

Universidad de Concepción
Dirección de Postgrado
Facultad de Ciencias Químicas
Programa Doctorado en Ciencias Geológicas

Geomorfología Tectónica del Frente Andino Occidental (FAO) entre los 35°S y 38°S en Chile.
Tectonic Geomorphology of the Western Andean Front (WAF) between 35°S and 38°S in Chile.

Tesis para optar al grado de Doctor en Ciencias Geológicas

Jorge Adrián Oviedo Reyes

Profesor guía: Dr. Joaquín Cortés
Profesor co-guía: Dr. Alfonso Fernández

Concepción-Chile
2024

"The mask of self-deception was no longer a mask for me, it was a part of me." "I have not a care of my own, but I am more restless than if I had." "For I knew that the King in Yellow had opened his tattered mantle and there was only God to cry to now."

Robert W. Chambers

The King in Yellow

"Santiago no es el final del Camino, si no el principio"

Paulo Coelho

Agradecimientos

Este documento expresa en sí mismo años de trabajo. Involucro aquí todo lo que he aprendido desde niño, joven y adulto. Soy una persona afortunada, conté con el apoyo de muchas personas en el transcurso de este proceso, su cariño hacia mí siempre será recompensando. Chile ha sido una gran experiencia, su paisaje es inolvidable, su territorio y sus gentes hacen que sea un país para vivir. Concepción, una ciudad que siempre me recordó mi Bogotá.

Doy gracias especiales al Profesor Joaquín Cortes quien me apoyo para iniciar este viaje académico. Igualmente extiendo mis agradecimientos al Profesor Co- Guía Alfonso Fernández por su disposición a entregar soluciones, amabilidad y respeto. Agradezco el apoyo del Estado de Chile por financiar a través de la Agencia Nacional de Investigación y Desarrollo - Chile (ANID - Doctorado Nacional/2019- 21191037) y el proyecto Fondecyt Iniciación 11180509 del Profesor Guía Dr. Joaquín Cortes Aranda.

Resumen

Caracterizar la actividad neotectónica a lo largo de los frentes montañosos en orógenos activos es clave para comprender mejor las trayectorias de la evolución del paisaje, los acoplamientos climático-tectónicos y los peligros naturales. Uno de esos prominentes frentes montañosos es el Frente Andino Occidental (FAO) que se despliega a lo largo del occidente de la Cordillera de los Andes. Su estudio representa retos importantes para comprender el potencial sismogénico de las fallas corticales (con tendencia NNE y NW) que en principio se creen que controlan el alzamiento de la Cordillera Principal, al menos entre los 35°S-38°S. Su geomorfología comprende una compleja interacción entre el clima, tectónica y procesos de superficie, dando como resultado un paisaje que acopla estas variables a distintos ritmos.

Los resultados comprendidos en este estudio buscan descifrar a qué ritmo las variables acopladas ocurren dentro de la evolución del Frente Andino Occidental y en qué sectores son más visibles que otros. Para hacer esto, se partió de lo regional a lo local; inicialmente, se exploraron las señales de tectónica reciente a escala regional usando análisis topográfico a través de técnicas morfométricas. Luego de individualizar las áreas de interés, se procedió a identificar las geoformas que permitirían evaluar el grado de tectónica activa en el rango del Pleistoceno Tardío al Holoceno. En la primera parte de este estudio, se utilizaron modelos digitales de elevación (DEM) de 30 m de resolución para el análisis morfométrico del Frente Andino Occidental considerando la unión piedemonte-montaña hasta la divisoria de aguas regional. Las métricas derivadas del estudio de la unión del frente montañoso con el piedemonte (Smf) (línea planimétrica), la forma de los valles (aspecto altimétrico) (Vf), el índice de longitud de corriente-gradiente (SL), perfiles swath y el área de relieve local normalizado, permitieron identificar una segmentación del Frente Andino Occidental a partir del paralelo 36°S. Hacia el norte, un frente montañoso inactivo con una respuesta fluvial impulsada principalmente por el clima. Mientras que hacia el sur es un área en un estado transitorio de deformación por tectónica activa. Se propone aquí que, adicionalmente a las fallas NNE (p. ej., Fallas de Cachapoal y Huépil), existen unas fallas de carácter transversal (dirección NW) al Frente Andino Occidental que modulan la deformación reciente.

Posteriormente, el análisis del paisaje mediante índices de tectónica activa relativa (Iat, RTA) en el Frente Andino Occidental reveló con notable claridad el nivel de actividad tectónica de las fallas transversales con rumbo noroeste (p. ej., falla del rio Laja, Longaví-Achibueno ó del Rio Ñuble). Se observó que los índices morfométricos Smf/Vf e Iat/RTA proporcionan valiosas perspectivas sobre la actividad tectónica, cada uno con sus fortalezas particulares. Mientras Smf/Vf es especialmente útil en frentes montañosos, Iat/RTA abarca áreas más extensas; en conjunto, constituyen métodos eficaces para detectar áreas potencialmente activas, guiando estudios de campo y futuras líneas de investigación. Adicionalmente, el estudio de las interacciones entre morfometría e influencia climática demostró la importancia crucial de considerar el impacto del clima para evitar sesgos en la identificación de la tectónica activa, especialmente en los segmentos analizados. Un ejemplo significativo es el índice de empinamiento del canal (K_{sn}), que evidencia una correlación entre valores elevados de relieve local y transiciones entre distintos dominios geomorfológicos

Del escalamiento regional a lo local, se documentó que el área comprendida en la confluencia de los ríos Ñuble y Perquilauquén presenta evidencia de deformación reciente, avalada por la cartografía morfotectonica (índices de deformación, terrazas, escarpes de falla) y las dataciones OSL (Luminiscencia Ópticamente Estimulada). Se concluye que la Falla de San Fabián (SFF) se describe como una falla activa que configura un frente montañoso interno. Su actividad está modulada por la falla del río Ñuble, de tendencia noroeste, cuya compleja interacción ha dado lugar a la formación de una cuenca tipo pull-apart. Adicionalmente se probó, que los escarpes lineales del frente montañosos paralelo a la falla San Fabián, pertenecientes a la falla Cachapoal corresponden a un escarpe de flexura que evidencia plegamiento tectónicamente activo. La Falla de Cachapoal exhibe una notable variabilidad en sus tasas de levantamiento a lo largo de su extensión norte-sur. En el sector de Catillo, la tasa es de 0.89$\pm$0.06 mm/año. Esta disminuye considerablemente en el área de Zemita, donde se registra 0.36$\pm$0.04 mm/año. Sin embargo, en el escarpe de Nahueltoro, la tasa aumenta dramáticamente a 1.71$\pm$0.22 mm/año, lo que sugiere una actividad tectónica más intensa en este sector. En cuanto a la Falla de San Fabián, aunque no se dispone de tasas de levantamiento directas, las tasas de incisión del río Ñuble proporcionan información valiosa sobre la actividad tectónica asumiendo un acomplamiento tectonico-fluvial. Por lo tanto, durante el Pleistoceno tardío, estas tasas alcanzaron hasta 5.07$\pm$0.37 mm/año, indicando un período de intensa actividad. En el Holoceno, sin embargo, se observa una disminución significativa a 1.86$\pm$0.14 mm/año.

Esta investigación desde un enfoque cuantitativo y geológico en la región del Frente Andino Occidental de Chile (35-38°S) tiene una relevancia significativa tanto en el ámbito científico como en la planificación y seguridad pública. Estos hallazgos no solo avanzan nuestra comprensión de la tectónica andina, sino que también tienen importantes implicaciones para la evaluación del peligro

sísmico y proporcionan un valioso marco de referencia para el estudio de la formación de montañas desde la perspectiva de los Andes chilenos.

Abstract

Characterizing neotectonic activity along mountain fronts in active orogens is key to better understanding landscape evolution trajectories, climatic-tectonic couplings, and natural hazards. One such prominent mountain front is the Western Andean Front (WAF) that extends along the western side of the Andes Cordillera. Its study presents significant challenges in understanding the seismogenic potential of crustal faults (with NNE and NW trends) that are believed to control the uplift of the Principal Cordillera, at least between 35°S-38°S. Its geomorphology comprises a complex interaction between climate, tectonics, and surface processes, resulting in a landscape that couples these variables at different rates.

The results included in this study seek to decipher at what rate the coupled variables occur within the evolution of the Western Andean Front and in which sectors they are more visible than others. To do this, we moved from regional to local scale; initially, recent tectonic signals were explored at a regional scale using topographic analysis through morphometric techniques, and finally, using the highlighted areas, the arrangement of landforms corresponding to active faulting was identified in detail, at least during the Late Pleistocene to Holocene.

In the first part of this study, 30 m resolution digital elevation models (DEM) were used for the morphometric analysis of the Western Andean Front, considering the piedmont-mountain junction to the regional watershed. The metrics derived from the study of the mountain front-piedmont junction (Smf) (planimetric line), valley shape (altimetric aspect) (Vf), stream length-gradient index (SL), swath profiles, and normalized local relief area allowed the identification of a segmentation of the Western Andean Front from the 36°S parallel. To the north, an inactive mountain front with a fluvial response driven mainly by climate. While to the south, it is an area in a transient state of deformation due to active tectonics. It is proposed here that, in addition to the NNE faults (e.g., Cachapoal and Huépil Faults), there are transverse faults (NW direction) to the Western Andean Front that modulate recent deformation.

Subsequently, the landscape analysis using relative active tectonic indices (Iat, RTA) in the Western Andean Front revealed with notable clarity the level of tectonic activity of the northwest-

trending transverse faults, such as the Laja River Fault. It was observed that the morphometric indices Smf/Vf and Iat/RTA provide valuable perspectives on tectonic activity, each with its particular strengths. While Smf/Vf is especially useful in mountain fronts, Iat/RTA covers more extensive areas; together, they constitute effective methods for detecting active deformation, guiding field studies and future lines of research. Additionally, the study of interactions between morphometry and climatic influence demonstrated the crucial importance of considering climatic impact to avoid biases in identifying active tectonics, especially in the analyzed segments. A significant example is the channel steepness index (K_{sn}), which shows a correlation between high local relief values and transitions between different geomorphological domains.

From regional to local scaling, it was documented that the area comprised in the confluence of the Ñuble and Perquilauquén rivers presents evidence of recent deformation, supported by morphotectonic mapping (deformation indices, terraces, fault scarps) and OSL (Optically Stimulated Luminescence) dating. It is concluded that the San Fabián Fault (SFF) is described as an active fault that configures an internal mountain front. Its activity is modulated by the northwest-trending Ñuble river fault, whose complex interaction has led to the formation of a pull-apart basin. Additionally, it was proven that the linear scarps of the mountain front parallel to the San Fabián fault, belonging to the Cachapoal fault, correspond to a flexural scarp that evidences tectonically active folding.

The Cachapoal Fault exhibits notable variability in its uplift rates along its north-south extension. In the Catillo sector, the rate is 0.89$\pm$0.06 mm/year. This decreases considerably in the Zemita area, where 0.36$\pm$0.04 mm/year is recorded. However, at the Nahueltoro scarp, the rate increases dramatically to 1.71$\pm$0.22 mm/year, suggesting more intense tectonic activity in this sector. Regarding the San Fabián Fault, although direct uplift rates are not available, the incision rates of the Ñuble River provide valuable information about tectonic activity assuming a tectonic-fluvial coupling. Therefore, during the late Pleistocene, these rates reached up to 5.07$\pm$0.37 mm/year, indicating a period of intense activity. In the Holocene, however, a significant decrease to 1.86$\pm$0.14 mm/year is observed.

This research from a quantitative and geological approach in the Western Andean Front region of Chile (35-38°S) has significant relevance both in the scientific field and in public planning and safety. These findings not only advance our understanding of Andean tectonics but also have important implications for seismic hazard assessment and provide a valuable framework for studying mountain building from the perspective of the Chilean Andes.

Tabla de contenidos

Agradecimientos i

Resumen ii

Abstract v

Capítulo 1 Introducción 2

1.1 Planteamiento del problema . . . 3
1.2 Hipótesis . . . 9
1.3 Objetivo General y Específicos . . . 9
1.3.1 Objetivo general . . . 9
1.3.2 Objetivos específicos . . . 9
1.4 Organización de la Tesis . . . 9
1.5 Metodología . . . 10

Capítulo 2 Geomorphic signatures of neotectonic activity along the Western Andean Front in the Chilean Andes (35°S to 37°S) 13

2.1 Introduction . . . 15
2.2 Regional Geologic and Climate Setting . . . 16
2.3 Methods . . . 19
2.3.1 Topography Analysis . . . 20
2.3.2 Rock strength (RS) and mean annual precipitation (MAP) . . . 20
2.3.3 Stream length-gradient index (SL) . . . 21
2.3.4 Morphometric indicators of relative active tectonics . . . 22
2.3.5 Normalized Relief Area (NRA) . . . 25
2.4 Results . . . 27
2.4.1 Geomorphological analysis from swath profiles . . . 27
2.4.2 Rock strength (RS), mean annual precipitation (MAP), and SL . . . 29
2.4.3 Morphometric indicators of relative active tectonics . . . 30

2.4.4 Topographic trends and Normalized Relief Area . . . 32
2.5 Discussion . . . 35
2.5.1 Topographic patterns linked to deformation . . . 35
2.6 Relative active tectonics from geomorphic indices . . . 36
2.6.1 Geomorphic signatures to Tectonic and/or Climate forcing . . . 40
2.6.2 Neotectonic structures for WAF between 35° S - 37° S . . . 42
2.7 Conclusions . . . 43
2.8 Authors Contributions . . . 43
2.9 Acknowledgements . . . 44

Capítulo 3 Deciphering Climate and Tectonic Signals on Landscapes through Morphometric Analysis: Insights from western slope of Principal Cordillera, 35°S to 38°S, Chile 45

3.1 Introduction . . . 46
3.2 Regional Setting . . . 48
3.3 Data and Methods . . . 52
3.3.1 Mountain front sinuosity (Smf) . . . 52
3.3.2 Valley floor width-to-height ratio (Vf) . . . 53
3.3.3 Asymmetry Factor (AF) . . . 53
3.3.4 Basin Elongation Ratio (Re) . . . 55
3.3.5 Hypsometry . . . 56
3.3.6 Topographic and river profile analysis . . . 57
3.3.7 Polynomial regression by machine learning . . . 59
3.3.8 Rock Strength (RS) – Mean Annual Precipitation (MAP) . . . 60
3.3.9 Relative tectonic activity index (Iat-RTA) . . . 60
3.4 Results . . . 61
3.4.1 Smf/Vf ratio . . . 61
3.4.2 Drainage-basin asymmetry factor (AF) . . . 63
3.4.3 Basin Elongation Ratio . . . 67
3.4.4 Hypsometric curve and integral - statistical moments . . . 68
3.4.5 Topography and channel-steepness index (K_{sn}) and normalized river profiles . . . 71
3.4.6 RS-MAP patterns . . . 80
3.4.7 Relative tectonic activity index patterns . . . 84
3.5 Discussion . . . 88

3.5.1 Spatial variation in tectonic activity . . . 88
3.5.2 Morphometric properties and their response to climate forcing . . . 90
3.5.3 Fault Segmentation and growth from morphometric properties . . . 92
3.6 Conclusions . . . 93

Capítulo 4 Morphometric analysis detects faulting styles imprinted on geomorphic features: Example from the Western Andean Front (35°S-38°S), central Chile 97
4.1 Introduction . . . 98
4.2 Methodology . . . 99
4.3 Results . . . 104
4.4 Discussion . . . 106
4.5 Conclusions . . . 111

Capítulo 5 Quantifying Late Quaternary Fluvial Incision Rates in the South-Central Andes (∼36°S): A Record of Uplift, Active Faulting, and Mountain Front Migration 113
5.1 Introduction . . . 115
5.2 Materials and Methods . . . 117
5.2.1 Morphotectonic mapping . . . 117
5.2.2 Structural Analysis . . . 117
5.2.3 Drainage Analysis . . . 117
5.2.4 OSL Sampling and Dating of Terraces . . . 118
5.3 Morphotectonic mapping and structural style . . . 119
5.4 Geomorphology of Ñuble and Perquilauquén rivers . . . 123
5.5 Fluvial response to low Quaternary active folding . . . 127
5.6 River incision and uplift rates . . . 128
5.7 Discussion . . . 130
5.8 Conclusions . . . 131

Capítulo 6 Discussion 146
6.1 Landscape Response to Tectonic and Climatic Forcing . . . 147
6.2 Spatial Variation in Tectonic Activity . . . 148
6.3 Methodological Contributions . . . 152
6.4 Uplift Rates and Deformation Patterns . . . 153

Capítulo 7 Conclusions **156**

Referencias **160**

Índice de figuras

1-1 Marco tectónico del margen chileno entre los 30°S y 42°S. Cordillera de la Costa (CC): 60-80 km de ancho con picos que alcanzan hasta 700 m. Valle Central (VC): 20-60 km de ancho con una altitud promedio de alrededor de 200 m, llena de sedimentos cuaternarios. Cordillera Principal (**PC)**: 50-100 km de ancho con picos que alcanzan hasta 3,953 m sobre el nivel del mar. **FSR**: Falla de San Ramón; **FCAO**: Falla de Cabalgamiento Andino Occidental; **SFAC**: Sistema de Fallas de Antiñir-Copahue; **DBB**: depresión del Bío Bío; **DL**: depresión de Loncopué; **CN**: Cordillera de Nahuelbuta; **FLn**: Falla de Lanalhue; **SFLO**: Sistema de Fallas de Liquiñe Ofqui; **FPCA**: Falla Plegada y Corrida de Agrio; **FPCM**: Falla Plegada y Corrida de Malargüe; Dorsal de Huincul; **ZFBB**: Zona de Falla del Bío Bío; **LnC**: Lineamiento de Cortaderas. 5

1-2 Dos modelos conceptuales en conflicto de los Andes a 33.5°S de latitud (Tomado de Riesner et al., 2018). (a) Modelo de vergencia hacia el este propuesto por Giambiagi et al. (2014). (b) Modelo de orógeno de doble vergencia con una vergencia primaria dominante hacia el oeste propuesto por Armijo et al. (2010). CC = Cordillera Costera; CD = Depresión Central; FTB Andino Occidental = cinturón de pliegues y cabalgamientos andino occidental; FC = Cordillera Frontal; FTB Aconcagua = cinturón de pliegues y cabalgamientos de Aconcagua; WAT = Cabalgamiento Andino Occidental. 6

2-1 Tectonic and structural features of the study area (dashed box) in the Central Andes of Chile (35°-37°S). Notable features in this region include the Coastal Cordillera (CC), a 60-80 km wide range with peaks up to 700 m; the flat Central Valley (VC), 20-60 km wide with an average altitude of 200 m, filled with Quaternary sediments; and the Principal Cordillera (PC), a 50-100 km wide range with peaks reaching up to 3953 m.a.s.l. The mountain-piedmont junction in the study area extends NNE parallel to Principal Cordillera and in agreement with inferred the Western Andean Thrust (WAT), like a southward extension of the San Ramon Fault (SRF). To the east the study area extends to regional watershed boundaries (red line) crossing the western flank of Principal Cordillera. The Central Valley in particular is strangled to the north by the relief, unlike to the south where it reaches its maximum width. Main volcanoes are highlighted (red triangles). SRF: San Ramon Fault; WAT: West Andean Thrust; **ACFZ**: Antiñir-Copahue Fault System; **BBT**: Bío Bío Trough; **LT**: Loncopué Trough; **ND**: Nahuelbuta Range; **LnF**: – Lanalhue Fault; **LOFZ**: Liquiñe Ofqui Fault System; **AFTB**: Agrio Fold Thrust Belt; **MFTB**: Malargüe Fold Thrust Belt; Huincul Ridge; **BBFZ**: Bío Bío Fault Zone; **CLn**: Cortaderas Lineament. . . . 17

2-2 Geologic map of the study area between 35°S and 37°S superimposed over hillshade from ALOS AW3D30 30 m,($https//www.eorc.jaxa.jp/ALOS/en/aw3d30/index.htm$), seismic events (gray-scale circles) are from IRIS data set (*epicentral data), faults are from SERNAGEOMIN, 2003; Melnick, Charlet, et al., 2006; Folguera et al., 2004; Cembrano and Lara, 2009; Maldonado et al., 2021. WAT: west Andean thrust;CaF: Cachapoal fault; LoLn: Longaví-Achibueno lineament; MeF: Mesamávida fault; Laln: Lajas lineament; HuF: Huépil fault. (*) All seismic data were downloaded through the IRIS earthquake browser system ($https://ds.iris.edu/ieb/$). 18

2-3 The location of the transverse swath profiles for the Western Andean front is shown (right figure). Each across swath profile (left figure) has a black line representing the mean elevation, grey areas marking the maximum and minimum elevation, and magenta lines displaying the local relief. Inclined surfaces Ts (summit surfaces) were identified along each profile (a to e). The landforms related to volcanic systems (Vn) and fault scarps (S) are identified. The regional drainage divide is indicated by the number one (1), and local drainage divides with the number two (2) for all profiles. Several interpreted NNE and NW-striking structures (magenta lines, right figure) were labelled with their vergence across profiles from our structural interpretations. The width of the active structures is delineated below each profile (grey bar). Note the internal mountain front (IMF, white line) and range bounding fault (with younger fault scarps) are depicted in the west of swath profiles (solid white line, c and d). Faults are from SERNAGEOMIN, 2003; Folguera et al., 2004; Cembrano and Lara, 2009; Maldonado et al., 2021. **WAT**: West Andean thrust;**CaF**: Cachapoal fault; **LoLn**: Longaví-Achibueno lineament;**MeF**: Mesamávida fault; **ÑrLn**: Ñuble lineament; **LaIn**: Lajas lineament; **HuF**: Huépil fault from Melnick, Charlet, et al., 2006 and Melnick and Echtler, 2006 27

2-4 Relationships between rock strength, mean annual precipitation and SL gradient channel index values for the Western Andean Front. (a) The rock strength map with five levels. A straight-line segment was used to connect the headwaters node to the outlet node to determine the main orientation of trunk channels. A rose diagram with the principal trend of the main channels is shown; (b) Mean annual precipitation – MAP distribution (after Bookhagen and Strecker (2008)). The names of the main rivers in the study area and the watersheds obtained from the MAP overlay are provided; (c) Simple Kriging predictive map of the distribution of SL values obtained with the SLiX tool (Piacentini et al., 2020) for the main channels of the study area; (d) Lithological – precipitation map obtained from weighted sum between rock strength and precipitation pixels values (pixel resolution 5 km approximately) with overlay extracted SL anomalies. The Vf position of topographic cross-sections of the valleys (green dots). The areas where SL anomalies are found were compared with the lithological - precipitation map to infer their possible tectonic (red polygons) or lithological controls (yellow polygons). The Maule (M) and Lontué (L) river basins are highlighted as areas with a significant presence of anomalies. The main lakes in the western side area are Maule (north) and Laja (south). **DGQZ Vn**: Descabezado Grande and Quizapú Volcanoes. **TSP Vn**: Tatara San Pedro Complex. **LON Vn**: Nevado de Longaví Volcano. **NC Vn**: Nevados de Chillán Volcanic Complex. **AN Vn**: Antuco Volcano. 28

2-5 (a) Polynomial regression predicted by machine learning for the Smf data vs distance: training data 70%, test data 30% and a curve with order 8. Note that the generalized (EG) and training error (ET) are close to 1 and very close to each other. The classes are differentiated by ranges proposed in this study; the number of mountain front is highlighted (Table 2.1). (b) Power-law distribution for Smf data in the WAF. The parameters of PDF are: $\alpha = 3.211$; Xmin $= 1.18$. The goodness of fit was assessed using the likelihood ratio between power-law's family distributions. (c) Cumulative distribution function is shown. (d) Polynomial regression predicted by machine learning for the Vf data vs distance: training data 60%, test data 40% and a curve with order 5. (e) Stretched exponential distribution (right) for Vf data in the WAF. The parameters of PDF are $\beta = 0.726$; $\lambda = 1.6206$; Xmin $= 0.06$. The goodness of fit was assessed using the likelihood ratio between power-law's family distributions. (f) Cumulative distribution function is shown. (g) Linear regression of valley-floor width (Vfw) and drainage-basin size in WAF. Watersheds of equivalent sizes exhibit a spectrum of both high low Vfw values. A total of 122 data for 97 basins were calculated. The starting point zero in the plot is located in the outlet of the basin 97. **LaIn**: Lajas lineament; **HuF**: Huépil fault; **CaF**: Cachapoal fault; **LoLn**: Longaví-Achibueno lineament; **MeF**: Mesamávida fault; **WAT**: West Andean Thrust. 31

2-6 (a) Tectonic activity classes of mountain fronts in the Western Andean front between 35° and 37° S. PC: Main cordillera, VC: Central Valley, CC: coastal cordillera. The values used to define the classes are shown in Table 1. Catillo (Qtc) and Huépil (Qth) terraces are labelled. (b) Boxplot with Smf and Vf values combined in order to classify the relative tectonic classes in the Western Andean Front. The data are sorted from lowest to highest with reference to the Smf. The outliers in the plot are depicted by rhombus (around class 3). (c) Scatter plot depicts Smf/Vf data distribution, considering the mean value of Vf. Logarithmic regressions of Smf/Vf data distinguish two observed trends (a and b) in the dataset (magenta and blue lines, respectively). The grey zones are the uncertainty (2γ) displayed for the regional groups identified in the WAF between 35° and 37° S. Values > 4 in both metrics were excluded from this plot. The relative tectonic activity classes inferred in the boxplot are depicted in red rectangles. 33

2-7 Location of swath profiles along-strike mountain-piedmont junction in the Western Andean Front (left). The swath profiles (right) are numbered from north to south (SP1 to SP6) and include the segments used to calculate the Smf index (see Figure 2-6). Also, the points of the Vf index calculation are shown (green and white points). The alternating bands below the local relief curves in each profile (yellow and green bands) indicate the specific area for each Smf segment. We selected a swath width of 5 km and a step-size of 40 m to make the areas under the curve comparable between segments. Additionally, each segment is highlighted according to its tectonic class (see Figure 2-6). The transverse hypsometric integral (THi) is shown in the lower part for each swath profile, areas exceeding THi values $>$ 0.5 are highlighted (pink colour). Note how segments with active tectonic class 1 have V-shaped valleys (Vf $>$ 0.5) and THi $>$ 0.5. A. Descabezado Grande and Quizapu volcanoes. B. Nevado de Longaví volcano. C. Nevados de Chillán volcanic complex. D. Antuco Volcano. . 35

2-8 Vf vs. Normalized relief area plot. Every segment is coloured by tectonic activity classes from class 1 to class 3 (black, grey and white circles). 1A uplift » incision – leading to a transient state. 1B. Tectonic-fluvial coupling – leading to a highly dissected landscape, high elevations maintains under high river incision processes. 2A lateral erosion by river processes – leads to a broader valley floor. Segments 5, 6, and 7 are inactive mountain fronts with high incision (magenta arrow). 37

2-9 Neotectonic structural Setting interpreted in the Western Andean front. Several structural elements such as faults and folds are taken from official geological maps (SERNAGEOMIN, 2003). The structural elements related to the Huépil fault, and those associated with the vicinity of the Antuco volcano (normal faults) are taken from Melnick, Charlet, et al. (2006) and Melnick, Rosenau, et al. (2006). The ACFZ trace information in the Eastern flank of Cordillera Principal is taken from Folguera et al. (2004). **HuF**: Huépil fault, **ACFZ**: Antiñir- Copahue fault system, **CaF**: Cachapoal fault, **MeF**: Mesamávida fault, **LaF**: Laja River fault, **NrF**: Ñuble river fault, **LoF**: Longaví-Achibueno fault, **WAT**: west Andean thrust, **CLn**: Cortaderas lineament, **U**: uplifted side, **D**: Down-dropped side. 38

3-1 Tectonic and structural features of the study area (blue box) in the Central and Southern Andes of Chile (35°-38°S) (Modified from Oviedo-Reyes et al. (2024)). Notable features in this region include the Coastal Cordillera (CC), Central Valley (VC), and the Principal Cordillera (PC). The mountain-piedmont junction in the study area extends NNE parallel to Principal Cordillera and in agreement with the Huépil and Cachapoal faults with the Western Andean Thrust (WAT). Main volcanoes are highlighted (orange triangles). **HuF**: Huépil fault; **CaF**: Cachapoal fault; **WAT**: West Andean Thrust; **SRF**: San Ramon fault; **ACFZ**: Antiñir-Copahue fault System; **BBT**: Bío Bío Trough; **LT**: Loncopué Trough; **ND**: Nahuelbuta Range; **LnF**: – Lanalhue fault; **LOFZ**: Liquiñe Ofqui Fault System; **AFTB**: Agrio Fold Thrust Belt; **MFTB**: Malargüe Fold Thrust Belt; Huincul Ridge; **BBFZ**: Bío Bío fault zone; **CLn**: Cortaderas Lineament. 49

3-2 Geologic map of the study area between 35°S and 38°S superimposed over hillshade from ALOS AW3D30 30m (modified from Oviedo-Reyes et al. (2024)) Geological map from Sernageomin (2003). Main volcanoes are highlighted (red triangles). **ACFZ**: Antiñir- Copahue fault system; **WAT**: West Andean Thrust; **CaF**: Cachapoal fault; **LoF**: Longaví-Achibueno Fault; **MeF**: Mesamávida Fault; **ÑrF**: Ñuble River fault; **LaF**: Laja River fault; HuF: Huépil fault.; **LLFS**: Lago Laja fault system. **PC**: Principal Cordillera, **VC**: Central Valley, **CC**: Coastal Cordillera. In the figure, the grid is based on the WGS 1984 UTM Zone 19S reference system, while the DEM is projected with a scale in meters. 50

3-3 Diagrams of the morphometric indices applied in the WSPC. Each index is graphically represented considering the parameters for computing them. The uplift rate inferred from the individual analysis of each metric is indicated. 54

3-4 Spatial distribution of the basins with Vf positions and trunk channels along the study area between 35° and 37° S (from Oviedo-Reyes et al. (2024)). Coastal Cordillera (CC), Central Valley (VC), and the Principal Cordillera (PC) are depicted. Basin 11: Lontué River; Basin 25: Maule River; Basin 36: Achibueno River; Basin 61: Ñuble River ; Basin 86: Laja River. Drainage basins from 30 to 41 belong Longavi-achibueno river system. 62

3-5 Smf and Vf indexes along the Western Andean Front by Oviedo-Reyes et al. (2024). Notice how while there is an increase in Smf values to the north, the Vf values decrease. Smf range data from 1.06 to 13.06. Vf range data from 0.06 to 8.36 (see Figure 3-4 to Vf positions). 63

3-6 Asymmetry Factor and Basin Elongation Ratio (Re) Indices for the Western Andean Front. Note the similarities between the AF and Re curves calculated from the polynomial regression, with curves of order 5 and 6, respectively. A. The AF data range from 0 to 35. Peaks within the original curve do not reveal a clear trend; however, a slight increase towards the north (MeF and WAT) is noted. B. The Re data range from 0.45 to 0.87, with a slight increase similar to the AF index. Both curves indicate a slight correlation between basin shape and tilting: the higher the elongation, the more tilted the basins are. 64

3-7 Asymmetry factor distribution along the drainage basin in the study area. In dark grey the basins taken on the right are shown below, while the areas on the left are in light grey (see Figure 3-4 to drainage basins position). The size of the arrows does not indicate greater tilting, their size varies to make interpretation easier. 65

3-8 Hypsometric Curve and graphical representation of Sk and Kur Statistical Moments (lower part). The IH index data range from 0.24 to 0.56. A set of low IH values is observed towards the CaF, LoF, and MeF sectors, contrasting with high IH values towards both the southern end of the study area and the north. 68

3-9 Statistical moments and its variations along north-south in the study area. Skewness (Sk) (range of data: -0.382 to 1.078), Kurtosis (Kur) (range of data: 1.943 to 3.72), Density Skewness (Dsk) (range of data: -0.414 to 1.078) and Density Kurtosis (range of data: 1.351 to 3.089) (Dkur) Statistical Moments varying in similar trends over south, central and north sections subdivided here the WSPC. The mean values for each statistical moment are displayed in A, B, C and D plots. 70

3-10 Hypsometric curves ranked using their morphological changes along the curve. To classify curve shapes, reference points (A, B, B', C, C') were used. Convex curves rise above the midpoint of AB' and stay above B'C'. Convex mouth curves sit below the midpoint of AB' but remain above BC', staying convex above point C'. S-shaped curves generally lie below AC' and cross over C'C. Concave curves remain below BC. 71

3-11 Hypsometric curves ranked using their fault location. Note how the Huepil fault sector, the Laja river and WAT present curves from convex to convex to the mouth. In contrast, MeF, LoF, CaF sectors show wider ranges of curves from highly eroded basins (concave) to weakly eroded basins (convex). 72

3-12 Hypsometric curves mapped according to the classification proposed in this study. The hypsometric curves, classified according to the proposed method in this study, highlight that most concave basins are located in the fault sectors of MeF, LoF, and the northern part of CaF. In contrast, other sectors display moderately eroded zones. The presence of convex curves near the mouth suggests a landscape response to tectonic uplift (landscape rejuvenation). 73

3-13 Regional topographic metrics in the Western Slope of the Principal Cordillera. A. Slope-Angle Variability. High degree of slope angle variability, predominantly shown in red and orange shades. B. Local Relief. The Maule rivers (M) and Lontué (L) are depicted in both figures to reference. PC: Principal Cordillera, VC: Central Valley, CC: Coastal Cordillera. 74

3-14 K_{sn} variations and outlet elevation of each drainage basin in the study area. A. K_{sn} steepness index show a range of data from 21.612 to 173.222$m^{0.9}$. B. Note how a decrease in the elevation of the drainage basin outlet is observed in the central part of the WAF, with a slight peak over some basins associated with the LoF trace. . . 75

3-15 K_{sn} map and knickpoints observed in two different sectors in the study area. **A**. Map of K_{sn} patterns on structural map proposed by Oviedo-Reyes et al. (2024) and overlay on DEM- 30m. **B**. The map shows the distribution of K_{sn} and knickpoint values superimposed on the local relief map, with contour lines at 500 meters (gray curves) and 800 meters (black curves). This sector, located along the San Fabian Fault (SFF), is recognized as the internal mountain front parallel to the Cachapoal Fault. Knickpoints are projected where K_{sn} values transition from low to high downstream along the rivers. **C**. The map shows the distribution of K_{sn} and knickpoint values superimposed on the local relief map, with contour lines at 500 meters (gray curves) and 800 meters (black curves). Sector of the Maule River over its trunk channel, where the distribution of the knickpoints can be observed at approximately the same elevation. One of the areas where there is evidence of glacial dominance is highlighted. **D**. Topographic profile approximately along the course of the Maule River (trunk channel) locating the elevations of the knickpoints. The trend of the points is statistically analyzed with Loess (magenta curve). 76

3-16 Cf% and C_{max} indexes calculated from Normalized River Profiles in the study area. A. C_{max} pattern distribution with polynomial regression curve. The maximum distance between the river profile and the imaginary line between upper and lower reach increase toward the central sector of the study area. B. Concavity factor (%) that represents the area between the curves of the normalized river profile and the line that connects the upper reach and lower reach. 77

3-17 Scatter plot of C_{max} and dL of normalized stream profiles for drainage basins of the. Cf% and C_{max} indexes calculated from Normalized profiles from rivers in the WSPC. CS: Convex Shape, CM: Convex Mouth, TS: Transient State, PG: Poorly Graded Profile, GR: Well Graded Profile. 78

3-18 Convex to straight profiles in the Western Slope of the Principal Cordillera. Each profile include the position of C_{max}, dL and Cf% (yellow area) and sorted according to the trend in Figure 3-17. 79

3-19 Normalized river profiles with convex mouth shape along Western Slope of the Principal Cordillera. Each profile include the position of C_{max}, dL and Cf% (yellow area) and sorted according to the trend in Figure 3-17. 80

3-20 Normalized river profiles with poorly graded shape. Each profile include the position of C_{max}, dL and Cf% (yellow area) and sorted according to the trend in Figure 3-17. 81

3-21 Normalized river profiles with transient state signal. Each profile include the position of C_{max}, dL and Cf% (yellow area) and sorted according to the trend in Figure 3-17. 82

3-22 Normalized river profiles with graded profile shape. Each profile include the position of C_{max}, dL and Cf% (yellow area) and sorted according concavity factor (Cf%). . . 83

3-23 Normalized river profiles with graded profile shape. Each profile include the position of C_{max}, dL and Cf% (yellow area) and sorted according concavity factor (Cf%). . . 84

3-24 Normalized river profiles with graded profile shape. Each profile include the position of C_{max}, dL and Cf% (yellow area) and sorted according concavity factor (Cf%). . . 85

3-25 Relationships between rock strength (RS) and mean annual precipitation (MAP) along the Western Slope of the Principal Cordillera (WSPC) (modified from Oviedo-Reyes et al. (2024). A. Rock strength levels. B. RS+MAP raster obtained from weighted sum between RS and MAP pixels values (∼5km). C. MAP- mean annual precipitation in a 0.05° latitude-longitude grid (approximately 5 km) spanning 1979 to 2019. 86

3-26 Relative active tectonics index for the Western Slope of the Principal Cordillera. A. Iat – defined by El Hamdouni et al. (2008) B. RTA index defined by Matoš et al. (2016). Note the internal mountain front (IMF, white line) and range bounding fault (with younger fault scarps) are depicted in the west of swath profiles (solid white line, c and d). Faults are from SERNAGEOMIN (2003), Melnick and Echtler (2006), Melnick, Charlet, et al. (2006), Folguera et al. (2004), Cembrano and Lara (2009), and Maldonado et al. (2021). **ACFZ**: Antiñir- Copahue fault system; **WAT**: West Andean Thrust; **CaF**: Cachapoal fault; **LoF**: Longaví-Achibueno Fault; **MeF**: Mesamávida Fault; **ÑrF**: Ñuble River fault; **LaF**: Laja River fault; **HuF**: Huépil fault.; **LLFS**: Lago Laja fault system **PC**: Principal Cordillera, **VC**: Central Valley, **CC**: Coastal Cordillera. 87

3-27 Panoramic view looking northeast over the La Mina sector, illustrating the transition between geomorphic domains. The knickpoints, marked by white dots, are situated at 2200 masl, defining the boundary between these domains. At the bottom of the image, the Maule River flows 1200 meters below the knickpoints. (Image modified from Google Earth). 91

3-28 Variations in morphometric indices along the Huépil Fault trace. Fault terminations are highlighted (yellow box). Related basins are named e.g. B79 (see Figure 3-4). . 94

3-29 Variations in morphometric indices along the San Fabian Fault trace. Fault terminations are highlighted (yellow box). Related basins are named e.g. B79 (see Figure 3-4). 95

3-30 Variations in morphometric indices along the Mesamávida Fault trace. Fault terminations are highlighted (yellow box). Related basins are named e.g. B79 (see Figure 3-4). 96

4-1 Tectonic and structural features for Western Andean Front in Chilean Andes (32-40°S). A. Three main morphotectonics features are displayed: Coastal Cordillera (CC), a 60-80 km wide range with peaks up to 700 m, Central Valley (VC), 20-60 km wide with an average altitude of ∼200 m, filled with Quaternary sediments, and the Principal Cordillera (PC), a 50-100 km wide range with peaks reaching up to ∼3953 m.a.s.l. Main volcanoes are highlighted (red triangles). **SRF**: San Ramon Fault; **WAT**: West Andean Thrust; **ACFZ**: Antiñir-Copahue Fault System; **BBT**: Bío Bío Trough; **LT**: Loncopué Trough; **ND**: Nahuelbuta Range; **LnF**: – Lanalhue Fault; **LOFZ**: Liquiñe Ofqui Fault System; **AFTB**: Agrio Fold Thrust Belt; **MFTB**: Malargüe Fold Thrust Belt; Huincul Ridge; **BBFZ**: Bío Bío Fault Zone; **CLn**: Cortaderas B. Tectonic activity classes for WAF (35-37°S) and location of Vf index measurements (Modified from Oviedo-Reyes et al. (2024)). The mountain-piedmont junction in the study area extends NNE parallel to Principal Cordillera and in agreement with inferred the Western Andean Thrust (WAT). 100

4-2 Plot of Smf vs. Vf for Western Andean Front in Chile and several authors in different tectonic settings following the procedures from Silva et al. (2003). A total amount of 230 mountain front data have been used for this plot. A. Faulting styles proposed by Silva et al. (2003) from morphometric properties extracted from mountains fronts in different structural domains. Regression lines and equations for different styles of faulting in regional groups are displayed (lower left) B. Data from normal faulted fronts (lines 1a, 3a), the arrow indicates the predominance of the data. The blue line 1(b) highlights the trend of mountain fronts associated with strike-slip faulting. Here used as reference to discriminate the different structural domains. C. Strike-slip faulted fronts data (lines 1b, 3b). D. Reverse faulted fronts data (lines 2a and 2b). E. Western Andean Front morphometric data and tectonic activity classes (green box) (Oviedo-Reyes et al., 2024). The gray zones are the uncertainty (2σ) displayed for the regional groups identified in the WAF between 35° and 38° S and corresponding equations (magenta). Vf values > 4 and Smf > 5 were excluded from this plot. 105

4-3 Structural Setting and active tectonics interpreted in this study from Smf/Vf ratio (modified from Oviedo-Reyes et al. (2024)). The uplifted areas with higher tectonic activity are highlighted (orange) (See Table 1). **HuF**: Huépil Fault, **ACFZ**: Antiñir-Copahue Fault System, **CaF**: Catillo Fault, **MeF**: Mesamávida Fault, **LaLn**: Laja River Fault, **LnNr**: Ñuble River Fault, **LoLn**: Longaví-Achibueno Fault, **WAT**: West Andean Thrust, **CLn**: Cortaderas Lineament, **U**: Uplifted side, D: Down-Dropped side. 107

4-4 Curves of the first-derivatives applied to the two clusters identified in the WAF. A. First-derivative from the equation Vf = 1.76Ln(Smf) + 0.346 related to NNE-striking fronts (blue line). B. First-derivative from the equation Vf = 1.106Ln(Smf) + 0.0078 related to Nw-striking fronts (red line) C. First-derivative which represents a theoretical equation Vf = 0.1Ln(Smf) + 0.1 (green line). Note the distance at the starting point of the curves (D1), and the smaller range at the end of the curves (D2). 110

5-1 Mapped faults and horizontal shortening strain axes calculated in the Western Andean Front (WAF). Internal Mountain Front and Range Bounding Fault are depicted in the main traces. 116

5-2 Morphotectonic map of the study area. Detailed zoom zones (a and b) are depicted. From bedrock to most recent deposits are displayed in the legend (right side). The symbology include (bottom) tracks all morphotectonic elements and useful information. 120

5-3 Detailed morphotectonic map zooms **a**. Northern sector Cachapoal fault (CAF). **b**. Southern east sector of the San Fabián fault (SFF). Time are depicted with age of deposits (OSL) in terraces. 121

5-4 Structural and geomorphological sketch of the Internal Mountain Front (IMF) and Regional Basal Front (RBF) in the south-central Andes. For location references, see Figure 5-2. The Catillo sector (upper figure) exhibits Quaternary folding that has produced a flexural scarp, uplifting this area since at least the Late Pleistocene. In the southern Nahueltoro sector (lower figure), a similar pattern is observed, influenced by a strike-slip tectonic regime from NW-striking structures. Geomorphological features related to deformation are highlighted, considering their positions within the IMF and RBF (yellow and pink boxes). 123

5-5 Longitudinal profiles of mapped river terraces along Perquilauquén and Ñuble rivers. We followed the procedures of Angster et al. (2020) to obtain terraces profiles. We used 100 m of distance between point elevation extraction. The elevated terraces in the IMF front can distinguished in both river system. Note the difference in elevations between Ñuble and Perquilauquén rivers. **a**. Perquilauquén River in the northern area, T1 to T6 terraces are depicted. **b**. Ñuble River terraces from T1 to T7. 124

5-6 Drainage system in the study area. a. Distribution of stream course related to Perquilauquén and Ñuble rivers. Dendrithic, Parallel-subparallel and rectangular drainages can be distinguished. b. "Straightened" method or rectification of the drainage systems using nodes and sense the darainage. The orders come from the rectification procedure, and are grouped by colour. 125

5-7 Comparison between order classification from "Straightened" method of the drainage system (a to e), lineaments and joints in the study area. 126

5-8 Extracted drainage orientations setting by sectors of Quaternary deposits from south to north (a to d). Mean trend vector is depicted for each rose diagram. 127

5-9 Comparison between Zemita drainage network (left) and joints from field data in Abanico Formation (right). 127

S1 Slope and TRI maps for the study area. a. Distribution of slope in the study area. The highest elevations are located to southeast section. b. TRI permits to mapping structural features adequately. Perquilauquén and Ñuble Rivers are depicted in blue. 135

S2 Drone image of the San Fabián fault (SFF) and its morphotectonic deformation indices. View towards the east. Triangular (TF) and trapezoidal facets can be distinguished along the fault trace. An isolated relief is described as a pressure ridge, with a low relief (PR). From left to right, a transition in lithology is observed from Abanico Formation units (andesites) to granitoids, which form the highest elevations. 136

S3 Drone image of the terrace and alluvial gravel deposits of the Ñuble River near San Fabián de Alico. Two positions of the T4 terrace are observed. Meander formation only occurs in this segment, while along this sector, the Ñuble River has a straight course. T6 and T7 terraces are also highlighted. OSL dating of T6 reveals a similar age to T4A. 137

S4 Distribution of particle size of terraces and other deposits in the study area. Triangular diagrams based on Sneed and Folk (1958) from C: Compact, P:Platy, and E:Elongated.Using TRI-PLOT excel spreadsheet from Graham and Midgley (2000). Note the majority of clast range from compact bladed, elongated and platy shapes. . 138

S5 Zingg (1935) particle shape classification using the ratios of the three main axes of a clast a,b and c. Particle shape from disk shape to spherical. 139
S6 Minor structures on fault planes of the Loma Linda fault (a, b, c) and San Fabian fault (d, e, f). Riedel (R), antithetic Riedel (R'), and lunate fractures (la) are observed across the fault planes. Slip direction is determined using criteria established by Petit (1987). Arrows indicate sense of movement of missing block. 140
S7 Projection of terrace elevation in the Perquilauquen River. 144
S8 Projection of terrace elevation in the Ñuble River. 145

Índice de tablas

2.1 Range of data used to define the relative active tectonic classes for the Western Andean Front between 35° and 36° S. The length of each segment is the same parameter Lmf used to calculate the sinuosity of the mountain front. For each segment the different metrics calculated to evaluate the active tectonics, the mean and standard deviation per section are differentiated, some segments do not show Vf values because no major drainage is developed on the studied segment; therefore, no value appears on the Smf/Vf plots (*). ND = No Data. 24

2.1 Continued. 25

2.2 Segments used to calculate the normalized relief area using local relief curve in swath profiles in the WAF. The length of each segment is ∼Lmf parameter in the Smf calculation. The normalized area is calculated using the length of each segment from Smf. We associated the values of normalized relief area with its tectonic class and Vf values to compare the incision and/or uplifting. 36

3.1 Basins and related morphometric parameters for the Western Slope of the Principal Cordillera. For the study 97 basins were calculated the following indices: Mountain Front Sinuosity (Smf), Valley Floor Width-to-Height Ratio (Vf), Asymmetry Factor (AF), Basin Elongation Ratio (Re), Hypsometry and Statistical Moments, K_{sn}, Concavity (C_{max}), Concavity Factor (Cf%), and Distance from Source (Δ L) from normalized river profiles. Additionally, the table includes the outlet elevation of basins, area, and Tectonic Relative Index (Iat). 66

3.1 Continued. 67

4.1 Range of data used to calculate logarithmic regression lines for the Western Andean Front between 35° and 36° S (modified from Oviedo-Reyes et al. (2024)). Some segments do not show Vf values because no major drainage is developed on the studied segment; therefore, no value appears on the Smf/Vf plots (*). ND = No Data. 102

4.1 Continued. 103

4.2 Results for KS-test for Smf/Vf values in the WAF and published work worldwide. For the data we used a significance level $\alpha = 0.05$. H0 = Null Hypothesis, H1 = Alternative Hypothesis.* Data grouped by structural domain. 109

5.1 Ages and erosion rates derived from the Perquilauquén and Ñuble river terraces. . . 129

5.2 Age constraints to CAF linear scarps. 129

S1 Equivalent dose (De), annual dose rate (Da) and calculated OSL ages for each sample. Ages have been calculated for Quartz grains with size ranging between 180-250 µm. 133

S2 Results of the solution of the stress tensors obtained from the analysis of striated planes 141

S3 Database of brittle deformation in the Internal Mountain Front 142

S4 List of sand samples collected for OSL. The amount of Qz per sample is indicated. . 143

6.1 Comparison between structural domains along Western Andean Thrust. 154

Capítulo 1

Introducción

Introducción

1.1 Planteamiento del problema

La Cordillera de los Andes, extendiéndose por más de 7.000 km a lo largo del margen occidental de América del Sur, se erige como la cadena montañosa continental más larga de la Tierra. Este impresionante cinturón orogénico es el resultado de la convergencia durante 200 Ma (p. ej., Gansser, 1973; Isacks, 1988) entre las placas de Nazca y Sudamericana, una interacción tectónica que ha moldeado profundamente el paisaje y la geología de la región. La subducción de la placa oceánica de Nazca bajo la placa continental Sudamericana ha llevado a una intensa deformación, magmatismo y levantamiento, dando lugar a la diversa topografía y las complejas características estructurales observadas a lo largo del margen andino.

A lo largo del margen chileno, esta colisión ocurre a una velocidad de 66 mm por año (Angermann et al., 1999) con una orientación de convergencia de N78°E (p. ej., Cisternas et al., 2005; Moreno et al., 2012). Una de las más notables expresiones de esta interacción entre placas es la presencia de zonas volcánicas (norte y sur de Chile) y su ausencia (segmento de placa plana Pampeana) de acuerdo con el ángulo en el que subduce la Placa de Nazca. De norte a sur: hasta los 27°S, una losa inclinada de 30° hacia el este; entre los 27.5-33°S con una losa sub-horizontal, entre los 33-36°S de nuevo un ángulo promedio de 30° hacia el este y finalmente entre los 36- 46°30'S una losa inclinada entre los 30-40° (López et al., 1997). Se ha establecido una relación causal ampliamente reconocida entre el desarrollo del segmento de placa plana Pampeana y la dorsal de Juan Fernández que se extiende en dirección oeste-este (Yáñez et al., 2002).

La importancia de esta segmentación del margen andino radica, como ya se mencionó, en la ocurrencia de volcanismo y el carácter neotectónico de cada región. Al norte, la neotectónica se caracteriza principalmente en fallas corticales orientadas paralelamente a la fosa (p. ej., Zona de Falla de Atacama), donde se destacan la falla del Salar del Carmen, la falla de Mejillones y de Caleta Herradura (e.g., González et al., 2003; Cortés et al., 2012). En el segmento de placa plana Pampeana, fallas activas con importantes tasas de acortamiento han sido identificadas en la Precordillera y las Sierras Pampeanas (Costa, 1992), con deformación Cuaternaria evidenciada en superficie principalmente entre los 30-33°S (Costa et al., 2001, 2006). Este Frente Andino Oriental recientemente ha sido evaluado usando índices geomorfológicos con el fin de reconocer la distribución a largo plazo de sus tasas relativas de deformación (Rimando and Schoenbohm, 2020).

Sobre la misma latitud en el Antearco, se ha establecido deformación Cuaternaria a los 33°S (Cerca a la ciudad de Santiago – Chile) controlada por la Falla San Ramón (Figure 1-1), específicamente donde los sedimentos cuaternarios y más antiguos de la Depresión Central son cabalgados por las rocas deformadas de la Cordillera Principal (Formación Abanico; Eoceno-Mioceno) (Armijo et al., 2010; Vargas et al., 2014). Hacia el norte (32,5°S), se considera como extensión de la Falla San Ramon, el sistema estructural de Pocuro donde la falla Cariño Botado presenta evidencias de rompimiento en superficie (Estay et al., 2023), similares a las reportadas en trinchera por Vargas et al. (2014) para la falla de San Ramón. El ángulo de inclinación propuesto para la falla de San Ramón es de 65° con dirección este (Armijo et al., 2010; Estay et al., 2023), con una expresión en superficie del trazo en escarpes semicontinuos (∼60 m de altura) que se extienden alrededor de 40 km desde el Rio Mapocho hasta el Rio Maipo. Esta expresión en superficie también revela una sismicidad importante bajo la Cordillera Principal a unos 10 km de profundidad y una sismicidad más profunda (∼15 km), alineadas con el cabalgamiento principal de los Andes al oeste, paralela al escarpe de la falla de San Ramón (SRF). Con esta evidencia creciente de actividad tectónica, se deja entrever que la topografía (al menos en el margen chileno) de este orógeno fue creado por un sistema de fallas frontales de cabalgamiento (p. ej., Armijo et al., 2010; Riesner et al., 2017). No obstante, descripciones iniciales (p, ej., Muñoz and Charrier, 1996) mencionan que este Frente Andino Occidental (FAO) (15°S y 20°S) se encuentra estructuralmente controlado por un sistema de cabalgamiento con vergencia hacia el oeste iniciado al menos en el Mioceno. Esta estructura de cabalgamiento multi-kilométrica (Armijo et al., 2010) se extendería de norte a sur, hasta los 38°S, sensu strictu un sistema de cabalgamiento (FCAO, Figura1-1) con vergencia hacia el oeste ha influido en la evolución del Frente Andino Occidental desde el Oligoceno (Riesner et al., 2017; Armijo et al., 2010).

En el reconocimiento de esta estructura kilométrica juega un papel importante en el entendimiento del modelo conceptual de los Andes(Figure 1-2). El modelo de vergencia hacia el este propuesto por Giambiagi et al. (2014) y el modelo de orógeno de doble vergencia propuesto por Armijo et al. (2010) presentan visiones contrastantes sobre la evolución tectónica de los Andes a ∼33.5°S de latitud (Riesner et al., 2017) (Figura1-2). Giambiagi et al. (2014) describen una evolución en dos fases, donde el cinturón de pliegues y cabalgamientos de Aconcagua (FTB) sirve como la estructura frontal principal. Inicialmente, desde ∼25 a ∼10 Ma, se produjo la deformación y el levantamiento en la cuenca del antearco y el FTB de Aconcagua, mientras que la cuenca del antepaís oriental ocurría subsidencia (posición actual Cordillera Frontal). Desde 10 Ma hasta el presente, la deformación se propagó hacia el este, conduciendo a la exhumación tardía de la Cordillera Frontal. En contraste, Armijo et al. (2010) sugieren una deformación continua hacia el oeste durante los últi-

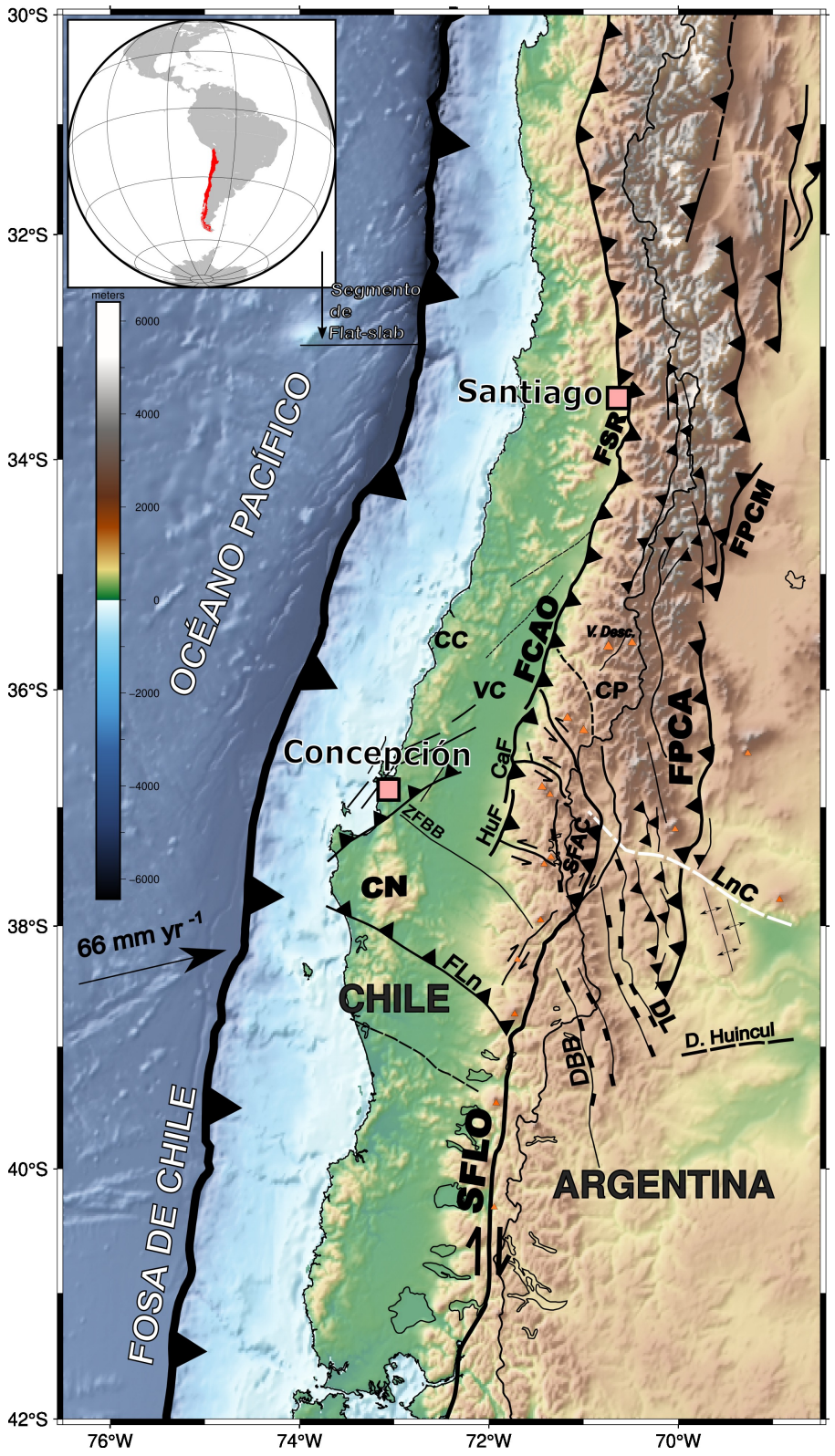


Figure 1-1: Marco tectónico del margen chileno entre los 30°S y 42°S. Cordillera de la Costa (CC): 60-80 km de ancho con picos que alcanzan hasta 700 m. Valle Central (VC): 20-60 km de ancho con una altitud promedio de alrededor de 200 m, llena de sedimentos cuaternarios. Cordillera Principal (**PC**): 50-100 km de ancho con picos que alcanzan hasta 3,953 m sobre el nivel del mar. **FSR**: Falla de San Ramón; **FCAO**: Falla de Cabalgamiento Andino Occidental; **SFAC**: Sistema de Fallas de Antiñir-Copahue; **DBB**: depresión del Bío Bío; **DL**: depresión de Loncopué; **CN**: Cordillera de Nahuelbuta; **FLn**: Falla de Lanalhue; **SFLO**: Sistema de Fallas de Liquiñe Ofqui; **FPCA**: Falla Plegada y Corrida de Agrio; **FPCM**: Falla Plegada y Corrida de Malargüe; Dorsal de Huincul; **ZFBB**: Zona de Falla del Bío Bío; **LnC**: Lineamiento de Cortaderas.

mos ~20-25 millones de años, considerando al FTB de Aconcagua como una estructura secundaria transportada pasivamente sobre el alto del basamento de la Cordillera Frontal. Este modelo implica una exhumación temprana y continua de la Cordillera Frontal desde ~20-25 Ma, manteniendo una vergencia dominante hacia el oeste a lo largo de la historia del orógeno.

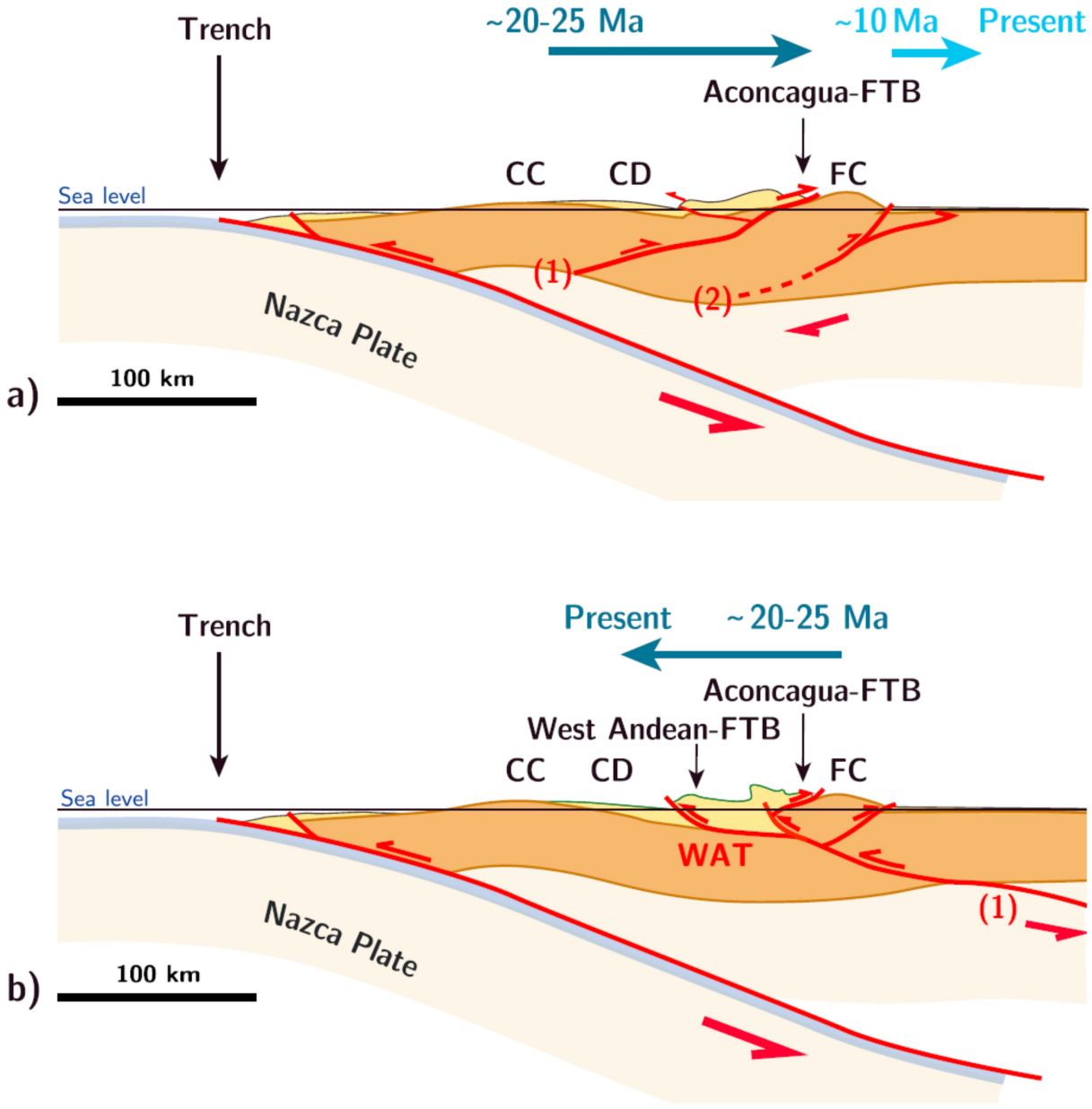


Figure 1-2: Dos modelos conceptuales en conflicto de los Andes a 33.5°S de latitud (Tomado de Riesner et al., 2018). (a) Modelo de vergencia hacia el este propuesto por Giambiagi et al. (2014). (b) Modelo de orógeno de doble vergencia con una vergencia primaria dominante hacia el oeste propuesto por Armijo et al. (2010). CC = Cordillera Costera; CD = Depresión Central; FTB Andino Occidental = cinturón de pliegues y cabalgamientos andino occidental; FC = Cordillera Frontal; FTB Aconcagua = cinturón de pliegues y cabalgamientos de Aconcagua; WAT = Cabalgamiento Andino Occidental.

A pesar de estas diferencias conceptuales, se tiene el consenso de que la Cordillera Principal es controlada en su borde occidental por una estructura tectónicamente activa. Sin embargo, hasta

este punto solo se abordado la evidencia en superficie de los procesos de deformación activa a lo largo del margen chileno, y no su expresión topográfica y las relaciones entre erosión y tectónica. Uno de los primeros trabajos en reconocer la respuesta erosiva al alzamiento fueron Farías et al. (2008) quienes reconocen una respuesta a largo plazo de los ríos, de más de 7 Ma, que dejan una señal transitoria discriminada en la red de drenaje. En este aspecto recientemente, Harries et al. (2023) propone que los ríos de la vertiente occidental de la Cordillera Principal (Andes chilenos) (35-36°S) responden al alzamiento incisando verticalmente y propagando esta verticalidad aguas arriba. Esta respuesta de los drenajes corresponde a un interacción compleja entre la tectónica, clima, erosión y topografía; que, en mecanismos de retroalimentación positivos o negativos, un proceso (endógeno o exógeno) desencadena una respuesta de incremento o retroceso de otro. Por ejemplo, Stalder et al. (2020) reporta altas tasas de erosión (2 km/Ma) durante el Pleistoceno entre los 32-36°S, que reconoce como resultado del acoplamiento de erosión (glaciar y fluvial), alzamiento isostático y tectónica activa. No obstante, si bien estos trabajos evalúan la respuesta erosiva a un posible alzamiento (p.ej., Harries et al., 2023; Stalder et al., 2020) no se define el carácter neotectonico de las posibles fallas causantes de estas señales entre los 35-38°S.

Estudios anteriores sugirieron que, al menos desde el Mioceno tardío, las fallas inversas con una orientación NNE y un buzamiento hacia el este controlan el segmento más al sur del FAO entre los 35°S y 39°S (Radic, 2010).Encinas et al. (2021) propone un modelo de evolución que sugiere una historia tectónica compleja del antearco en el centro-sur de Chile (37-42°S) durante el Cenozoico tardío. Según este modelo, tras un período de tectónica extensional en el Oligoceno-Mioceno temprano, ocurrió una fase compresiva importante alrededor de los 19 Ma, causando la deformación de estratos más antiguos y el crecimiento de la Cordillera Andina. La activación del Cabalgamiento Andino Occidental, una falla de empuje mayor en el límite entre la Depresión Central y la Cordillera Principal, provocó un levantamiento significativo del flanco occidental de los Andes desde al menos el Plioceno hasta el presente ($\sim$5Ma). Esto desencadenó una subsidencia por flexura, acumulando gruesos depósitos sedimentarios en el antearco durante el Plio-Pleistoceno. El aumento repentino del flujo de sedimentos hacia la fosa oceánica causó un cambio de no-acreción o erosión por subducción a acreción en el margen, dando origen a la Cordillera de la Costa como un alto de antearco en los últimos 2 Ma (Encinas et al., 2021).Cabe señalar que, si bien el modelo de evolución propuesto por Encinas et al. (2021) está respaldado por datos geocronológicos (U–Pb, LA-ICP-MS) obtenidos de unidades que afloran al oriente de la Cordillera de la Costa (p. ej., la Formación Rodados Multicolores), este presenta una limitación importante. El modelo carece de información específica sobre el trazo principal de la falla de empuje andino occidental. Esta falta de detalle sobre la geometría y ubicación precisa de la estructura tectónica clave genera cierta incertidumbre en la

interpretación de la evolución tectónica regional.

Dentro de las investigaciones que documentan deformación reciente en estas estructuras NNE, Melnick and Echtler (2006) destacan por haber identificado la Falla de Huépil (∼37°10') como una estructura compresiva.Esta falla presenta plegamiento en su flanco oriental y un escarpe estructural que actúa como una geoforma diagnóstica. Posteriormente, Maldonado et al. (2021) reporta una base de datos de fallas activas, donde se distinguen las fallas de Mesamávida y Cachapoal (36-36°30'). La falla de Mesamávida en la comuna de Longaví (∼36°S) presenta un escarpe de aproximadamente 8 km de longitud con escarpes entre 3 a 7 metros delimitados al NE-SW por depósitos aluviales (Sepúlveda et al., 2019; Cortes-Aranda et al., 2021). Este tipo de escarpes caracterizan el Frente Andino Occidental (FAO) entre los 35-38°S, principalmente por su orientación NE a NNE formados en depósitos recientes (aluviales y volcánicos) con una impronta topográfica similar a los que se observan a los 33°S (Falla San Ramón).

El Frente Andino Occidental (FAO) es un paisaje distintivo que ocupa la región entre el Valle Central (o Depresión Central) y el flanco occidental de la Cordillera Principal, extendiéndose desde los 15°S hasta los 39°S. Abarca los primeras elevaciones topográficas de la Cordillera Principal, marcando la transición desde el Valle Central relativamente plano hacia el terreno montañoso. Un componente esencial del FAO es su zona de piedemonte, que comprende el área de transición donde el frente montañoso se encuentra con las tierras bajas adyacentes. La zona de piedemonte en el FAO, particularmente entre ∼35° y 38°S, se caracteriza por que en dicha transición se encuentran diferentes expresiones del relieve como facetas triangulares, basculamiento de abanicos aluviales, terrazas erosivas y una serie de escarpes lineales de tendencia generalmente NE a NNE (e.g., escarpe Mesamávida, Cachapoal). Según la evidencia geológica y el conocimiento actual, una pregunta abierta es ¿En qué medida estas formas de relieve están relacionadas o influenciadas por la actividad tectónica asociada a la Falla de Cabalgamiento Andino Occidental (FCAO) entre los 35-38°S?

Esta disertación se ocupa de entender cuáles son las señales de actividad neotectónica en el Frente Andino Occidental (FAO), entre los 35°s y 38°S, desde una perspectiva de la morfometría, enfocada a la cuantificación del paisaje; y desde la morfotectónica identificando la distribución y edad de las geoformas de acuerdo con los patrones de falla. El enfoque aplicado consistió en la detección regional (∼300 km) de sectores con altos patrones de deformación, para posteriormente evaluar de manera particular su potencial influencia tectónica. Pero ¿Por qué estudiamos este frente montañoso? La respuesta es porque cartografiando los trazos de fallas activas en estos frentes montañosos es importante para la evaluación del riesgo sísmico, principalmente en zonas pobladas, pero también para obras de infraestructura como carreteras, puentes, centrales nucleares, represas y minería. Se espera que lo contenido aquí sea una herramienta para evaluar y diagnosticar potenciales

riesgos para las comunidades, y que sirva al desarrollo de la planificación del territorio de las regiones involucradas.

1.2 Hipótesis

Durante el Cuaternario, el Frente Andino Occidental (FAO) entre los 35° y 38° S ha experimentado un levantamiento tectónico debido a fallas de cabalgamiento con orientación NNE. Estas fallas, activas durante el Cuaternario, no solo formaron escarpes como resultado de ciclos de terremotos, sino que también mostraron distintos niveles de actividad tectónica. Dichos niveles han dejado firmas morfométricas específicas y evidencias morfológicas en el FAO, sugiriendo una actividad compleja y variada (p.ej., clima), que no se limita exclusivamente a procesos sismogénicos.

1.3 Objetivo General y Específicos

1.3.1 Objetivo general

Evaluar la deformación cuaternaria en el Frente Andino Occidental (FAO) entre los 35°S y 38°S, en el marco de los procesos tectónicos y de superficie que operan en el área.

1.3.2 Objetivos específicos

- Distinguir los segmentos tectónicos activos del Frente Andino Occidental a partir de técnicas morfométricas.
- Discutir el estilo de fallamiento y cinemática asociada de las principales fallas que impulsan la elevación.
- Caracterizar los principales rasgos morfotectónicos (escarpes-terrazas) que indican los procesos de levantamiento durante el Cuaternario Tardío.
- Estimar las tasas de elevación del Cuaternario Tardío.

1.4 Organización de la Tesis

Esta tesis fue escrita en capítulos independientes pero relacionados (Capítulos 2 al 4) preparados para ser sometidos a revistas internacionales revisadas por pares. Entre estos el capítulo 2 fue

publicado en la revista Earth, Surface Processes and Landforms - ESPL (Volumen 49, Número 7), y el capítulo 3 sometido al Journal of South American Earth Sciences - JSAMES en el número especial "Geomorfologia de los Andes de Argentina y Chile". De las secciones mencionadas se desprende el capítulo de cartografía morfotectónica (Capitulo 5), que integra todo el trabajo de terreno y se encuentra en fase de preparación. Este capítulo (Capitulo 1) contiene una visión general introduciendo al lector al planteamiento del problema, a la hipótesis, objetivos principales y generales, además de una síntesis de la metodología.

Los capítulos del 2 al 4, al estar preparados para publicación en revistas, están escritos en inglés y tienen un contenido transversal: resumen, introducción, metodología, discusión y conclusiones. Dado que las metodologías se encuentran bien definidas en estos capítulos, se incluye una sección posterior con una breve síntesis de los métodos.

En el Capítulo 2 se discuten tanto las principales evidencias morfométricas de tectónica activa de la unión piedemonte-montaña en el FAO, como su ajuste transitorio al clima. El Capítulo 3 determina la respuesta de la vertiente occidental de la Cordillera Principal a la interacción entre clima, erosión, tectónica activa y la posible señal de rebote isostático. Posteriormente, en el Capítulo 4, se abre un nuevo frente de estudio explorando cómo la cinemática de una falla influencia parámetros morfométricos, y cómo estos podrían ser utilizados para catalogar de manera indirecta el estilo de falla que afecta un frente montañoso. El Capítulo 5 muestra un mapa de la zona de deformación definido a partir del análisis morfométrico (Capítulos 2 y 3), y que integra información frágil (Sectores de Cachapoal, San Fabián, Nahueltoro, entre otras), dataciones OSL, sedimentología y geología general. En el Capítulo 6, una discusión abordando los hallazgos principales, preguntas sin resolver y trabajo a futuro.

1.5 Metodología

La morfometría calculada para la zona de estudio tuvo como base topográfica el modelo digital de elevación ALOS AW3D30 de 30 metros de resolución (versión disponible de enero del 2021). Para el cálculo de los índices mencionados en los capítulos 2, 3 y 4 se usó ArcGIS Pro (version3x.) con herramientas de complemento (add-in) como CalHypso (Pérez-Peña et al., 2009), SwathProfiler (Pérez-Peña et al., 2017) y funcionalidades del SIG. Python fue una herramienta para el análisis de datos, y la creación de scripts para calcular algunos índices como los perfiles normalizados de los ríos, o regresiones polinomiales por aprendizaje de máquina. Para calcular el índice de verticalidad del canal (Ksn) se usó la herramienta Kit de Análisis Topográfico para TopoToolbox (TAK) desarrollado en Matlab por Forte and Whipple (2019).

Para el capítulo 2, se evaluó con morfometría la unión piedemonte-montaña del FAO siguiendo los estudios clásicos de Bull and McFadden (1977) and Rockwell et al. (1985), y más recientes como el Yıldırım (2014) donde se mide planimétricamente la sinuosidad del frente montañoso y altimétricamente las diferencias topográficas de un corte de los valles próximos a esta unión piedemonte montaña. Los índices aplicados son apropiados para identificar alzamientos activos en los frentes montañosos y geoformas en el piedemonte que resultan de un alzamiento y caída del nivel base (E. Keller and Rockwell, 2022). No obstante, con el fin de evaluar posibles señales transitorias que se ajustaran al levantamiento de procedió a usar el índice de longitud de corriente-gradiente (SL) o índice de Hack. Este índice proviene de una familia de métricas de canal (p. ej., Ksn, factor de concavidad Cf%) que permite evaluar en los perfiles longitudinales, interpolando estos datos vía kriging, áreas extensas con relativo éxito (Demoulin, 1998).No obstante, los valores obtenidos en estas métricas deben ser comparados con mapas de precipitación y litología para descartar posibles controles. Para esto, se usó un mapa de dureza de la roca y el mapa de la distribución de la precipitación media anual (MAP siglas en inglés) comparado con valores alto del índice SL. Para dar un paso adicional en el análisis regional se propuso integrar ambos mapas (litología + precipitación) que integra una sola señal medida en niveles de probabilidad dando mayor relevancia a la litología (Whipple et al., 2000). Un paso importante para entender los patrones topográficos, fue el uso de los perfiles en franja (swath siglas en inglés) que permitió extraer tres elementos importantes: la curva del relieve local y sus relaciones con el máximo-mínimo topográfico, transversal hipsométrica mejorada (Pérez-Peña et al., 2017) que permitió evaluar el estado de transitoriedad ante un posible ajuste tectónico, y finalmente el área normalizada del relieve, una nueva métrica propuesta en este trabajo para cuantificar adimensionalmente la cantidad de incisión. Este último índice evalúa el paisaje a largo plazo, reflejando la acumulación de incisión, y que debe ser comparado con el índice Vf, que refleja incisión a corto plazo.

En el capítulo 3, se aplicó una metodología más amplia buscando identificar las señales de esos estados transitorios del paisaje ante la tectónica activa. Además, se apuntó a buscar las señales dentro de los tramos de falla en dirección NW (p, ej., Radic, 2010). Se aplicaron dos métodos para establecer un único índice de tectónica activa relativa: Iat y el RTA. Ambos índices usan aproximaciones distintas, el primero (Iat) integra los índices (siete en total) en un promedio por clases, con una operación aritmética sencilla; el segundo (RTA) por su parte, se genera una comprende la superposición de rásteres (9 en total) con la ventaja que integra los siete del Iat más los rásteres de variabilidad del ángulo de la pendiente y relieve local. Dentro de los índices calculados se encuentra el de mayor uso actualmente por su potencial en la identificación en los patrones de deformación como es el índice de verticalidad del canal (Ksn channel steepness index)

propuesto por Wobus, Tucker, and Anderson (2006) que es equivalente al índice SL de Hack. Su diferencia radica en que el Ksn considera el área de la cuenca aguas arriba, mientras que el SL no lo hace. Esto significa que el índice Ksn puede proporcionar más información sobre la historia de la erosión y el transporte de sedimentos en el sistema fluvial, lo cual puede ser útil para comprender los procesos geomórficos a largo plazo ante un alzamiento tectónico. Otros índices considerados fueron la integral y curva hipsométrica, que a diferencia de otros índices es de tipo volumétrico y concede una evaluación del paisaje y su estado erosional (Strahler, 1952). Los índices de basculamiento (AF), elongación de las cuencas (Re), sinuosidad del frente montañosos (Smf) y relación ancho-alto de los valles (Vf) también fueron aplicados dentro de la metodología. Los perfiles normalizados de los ríos (Demoulin, 1998) fueron extraídos de la base topografica y analizados con un script en Python para obtener los parámetros Cmax Cf% y dL.

El capítulo 4 usa los datos de la relación de la sinuosidad del frente montañoso (Smf) y la relación alto-ancho dell valle (Vf) siguiendo los procedimiento de Silva et al. (2003). Estos procedimientos fueron realizados usando código en Python para realizar regresiones logarítmicas.

En el capítulo 5 se integran técnicas de cartografía geológica especializada a través de mapas morfotectónicos. Un mapa morfotectónico es un tipo especializado de mapa geológico que se centra en la representación de las características superficiales (morfología) de la Tierra en relación con los procesos tectónicos subyacentes (p. ej., Panizza et al., 1987). El término «morfotectónica» combina «morfología», que se refiere al estudio de las formas del relieve, con «tectónica», que implica los procesos relacionados con los movimientos de la corteza terrestre. Un mapa morfotectónico ofrece una representación visual de cómo la deformación activa modela el paisaje. Usando la base topográfica de 30m de resolución, imágenes de satélite Landsat 7, pares estereográficos recuperados desde Google Earth, y un modelo digital de elevación LiDAR (5m) proporcionado por Arauco, se procedió a interpretar las geoformas asociadas a la deformación usando una simbología específica (p.ej., Panizza et al., 1987). La simbología fue integrada usando diferentes caracteres y símbolos reconocidos en diferentes servicios geológicos como por ejemplo el Servicio Geológico Colombiano (Diederix et al., 2010). Posterior a este mapa se realizaron dos campañas a terreno (diciembre-2022 y enero-2023) para recolectar información sedimentológica, estructural, dataciones y geología regional). Esta información fue procesada en gabinete, teniendo como resultado un mapa morfotectónico con comprobación de terreno, nueve dataciones OSL sobre terrazas y escarpes, e información sobre la cinemática de algunos trazos de falla usando deformación frágil.

Capítulo 2

Geomorphic signatures of neotectonic activity along the Western Andean Front in the Chilean Andes (35°S to 37°S)

Geomorphic signatures of neotectonic activity along the Western Andean Front in the Chilean Andes (35°S to 37°S)[1]

Jorge Adrián Oviedo-Reyes[1]; Joaquín Cortes Aranda[1]; Alfonso Fernandez[12]; José Vicente Pérez-Peña[3]; Laura Flores[4]

[1]Departamento de Ciencias de la Tierra, Universidad de Concepción, Concepción, Chile

[2]Departamento de Geografía, Universidad de Concepción, Concepción, Chile

[3]Departamento de Geodinámica, Universidad de Granada, Granada, Spain

[4]Leibniz Centre for Agricultural Landscape Research (ZALF), Müncheberg, Germany

How to cite this article: Oviedo-Reyes, J.A., Cortés-Aranda, J.,Fernandez, A., Perez-Peña, J.V. & Flores, L. (2024) Geomorphic signatures of neotectonic activity along the Western Andean Front in the Chilean Andes (35°S to 37°S). Earth Surface Processes and Landforms, 49(7), 2205–2228. Available from: https://doi.org/10.1002/esp.5825

Abstract

Characterizing neotectonic activity along mountain fronts in active orogens is the key to better understanding trajectories of landscape evolution, climatic-tectonic couplings and natural hazards. One such prominent mountain front is the Western Andean Front (WAF), which defines the boundary between two main physiographic units along the Chilean Andes (15°S to 39°S): the Central Depression and Principal Cordillera. This study analyses the geomorphic imprints of neotectonic fault activity in the WAF between 35°S and 37°S. We used several topographic metrics, including the mountain-front sinuosity index (Smf), the valley floor width-to-height ratio (Vf) and the stream length-gradient (SL) index to gain information about the regional dis- tribution of deformation patterns and its relative tectonic activity for distinctive seg- ments. In addition, a raster map combining rock strength (RS) and mean annual precipitation (MAP) allowed discriminating lithology-climate vs. tectonics influence on SL anomalies from catchments spanning from the main deformation zone to the regional drainage divide. We use the local relief and swath profiles to quantify the incision and transient state of mountain fronts to evaluate the geomorphic response to tectonic and/or climatic input. Our analysis highlights significant variations from north to south, delineating two distinct segments with different topographic, geo- morphic and geometric fault characteristics. These segments are indented at approxi- mately 36°S. From north to south, there is a segment with an inactive thrust front with a primarily climate-driven fluvial response over long timescales and a second segment with a transient state adjusting to relatively high uplift rates. Morphometric data

[1]Published article in Earth Surface Proocesses and Landforms - ESPL

analysis, DEM-based morpho-structural maps, geological maps and previous research support the interpretation of two sets of neotectonic faults: (1) NNE- striking reverse faults with a dextral slip component and (2) NW-striking sinistral slip faults, likely a response to deformation partitioning caused by oblique subduction on a continental margin.

KEYWORDS:Geomorphic indices; Swath profiles; Local relief; Tectonic activity; Fluvial incision; Hypsometry; Western Andean Front; Forearc

2.1 Introduction

Along mountain fronts, the assessment of seismic hazards relies significantly on understanding the structural evolution and the extent of localized active faulting (e.g., Bull and McFadden, 1977; E. Keller and Pinter, 2002; E. Keller and Rockwell, 2022). Morphometric analyzes aid in understanding the evolution and localization of deformation along active mountain fronts (Bull and McFadden, 1977; Rockwell et al., 1985; El Hamdouni et al., 2008; Pérez-Peña et al., 2010; Giaconia et al., 2012; Scotti et al., 2014; Gaidzik and Ramírez-Herrera, 2017; Rimando and Schoenbohm, 2020; Erbello et al., 2022). Using computational capabilities to leverage geomorphic indices from digital elevation models offers a swift and cost-effective regional assessment of active tectonics (E. Keller and Rockwell, 2022). This approach provides a comprehensive understanding of active tectonics in large areas, pinpointing sites of interest for further investigation through Quaternary chronology and paleo-seismological trench analysis. Although these geomorphic indices are not a substitute for establishing the Quaternary chronology and deriving rates of processes in a regional assessment (E. Keller and Rockwell, 2022), their application provides reasonable empirical evidence to study and classify relative active tectonics (Rockwell et al., 1985; Prizomwala et al., 2016; García-Delgado and Velandia, 2020; Krystopowicz et al., 2020), allowing first-order inferences on landscape response to mountain-front faulting (Bull, 2007).

An example of deformation along active mountain fronts is the Western Andean Front (WAF) in the Chilean Andes (15°S to 39°S; Figure 2-1), a well-constrained morphological feature between two main physiographic units: the Central Depression (or Central Valley) and the Principal Cordillera. Between 15°S and 20°S, the WAF has been considered structurally controlled by a west-verging thrust system initiated in the Miocene, although likely older (e.g., Muñoz and Charrier, 1996). At 33.3°S, a west-verging thrust system has influenced the WAF evolution since the Oligocene (Riesner et al., 2017; Armijo et al., 2010). The San Ramón - Pocuro Fault (Figure 2-1), known as the

westernmost structure in the system (Vargas et al., 2014), is an active fault linked with two Mw >7 earthquakes during the last 20 ka. Previous research proposed that Late Miocene NNE-striking east-dipping reverse faults control the southernmost segment of the WAF between 35°S and 39°S (Radic, 2010). A recent mapping database revealed some active structures between 35°S and 37°S (Maldonado et al., 2021); however, the presence of fault scarps underscores the need to assess the activity of the entire fault zone for two key reasons. Firstly, uncertainty remains regarding the Western Andean Front (WAF) faulting style. Secondly, the regional neotectonics imprint of the WAF between these latitudes has not been analyzed to date. This lack of analysis precludes accurate assessments of the seismogenic potential of this region since it covers a densely populated area where several critical infrastructural facilities (like hydropower plants, mining, and forestry) are closely located, with many being vulnerable to seismic activities.

This study investigates neotectonic activity along the Western Andean Front (35°S-37°S) and its north-south landscape response variability. Utilizing DEM-based morphometric analysis, we derive indexes to identify topographic features and interpret geomorphic responses. The study establishes a regional structural framework using a DEM-based morpho-structural map and existing geological data. Our findings provide an initial understanding of WAF neotectonics southwards of the San Ramón Fault, offering valuable insights for seismic hazard assessment and identifying key sites for future studies on individual fault strands.

2.2 Regional Geologic and Climate Setting

The Andean Mountain Range results from the convergence of the Nazca and South American plates at a 66 mm/yr rate along an N78°E-oriented vector (Angermann et al., 1999; Kendrick et al., 2003). Along the Chilean Andes (15°S to 39°S), the Western Andean Front (WAF) is a physiographic feature that defines the transitional border between the Central Depression (or Central Valley) and the Principal Cordillera. Dominantly consisting of west-dipping mountain slopes and a piedmont surface, between 35°S and 37°S the WAF is an NNE-striking mountain front. Meanwhile the Principal Cordillera progressively decreasing in altitude southwards, from $\sim$ 3000 m to $\sim$ 1000 m (Montgomery et al., 2001).

The Central Valley consists of a depression filled with Quaternary sediments and an ignimbrite cover of 500 m thick. In turn, the Principal Cordillera features, from west to east, Cenozoic (Abanico and Farellones formations) to Mesozoic volcano-sedimentary sequences. Miocene intrusives are emplaced into these stratified rocks (e.g., SERNAGEOMIN, 2003; Farías et al., 2008; Armijo et al., 2010; Figure 2-2).

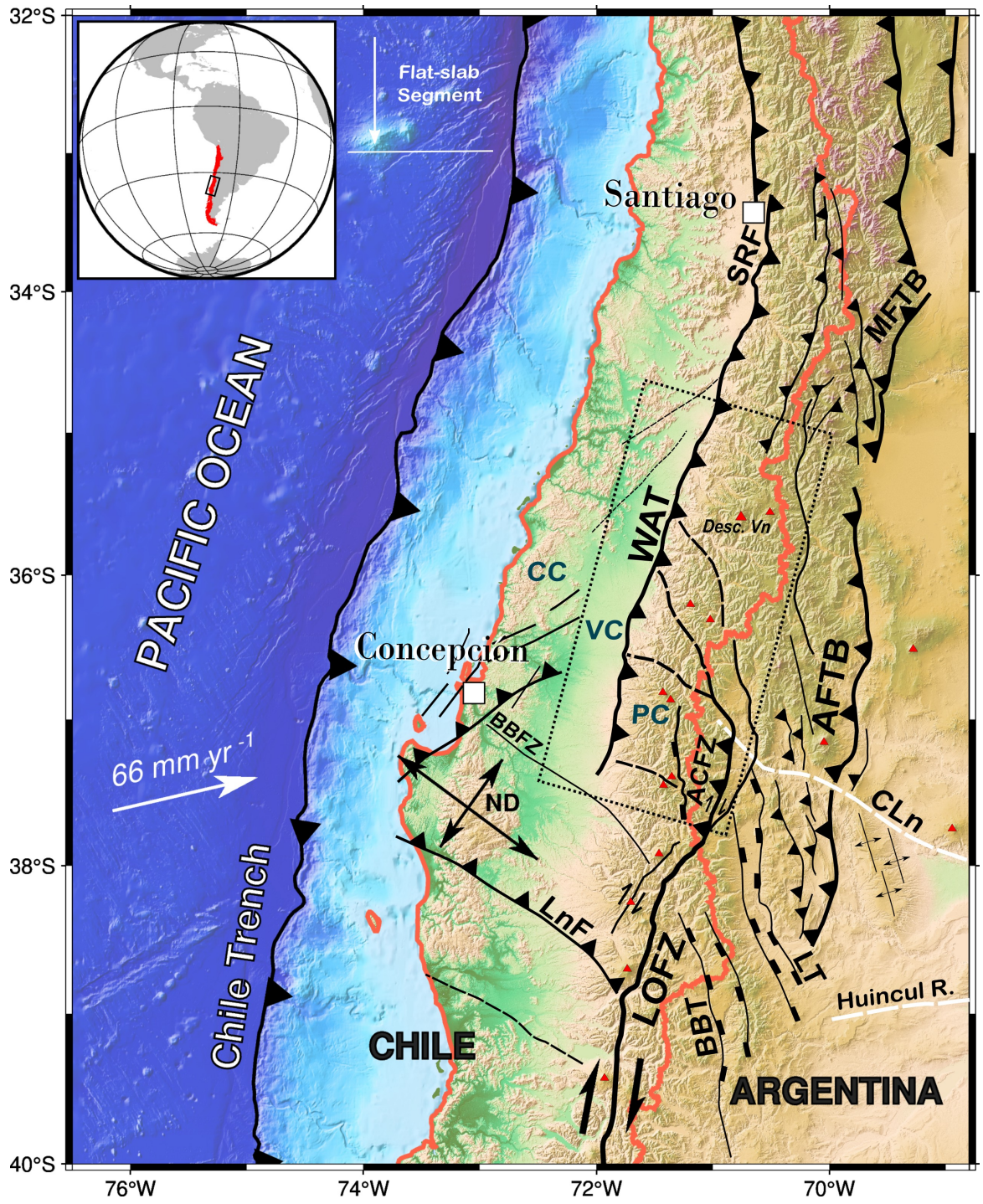


Figure 2-1: Tectonic and structural features of the study area (dashed box) in the Central Andes of Chile (35°-37°S). Notable features in this region include the Coastal Cordillera (CC), a 60-80 km wide range with peaks up to 700 m; the flat Central Valley (VC), 20-60 km wide with an average altitude of 200 m, filled with Quaternary sediments; and the Principal Cordillera (PC), a 50-100 km wide range with peaks reaching up to 3953 m.a.s.l. The mountain-piedmont junction in the study area extends NNE parallel to Principal Cordillera and in agreement with inferred the Western Andean Thrust (WAT), like a southward extension of the San Ramon Fault (SRF). To the east the study area extends to regional watershed boundaries (red line) crossing the western flank of Principal Cordillera. The Central Valley in particular is strangled to the north by the relief, unlike to the south where it reaches its maximum width. Main volcanoes are highlighted (red triangles). SRF: San Ramon Fault; WAT: West Andean Thrust; **ACFZ**: Antiñir-Copahue Fault System; **BBT**: Bío Bío Trough; **LT**: Loncopué Trough; **ND**: Nahuelbuta Range; **LnF**: – Lanalhue Fault; **LOFZ**: Liquiñe Ofqui Fault System; **AFTB**: Agrio Fold Thrust Belt; **MFTB**: Malargüe Fold Thrust Belt; Huincul Ridge; **BBFZ**: Bío Bío Fault Zone; **CLn**: Cortaderas Lineament.

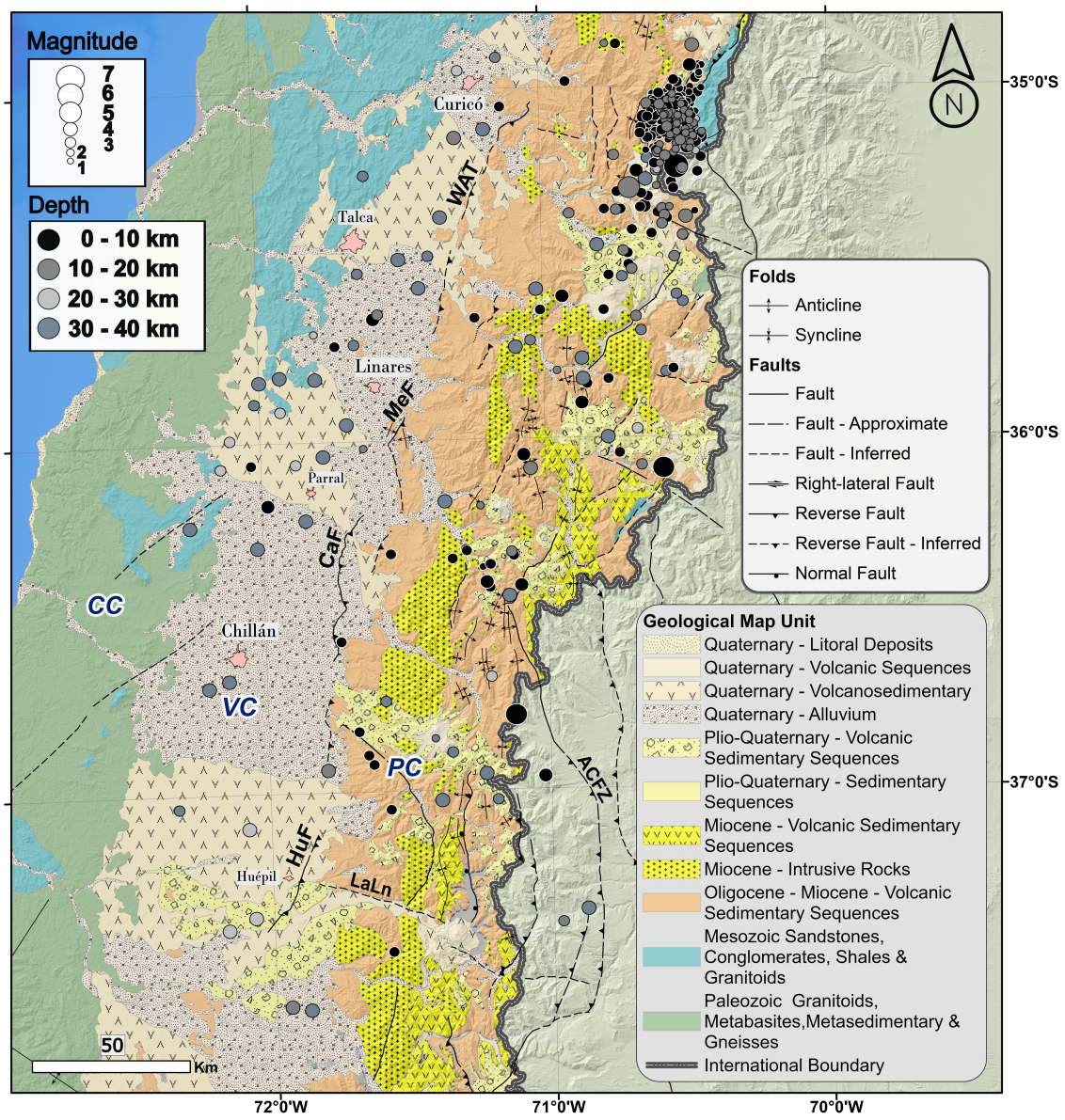


Figure 2-2: Geologic map of the study area between 35°S and 37°S superimposed over hillshade from ALOS AW3D30 30 m,($https//www.eorc.jaxa.jp/ALOS/en/aw3d30/index.htm$), seismic events (gray-scale circles) are from IRIS data set (*epicentral data), faults are from SERNAGEOMIN, 2003; Melnick, Charlet, et al., 2006; Folguera et al., 2004; Cembrano and Lara, 2009; Maldonado et al., 2021. WAT: west Andean thrust;CaF: Cachapoal fault; LoLn: Longaví-Achibueno lineament; MeF: Mesamávida fault; Laln: Lajas lineament; HuF: Huépil fault. (*) All seismic data were downloaded through the IRIS earthquake browser system ($https://ds.iris.edu/ieb/$).

From 36°S to 36°38'S, NNE-striking structures have been interpreted on the western edge of the WAF (Figure 2-1). These structures with their respective vergences are structural features inherited from ancient extensional basins during Oligocene-Miocene, where they subsequently underwent tectonic inversion during Late Miocene (Radic, 2010). Recently, these structures have been documented as potentially active based on parallel scarps to the mountain front (Maldonado et al., 2021). From this, the Mesamávida (MeF) and Cachapoal (CaF) faults are inferred as high angle reverse faults (Figure 2-2) with a length of ∼27 km and ∼44km, respectively. Despite this localized

evidence of active structures, the activity of the entire fault segments is still unknown (e.g., Quaternary chronology, slip rate). At 37°15'S, Melnick, Charlet, et al., 2006 reported an NNE-striking anticline cut by a parallel reverse fault (Huépil Fault; HuF), interpreted as a neotectonic reverse fault.

In addition, NW-structures cutting the NNE faults orthogonally are interpreted as weak zones related to the development of magmatism in Pliocene to Holocene times (e.g., the Nevados de Chillán volcanic complex) (Radic, 2010; Lupi et al., 2020). These structures are recognized, such as the basement boundary reactivated during the Andean Deformation (Ramos and Kay, 2006; Cembrano and Lara, 2009).

While seismic data for the study area is lacking, seismic catalogs show seismic activity near the Principal Cordillera axis and within the Central Valley (Bohm et al., 2002; Olivar et al., 2022). Seismic events in the Principal Cordillera are sparse and shallow (∼40 km depth) (Figure 2-2), while those in the Central Valley are associated with subduction processes (Asch et al., 2006).

Regarding the climate, the Andes play a key role in the 'Arid Diagonal' prominent on the western side of the northern and central Andes, an extensive SE direction arid strip from the Pacific in Peru to the Atlantic in NE Patagonia (43°S) (Abraham et al., 2020). Prevailing winds bring Amazon moisture (e.g., South American Monsoon) to eastern Andean slopes, causing higher precipitation. As air descends the western slopes, it dries, creating arid/semi-arid areas. In the southern Andes, this pattern inverts as winter precipitation is influenced by westerlies. Thus, south of 35°S, rainfall is primarily from Pacific storms hitting the western slopes, while eastern areas experience reduced rainfall due to the barrier effect (Stalder et al., 2020). The study area has a Mediterranean climate - warm, dry summers and cool, wet winters. However, local topography and elevation cause regional variations (e.g., Montgomery et al., 2001).

2.3 Methods

We utilize landscape morphometric ratios for semi-quantitative analysis of large localized tectonic displacements in the WAF. Geomorphic metrics, such as mountain-front sinuosity index (Smf) and valley floor width-to-height ratio (Vf), classify tectonic activity classes and capture recent deformation along the mountain front (∼1.8 Ma) (Bull, 2007). We combine the stream length - gradient index (SL) (Hack, 1973) with lithology and Mean Annual Precipitation (MAP) to identify deformation from catchments spanning from the fault to the main drainage divide capture. Elevation data from 14-km-wide and 145-km-long orogen-perpendicular swath profiles across the WAF are analyzed. Additional strike-parallel swath profiles along the WAF edge were obtained to assess spatial varia-

tions in fluvial incision. Topographic analysis is conducted using the ALOS AW3D30 DEM (30m, released in January 2021), chosen for its superior accuracy in steep mountainous regions compared to SRTM and TanDEM-X (Schwanghart and Scherler, 2017; Tarolli and Mudd, 2020; M. Li et al., 2023)

2.3.1 Topography Analysis

We extracted five 14 km wide and 145 km long swath profiles, starting 25 km west of the mountain-piedmont junction for consistent landscape analysis. The Swath-Profiler tool in ArcGIS 10.7 (Pérez-Peña et al., 2017) was used for topographic parameter extraction. A Savitzky–Golay filter (window size: 31 points, polynomial order: 3) was applied to the profiles using the Scipy function (Virtanen et al., 2020). The filter, similar to a moving average, reduced noise in the data (Jewell, 2016).

Each profile displays maximum, minimum, and mean elevations. Local relief, calculated as the difference between maximum and minimum elevations (Masek et al., 1994), quantifies Quaternary fluvial incision (105 to 106 years). High local relief and wider profile variations indicate potential tectonic uplift or significant incision (Molin et al., 2004; Pérez-Peña et al., 2017).

2.3.2 Rock strength (RS) and mean annual precipitation (MAP)

The impact of lithology on geomorphic indices interpretation has been widely discussed in various tectonic settings (Yıldırım, 2014; Bursztyn et al., 2015; Gao et al., 2023). For example, interpretation of Ksn (steepness index) or SL (Hack index) maps can be obscured by scattered anomalous values reflecting localized controls like lithologic knickpoints or landslide dams (Troiani et al., 2014; Demoulin, 1998). To isolate the regional SL signal, we employed GIS to create an integrated raster weighting rock strength and precipitation. This raster integrated a rock strength map (RS) with five classes based on Selby (1980) measures and Mean Annual Precipitation (MAP) with four classes based on available data quantiles (up to 254 mm/year).

To identify the main lithological features, we utilized the Chilean Geological chart (1:1,000,000 scale, SERNAGEOMIN, 2003) and generated a rock strength map (RS). From existing geological maps in the study area, rock strength was considered using rock type and constituent material (matrix, crystals, grains, cement). Our lithological matching was compared with similar studies (e.g.,El Hamdouni et al., 2008; Yıldırım, 2014; Bursztyn et al., 2015). For instance, dolerites in Selby's classification rated up to 87 (high strength), aligning closely with observed basaltic andesites and andesites in the field. Comparisons with basalts in a Colorado Plateau fluvial transect suggested a rock strength between 75 and 78 (Selby's classification), categorizing the rocks as high strength

(Bursztyn et al., 2015). We established five-rock strength levels from very low (unconsolidated deposits) to very high (intrusive and metamorphic rocks) (El Hamdouni et al., 2008; Bursztyn et al., 2015). However, the classification is regionally dependent (Figure 2-1), with slight modifications to parameters. Bursztyn et al., 2015 suggest systematic and coherent changes in rock strength corresponding to both age (burial) and rock type.

We acquired precipitation data (MAP) from the Center for Climate and Resilience Research CR2MET ($https://www.cr2.cl/datos-productos-grillados/$) in a 0.05º latitude-longitude grid (approximately 5 km) spanning 1979 to 2019 (Alvarez-Garreton et al., 2018). To enable convenient comparison, we converted RS map data to pixels matching the resolution of the MAP data (~5 km).

Our method acknowledges the fundamental role of lithology in erosion processes (e.g., Whipple et al., 2000; Gao et al., 2023). Through this approach, we generated a unified raster incorporating both lithology and precipitation information. This normalized raster, preserving the proposed rock strength levels, aims to identify high-strength lithological units with increased accumulated precipitation. Consequently, the findings will enable us to infer regional-scale relationships among lithology, precipitation, and the SL Hack index. A sensitivity analysis assessed different weightings on the final weighted sum raster, using normalized lithology and MAP rasters. The correlation coefficient between various pairs of output rasters was calculated to observe changes with varying weighting schemes (e.g., 50%RS – 50% MAP, 60%RS – 40% MAP). Based on this analysis, a weighted sum of 60% and 40% was chosen due to higher values in r and R2.

2.3.3 Stream length-gradient index (SL)

The Stream Length - Gradient Index is defined by Hack (1973) as:

$$SL = \frac{\Delta HxL}{\Delta L} \tag{2.1}$$

where L is the stream length measured from the watershed divide to the midpoint of a given reach. ΔH is the altitude difference between the ends of the reach, and ΔL is the reach's length (Hack, 1973). The SL index correlates with stream power based on channel slope and length, influencing the overall correlation with stream power (Hack, 1973; Azor et al., 2002; Pérez-Peña et al., 2009). It results from multiplying the channel slope at a specific point by the channel length, measured along the longest stream above the calculation point (Hack, 1973). Changes in gradient-index values along a well-adjusted channel profile typically signify differences in bedrock (erosional resistance), introduced load, or regional deformation due to active tectonics (Hack, 1973; Azor et

al., 2002; Burbank and Anderson, 2011). Sudden increases in the index characterize over-steepened reaches along a stream, potentially associated with recent tectonic activity (E. Keller and Pinter, 2002; Pérez-Peña et al., 2009).

The DEM was analyzed in ESRI ArcGIS, extracting the drainage network with ArcHydroTools and the D8 flow algorithm (O'Callaghan and Mark, 1984) for 97 basins (e.g., García-Delgado and Velandia, 2020; Erbello et al., 2022). The SL index was computed using the SLiX tool (Piacentini et al., 2020) with a constant ΔL of 50 m for each reach, generating a shapefile of points for the trunk and tributary channels of the studied basins.

Spatial interpolation via ordinary kriging (Cressie, 1990) predicts SL values throughout the study area, extending beyond observed data points (e.g., Mahmood and Gloaguen, 2012; Peronace et al., 2018). SL anomalies, identified using histogram classification for outliers (Troiani et al., 2014), were assessed through raster algebra in ESRI ArcGIS, extracting pixels with the highest SL values (>1500). Comparing SL anomalies with RS and MAP data allowed discussions on their significance in relation to lithological strength, tectonic control, and precipitation patterns (e.g., Azor et al., 2002; E. Keller and Pinter, 2002; Różycka et al., 2021).

2.3.4 Morphometric indicators of relative active tectonics

The mountain-front sinuosity index (Smf) and valley floor width-to-height ratio (Vf) are morphometric measures used to assess tectonic and erosional processes along active mountain fronts (Bull and McFadden, 1977; Bull, 2007; E. Keller and Rockwell, 2022). Smf, defined as the ratio of planimetric length along the mountain-piedmont junction (Lmf) to the straight-line mountain front (Ls), defined as:

$$Smf = \frac{Lmf}{Ls} \tag{2.2}$$

The Smf index indicates the balance between erosional processes and tectonic uplift at a mountain front scale (Bull and McFadden, 1977). Smf $<$ 1.4 indicates potential tectonic activity and is the upper limit defining tectonically controlled segments (e.g., Wells et al., 1988). Typically, higher Smf values (>3) denote more sinuous segments associated with cessation of faulting or high erosion rates (Bull and McFadden, 1977). Smf changes require long periods from early to middle Pleistocene (125ka to ∼1.8Ma) (Bull, 2007; E. Keller and Rockwell, 2022), given the gradual slope modifications by geomorphic processes. On average, the mountain front experiences a one-kilometer retreat after a period exceeding 1 Ma (Bull, 2007). The segment classification criteria include geomorphic changes, steps, bends (E. Keller and Rockwell, 2022), geology, local morphology scarps and mapped faults.

To delimit the planimetric line, a GIS-processed DEM-derived slope map is calculated. Slopes under 10° indicate recent deposits, while those exceeding 10° denote bedrock mountain front slopes. The aspect map was employed to prevent segmentation biases, distinguishing mountainous slopes and delineating the mountain-piedmont junction line and basin outlet. Smf was computed for 45 segments along the Western Andean Front (WAF) to analyze variations.

On the other hand, the Vf index, representing valley cross-section shape and maturity, is defined by the ratio of valley width (Vfw) to the sum of left (Eld) and right (Erd) divided elevations with the elevation of the valley floor (Esc). Bull and McFadden (1977) define it as:

$$Vf = \frac{2Vfw}{(Eld - Esc) + (Erd - Esc)} \tag{2.3}$$

This index distinguishes V-shaped valleys (Vf<0.5) resulting from rapid uplift and high fluvial incision from U-shaped valleys (high Vf values), indicating less incision and degradation processes (e.g., Bull, 2007; Burbank and Anderson, 2011). The Vf index is useful for short-term assessment (10 – 125ka) of changes in uplift rate and differences in erosion patterns (Bull, 2007). Valley cross-sections were obtained using ESRI ArcGIS procedures (Rimando and Schoenbohm, 2020) and Python scripting. Vf measurements were performed at a distance of $\sim$ 0.5km to 1 km upstream from the outlet of 97 drainage basins (e.g., Bull and McFadden, 1977; Rimando and Schoenbohm, 2020). For narrow Vfw (<50 m), we additionally used information extracted from Google Earth and topographic maps to delimit the width of the valley accurately. Three main Vf classes were considered: class 1 (Vf $\leq$ 0.5), indicating incision and uplift (Bull, 2007; Burbank and Anderson, 2011), class 3 (Vf $\geq$ 1) reflecting degradation dominance, and class 2 (0.5 $<$ Vf $<$ 1) representing intermediate values (e.g., Silva et al., 2003; El Hamdouni et al., 2008; Dehbozorgi et al., 2010).

Polynomial regression using machine learning was employed to assess variations in both Smf and Vf along the Western Andean Front (WAF). For Smf, Python code from the Scikit-learn library was used (Pedregosa et al., 2011), with a training/testing split data of 70%/30%, K-fold cross-validation (CV) iterations set at 5, and a polynomial order of 8 determined through a complexity vs. generalization error plot. This approach ensured a well-generalizing model with accurate predictions. A polynomial regression curve of order 5 was applied for Vf, considering training data (60%), test data (40%), and 10 consecutive CV iterations. These methodologies allowed for the identification of meaningful patterns in both Smf and Vf along the WAF.

Table 2.1: Range of data used to define the relative active tectonic classes for the Western Andean Front between 35° and 36° S. The length of each segment is the same parameter Lmf used to calculate the sinuosity of the mountain front. For each segment the different metrics calculated to evaluate the active tectonics, the mean and standard deviation per section are differentiated, some segments do not show Vf values because no major drainage is developed on the studied segment; therefore, no value appears on the Smf/Vf plots (*). ND = No Data.

Mountain Front	Smf	Basins	Vf	Vf (Mean)	σn- 1	Orientation of Front	Front Length (Ls)	Tectonic activity Class	Tectonic Offset Type	Temporal Classification
1	3,77	1 2 3 4	0,69 6,65 0,30 3,05	2,673	2,914	Curving E - S46E to N48E	19,88	3	Vertical Uplift	Pre-Quaternary
2	2,47	5	1,11	1,11	ND	N59W to N4W	20,06	2	Vertical Uplift	Pre-Quaternary
3	1,51	*	*	*	*	Curving S47W - N49W to N69E	25,15	2	Vertical Uplift	Pre-Quaternary
4	1,24	6 7 8	0,41 0,92 0,47	0,597	0,277	N21E	11,58	1	Vertical Uplift	Quaternary
5	8,81	9 10 11 12a 12b 13 14	0,40 0,42 0,62 0,16 0,14 0,23 0,73	0,386	0,227	N25E to N54E	24,70	3	Vertical Uplift	Pre-Quaternary
6	13,06	15 16 17 18 19 20a 20b 21a 21b 22a 22b 23 24 25 26a 26b	0,22 0,25 0,54 0,44 0,22 0,47 0,25 0,35 0,80 0,41 1,25 0,26 0,07 1,64 0,25 0,15	0,473	0,424	N6E to N32E	24,72	3	Vertical Uplift	Pre-Quaternary
7	3,50	27	0,19	0,191	ND	N12E to N24E	23,71	3	Vertical Uplift	Pre-Quaternary
8	1,94	28	0,58	0,576	ND	Curving N78W to N9W	10,93	2	Vertical Uplift	Pre-Quaternary
9	1,75	29 30a	0,40 8,06	4,228	5,413	N53E	13,31	2	Vertical Uplift	Quaternary
10	1,54	31a 42 43 44	1,09 0,28 3,25 3,39	2,003	1,558	N24E	10,30	2	Vertical Uplift	Quaternary
11	5,08	45a 45b 46 47a 47b 48 49	0,73 0,84 0,89 0,56 5,84 0,26 1,08	1,458	1,950	N10W to N8E	14,84	3	Vertical Uplift	Pre-Quaternary
12	1,31	*	*	*	*	N10W	12,18	1	Vertical Uplift	Quaternary
13a	1,42	30b 32	0,45 2,25	1,350	1,273	N40E	21,63	2	Vertical Uplift	Pre-Quaternary
13b	1,22	*	*	*	*	N48W	5,61	1	Lateral displacement	Quaternary
13c	1,42	31b	1,16	1,160	ND	N36E	5,28	2	Vertical Uplift	Pre-Quaternary
14	1,63	32 33a 33b 34	1,17 0,49 0,29 0,94	0,724	0,403	N30W	11,44	2	Lateral displacement	Quaternary
15	1,87	35 36	0,85 1,53	1,190	0,486	N10W	11,09	2	Lateral displacement	Quaternary
16	1,66	37 38	0,09 0,23	0,156	0,099	N32W	11,34	2	Lateral displacement	Quaternary
17	1,12	39 40 41	0,10 0,17 0,38	0,215	0,150	Curving N3W to N16W	13,06	1	Lateral displacement	Quaternary

Table 2.1: Continued.

Mountain Front	Smf	Basins	Vf	Vf (Mean)	σn- 1	Orientation of Front	Front Length (Ls)	Tectonic activity Class	Tectonic Offset Type	Temporal Classification
18	1,14	*	*	*	*	N25E to N45W	14,59	1	Lateral displacement	Quaternary
19	1,45	50	0,46	0,46	ND	N83W	11,09	2	Vertical Uplift	Quaternary
20	2,68	51a 51b 52 53 54	0,93 0,43 1,57 6,22 0,60	1,950	2,425	N32E to N56E	14,35	2	Vertical Uplift	Pre-Quaternary
21	2,74	55 56 57 58	0,52 0,06 0,40 0,57	0,388	0,229	N18W to N16E	16,78	2	Lateral displacement	Pre-Quaternary
22	1,44	59 60	0,38 0,20	0,291	0,125	N24W	14,30	2	Lateral displacement	Quaternary
23a	2,01	61 63c	1,71 1,55	1,631	0,115	N15E to N42E	13,21	2	Vertical Uplift	Pre-Quaternary
23b	1,31	62 63a 63b	0,43 0,30 0,48	0,402	0,090	N12W	11,97	1	Vertical Uplift	Quaternary
23c	1,26	*	*	*	*	N82W	22,06	1	Lateral displacement	Quaternary
24a	1,64	64b 65b 65c	0,39 1,76 2,03	1,392	0,880	N19E to N41E	10,08	2	Vertical Uplift	Pre-Quaternary
24b	1,69	64a 65a	0,34 0,65	0,498	0,222	N31E	8,10	2	Vertical Uplift	Quaternary
25a	2,41	66b 66c 67b	0,34 1,28 1,64	1,085	0,669	N20E	14,19	2	Vertical Uplift	Pre-Quaternary
25b	1,57	66a	1,29	1,29	ND	N24W to N12E	10,64	2	Vertical Uplift	Quaternary
25c	2,09	67a	2,73	2,73	ND	N50W	6,87	2	Vertical Uplift	Pre-Quaternary
26	1,26	68 69a 69b 70	1,45 0,50 1,14 0,23	0,830	0,566	N16W to N27E	8,18	1	Vertical Uplift	Quaternary
27	1,28	71a 71b 72a 72b	0,27 0,56 0,44 0,13	0,350	0,186	N5E	7,70	1	Vertical Uplift	Quaternary
28	2,22	73 74 75	0,30 0,46 0,51	0,425	0,111	Curving E - N9W to W	13,27	2	Vertical Uplift	Quaternary
29	1,28	76 77	0,23 0,29	0,258	0,042	Curving N60E to S78E	12,09	1	Vertical Uplift	Quaternary
30	1,25	78	0,32	0,32	ND	Curving N24W -	14,37	1	Vertical Uplift	Quaternary
31	1,26	79 80	0,63 0,81	0,72	0,129	S82W to N57W	11,23	1	Vertical Uplift	Quaternary
32	1,06	81a 81b 82	0,65 0,49 0,20	0,445	0,231	N71W	11,45	1	Vertical Uplift	Quaternary
33	1,51	83 84	0,13 0,36	0,248	0,162	N71W	10,05	2	Lateral displacement	Quaternary
34	1,40	85 86	0,27 0,19	0,232	0,058	N62W	8,77	1	Lateral displacement	Quaternary
35	1,15	87 88a 88b	0,12 0,40 0,21	0,244	0,142	N38W to N86W	10,49	1	Lateral displacement	Quaternary
36	1,32	89	0,33	0,33	ND	N67W	8,60	1	Lateral displacement	Quaternary
37	1,40	90 91	0,37 0,45	0,412	0,057	N53E	10,51	1	Vertical Uplift	Quaternary
38	1,64	92 93 94 95	0,23 0,21 0,51 1,12	0,517	0,426	N19E	13,25	2	Vertical Uplift	Quaternary
39	1,18	96 97	0,43 0,36	0,394	0,054	N70W	10,53	1	Vertical Uplift	Quaternary

We analyze the distribution of Smf and Vf values through boxplot diagrams and logarithmic regression analysis to define classes of tectonic activity following previous studies (e.g., Bull and McFadden, 1977; Rockwell et al., 1985; Silva et al., 2003; Yıldırım, 2014). A mean Vf value was determined for Smf segments crossed by more than one single basin (Table 2.1). The classes are as follows: Class 1 (Tectonically active) - Low values of Smf $\leq$ 1.4 and Vf $\leq$ 0.5, Class 3 (Slightly or inactive) – with high values of Smf $>$ 3.0 and Vf $\geq$ 1.0, and Class 2 (Moderately active mountain front) with the intermediate values of Smf and Vf.

2.3.5 Normalized Relief Area (NRA)

To expand our analysis, we link tectonic classes and the local relief curve. Local relief is the residual between the maximum and minimum topography (Masek et al., 1994) and often indicates mountain

ranges or extensively dissected landscapes experiencing significant incision and/or uplifting over long timescales (105 to 106 years) (Molin et al., 2004; Azañón et al., 2015). We focused on assessing the area under the curve of local relief profiles using swath profiles obtained along the strike of the mountain-piedmont junction. To do comparable adjacent segments in the WAF using Smf segmentation we normalized the area under each curve using the following relationship:

$$NRA = \frac{\int_a^b |LR(x)|\, dx}{L} \tag{2.4}$$

where NRA is the normalized relief area, LR (x) is the absolute value of local relief, [a,b] is defined for Smf, and L the apparent length that ensures a dimensionless measure for the NRA. L approximates the extent of Lmf in Smf calculations for each segment, determined using the length from the base line trace due to the complexity of processing swath data with the SwathProfiler algorithm (e.g., Pérez-Peña et al., 2017). Major segments were determined based on inferred structural domains (e.g., NW and NE fault-generated mountain fronts). Six major swath profiles (SP1=201km, SP2=47km, SP3=100km, SP4=73km, SP5=80km, SP6=60km) were calculated from north to south, extracting main topographic features (maximum, minimum, and mean elevations) as described in section 2.3.1. Swath profiles run along-strike the mountain-piedmont junction with a 5 km swath width for each section. Each normalized data is plotted against mean Vf values for each segment, assigning a previously defined tectonic class for each.

Additionally, we explore the relationships between mean elevation respect maximum and minimum elevations. To do this, we applied Enhanced Transverse Hypsometry Index (THi*) where using deviations values in HI* across transects could indicate a transient state of adjustment to higher uplift rates (Pérez-Peña et al., 2017):

$$THi^* = (HI^* - 0.5)w_i + 0.5 \tag{2.5}$$

where HI* is the re-scaling HI values between 0.2 and 0.8, and wi represents a weighting factor for a specific transect or location considering the variations in local relief. The THi* index is provided by the Swath-Profiler add-in tool in ArcGIS 10.7.

$$Hi^* = \frac{(HI - 0.2)}{0.8 - 0.2}, w_i = 0.2\ln(RLR) + 0.1, RLR = \frac{LR_i}{LR_{max}} \tag{2.6}$$

2.4 Results

2.4.1 Geomorphological analysis from swath profiles

Here the WAF spans 311 km in a straight line, with a nearly uniform width of about 58 km, except near the Maule River at 35°42'S, where it expands to around 100 km (Figure 2-3). WAF trends in the NNE direction between 37°14'S (near Huépil) and 36°09'S (near Parral), shifting closer to the NE direction as it extends northward.

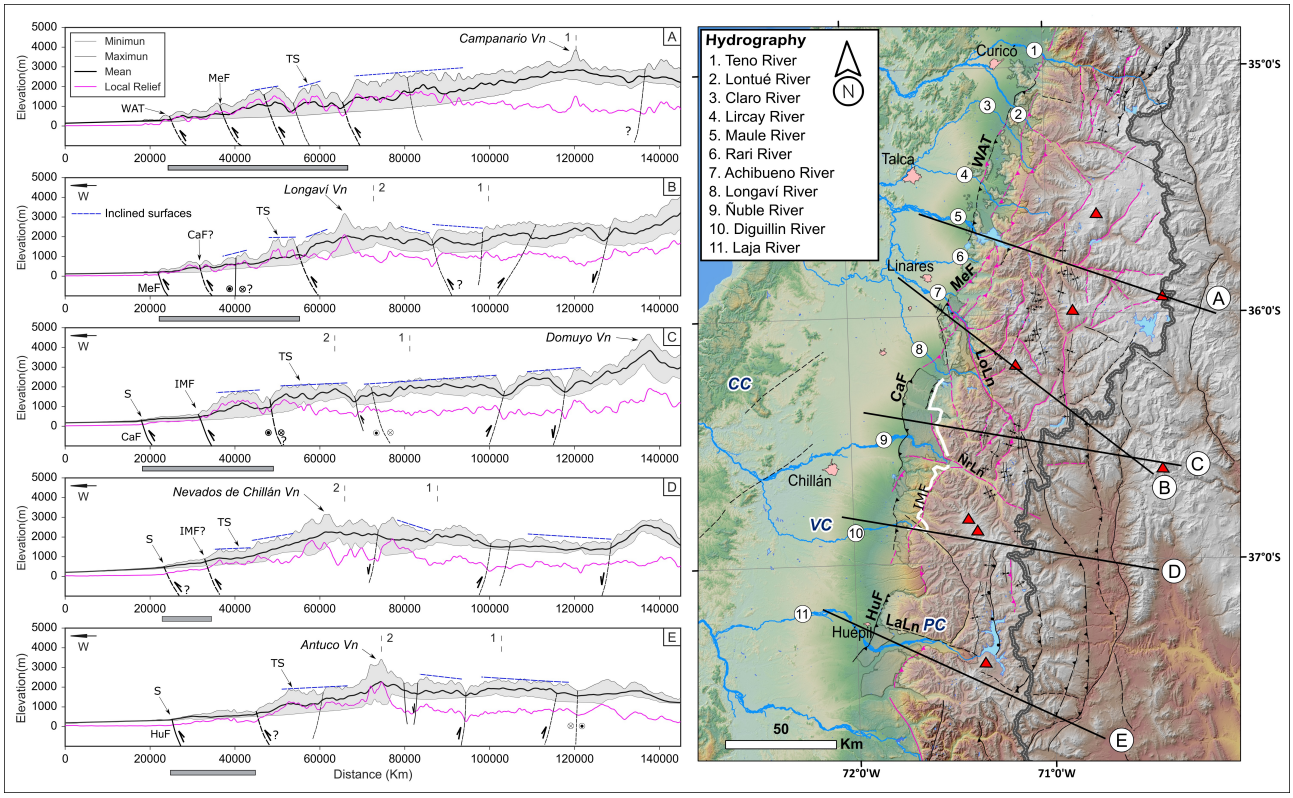


Figure 2-3: The location of the transverse swath profiles for the Western Andean front is shown (right figure). Each across swath profile (left figure) has a black line representing the mean elevation, grey areas marking the maximum and minimum elevation, and magenta lines displaying the local relief. Inclined surfaces Ts (summit surfaces) were identified along each profile (a to e). The landforms related to volcanic systems (Vn) and fault scarps (S) are identified. The regional drainage divide is indicated by the number one (1), and local drainage divides with the number two (2) for all profiles. Several interpreted NNE and NW-striking structures (magenta lines, right figure) were labelled with their vergence across profiles from our structural interpretations. The width of the active structures is delineated below each profile (grey bar). Note the internal mountain front (IMF, white line) and range bounding fault (with younger fault scarps) are depicted in the west of swath profiles (solid white line, c and d). Faults are from SERNAGEOMIN, 2003; Folguera et al., 2004; Cembrano and Lara, 2009; Maldonado et al., 2021. **WAT**: West Andean thrust;**CaF**: Cachapoal fault; **LoLn**: Longaví-Achibueno lineament;**MeF**: Mesamávida fault; **ÑrLn**: Ñuble lineament; **LaLn**: Lajas lineament; **HuF**: Huépil fault from Melnick, Charlet, et al., 2006 and Melnick and Echtler, 2006

The WAF is deeply incised by drainage systems (areas from 2.24 km^2 to 5574 km^2), primarily oriented at about N77°W, nearly perpendicular to the western flank of the Principal Cordillera (Figure 2-3). Drainages with WSW to SW orientation are subordinate and mainly found in the periphery of

the Laja and Longaví - Achibueno rivers (Figure 2-4A).

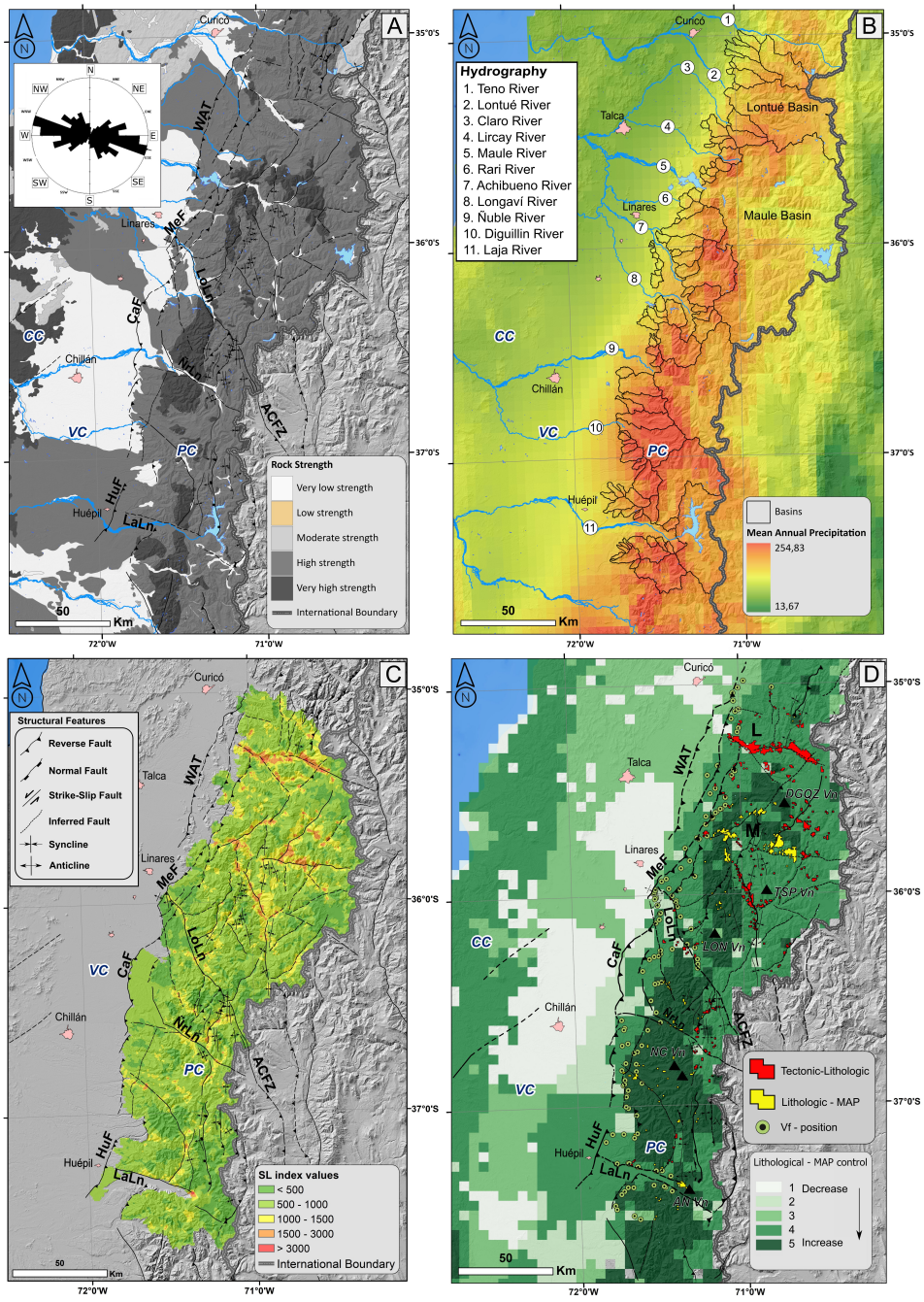


Figure 2-4: Relationships between rock strength, mean annual precipitation and SL gradient channel index values for the Western Andean Front. (a) The rock strength map with five levels. A straight-line segment was used to connect the headwaters node to the outlet node to determine the main orientation of trunk channels. A rose diagram with the principal trend of the main channels is shown; (b) Mean annual precipitation – MAP distribution (after Bookhagen and Strecker (2008)). The names of the main rivers in the study area and the watersheds obtained from the MAP overlay are provided; (c) Simple Kriging predictive map of the distribution of SL values obtained with the SLiX tool (Piacentini et al., 2020) for the main channels of the study area; (d) Lithological – precipitation map obtained from weighted sum between rock strength and precipitation pixels values (pixel resolution 5 km approximately) with overlay extracted SL anomalies. The Vf position of topographic cross-sections of the valleys (green dots). The areas where SL anomalies are found were compared with the lithological - precipitation map to infer their possible tectonic (red polygons) or lithological controls (yellow polygons). The Maule (M) and Lontué (L) river basins are highlighted as areas with a significant presence of anomalies. The main lakes in the western side area are Maule (north) and Laja (south). **DGQZ Vn**: Descabezado Grande and Quizapú Volcanoes. **TSP Vn**: Tatara San Pedro Complex. **LON Vn**: Nevado de Longaví Volcano. **NC Vn**: Nevados de Chillán Volcanic Complex. **AN Vn**: Antuco Volcano.

Analysis of five swath profiles in Figure 2-3, show WAF exhibits inclined surfaces mainly facing west (Ts). Some of these Ts surfaces (sense relict surfaces, e.g., Farías et al., 2008) are displaced by mapped faults from 200 to 400m. The highest local relief values, also coinciding with the highest precipitation and presence of Miocene intrusive units, are observed in the westernmost portion of the WAF. Profiles A, B, and C demonstrate the correlation between the upward deflection of the mean elevation, high local relief, and mapped faults.

This correlation led us to interpret the position of unknown active structures in the WAF (e.g., Wobus, Whipple, and Hodges, 2006). Instead, to the south, the identification of active structures is limited to a shorter zone, predominantly located near the mountain-piedmont junction (D and E, Figure 2-3). West-facing scarps in Catillo (CaF, 36°17'S) and Huépil (HuF, 37°14'S) (heights of approximately 50 m and 30 m, respectively) can be distinguished from the swath profiles (Figure 2-3C and E). These morphological features are associated with terrace deposits, ranging from 10 km wide and 40 km long in the Catillo area to approximately 7 km to 9 km wide and 19 km long in the Huépil locality (e.g., Melnick and Echtler, 2006).

2.4.2 Rock strength (RS), mean annual precipitation (MAP), and SL

The study area consists of 77% high strength rocks (e.g., basaltic andesites, andesites, dacites, ignimbrites) and 23% of very high strength rocks (e.g., granitoids)(Figure 2-4A). Rock strength go higher up to the main drainage divide and lower in the Central Valley, where alluvium and volcanic ash deposits are mainly exposed (Figure2-4A). Concerning RS calculation, 22.1% of the locations where Vf was computed are associated with rocks exhibiting very high strength. Additionally, 77.9% of these sites are situated within regions characterized by high-strength lithologies (Figure 2-4D).

The regional distribution of SL indicates that the most significant variations occur in the northern sector of the study area, specifically in the Maule River (35°43'S) and predominantly along the central section of the western flank of the Principal Cordillera (Figure 2-4C).

We categorized rock strength and precipitation into five levels (Figure 2-4D), where 4 and 5 are the study foci in the WAF and represent high-strength lithologies (e.g., granitic bodies, andesitic or basaltic rocks) with significant rainfall >90 mm/year. We counted the number of SL (anomalies) pixels falling into these levels. The results show that anomalies were attributed to either tectonic-lithologic (67.7%) or lithologic-precipitation signals (32.3%). Statistically, most SL anomalies related to a tectonic-lithologic origin are clustered along the rivers north of the study area.

Otherwise, highest SL values ($\geq$ 1500) are located in the vicinity of faults traces where these anomalies occur at same altitude in different basins (Figs. 4C and 4D). These anomalies are

consistent with NNE and NW-oriented fault traces (e.g., MeF, LoLn, Figure 2-4D). In contrast, SL anomalies clustered within the maximum rainfall and the very high-strength rocks (lithologic – MAP control, Figure 2-4D) areas are spread along the study area coincident with the central section of the western flank of the Principal Cordillera.

2.4.3 Morphometric indicators of relative active tectonics

In Table 2.1, Smf results and related parameters per segment are presented. North of 35°51'S, the average segment length is 20.09 km, considering inselbergs and embayment piedmont; southwards, it is 11.64 km. Machine learning-based polynomial regression confirms a northward-increasing trend in Smf data (Figure 2-5A). Conducting a likelihood ratio test, we compared various distributions within the power-law family to assess the fit of the distribution, demonstrating a robust fit to a power-law distribution (PDF, Figure 2-5B). The power-law distribution suggests a higher likelihood of straight mountain fronts than sinuous ones for the WAF. The cumulative distribution function (CDF) curve reveals that 28.6% of Smf values indicate tectonically controlled segments (Smf<1.4) (Figure 2-5C). Also, the CDF shows that 85% of data falls below Smf values of 3.0. This threshold is exceeded in 35°51'S (MeF) in Linares City (Figure 2-5A).

Examining Vf trends, machine learning-based polynomial regression reveals a subtle northward-increasing pattern for values up to 35°51'S in the MeF area (Figure 2-5D). Variations in Vf values are notable among closely located basins, such as MeF and LoLn (Figure 2-5D). The highest Vf values are concentrated between 35°51'S and 36°40'S, whereas sectors like LaLn and HuF demonstrate more consistent Vf values (<0.5 and class 1, Figure 2-5D). Notably, low Vf values (<0.5, V-shaped valleys) tend to coincide with high Smf values (>1.4; sinuous mountain fronts; Table 2.1). The likelihood ratio favors a stretched exponential fit due to heavy tails (Figure 2-5E), suggesting a higher likelihood of V-shaped valleys than U-shaped valleys. According to the CDF, 56% of WAF valleys have a V-shaped morphology (Vf <0.5); meanwhile, 33% of Vf values exceed a threshold of Vf > 1.0 (U-shaped valleys) (Figure 2-5F). In general, Vf values range from 0.06 to 8.06.

Here, we explored valley-floor width (Vfw) in relation to drainage basin size in the WAF (Figure 2-5G). Unlike conventional patterns, smaller catchments in the WAF show valley-floor widths similar to larger ones (see supplementary data). Subdividing into 'Small' and 'Large' subsets showed significant outcomes in the former, challenging the direct link between valley-floor width and basin size in the WAF, suggesting the need for alternative explanations.

Between ~36°52'S and ~37°33'S, Class 1 is characterized by low Smf and Vf indices (HuF, Figure 2-6), alongside intermediate to high SL values (>1000) (Figure 2-4C) in areas towards

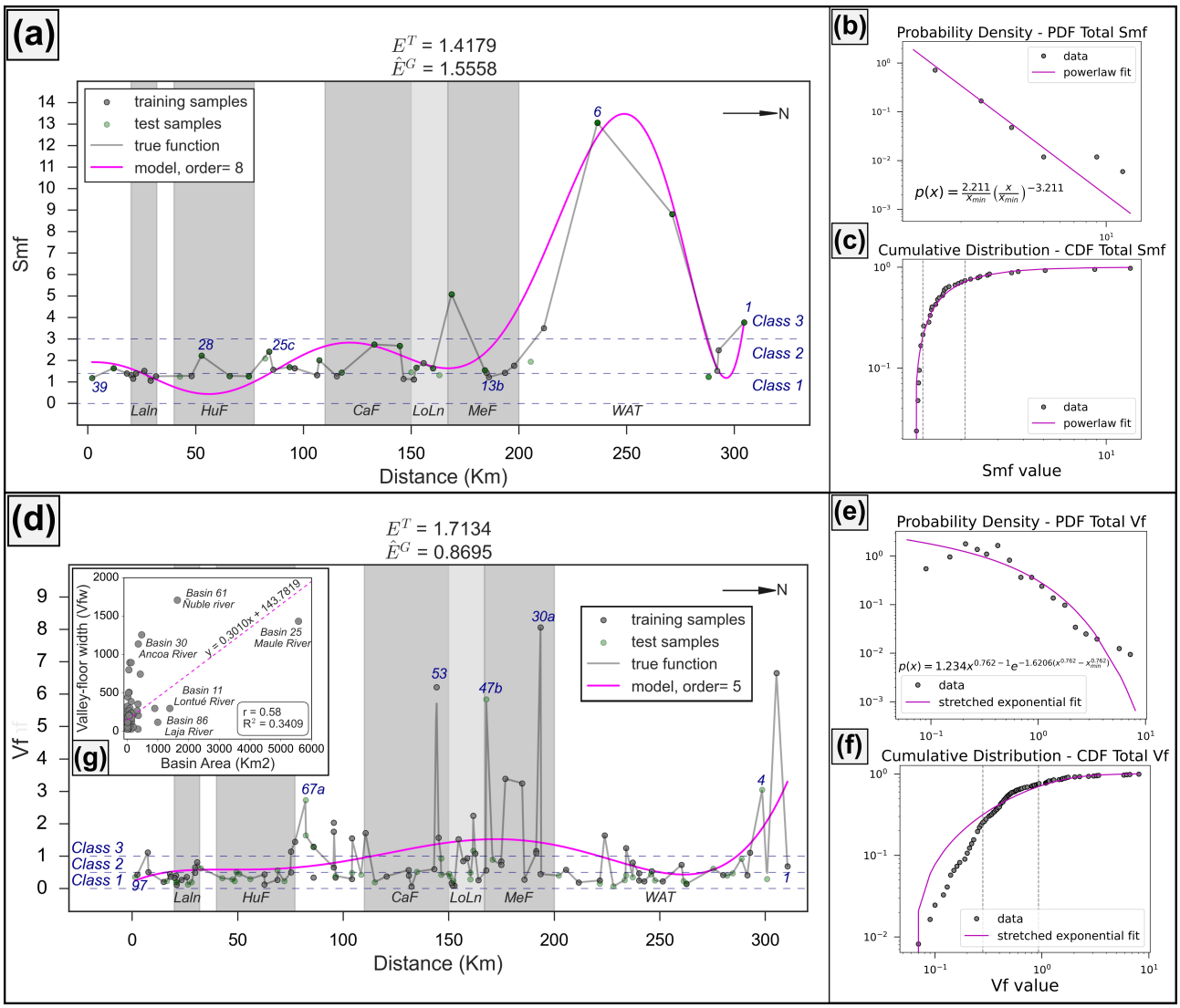


Figure 2-5: (a) Polynomial regression predicted by machine learning for the Smf data vs distance: training data 70%, test data 30% and a curve with order 8. Note that the generalized (EG) and training error (ET) are close to 1 and very close to each other. The classes are differentiated by ranges proposed in this study; the number of mountain front is highlighted (Table 2.1). (b) Power-law distribution for Smf data in the WAF. The parameters of PDF are: $\alpha = 3.211$; Xmin = 1.18. The goodness of fit was assessed using the likelihood ratio between power-law's family distributions. (c) Cumulative distribution function is shown. (d) Polynomial regression predicted by machine learning for the Vf data vs distance: training data 60%, test data 40% and a curve with order 5. (e) Stretched exponential distribution (right) for Vf data in the WAF. The parameters of PDF are $\beta = 0.726$; $\lambda = 1.6206$; Xmin = 0.06. The goodness of fit was assessed using the likelihood ratio between power-law's family distributions. (f) Cumulative distribution function is shown. (g) Linear regression of valley-floor width (Vfw) and drainage-basin size in WAF. Watersheds of equivalent sizes exhibit a spectrum of both high low Vfw values. A total of 122 data for 97 basins were calculated. The starting point zero in the plot is located in the outlet of the basin 97. **Laln**: Lajas lineament; **HuF**: Huépil fault; **CaF**: Cachapoal fault; **LoLn**: Longaví-Achibueno lineament; **MeF**: Mesamávida fault; **WAT**: West Andean Thrust.

the mountain-piedmont junction (segments 27 to 39). North of 37°33'S, significant differences in Quaternary activity are observed between the internal mountain front (S20 to S25a, Figure 2-6B) and the range-bounding fault (S23b to S25c, Figure 2-6). The most segments fall into class 2 comparing Smf values. A higher occurrence of straight segments (Smf: 1.308 - 1.688) is noted along the Cachapoal Fault (CaF, Figure 2-2 and 2-6B), contrasting with more sinuous segments

along the internal mountain front (Smf: 1.442 – 2.408). The same for Vf, along the Cachapoal Fault, shows the lowest ($\leq$ 0.5) compared to the internal mountain front (>1.0). Isolated patches of high SL values (>1000) are observed along the described mountain fronts.

Tectonically inactive segments (class 3) occur north of 35°51'S, characterized by inselbergs and embayment piedmont (Figure 2-6). Here, Vf values are low (mean = 0.41), and larger basins like Lontué (basin 11, Table 2.1) have intermediate values (Vf = 0.62). Tectonic classes were mapped using Smf (Figure 2-5A) (Silva et al., 2003). Each class is associated with a tectonic offset type and temporality (Table 2.1). The NW LaLn lineament prefers active segments (Smf: 1.06 - 1.51; Vf: 0.12 to 0.81). Instead, the LoLn segment shows distinct moderately active segments (Smf: 1.12 - 1.87; Vf: 0.09 to 1.53).

Figure 2-6C illustrates a notable dispersion in Smf/Vf data, suggesting the presence of probable outliers. However, Smf/Vf data analysis along the WAF reveals distinct clusters. These persist regardless of the tectonic class of the front (Figure 2-6C, trends A and B) (e.g., Silva et al., 2003). The observed clusters signify two prevalent valley shapes along the WAF: V-shaped characterized by the equation Vf = 1.106Ln(Smf) + 0.078(R2 = 0.83). (trend B), and U-shaped follows the equation Vf = 1.76Ln(Smf) + 0.346 (R2 = 0.91) (trend A) (e.g., Yıldırım, 2014).

2.4.4 Topographic trends and Normalized Relief Area

The NW-trending mountain fronts exhibit elevations ranging from 504 m to 2751 m for the LaLn lineament and 296 m to 1887 m for the LoLn lineament (SP6 and SP2, Figure 2-7). The relief variation may reflect lithological differences or elevation change modulated by the volcanic centers along segment LaLn (Figure 2-2). Meanwhile, in NNE profiles, elevation ranges from 175m to 1656 m. Note that the SP1 profile shows significant relief accumulation and the lowest elevations in the study area with a notable depression at 36°S considered a depocenter (Figure 2-7). Also, SP1 shows a distinct topographic transition between S9-S10 unrelated to lithology (Figure 2-7), aligning with Rio Ancoa/Achibueno outlets and causing lower relief (S10-S11). This transition marks more active segments (class 2), coinciding with the lowest values of THi*. Elongated terrace deposits ($\sim$200m) follow the LoLn lineament (SP2, Figure 2-7). SP2 has a similar transition towards SE with higher elevations from granitoids. Minimum elevations suggest an ancient NW Achibueno-Longaví connection related to piracy processes.

In NNE-trend SP3, lithological changes drive physiographic variations. Lower elevations coincide with volcano-sedimentary sequences, while more erosion-resistant granitoid bodies contribute to increased relief. SP4 and SP5 consistently exhibit topographic changes in their southern sections,

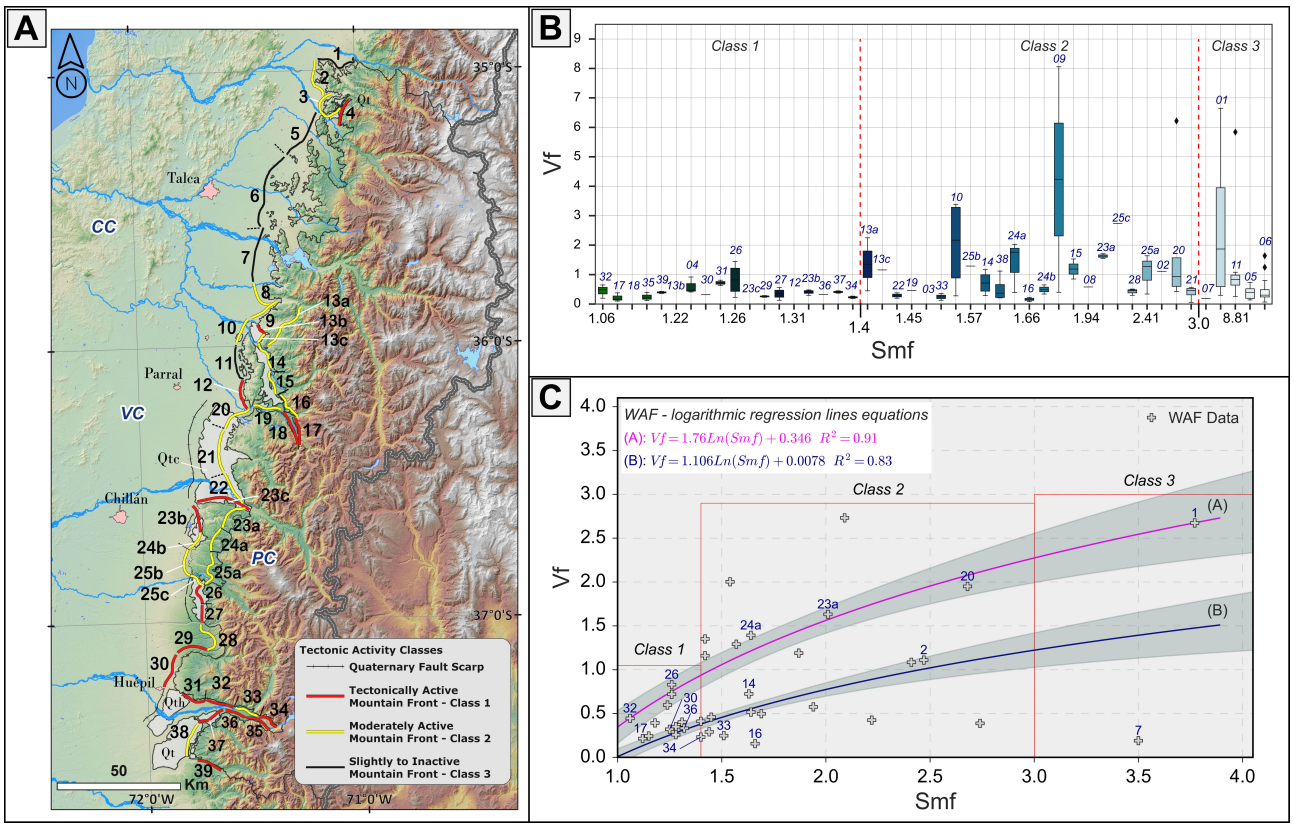


Figure 2-6: (a) Tectonic activity classes of mountain fronts in the Western Andean front between 35° and 37° S. PC: Main cordillera, VC: Central Valley, CC: coastal cordillera. The values used to define the classes are shown in Table 1. Catillo (Qtc) and Huépil (Qth) terraces are labelled. (b) Boxplot with Smf and Vf values combined in order to classify the relative tectonic classes in the Western Andean Front. The data are sorted from lowest to highest with reference to the Smf. The outliers in the plot are depicted by rhombus (around class 3). (c) Scatter plot depicts Smf/Vf data distribution, considering the mean value of Vf. Logarithmic regressions of Smf/Vf data distinguish two observed trends (a and b) in the dataset (magenta and blue lines, respectively). The grey zones are the uncertainty (2γ) displayed for the regional groups identified in the WAF between 35° and 37° S. Values > 4 in both metrics were excluded from this plot. The relative tectonic activity classes inferred in the boxplot are depicted in red rectangles.

with SP4 indicating southward elevation accumulation along the piedmont-mountain junction, likely due to higher uplift rates. SP5 shows an offset between fronts along the Laja River valley.

Upward deflections of mean elevation towards maximum topography (e.g., Wobus, Whipple, and Hodges, 2006) are evident along profiles (SP1 to SP6), correlating with THi* values > 0.5 (e.g., Pérez-Peña et al., 2017) (Figure 2-7). Tectonically controlled segments (class 1) predominantly exhibit this relationship, with moderate occurrences in segments of moderate and inactive tectonics. Consistent THi* values are observed in study segments S27 to S30 (SP4-SP5, Figure 2-7), mainly classified as tectonic activity class 1, featuring low Vf values (Vf $<$0.5) (Huepil Fault, HuF), suggesting a transient state adjusting to uplifting (Figure 2-7 and Figure 2.8). A similar trend is noted in segments S23b to S25b (SP4), aligning with the Cachapoal Fault trace (CaF, Figs. 2-2 and 2-3). This feature is also observed in the internal mountain front (S24a to S25a; SP3), displaying moderate active tectonics with slightly continuous anomalies and V to U-shaped valleys.

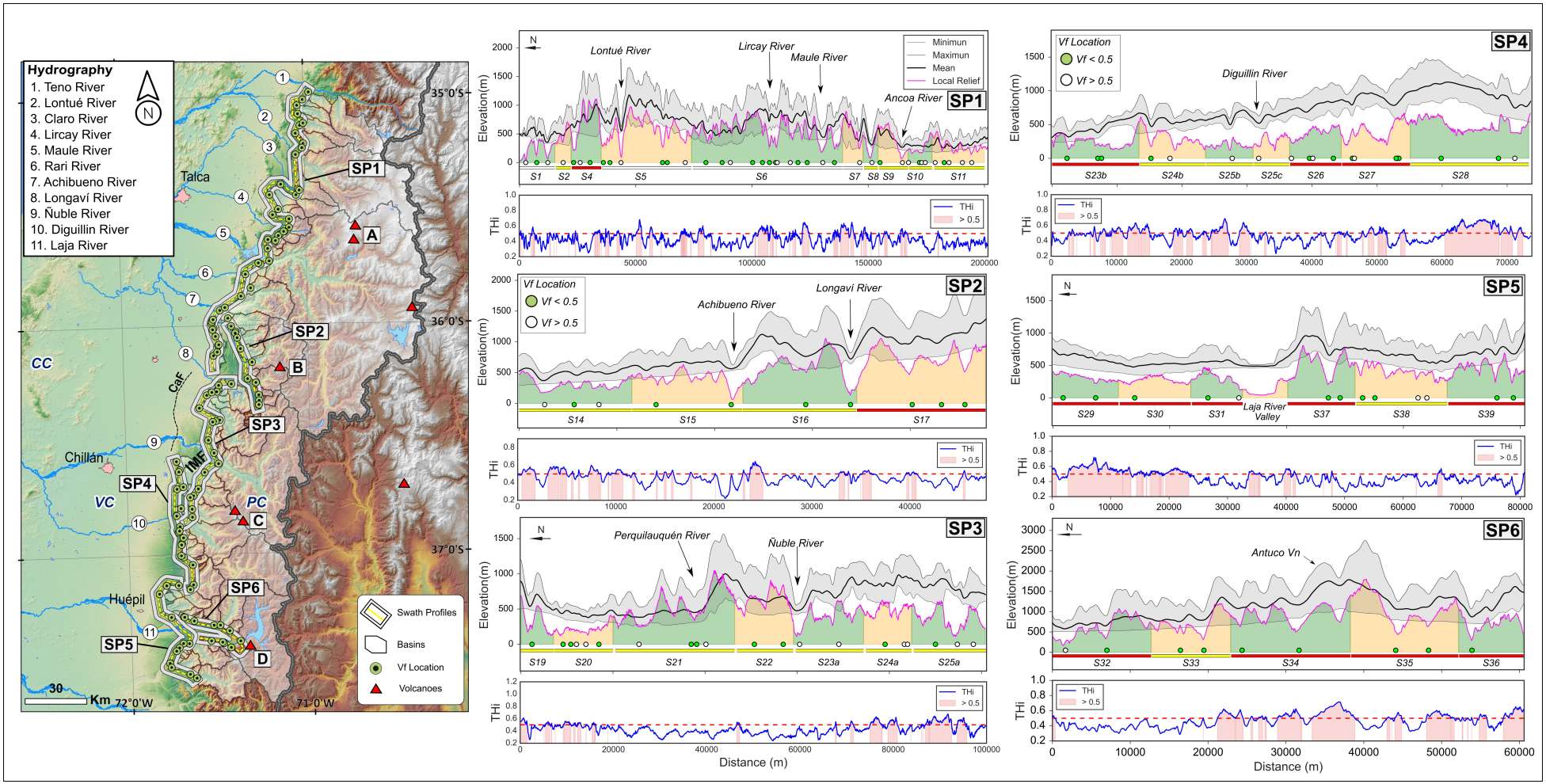

Hydrography
1. Teno River
2. Lontué River
3. Claro River
4. Lircay River
5. Maule River
6. Rari River
7. Achibueno River
8. Longaví River
9. Ñuble River
10. Diguillin River
11. Laja River
Talca
Chillán
Huépil
CC
VC
CaF
IMF
PC
SP1
SP2
SP3
SP4
SP5
SP6
A
B
C
D
35°0'S
36°0'S
37°0'S
72°0'W
71°0'W
30 Km
Swath Profiles
Basins
Vf Location
Volcanoes
Lontué River
Lircay River
Maule River
Ancoa River
Achibueno River
Longaví River
Perquilauquén River
Ñuble River
Diguillin River
Laja River Valley
Antuco Vn
Minimun
Maximun
Mean
Local Relief
Vf < 0.5
Vf > 0.5
THi
> 0.5
Elevation(m)
Distance (m)

Figure 2-7: Location of swath profiles along-strike mountain-piedmont junction in the Western Andean Front (left). The swath profiles (right) are numbered from north to south (SP1 to SP6) and include the segments used to calculate the Smf index (see Figure 2-6). Also, the points of the Vf index calculation are shown (green and white points). The alternating bands below the local relief curves in each profile (yellow and green bands) indicate the specific area for each Smf segment. We selected a swath width of 5 km and a step-size of 40 m to make the areas under the curve comparable between segments. Additionally, each segment is highlighted according to its tectonic class (see Figure 2-6). The transverse hypsometric integral (THi) is shown in the lower part for each swath profile, areas exceeding THi values > 0.5 are highlighted (pink colour). Note how segments with active tectonic class 1 have V-shaped valleys (Vf > 0.5) and THi > 0.5. A. Descabezado Grande and Quizapu volcanoes. B. Nevado de Longaví volcano. C. Nevados de Chillán volcanic complex. D. Antuco Volcano.

Significant variations in NRA values exist from north to south across SP1 to SP6 segments (Table 2.2). A Vf vs NRA plot was conducted considering active tectonic classes and THi* values (> 0.5) (Figure 2-8), revealing distinct patterns along the WAF strike, reflecting variations in uplift and incision. The mean NRA value (463.54) is used as a boundary to differentiate the trend of higher incision. A boundary is drawn at Vf $= 0.5$ to associate the valley shape and NRA. Class 1 active tectonics links to a broad range of normalized relief areas with V-shaped valleys (Vf <0.5) (1A, 1B, Figure 2-8). The normalized relief area decreases as the morphology of the valleys becomes U-shaped.

2.5 Discussion

2.5.1 Topographic patterns linked to deformation

West-facing scarps in Quaternary deposits, like Huepil and Catillo, provide key neotectonic evidence. Swath profile analysis reveals upward deflections in mean elevation and local relief, indicative of terrace uplift by the migrating Andean front (Figs. 3C and 3D). This also shows two previously unknown active structures: the northward extension of the Mesamávida fault (36°S) (MeF, Figs. 2-3A, and 2-3B) and an interpreted internal mountain front from 36°13' to 36°58'S (IMF, Figs. 2-3C and 2-3D) (e.g.,Wobus, Whipple, and Hodges, 2006). The IMF evidence supports interpreting the Cachapoal Fault as a range-bounding fault (e.g.,Ikeda, 1983; E. Keller and Pinter, 2002). We observe increasing deformation northward with more fault strands (Figure 2-3), explained by differential shortening across the WAF (Carretier et al., 2018). Linking scarps with swath profile analysis provides key insights into active structures and quaternary deformation patterns. Further structural mapping and geochronology could better constrain the kinematics and timing of these neotectonic features.

Table 2.2: Segments used to calculate the normalized relief area using local relief curve in swath profiles in the WAF. The length of each segment is ∼Lmf parameter in the Smf calculation. The normalized area is calculated using the length of each segment from Smf. We associated the values of normalized relief area with its tectonic class and Vf values to compare the incision and/or uplifting.

NRA Segments	Segment Smf	Area (Km^2)	Length (Km)	Normalized Relief Area (m)	Vf	Smf	Tectonic Class
SP1	S1	3,66	15,20	240,57	2,67	3,77	3
	S2	3,38	6,91	489,82	1,11	2,47	2
	S4	9,85	13,04	755,75	0,6	1,24	1
	S5	22,47	38,80	579,16	0,39	8,81	3
	S6	36,87	65,00	567,29	0,47	13,06	3
	S7	5,02	8,78	572,21	0,19	3,5	3
	S8	2,01	6,50	309,56	0,58	1,94	2
	S9	5,37	12,92	415,46	4,23	1,75	2
	S10	2,78	10,31	269,99	2	1,54	2
	S11	6,46	22,54	286,49	1,46	5,08	3
SP2	S14	3,58	11,56	309,99	0,72	1,63	2
	S15	4,53	11,32	400,00	1,19	1,87	2
	S16	6,82	11,67	584,25	0,16	1,66	2
	S17	9,75	13,15	741,55	0,22	1,12	1
SP3	S19	2,36	7,12	331,09	0,46	1,45	2
	S20	2,77	12,88	214,97	1,95	2,68	2
	S21	14,11	26,41	534,32	0,39	2,74	2
	S22	8,12	12,76	636,03	0,29	1,44	2
	S23a	6,11	15,24	400,90	1,63	2,01	2
	S24a	5,06	10,39	487,01	1,39	1,64	2
	S25a	5,90	16,23	363,36	1,09	2,41	2
SP4	S23b	3,24	13,40	242,11	0,4	1,31	1
	S24b	3,11	10,19	305,35	0,5	1,69	2
	S25b	1,43	7,35	194,43	1,29	1,57	2
	S25c	1,51	5,58	271,05	2,73	2,09	2
	S26	3,01	7,99	376,99	0,83	1,26	1
	S27	2,60	7,75	335,03	0,35	1,28	1
	S28	10,52	21,08	499,12	0,43	2,22	2
SP5	S29	3,56	11,23	316,66	0,26	1,28	1
	S30	3,38	12,36	273,25	0,32	1,25	1
	S31	2,76	8,90	310,12	0,72	1,26	1
	S37	6,01	11,55	520,41	0,41	1,4	1
	S38	6,36	15,75	403,62	0,52	1,64	2
	S39	6,05	13,29	455,16	0,39	1,18	1
SP6	S32	7,75	12,68	611,13	0,45	1,06	1
	S33	7,31	10,19	716,96	0,25	1,51	2
	S34	14,24	15,41	924,17	0,23	1,4	1
	S35	14,74	13,87	1062,86	0,24	1,15	1
	S36	6,01	8,37	718,54	0,33	1,32	1

2.6 Relative active tectonics from geomorphic indices

This study exploits Smf/Vf ratio to identify tectonic activity (Figure 2-6) and the SL index to assess deformation across the WAF from catchments spanning the faults to drainage divides (Figure 2-4). Results support the neotectonic character of Huepil and Cachapoal faults (Melnick and Echtler, 2006; Maldonado et al., 2021) (Figure 2-9), expanding understanding of mountain fronts deformation patterns (Class 1 and 2) adjacent to observed scarps. Notably, isolated SL anomalies along the mountain front (Figure 2-4C) suggest potential localized deformation accumulation without upstream propagation (Figure 2-4C, 2-4D). Our results also show that the NW-trending LaF, ÑrF, and LoF faults (Figure 2-9), previously recognized as lineaments, are potentially active structures traversing the Andean front (Class 1 and 2, Figure 2-6). The lack of direct and reliable age con-

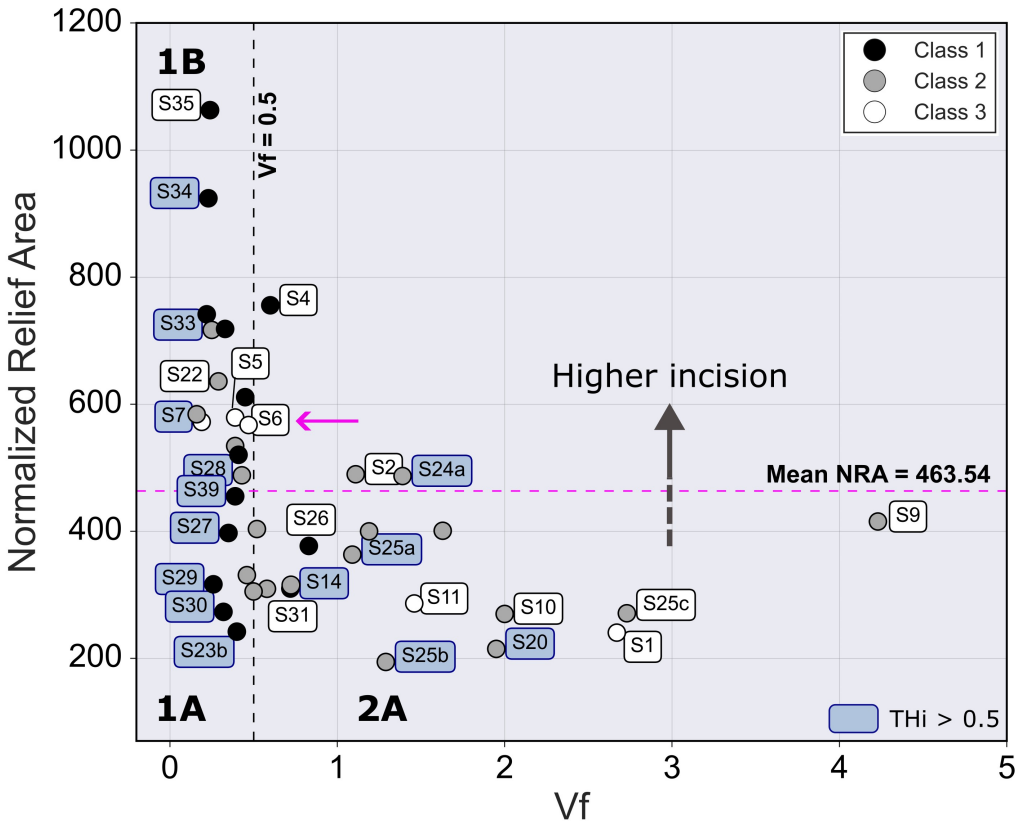


Figure 2-8: Vf vs. Normalized relief area plot. Every segment is coloured by tectonic activity classes from class 1 to class 3 (black, grey and white circles). 1A uplift » incision – leading to a transient state. 1B. Tectonic-fluvial coupling – leading to a highly dissected landscape, high elevations maintains under high river incision processes. 2A lateral erosion by river processes – leads to a broader valley floor. Segments 5, 6, and 7 are inactive mountain fronts with high incision (magenta arrow).

straints raises questions about the timing of Andean front migration in the Cachapoal fault sector (Figure 2-3C) and the synchronicity of Quaternary deformation along the WAF between 36-37°S. Here, the assumption is that faulting occurred synchronously along the WAF (35°S-36°S) since the Late Miocene (Farías et al., 2008; Carretier et al., 2018; Stalder et al., 2020).

In regions north of 35°51'S, tectonically inactive segments (Class 3) are identified, characterized by the prevalence of inselbergs and embayment piedmont in the landscape (Figure 2-6). Mountain front sinuosity (Smf) trends indicate highly sinuous fronts (3.499 to 13.059) (Figs. 2-5A and 2-6), corroborated by field observations and satellite imagery interpretation. We settle preliminary that not all west-verging thrust faults, which accommodated Andean uplift, are tectonically active (e.g., Farías et al., 2008; Armijo et al., 2010; Harries et al., 2023). Unexpectedly, low to intermediate Vf values (Vfmean = 0.41, Table 1) were observed in the catchments related to this inactive thrust front (Figure 2-5D).

Findings are subject to a limitation concerning the glaciers and their role in carving out the U-shapes of the mountain front. Although some valleys in the area may preserve evidence of glacial activity, their Holocene morphology is mainly controlled by fluvial erosion (Rehak et al., 2010). In

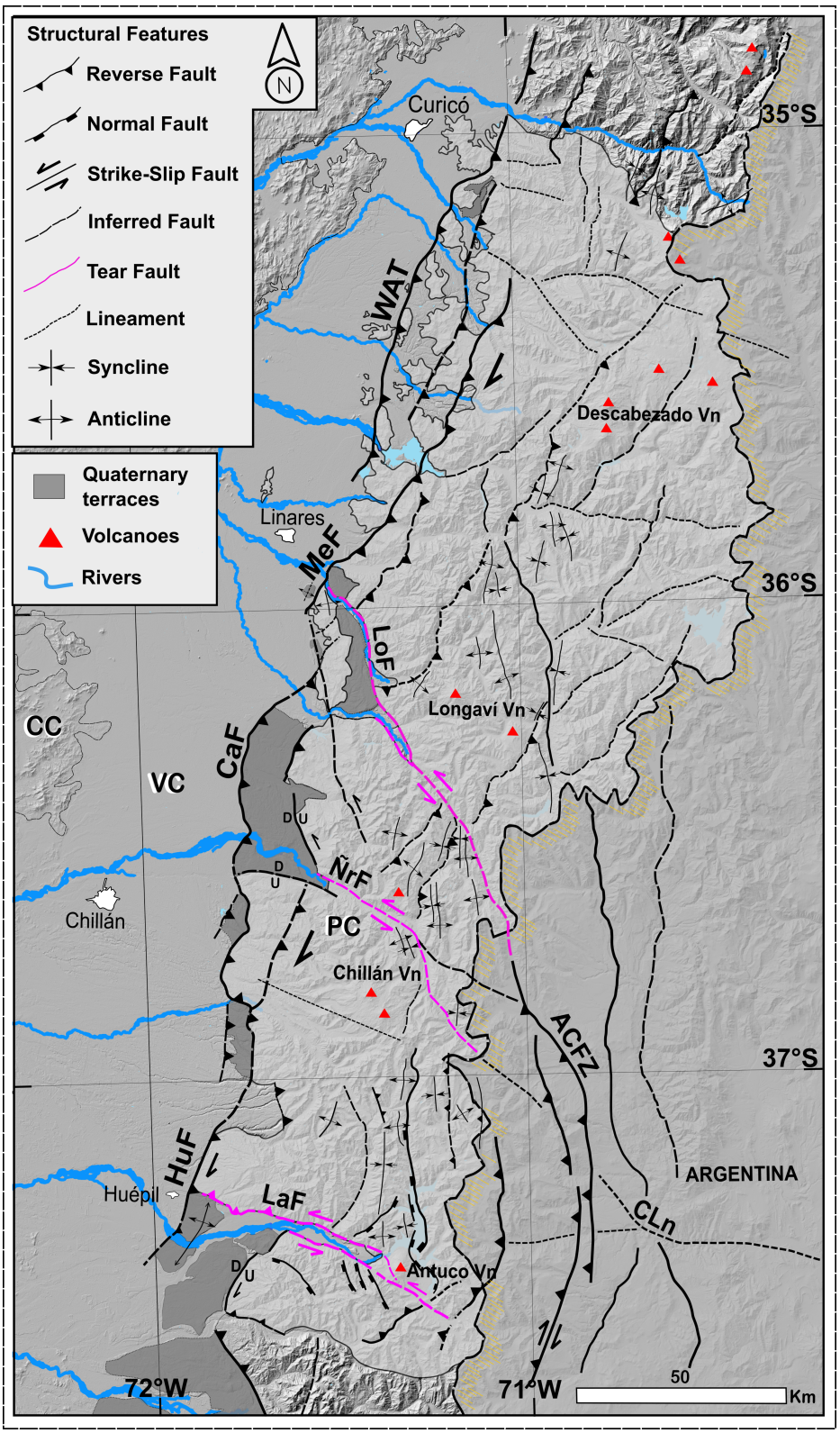


Figure 2-9: Neotectonic structural Setting interpreted in the Western Andean front. Several structural elements such as faults and folds are taken from official geological maps (SERNAGEOMIN, 2003). The structural elements related to the Huépil fault, and those associated with the vicinity of the Antuco volcano (normal faults) are taken from Melnick, Charlet, et al. (2006) and Melnick, Rosenau, et al. (2006). The ACFZ trace information in the Eastern flank of Cordillera Principal is taken from Folguera et al. (2004). **HuF**: Huépil fault, **ACFZ**: Antiñir- Copahue fault system, **CaF**: Cachapoal fault, **MeF**: Mesamávida fault, **LaF**: Laja River fault, **NrF**: Ñuble river fault, **LoF**: Longaví-Achibueno fault, **WAT**: west Andean thrust, **CLn**: Cortaderas lineament, **U**: uplifted side, **D**: Down-dropped side.

addition, at the Pleistocene timescale, glaciers in the area only carved U-shaped valleys higher in the Cordillera (Wobus, Tucker, and Anderson, 2006), and at least during the Holocene, ice bodies would have occurred as mountain glaciers, not valley glaciers (Price et al., 2022). Moreover, our results challenge the direct correlation between valley-floor width and catchment size in the WAF (e.g., Figure 2-5G). Tectonically active segments (e.g., S27 to S30) exhibit V-shaped valleys with floor widths ranging from 30 to 200 m and steeper hillslopes, resulting in Vf < 0.5. In similar conditions (e.g., S10, S11), Vf > 1.0 (moderately to inactive segments) (Figure 2-6, and supplementary data), indicating a dependence of Vf-index by uplift rates along the front (Bull, 2007). Nevertheless, the question arises: why do valleys exhibit a V-shape in the context of an inactive thrust front?

From tectonic perspective, SL anomalies in the hanging block of NNE-striking reverse faults, particularly along the Mesamávida fault trace (35°15'S to 35°51'S), indicate vertical uplift (MeF, Figure 2-4). We find consistent evidence to interpret these anomalies as mixed tectonic-lithological control (e.g., Farías et al., 2008), either for the described knickzones or for the piedmont-mountain junction (Figure 2-4D). Spatially, these knickzones are distributed in the same band as the Vf positions (Vfmean $= 0.41$), and correlate with uniform rock strength and precipitation (Figure 2-4D).

Considering the time sensitivity of the Vf index (10-125 ka), we can speculate a potential Quaternary faulting reactivation with low uplift rates insufficient to place straighten the mountain front (Bull, 2007). Furthermore, upward deflections and high local relief positions observed in swath profiles (MeF, Figure 2-3A) supports this interpretation. This finding adds to growing evidence that rivers have responded to fault uplift in the WAF by generating a propagating knickzone proximal to the fault, and widening river valleys upstream, distal from the fault (Harries et al., 2023).

On the other hand, the Lontué and Maule rivers show SL anomalies upstream approximates the location of the drainage divide (Figure 2-4). The erosion patterns are highly influenced by spatial variability of rock strength (Farías et al., 2008), this non-tectonic controls can be misleading interpretations on channel metrics. Precisely, these steeper channels coincide spatially with plutonic rock outcrops (Miocene) or lava flows from recent eruptions exposed on the surface (e.g., Descabezado Grande and Quizapú volcanoes) (e.g., Harries et al., 2023), which runs along the central section of the western flank of the Principal Cordillera (Figures 2-4C and 2-4D). Although, this anomalies can be also detected in steep erosional topography near volcanic complexes induced by glacial erosion (Singer et al., 1997) (TSP Vn, Figure 2-4D). Further, we suspect that some tectonic-lithologic anomalies observed along the Maule and Lontué river basins (at 35°44', Figure 2-4D) may be attributed to landslides (upstream flow obstruction) triggered by natural processes or the effects of the Colbún dam (e.g., Troiani et al., 2014).

Frequent landslides in this region are primarily attributed to steep valley slopes resulting from deep glacial and fluvial incision (Charrier et al., 2019). This rugged topography indicates glaciers significantly impact the highest areas and volcanic centers, influencing channel metrics.

2.6.1 Geomorphic signatures to Tectonic and/or Climate forcing

On the western side of the drainage divide of the Principal Cordillera (32-36°S), recent studies have reported that low exhumation rates during the late Miocene to late Pliocene (0.1-0.25 km/Ma) dramatically surge to values exceeding 2 km/Ma in the Pleistocene (Stalder et al., 2020). The main hypothesis that would explain this phenomenon is a positive feedback mechanism between long-term climate gradient, which emerges as a significant factor in shaping the morphological response of valleys, and tectonically-driven rock uplift (Stalder et al., 2020; Harries et al., 2023). Thus, glacial erosion and precipitation, coupled with isostatic rock uplift and active tectonics, contribute to the observed high Pleistocene erosion rates on the western side of the Andes (32-36°S) (Stalder et al., 2020).

Figure 2-8 illustrates our main result, displaying systematic variations in several morphometric properties (Smf, Vf, NRA, THi*) along the WAF mountain-piedmont junction. The Vf index is effective for short-term assessment, quantifying erosion pattern differences from the Holocene-Pleistocene boundary to 125 ka (late Pleistocene) (Bull, 2007; Pedregosa et al., 2011). Normalized relief area (NRA) represents cumulative vertical differences in elevation along each segment, indicating long-term landscape response to river incision (e.g., Molin et al., 2004; Pérez-Peña et al., 2017). As Vf increases, NRA values decrease (Figure 2-8). As NRA increases, it indicates more intense geomorphic processes (erosion). These Vf/NRA signals are complemented with metrics related to tectonic perturbation: tectonic activity classes and hypsometry (THi*). We assume deformation concentrates on the WAF edge, analyzing fault-generated mountain fronts along their strike. We present different scenarios depicting landscape responses to tectonic and/or climatic forcing.

The first scenario (1A, Figure 2-8) clustered segments from S27 (36°52'S) to S30 (Huepil Area, 37°33'S) display geomorphic signatures that strongly indicate active tectonic processes. These include straight mountain fronts (Class 1, Smf $<$1.4), V-shaped valleys (Vf $<$ 0.5), lower NRA values, and a noticeable upward deflection in mean elevation (THi* values $>$ 0.5) (Figs. 2-7 and 2-8). Our findings align with previous studies interpreting the Huépil Fault as a Quaternary contractional structure (Melnick and Echtler, 2006). Lower NRA values ($\sim$NRA$<$463.54) and an enhanced transverse hypsometry index (THi$^*>$0.5) in scenario 1A (Figure 2-8) indicate a young transient landscape (e.g., Wobus, Whipple, and Hodges, 2006; Pérez-Peña et al., 2017). If our

interpretations of incision (NRA) and hypsometry (THi*) are accurate, we can speculate that the uplift tends to outpace the incision (Carretier et al., 2018). Consequently, the presence of V-shaped valleys suggests active river downcutting induced by tectonic activity (Bull, 2007) (Figs. 2-6B, 2-7, and 2-8).

In scenario 1B (Figure 2-8), two interpretations emerge. Firstly, a tectonic-fluvial coupling response, with higher NRA, V-shaped valleys (Vf $<$ 0.5), and a straight mountain front (Class 1 or 2, Smf $\sim$ 1.4), indicating a close interaction between tectonic and fluvial processes. The fluvial network actively adjusted to rapid uplift, maintaining V-shaped valleys with increased incision, suggesting relatively high erosion rates in these mountain fronts. However, high THi* values ($>$0.5) in some segments (S33 and S34, Figure 2-7) suggest that erosion rates are not keeping pace with the uplift rate (e.g., Burbank and Anderson, 2011). This interpretation should be approached with caution, as other factors can impact local relief. For example, the NW-striking Laja River Fault, which runs the course of the Laja River (Figure 2-3), implies that fluvial erosion along the main channel may be impacting the local base-level of the drainage system, influencing both valley narrowing (Vf) and incision (NRA). Relief increase may also be linked to east-west active volcanic processes (e.g., Antuco and Sierra Velluda volcanoes) and lithological changes (e.g., granitoids) (SP6, Figure 2-7). We dismiss these signs as characteristic of a transient state, emphasizing the significance of signals related to NNE active faults, such as the Lago Laja fault system (LLFS) (Melnick et al., 2006a). Some segments (e.g., S21 and S22) warrant further studies to validate our interpretation (SP3, Figure 2-7).

Secondly, our analysis identified an inactive thrust front north of 36°S (S5, S6, S7, Figure 2-7). This zone exhibits a highly dissected landscape with high NRA values and V-shaped valleys, indicating significant fluvial erosion. The discontinuity between low and high THi* values likely reflects the complex topography associated with embayment piedmonts and inselbergs in the region. These findings align with Pleistocene erosion rates of 2 km/Ma reported by Stalder et al. (2020), implying that active incision has lowered elevations here. North of 36°S, our results strongly support a climate-driven bedrock incision over long timescales rather than tectonic uplift driving incision (Stalder et al. (2020) and Harries et al. (2023)).

A third scenario (2A, Figure 2-8) considers the following interpretations: As we expect that, in inactive mountain fronts (Class 3), U-shaped valleys (mainly Vf $>$ 1.0) can be associated with a low amount of incision (NRA). The broadening of the valley floor and retreat of the valley walls due to lateral incision river and leaving behind a strath (aggradation processes) (Burbank and Anderson, 2011) would occur mainly in intervals of tectonic quiescence. It has been suggested that the channel width can adjust to changes in discharge or sediment composition in the absence of tectonic forcing

(Wobus, Tucker, and Anderson, 2006).

Some segments present high values of THi* (e.g., S25b, S25a, S20) with class 1 or 2 (Figure 2-8). This result could be attributed to the fact that streams are unable to incise vertically due to a delay in the removal of sediment covers in response to vertical displacement (Harries et al., 2023) and therefore could not attain their base level (Bull, 2007). Changes in valley shape (e.g., valley-floor width), here determined from the Vf index, may be explained in response to disequilibrium conditions imposed by high sediment supply where channel bed is protected from vertical incision ("cover effect") (Sklar and Dietrich, 2004; T. Li et al., 2020; Marcotte et al., 2021) or tectonically active induced (Wobus, Tucker, and Anderson, 2006; Turowski et al., 2008; Whittaker et al., 2007; Clubb et al., 2023). We suggest that the transient state in segments of the WAF (e.g., S25a and 25b) respond to alternating periods of high sediment supply and uplifting. The first mechanism involves a high input of sediment from lahars, originating from nearby volcanic centers (e.g., Nevados de Chillán Volcanic Complex)(e.g., Dixon et al., 1999), where valley widening is predominantly triggered by sediment deposition along low-slope valley floors (Clubb et al., 2023), and the second induced by rock uplift (SP3-SP4, Figure 2-7) that keeps a young relief (Smf = 1.57, S25b).

2.6.2 Neotectonic structures for WAF between 35° S - 37° S

Our findings serve as a proxy for establishing a regional neotectonic framework in the WAF (Figure 2-9). We identify major first-order active structures, including NNE-striking faults such as Huépil, Cachapoal, and Mesamávida faults (Figure 2-9). These faults exhibit predominantly reverse faulting with a strike-slip component. Second-order NW-striking structures are regionally associated with the western termination of the Cortaderas lineament, reactivated during Andean deformation (Ramos and Kay, 2006). These NW-trending faults, cutting the Principal Cordillera orthogonally, show characteristics ranging from strike-slip to oblique faulting (Figure 2-9) (e.g., Radic, 2010), consistent with strain partitioning models for the 34°S to 42°S region (Eisermann et al., 2021).

In this study, we highlight a distinct north-south neotectonic activity centered at 36°S, impacting the main WAF trend. The orientation of mountain fronts (N10°E) varies as the strike-slip fault shifts from N65°W (Laja and Ñuble faults) to N25°W (Longaví-Achibueno faults, Figure 2-9). The mostly inactive mountain front shows a primary direction between N25E to N45E (Figure 2-9), suggesting that deformation accommodation from large thrust systems involves strike-slip faulting, like tear faults. Supporting evidence includes significant mountain front offsets from 0.67 km to 22 km along the WAF until 36°S. These NW-striking structures, interpreted as antithetic Riedel faults, may induce clockwise rotation of WAF blocks (Eisermann et al., 2021).

NNE-striking structures align with the double-vergence of the Principal Cordillera, showing reverse faulting with a dextral strike-slip component. Brittle deformation slip data suggest a compressional state of stress (Quaternary) with a σ_1 striking from N-S to NNE – SSW (N013°$\pm$ 22°) from 33°S to 37°S (Lavenu and Cembrano, 1999), with recent activity on the Cachapoal and Huépil faults indicating thrust-front migration (Figs. 2-3 and 2-9). However, the spatial connection between the Cachapoal and Huépil faults remains uncertain due to limited detailed structural information, leaving the possibility of overlap and potential linkage to a significant crustal detachment at depth (e.g., Riesner et al., 2017).

2.7 Conclusions

This study provides a comprehensive analysis of Western Andean Front (WAF) neotectonics, revealing nuanced spatial variations in Quaternary tectonic activity from 35-37°S. Topographic analysis proves powerful for elucidating active structures, like the newly identified Mesamávida fault extension and internal mountain front (36°13'-36°58'S). This evidence supports reinterpreting the Cachapoal Fault as a major range-bounding structure.

Importantly, our integrated landscape analysis delineates two distinct morphotectonic segments, divided around 36°S. North of 36°S lies an inactive thrust front adjusted to long-term climate-driven fluvial processes. South of 36°S lies an actively uplifting transient landscape. This segmentation is delineated using the marked contrasts in normalized relief area (NRA), valley morphology (Vf), tectonic classes (Smf), and hypsometric variations (THi*) across the transition. Our quantification of these linked topographic markers represents an important advance for unraveling tectonic versus climatic impacts on Western Andean Front evolution.

While providing key constraints on seismic hazards and surface dating, our approach also establishes a quantitative baseline for disentangling the relative influences of uplift and erosion along active fronts. Further work should refine the neotectonic chronology and kinematics of faults and structures exposed by this study. Overall, our analysis provides a framework for decoding complex interactions between climate, tectonics, and topography in orogenic mountain fronts.

2.8 Authors Contributions

Jorge Adrián Oviedo-Reyes: Conceptualization, Methodology, Writing - original draft, Data collection, Visualization. **Joaquín Cortés-Aranda**: Conceptualization, Investigation, Supervision, Writing -original draft **Alfonso Fernández**: Conceptualization, Investigation, Supervision, Writing

-reviewing and editing. **José Vicente Perez-Peña**: Conceptualization, Investigation, Writing -reviewing and editing. **Laura Flores**: Data collection, Data Processing, Writing -reviewing and editing.

2.9 Acknowledgements

The main author would like to thank the Agencia Nacional de Investigación y Desarrollo (ANID - CHILE) and its national doctoral scholarship program for the year 2019 (21191037). We would also like to express our appreciation to the anonymous reviewers whose constructive feedback greatly enriched the quality of this work.

Capítulo 3

Deciphering Climate and Tectonic Signals on Landscapes through Morphometric Analysis: Insights from western slope of Principal Cordillera, 35°S to 38°S, Chile

Deciphering Climate and Tectonic Signals on Landscapes through Morphometric Analysis: Insights from western slope of Principal Cordillera, 35°S to 38°S, Chile[1]

Jorge Adrián Oviedo-Reyes[1]; Joaquín Cortes Aranda[1]; Alfonso Fernandez[12]; Laura Flores[4]

[1]Departamento de Ciencias de la Tierra, Universidad de Concepción, Concepción, Chile

[2]Departamento de Geografía, Universidad de Concepción, Concepción, Chile

[3]Leibniz Centre for Agricultural Landscape Research (ZALF), Müncheberg, Germany

Abstract This study investigates the neotectonic character of the Western Slope of the Principal Cordillera (WSPC) between 35°S and 38°S by integrating multiple geomorphic indices into a single relative active tectonic index. The results reveal distributed tectonic activity across NNE- and NW-oriented fault systems, with highly segmented fault morphology indicating ongoing growth and interaction. The landscape response to tectonic uplift is significantly influenced by the interplay of glacial erosion, precipitation, lithology and isostatic rock uplift. The study extends the understanding of glacial imprint on topography and proposes fault growth by segment linkage based on morphometric analyses. Detailed analysis of tectonic activity using morphometric properties identifies areas of concentrated uplift and likely potential trends of fault propagation. While geomorphic indices serve as preliminary tools for neotectonic investigations, their interpretation will be considering lithological and climatic controls. The research provides insights into the complex dynamics of the western flank of the Principal Cordillera and establishes a foundation for future detailed neotectonic studies in the region.

KEYWORDS: Relative tectonic activity index; Geomorphic indices; Normalized channel steepness; Local relief; Tectonic activity; Glacial Imprint

3.1 Introduction

Tectonic geomorphology is a crucial tool for identifying active faults and assessing seismic hazards, as well as studying landscape evolution (E. Keller and Pinter, 2002). On a regional scale, the initial approach involves assessing the relative tectonic activity classes in mountain fronts or other structural elements during the Quaternary (Bull and McFadden, 1977). This approach utilizes various geomorphological indices and landscape parameters derived from digital elevation models (DEM) and processed with geographic information systems (GIS). These tools enable regional surveys of recent tectonic deformation patterns associated with range-bounding fault zones (e.g., Silva et al.,

[1]Article in Preparation

2003; Pedrera et al., 2009; Dehbozorgi et al., 2010; Giaconia et al., 2012; Yıldırım, 2014; Matoš et al., 2016; Camafort et al., 2020; Rimando and Schoenbohm, 2020; Oviedo-Reyes et al., 2024).

Given the wide variety of morphometric indices, one approach to assess relative active tectonics involves evaluating the entire area rather than just along the mountain front (e.g., Bull and McFadden, 1977; Silva et al., 2003; Yıldırım, 2014; Oviedo-Reyes et al., 2024). This method assesses relative tectonic activity using a single index, such as relative tectonic activity index (Iat) (e.g., El Hamdouni et al., 2008; Dehbozorgi et al., 2010) or RTA (e.g., Matoš et al., 2016), which are computed as an average or overlay in GIS, respectively. The latter approach provides regional insights that are not fully captured by indices applied solely to the piedmont-mountain junction, such as mountain front sinuosity (Smf) and valley shape (Vf). This area is assessed using the drainage basin as the geomorphological unit, a natural and unmodifiable feature that provides a consistent and comprehensive framework for analysis using the available geomorphic indexes.

The western slope of the Principal Cordillera (WSPC) in the Chilean Andes comprise a significant geomorphological feature known as the Western Andean Front (WAF). The WAF is a distinct landscape that occupies the region between the Central Valley and the western flank of the Principal Cordillera, stretching from 15°S to 39°S. It encompasses the first topographical rises of the Principal Cordillera, marking the transition from the relatively flat Central Valley to the mountainous terrain. An essential component of the WAF is its piedmont zone, which encompasses the transitional area where the mountain front meets the adjacent lowlands. The piedmont zone in the WAF, particularly between $\sim$35° and 37°S, is characterized by a series of linear scarps of generally NE trend which formed in recent sedimentary deposits (alluvial and volcanic deposits)(e.g., Maldonado et al., 2021; Melnick and Echtler, 2006), and similar to those observed to the north, near the city of Santiago (e.g. Armijo et al., 2010; Vargas et al., 2014; Riesner et al., 2017). Preliminary hypothesis suggests that these morphotectonic landforms are controlled by several thrust faults with vergence towards the west during Quaternary span (e.g., Maldonado et al., 2021; Melnick and Echtler, 2006; Oviedo-Reyes et al., 2024), concordant with the same observations which were made along the San Ramon fault trace (e.g., Armijo et al., 2010; Vargas et al., 2014).

Along the piedmont-mountain junction between 35°S and 38°S, morphometric indicators such as mountain front sinuosity (Smf), valley shape (Vf), SL index channel metrics, and swath topographic profiles exhibit notable variations from south to north, with a distinct transition at approximately 36°S (Oviedo-Reyes et al., 2024). These variations indicate that north of 36°S, climatic factors primarily drive the changes, whereas south of this parallel, tectonic activity is the dominant influence. However, SL anomalies suggest a more non-tectonic control (e.g., lithology, landslides, dams) than uplifting, specifically from basin outlets to regional drainage divide (Oviedo-Reyes et al., 2024).

Another crucial aspect to consider is the uncertainty surrounding which signals within the drainage basins respond to active tectonics as proposed by Oviedo-Reyes et al. (2024), and whether these signals can be distinguished from those identified by other morphometric indices. Additionally, it remains unclear whether these signals offer novel insights into assessing areas beyond the mountain front.

The aim of this research is to conduct a comprehensive tectonic geomorphological analysis of the WSPC in the Chilean Andes between 35°S and 38°S. We apply a wide range of morphometric indices (e.g., hypsometry, basin asymmetry, basin elongation ratio, steepness index – Ksn, normalized profiles, local relief, slope-angle variability) and a relative tectonic activity index (such as IAT or RAT) across entire drainage basins to test the hypothesis proposed by Oviedo-Reyes et al. (2024) that landscape evolution north of 36°S is primarily controlled by climatic factors, while tectonic forces dominate south of this latitude. By evaluating the effectiveness of various geomorphic indices in distinguishing between climatic and tectonic signals, particularly beyond the piedmont-mountain junction, we aim to identify potentially active fault systems and provide a more nuanced understanding of the interplay between climate and tectonics in shaping the WSPC landscape during the Quaternary.

3.2 Regional Setting

The Forearc region in the southern central Andes (south of 33°S) is physiographically constituted into three trench-parallel continental morphotectonic features (Muñoz and Charrier, 1996; Rehak et al., 2010): Coastal Cordillera (CC), Central Valley (CV) and Principal Cordillera (PC) (Figure 3-1). Firstly, the Coastal Cordillera consists in the western flank mainly in Carboniferous to Jurassic metamorphic to intrusive basement covered by Miocene sedimentary succession to recent marine deposits, conversely in the eastern flank consists in east dipping Cretaceous sequences (e.g., SERNAGEOMIN, 2003; Farías et al., 2008; Armijo et al., 2010; Riesner et al., 2017). At 35°30'S the geological relationship between both flanks of the Coastal Cordillera changes to give way only to a Silurian to Permian metamorphic to intrusive basement with some Cretaceous intrusives. Secondly, the Central Valley particularly consist in a filled depression with Quaternary sediments and ignimbrite cover around ∼500 m (SERNAGEOMIN, 2003; Farías et al., 2008; Armijo et al., 2010; and references therein) and finally, the Principal Cordillera exhibits a Cenozoic sequences in the west to Mesozoic sequences in the most eastern portion, with variations N-S to Miocene intrusives. The Abanico Formation (Eocene-Miocene) extends from Central Valley to easternmost part of Principal Cordillera, this unit is overlying by Farallones Formation (Miocene) (e.g., SERNAGEOMIN, 2003;

Farías et al., 2008; Armijo et al., 2010) (Figure 3-2).

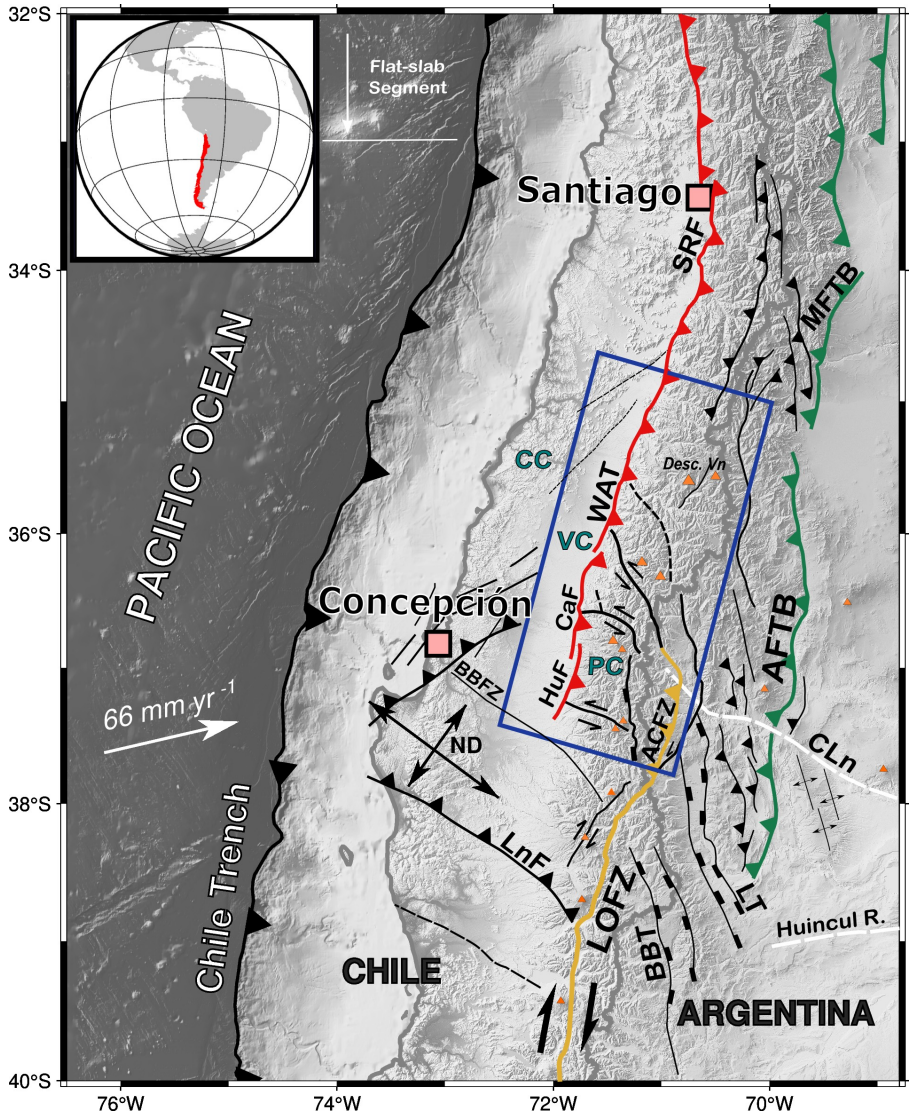


Figure 3-1: Tectonic and structural features of the study area (blue box) in the Central and Southern Andes of Chile (35°-38°S) (Modified from Oviedo-Reyes et al. (2024)). Notable features in this region include the Coastal Cordillera (CC), Central Valley (VC), and the Principal Cordillera (PC). The mountain-piedmont junction in the study area extends NNE parallel to Principal Cordillera and in agreement with the Huépil and Cachapoal faults with the Western Andean Thrust (WAT). Main volcanoes are highlighted (orange triangles). **HuF**: Huépil fault; **CaF**: Cachapoal fault; **WAT**: West Andean Thrust; **SRF**: San Ramon fault; **ACFZ**: Antiñir-Copahue fault System; **BBT**: Bío Bío Trough; **LT**: Loncopué Trough; **ND**: Nahuelbuta Range; **LnF**: – Lanalhue fault; **LOFZ**: Liquiñe Ofqui Fault System; **AFTB**: Agrio Fold Thrust Belt; **MFTB**: Malargüe Fold Thrust Belt; Huincul Ridge; **BBFZ**: Bío Bío fault zone; **CLn**: Cortaderas Lineament.

The Western Andean Front (WAF) consists of the landscape between the western flank of Principal Cordillera and the Central Valley. According to Armijo et al. (2010), the WAF near 33°S (nearby to Santiago) is controlled by the San Ramón fault, where Quaternary and older sediments are overthrusted by deformed rocks of the Principal Cordillera (Abanico Formation). The San Ramón fault is part of a west-vergent active fault propagation fold system, also known as the West Andean Thrust, parallel to the subduction zone and responsible for uplifting the highest portions of the Chilean Andes (Muñoz and Charrier, 1996; Armijo et al., 2010; Vargas et al., 2014). This system,

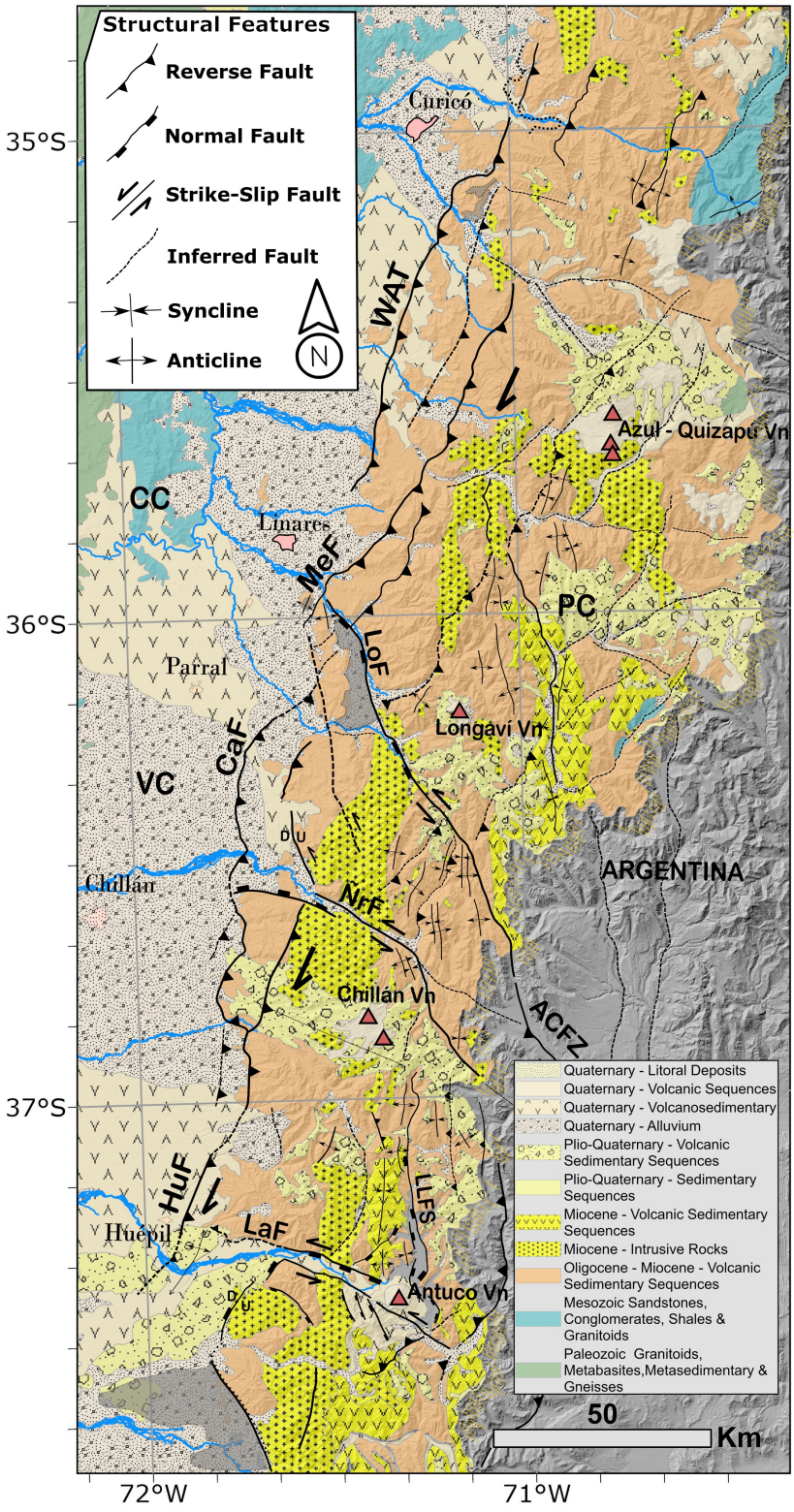


Figure 3-2: Geologic map of the study area between 35°S and 38°S superimposed over hillshade from ALOS AW3D30 30m (modified from Oviedo-Reyes et al. (2024)) Geological map from Sernageomin (2003). Main volcanoes are highlighted (red triangles). **ACFZ**: Antiñir- Copahue fault system; **WAT**: West Andean Thrust; **CaF**: Cachapoal fault; **LoF**: Longaví-Achibueno Fault; **MeF**: Mesamávida Fault; **ÑrF**: Ñuble River fault; **LaF**: Laja River fault; HuF: Huépil fault.; **LLFS**: Lago Laja fault system. **PC**: Principal Cordillera, **VC**: Central Valley, **CC**: Coastal Cordillera. In the figure, the grid is based on the WGS 1984 UTM Zone 19S reference system, while the DEM is projected with a scale in meters.

primarily west-vergent, was initially defined in northern Chile (15°-27°S) between 15 Ma and 4.8 Ma. Armijo et al. (2010) estimate a long-term average slip rate of 0.3 mm/yr for the San Ramón Fault, while Vargas et al. (2014) identified two major seismic events (Mw $>$ 7) in the past 19 ka.

Encinas et al. (2021) propose an evolution model that suggests a complex tectonic history of the forearc in south-central Chile (37-42°S) during the late Cenozoic. According to this model, after a period of extensional tectonics in the Oligocene-early Miocene, a significant compressive phase occurred around 19 Ma, causing the deformation of older strata and the growth of the Andean Cordillera. The activation of the Western Andean Thrust, a major thrust fault at the boundary between the Central Depression and the Principal Cordillera, caused significant uplift of the western flank of the Andes from at least the Pliocene to the present ($\sim$5 Ma). This triggered flexural subsidence, accumulating thick sedimentary deposits in the forearc during the Plio-Pleistocene. The sudden increase in sediment flux to the oceanic trench caused a change from non-accretion or subduction erosion to accretion at the margin, giving rise to the Coastal Cordillera as a forearc high in the last 2 Ma (Encinas et al., 2021).

Geomorphologically, the primary trunk channels exhibit a NW trend, nearly perpendicular to the main morphotectonic features (Figure 3-2). The NW trend of some river valleys likely indicates structural control by shear zones similar to the Cortaderas Lineament (Figure 3-1, Lupi et al., 2020; Oviedo-Reyes et al., 2024). These drainage systems follow the regional slope, depositing sediments in the Central Valley, primarily as alluvial fans. Sedimentary deposits are thicker on the WAF than on the western foothills of the Coastal Cordillera (e.g., Encinas et al., 2021).

On the other hand, the regional features of the drainage systems, as well as the quaternary within the principal valleys, and the deposits over the Central Valley, contain the geological record to understand how the western flank of the Principal Cordillera has been uplifted during the upper Pleistocene to the Holocene timespan. In addition, the main trunk channels have a NW trend nearly perpendicular to main morphotectonic features (Figure 3-2). For example, in the study area the Maule River basin is only which watershed boundaries borders the eastern slope of the Andes Mountain Range. Many sub-basins at south of 36°, smaller in size, are attached with these regional basins (e.g. Rio Diguillin, Lontué, Maule) but their trend is SW (Figure 3-2). As for the NW trend of some river valleys is probable that exists a structural control compatible with possible shear zones similar to the Cortaderas Lineament (Figure 3-1, Lupi et al., 2020; Oviedo-Reyes et al., 2024) (e.g. Laja River fault). These drainage systems run on the regional slope (e.g., minimum elevation), and consequently the sediments transported are deposited over the Central Valley mainly in alluvial fans. The thickness of these sedimentary deposits is greater on the WAF than on the western foothills of the Coastal Cordillera. However, the occurrence of terraces confined to the main valley of the

drainage systems, which present different levels recording changes in the base level, might also represent periods of aggradation by deglaciation, or others climatic factors occurred in the highest parts of the Andes.

On the other hand, the Andean Mountain Range exerts a profound influence on regional climate, manifesting most notably in the formation of the 'Arid Diagonal', a salient feature on the western flank of the northern and central Andes. It is an extensive and continuous arid strip that starts in the Pacific Ocean in Peru (south of Ecuador) and runs in SE direction up to the Atlantic Ocean, in the NE coast of Patagonia (43°S) (Abraham et al., 2020). The prevailing atmospheric circulation transports moisture from the Amazon Basin (e.g., South American Monsoon) to the eastern Andean slopes, engendering enhanced precipitation. Conversely, as air masses descend the western slopes, it becomes drier, creating conditions for arid or semi-arid environments in some areas. In the southern Andes, the arid diagonal undergoes a progressive inversion, with winter precipitation influenced by mid-latitude storm tracks or westerlies. Thus, south of 35°S, the annual rainfall is primarily influenced by mid-latitude storm tracks, delivering moisture from the Pacific to the western side of the Andes, while the eastern side experiences reduced rainfall due to the orographic barrier effect (Stalder et al., 2020; and references therein). As a result, in the study area, the climate is characterized by warm, dry summers and cool, wet winters (Mediterranean climate). However, local topography, elevation, and other factors contribute to variations within these regions (Montgomery et al., 2001).

3.3 Data and Methods

In this quantitative approach from morphometric analyses, we computed topographic parameters from Digital Elevation Model (DEM) – ALOS AW3D30 30 m, the choice of this digital model is based on the fact that the AW3D30 has recently been found to exhibit vertical and channel profile accuracy (comparing with SRTM and TanDEM-X models), which is reliable in steep mountain areas (Tarolli and Mudd, 2020) such as western slope in the southern central Andes.

3.3.1 Mountain front sinuosity (Smf)

The mountain-front sinuosity index (Smf) is defined by Bull and McFadden (1977) as:

$$Smf = \frac{Lmf}{Ls} \tag{3.1}$$

where Smf is the ratio of the planimetric length along the mountain-piedmont junction (Lmf) and the straight-line of the mountain front (Ls; Bull, 2007). The Smf reflects the balance between

erosional processes and tectonic uplift operating at the scale of a given mountain front (Bull and McFadden, 1977; E. Keller and Pinter, 2002; Bull, 2007) (Figure 3-3a). The values of this index are generally lower than 3 with higher values representing the most sinuous segments (Bull, 2007). Some studies have proposed that Smf < 1.4 are indicative of tectonically active fronts (Rockwell et al., 1985; Wells et al., 1988; Silva et al., 2003). In this study, we defined tectonically controlled mountain front segments using an upper limit of Smf < 1.5. We utilized data obtained by Oviedo-Reyes et al. (2024), who mapped a total of 45 NE to NW-oriented segments within the study area to compute Smf. These segments represent a combined length (Lms) of 609.52 km. North of 35°51´S, the average length of the mapped segments is 20.09 km, while south of this latitude, the mean segment length is 11.64 km.

3.3.2 Valley floor width-to-height ratio (Vf)

Vf is a morphological index that describes the shape of a valley cross-section and its degree of maturity. It is defined by Bull and McFadden (1977) as:

$$Vf = \frac{2Vfw}{(Eld - Esc) + (Erd - Esc)} \tag{3.2}$$

where Vfw is the valley width, Eld and Erd are the elevations of left and right divides, respectively, and Esc is the elevation of the valley floor (Figure 3-3b). This index has been considered to differentiate V-shaped valleys (Vf<0.5), usually resulting from high fluvial incision related to rapid uplift, from U-shaped valleys (high Vf values) reflecting less incision and degradation processes such as valley widening and ridge-crest lowering (e.g., Bull, 2007, 2011). In this study, we used the data obtained by Oviedo-Reyes et al. (2024), where Vf was determined at ∼0.5 to 1 km upstream from the outlet of the 97 drainage basins.

3.3.3 Asymmetry Factor (AF)

The asymmetry factor (AF) is a geomorphic index used to evaluate tectonic tilting in drainage basins (e.g., Hare and Gardner, 1985; El Hamdouni et al., 2008; Dehbozorgi et al., 2010; Pérez-Peña et al., 2010; Matoš et al., 2016; Saber et al., 2018; García-Delgado and Velandia, 2020). Here, we used the modified definition by Pérez-Peña et al. (2010):

$$AF = |50 - A_R * A_T/100| \tag{3.3}$$

where AR is the basin area to the right of the main channel facing downstream, and AT is the

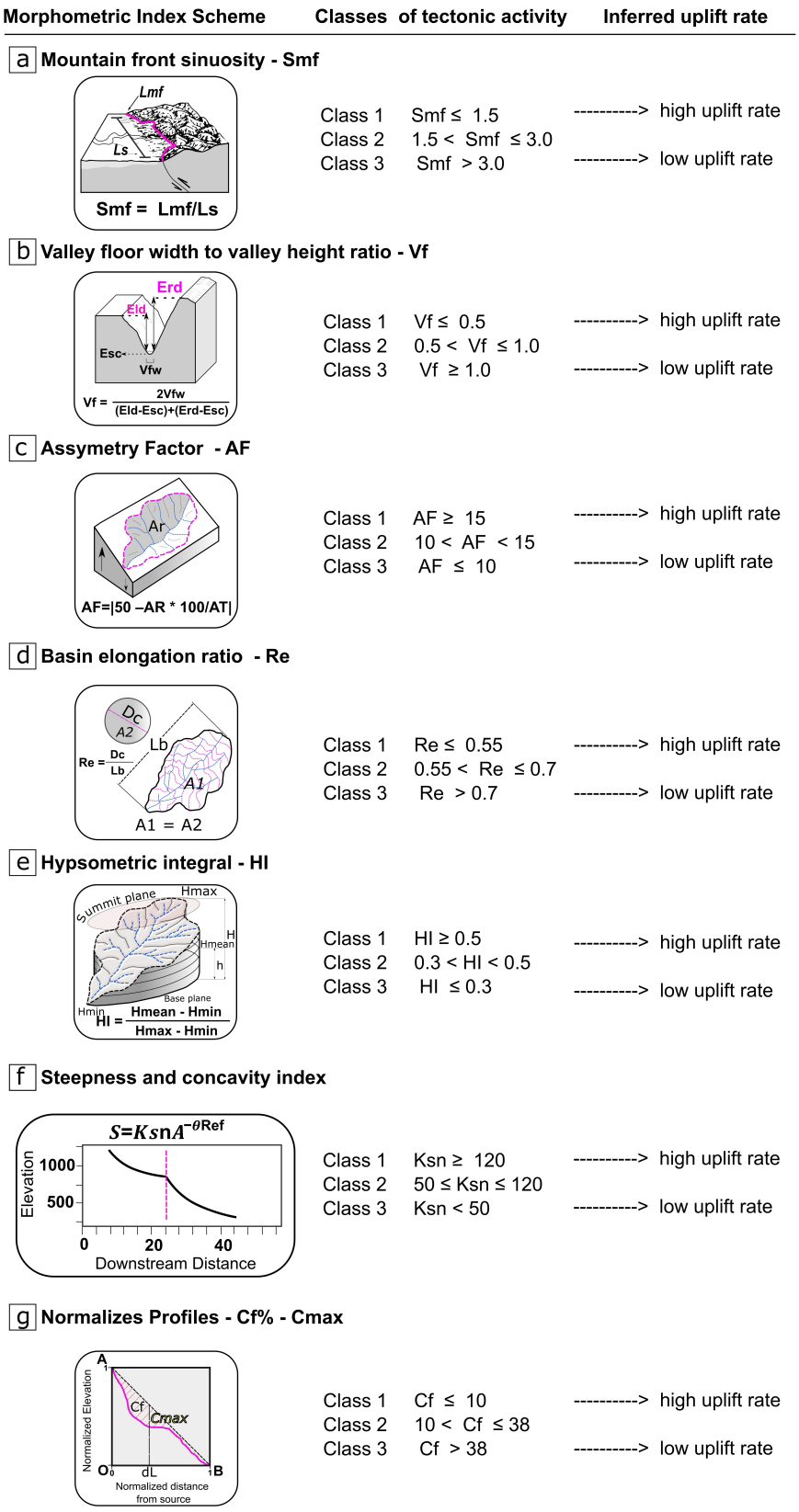


Figure 3-3: Diagrams of the morphometric indices applied in the WSPC. Each index is graphically represented considering the parameters for computing them. The uplift rate inferred from the individual analysis of each metric is indicated.

total basin area. Using the values around 50 indicating symmetric basins, while deviations suggest asymmetry due to tectonic tilting, lithological control, or differential erosion (E. Keller and Pinter, 2002; Pérez-Peña et al., 2010) (Figure 3-3c). Thus, the absolute deviation from perfect symmetry (AF = 50) and includes a vector indicating the asymmetry direction. They classified basins as: symmetric (AF $<$ 5), gently asymmetric (AF = 5–10), moderately asymmetric (AF = 10–15), and strongly asymmetric (AF $>$ 15). In order to apply the Iat and RTA indexes in the WSPC, we modified the range of the tectonic activity classes to normalize the data between morphometric indexes.

3.3.4 Basin Elongation Ratio (Re)

The elongation ratio (Re) is a dimensionless index that quantifies the planimetric shape of a drainage basin. It is widely used in tectonic geomorphology studies to infer tectonic activity and landscape evolution processes (e.g., Rimando and Schoenbohm, 2020; Krystopowicz et al., 2020). It is defined as the ratio of the diameter of a circle with the same area as the basin (Dc) to the maximum basin length (Lb):

$$Re = \frac{D_c}{L_b} = \frac{2}{L_b}\sqrt{\frac{A}{\pi}} \tag{3.4}$$

where Dc is the diameter of a circle with the same area as the basin; Lb is the maximum basin length (basin chord), measured as the longest distance between two points on the basin boundary and A correspond to the basin area (Figure 3-3d). The basin elongation ratios were obtained using ArcGIS procedures (Rimando and Schoenbohm, 2020); where the basin length (Lb) was calculated using the minimum bounding geometry such as an expression of the maximum extents of a two-dimensional object (e.g., drainage basin).

The elongation ratio ranges from 0 to 1, with values closer to 1 indicating a more circular basin shape (watershed steady), and values closer to 0 indicating a more elongated basin shape (watershed migrating). The index is used to infer tectonic activity, as elongated basins (Re = 0.5-0.7) are associated with high-relief and steep slopes characteristic of active uplift, while circular basins (Re $\approx$ 1) are associated with low-relief and gentle slopes characteristic of low uplift rates (Cannon, 1976; Ramírez-Herrera, 1998; Bull, 2007). Shapes defined by the elongation ratio are as follows: not elongated (0.85–1.0), slightly elongated (0.7–0.85), elongated (0.55–0.7), and highly elongated ($<$ 0.55) (Cannon, 1976).

3.3.5 Hypsometry

Hypsometry is the measurement and analysis of the elevation distribution of a land surface (Strahler, 1952; E. Keller and Pinter, 2002). The percentage hypsometric curve (area-altitude curve) correlates the horizontal cross-sectional area of a drainage basin with its relative elevation above the basin mouth (Strahler, 1952). The hypsometric curve is generated by plotting the proportion of total basin height (relative height) against the proportion of total basin area (relative area) (E. Keller and Pinter, 2002) and the hypsometric integral is defined as the area under the hypsometry curve (E. Keller and Pinter, 2002; Strahler, 1952).

One key attribute of the hypsometric curve is its independence from differences in catchment size and relief, as area and elevation are normalized to total area and total elevation, allowing for the comparison of drainage basins of varying sizes (Strahler, 1952). Constructing a hypsometric curve consider the cumulative distribution function of elevations in a region, with relative height (h/H) on the vertical axis and the relative area (a/A) on the horizontal axis (Figure 3-3e). Where, h is the elevation above the lowest point in the area, H is the total elevation range (difference between the highest and lowest points), a is the area above a given elevation, and A is the total area of the region. On the other hand, the hypsometric integral (HI) is calculated from three values using the following equation:

$$HI = \frac{H_{mean} - H_{min}}{H_{max} - H_{min}} \tag{3.5}$$

where H_{mean} is the mean elevation, H_{min} is the minimum elevation, and H_{max} is the maximum elevation. HI values range between 0 and 1. The hypsometric integral (HI) is known to be sensitive to uplift rates, erosional resistance of lithological units and climatological effects (Lifton and Chase, 1992; Masek et al., 1994; Chen et al., 2003). The effects of this variables in the HI response lies mainly on scale dependence, for example smaller basins tend to show stronger lithological control (100 km^2); instead, large scale basins (1000 km^2) showed more influence in a tectonic input (e.g., Lifton and Chase, 1992).

Using the ArcGIS extension CalHypso (Pérez-Peña et al., 2009), we extracted the hypsometric curve (HC), hypsometric integral (HI), and statistical moments (Skewness, kurtosis, density skewness, and density kurtosis) for 97 basins in the WSPC. Describing the shape of the hypsometric curve can be more informative than relying on a single value, such as the hypsometric integral (Zhang et al., 2020; Rimando and Schoenbohm, 2020). The HC shape is especially relevant because the hypsometric integral value tends to stabilize below 0.6 or 0.5 over time, even though different shapes

of hypsometric curves may correspond to these values (Rimando and Schoenbohm, 2020). However, previous studies showed that basin hypsometry is dependent on the shape or size of the catchment (Willgoose and Hancock, 1998; Korup et al., 2005; Cheng et al., 2012). In general, the shape of the hypsometric curve indicates the landscape's erosional stage. A convex shape suggests a relatively young area, while an S-shaped or concave curve indicates moderate to high erosion (E. Keller and Pinter, 2002). Despite the limitations, Cheng et al. (2012) demonstrated that HI and HC is useful to describe balance between erosion and uplift. To explore hypsometric curves in the study area, we analyzed four shape types based on five reference points according to normalized profile position: convex, convex-mouth, S-shaped, complex, and concave (e.g., Pérez-Peña et al., 2010). The convex-mouth shape is defined by point C' in the last section of the plot, while convex shapes rise before the basin midpoint (midpoint AB'). Concave curves lie below reference points, and S-shaped curves have a lower h/H ratio than convex-mouth shapes.

3.3.6 Topographic and river profile analysis

Topographic metrics derived from the DEM include local relief, slope-angle variability, and river profiles. Local relief was determined by calculating the difference between the minimum and maximum elevations within a 1.4 km radius, considering the average valley spacing among 97 basin outlets. We extracted a local relief map of the western slope of the Principal Cordillera to produce a general overview of the regional spatial variation in fluvial incision patterns (e.g., Masek et al., 1994; Scotti et al., 2014; Erbello et al., 2022). Slope-angle variability refers to the difference between the maximum and minimum slope angles within the study area. This was also calculated using a 1.4 km radius with the Spatial Analyst tool in ArcGIS Pro, utilizing the slope data from the DEM. Identifying incision patterns due to regional uplift using these DEM-based metrics (e.g., Montgomery and Brandon, 2002; Scotti et al., 2014) requires evaluating them in conjunction with other metrics like K_{sn} to achieve more comprehensive analysis (e.g., Clementucci et al., 2022).

Building on the methods described earlier, we analyze spatial variations in topography through planimetric indices (e.g., basin elongation ratio, asymmetry factor, mountain front sinuosity, valley shape) and volumetric indices (e.g., hypsometry). These indices primarily utilize drainage basins as geomorphological descriptors, considering their area and relative elevation to discriminate tectonic signals (e.g., Krystopowicz et al., 2020; Erbello et al., 2022). However, analyzing drainage networks through longitudinal profiles helps decipher the uplift history of an active mountain range (e.g., E. A. Keller, 1986; Demoulin, 1998; Wobus, Tucker, and Anderson, 2006; Mere and McPhillips, 2024). Here, we considered the detachment-limited stream-power incision model, expressed by the equation

(Howard, 1994; Whipple et al., 2000):

$$\frac{dz}{dt} = U - E = U - KA^m S^n \tag{3.6}$$

where E is channel incision of bedrock rivers, U is the rock uplift rate, K is the dimensional erodibility coefficient that encompasses the effects of lithology, climate, incision process, and hydrology (Whipple et al., 2000). A is upstream drainage area, S is the local channel slope, and the exponent m refers to watershed hydrology and n account for the physical process of incision (Howard, 1994 Whipple et al., 2013). The stream-power-based analysis assumes topographic steady state (dz/dt =0), such that uplift equals incision (E=U), and spatially uniform incision within the channel. The rearranged terms in the geometrical relationships of Flint's Law (Hack, 1973; Flint, 1974) the steady-state channel gradient can be described as follow (Figure 3-3f):

$$S = (\frac{U}{K})^{\frac{1}{n}} A^{\frac{m}{n}} = k_s A^{-\theta} \tag{3.7}$$

where θ the concavity index and the coefficient ks is called the profile steepness. θ is the river profile concavity and often fixed to a reference value ($0.4 < \theta_{ref} < 0.6$) (Croissant and Braun, 2014) to calculate the normalized channel steepness, which allows the comparison of rivers within a study area (e.g., Wobus, Tucker, and Anderson, 2006):

$$S = K_{sn} A^{\theta_{ref}} \tag{3.8}$$

The K_{sn} value can be used to infer variations in rock uplift rates for steady-state rivers within regions with constant or similar K, such as areas with comparable lithology and climate. The values of K_{sn} and concavity are estimated through logarithmic regression of channel slope and drainage area data. The Flint's equation is applicable only for drainage areas exceeding a critical threshold, Acr, which is variously interpreted as marking the transition from divergent to convergent topography or from debris flow to fluvial processes (Wobus, Tucker, and Anderson, 2006, and references therein). We used an Acr $> 1\ km^2$ and drainage basins with areas $> 2\ km^2$ to include some important zones such as Measamávida Fault. We adopted the Topographic Analysis Kit (TAK) in the TopoToolbox to extract topographic parameters using a $\theta_{ref} = 0.45$ (Forte and Whipple, 2019; Schwanghart and Scherler, 2014) and the ALOS DEM of 30 m resolution.

Alternatively, within river profile analysis techniques, the concavity factor (Cf) and maximal concavity (C_{max}) are particularly effective for assessing whether a stream has attained a graded profile, reflecting equilibrium conditions between erosion and sediment transport, but also can provide

insights into tectonic deformation. The shape of the stream profiles and their deviations from equilibrium are evaluated using the concavity factor (Cf), maximal concavity (C_{max}), and distance from the source ($\Delta l/L$) (Demoulin, 1998). The concavity factor (Cf), ranging from 0% (0.0) to 100% (0.5), indicates the 'eroded area' between the stream profile and a straight line connecting the source and mouth (Demoulin, 1998; Ruszkiczay-Rüdiger et al., 2009; Matoš et al., 2016). Similarly, the C_{max} parameter, ranging from 0 to 1, represents the normalized maximal elevation difference between the stream profile and the source-mouth line. High Cf and C_{max} values suggest streams are closer to a graded profile, while lower values may indicate recent active tectonics or lithological control (Demoulin, 1998; Ruszkiczay-Rüdiger et al., 2009) (Figure 3-3g). Based on graded rivers have a characteristic concave upward profile, with high concavity (Cf) and a maximal concavity (C_{max}) close to the source area (small dL). Deviations from this profile indicate external influences such as resistant bedrock or neotectonic activity (Holbrook and Schumm, 1999; Gelabert et al., 2005) through inflection features known as knickpoints (Whipple et al., 2000). The knickpoint yields changes in the concavity along the longitudinal profile (Pérez-Peña et al., 2017). We computed 97 normalized river profiles along the trunk channel of the study area using the ArcGIS Pro elevation profile tool and Python code to visualize the parameters C_{max}, Cf%, and ΔL for each profile.

3.3.7 Polynomial regression by machine learning

Machine Learning (ML) methods have been employed in various geoscientific applications, such as estimating debris flow volumes (Huang et al., 2020), regional mapping of soil parent material (Lacoste et al., 2011), and understanding the evolution of complex landforms (Brigham and Crider, 2022). ML methods predict or identify patterns using a sample of the data (training data) and then test the statistical model on a different set of observations (test data) (Bishop, 2007). To assess the regional trends of morphometric index values along the western flank of the Principal Cordillera, we applied polynomial regression with ML to thirteen parameters vs Distance. We utilized Python functions from the Scikit-learn library (Pedregosa et al., 2011), with the training data comprising 30% and the test data 70% of the Smf data to generate a statistical model. The model's performance was estimated using K-fold cross-validation (e.g., CV = 5), performed multiple times with different splits each time. A plot of complexity versus generalization error estimated via CV was created to determine the optimal polynomial order (e.g., degree 5). We validated the model's complexity by ensuring the generalization error (EG) closely matched the training error (ET).

3.3.8 Rock Strength (RS) – Mean Annual Precipitation (MAP)

Lithology significantly impacts geomorphic indices interpretation in various tectonic settings (Yıldırım, 2014; Bursztyn et al., 2015; Gao et al., 2023). Localized controls like lithologic knickpoints can obscure K_{sn} or SL map interpretation (Troiani et al., 2014; Demoulin, 1998). To isolate the regional tectonic signal, we used the integrated raster weighting rock strength and precipitation proposed by Oviedo-Reyes et al. (2024).

We generated a rock strength map (RS) from the Chilean Geological chart (SERNAGEOMIN, 2003), considering rock type and constituent material. Our lithological matching was compared with similar studies (e.g., El Hamdouni et al., 2008; Yıldırım, 2014; Bursztyn et al., 2015). We established five rock strength levels, acknowledging regional dependency. Precipitation data (MAP) was acquired from CR2MET (Alvarez-Garreton et al., 2018). RS map data was converted to match MAP resolution (∼5 km). Here, we reinterpreted the unified raster levels in terms of probability, categorizing them into five classes ranging from very low to high probability, adapting the approach proposed by Oviedo-Reyes et al. (2024). In our framework, the RS-MAP values represent the probability of encountering specific combinations of rock strength (high/low) and mean annual precipitation (high/low).

The primary purpose of the RS-MAP map is to integrate both rock strength and precipitation signals, facilitating rapid assessment of non-tectonic influences on landscape evolution. However, for a comprehensive interpretation of erosional processes, consultation of the individual base maps (rock strength and mean annual precipitation) remains essential.

3.3.9 Relative tectonic activity index (Iat-RTA)

Assessing active tectonics involves evaluating the entire area using indices such as the relative tectonic activity index (Iat) or RTA (e.g., El Hamdouni et al., 2008; Dehbozorgi et al., 2010; Matoš et al., 2016), which provide regional insights not fully captured by indices applied solely to the piedmont-mountain junction, like mountain front sinuosity (Smf) and valley shape (Vf). The relative tectonic activity index (Iat) defined by El Hamdouni et al. (2008) is calculated like an average of several geomorphic index classes (S/n) and is divided into four categories: Class 1 represents very high tectonic activity with S/n values between 1 and <1.5; class 2 indicates high tectonic activity with values of $1.5 \leq S/n < 2$; class 3 signifies moderately active tectonics with values of $2 \leq S/n < 2.5$; and class 4 denotes low tectonic activity with S/n values ≥ 2.5. We applied a hierarchical classification of seven morphometric indices into three classes, where class 1 indicates high tectonic activity and class 3 indicates low tectonic activity. Iat is an efficient tool

that does not require extensive calculation time, making it practical for large-scale regional studies. However, in ranking tectonic classes by morphometric index, local perturbations in topography due to tectonic deformation over the limits of deformation zones, such as rejuvenation, are not considered. This method generalizes deformation into a single value, as observed in hypsometric or normalized river profiles. Therefore, it is crucial to exercise caution when determining the classes for each geomorphic index, as these classifications depend on the specific range of data obtained for the study area. Despite these limitations, Iat remains a reliable tool for regional identification of tectonic activity, providing a broad overview of tectonic patterns.

On the other hand, the RTA index (Matoš et al., 2016) provides a more suitable and detailed framework for assessing regional tectonic activity compared to other indices. Utilizing GIS overlay techniques for its calculation, the RTA index integrates local relief and slope angle variability on a pixel-by-pixel basis. This granular approach captures the intricacies of topographic deformation, offering a more comprehensive view of regional tectonic activity. For instance, significant variations in tectonic activity can occur within the same basin from headwaters to the outlet, which the RTA index can effectively identify (e.g., Matoš et al., 2016). We used local relief, slope angle variability, and values of topographic metrics, including mountain front sinuosity (Smf), valley floor width-to-height ratio (Vf), asymmetry factor (AF), basin elongation ratio (Re), hypsometric integral, concavity factor (Cf), and mean K_{sn}. Following the procedures of Matoš et al. (2016), we normalized each morphometric parameter value and converted them into a raster, which was then summarized using the weighted sum procedure. The resulting raster was subdivided into four classes considering Iat range classification.

3.4 Results

3.4.1 Smf/Vf ratio

The results of Smf and Vf analyses, derived from Oviedo-Reyes et al. (2024), highlight significant north-south changes from 35°51'S in the study area. In the north, Smf values characterize inselbergs and piedmont embayments, while low Vf values ($<$0.5) indicate V-shaped valleys (Figure 3-4). The southern segment shows a transient state of the landscape with tectonically controlled segments, notably the Cachapoal Fault (CaF) and Huépil Fault (HuF). From morphometric indexes, the internal mountain front parallel to the CaF displays moderate to high tectonic activity (36°20'S), with the Huepil Fault exhibiting the most tectonic influence (Figure 3-5).

NW faults, such as the Laja River Fault (37°20', LaF), show active segments, while the Longaví-

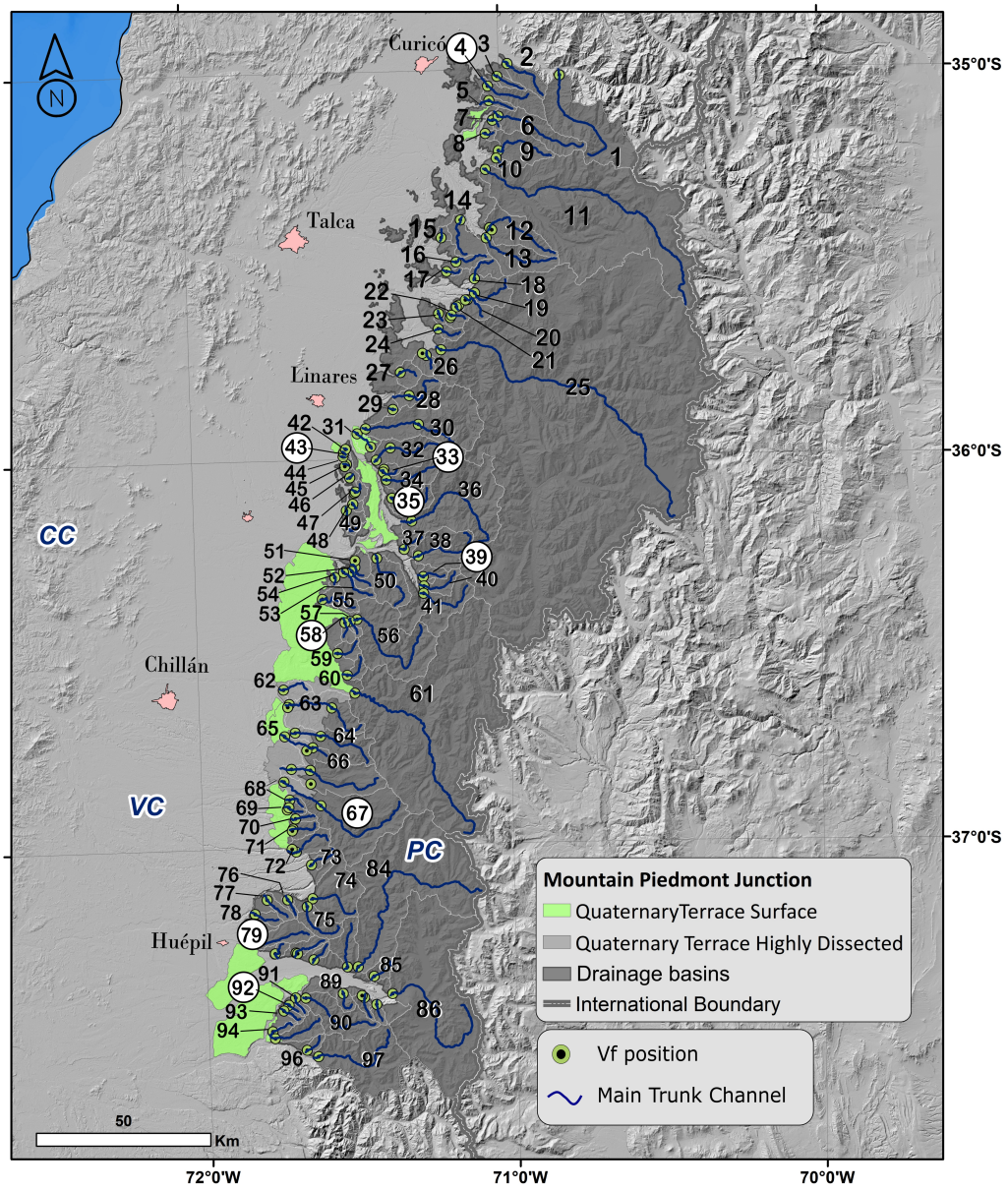


Figure 3-4: Spatial distribution of the basins with Vf positions and trunk channels along the study area between 35° and 37° S (from Oviedo-Reyes et al. (2024)). Coastal Cordillera (CC), Central Valley (VC), and the Principal Cordillera (PC) are depicted. Basin 11: Lontué River; Basin 25: Maule River; Basin 36: Achibueno River; Basin 61: Ñuble River ; Basin 86: Laja River. Drainage basins from 30 to 41 belong Longavi-achibueno river system.

Achibueno Fault (LoF) exhibits moderate activity (Oviedo-Reyes et al., 2024). By adjusting the upper limit of active tectonic segments to Smf = 1.5, we integrated four additional segments to the class 1 proposed by Oviedo-Reyes et al. (2024) shed light into new active segments in the internal mountain front of the CaF, for example, in the San Fabian sector, and and the NW tip of the LoF. Interestingly, the areas with the highest relative tectonic uplift are those at the tips of the NW faults, where these faults intersect with the NNE faults (Table 3.1).

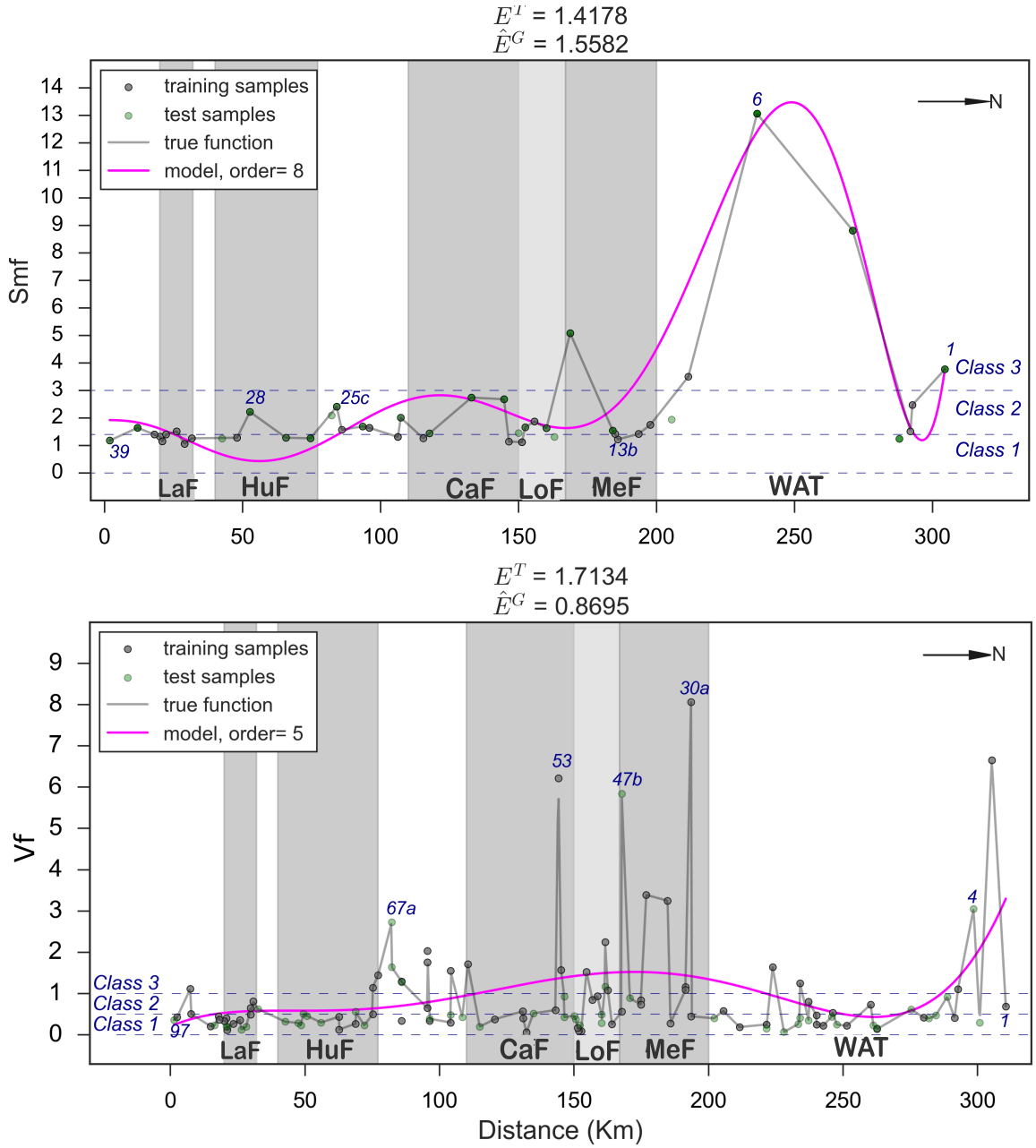


Figure 3-5: Smf and Vf indexes along the Western Andean Front by Oviedo-Reyes et al. (2024). Notice how while there is an increase in Smf values to the north, the Vf values decrease. Smf range data from 1.06 to 13.06. Vf range data from 0.06 to 8.36 (see Figure 3-4 to Vf positions).

3.4.2 Drainage-basin asymmetry factor (AF)

From north to south, the asymmetry factor fluctuates significantly along the distance, there are specific peaks and troughs, indicating areas of strongly asymmetry and symmetry (Figure 3-6). Notable peaks are observed around 0-50 km (LaF), 100-150 km (CaF), and 250-300 km (WAT). About 73% of the basins show some degree of tilting, 23% of the basins are symmetric. In the northern sector of the study area (WAT basins) are exhibited a predominant tilting towards the NNE, with occasional deviations to the NW (35°30'S, Figure 3-7). Notably, a NW tilting trend

is observed along the trace of the Longaví-Achibueno fault (LoF) on its right side, downstream of the drainage system (∼36°S). Notably, the NW termination of the Ñuble River fault also exhibits NW tilting, consistent with the fault kinematics proposed by Oviedo-Reyes et al. (2024). Further south, concentrated tilting is evident at the intersection of the Huepil fault and the Laja River fault (37°15') (Table 3.1).

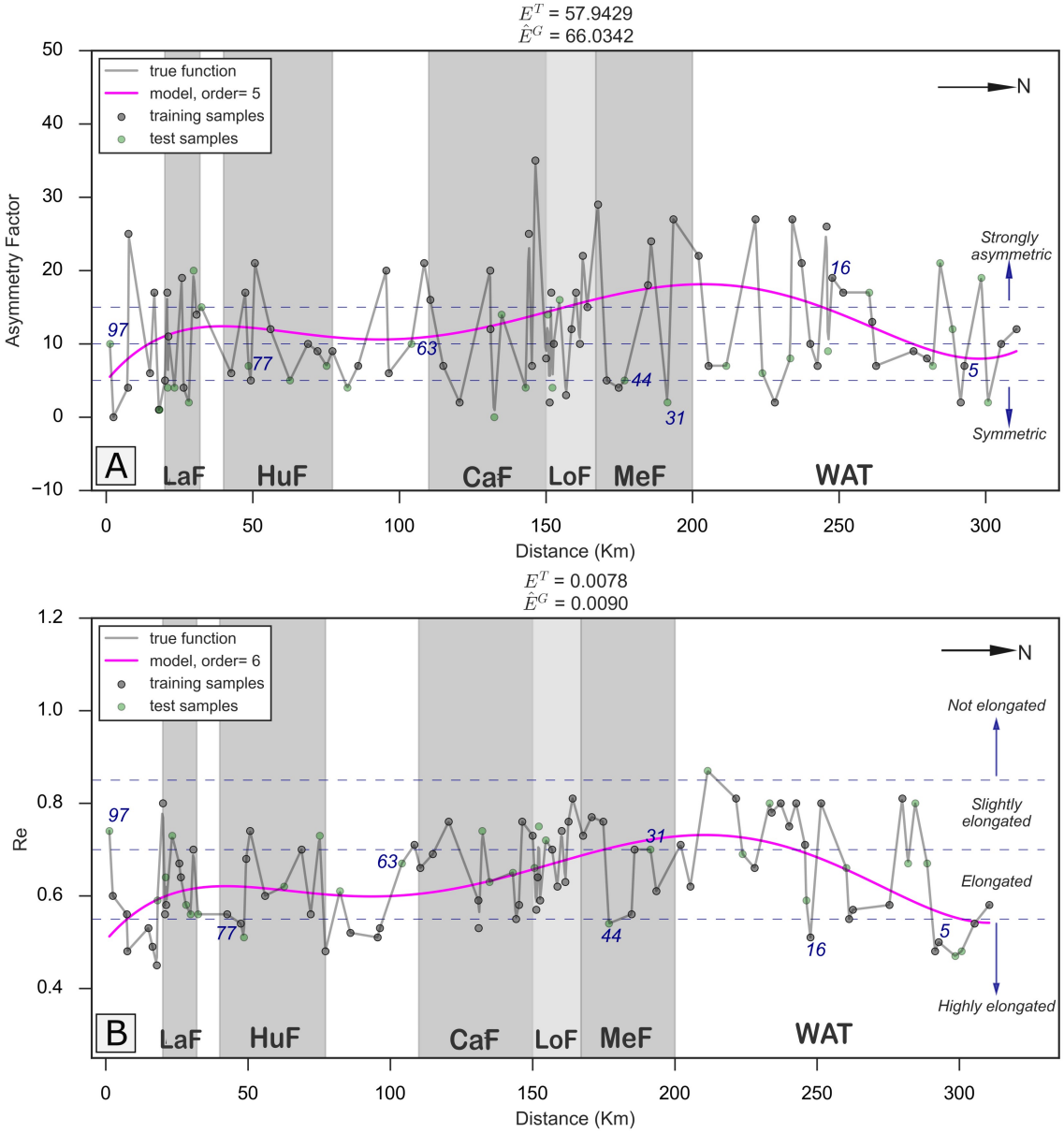


Figure 3-6: Asymmetry Factor and Basin Elongation Ratio (Re) Indices for the Western Andean Front. Note the similarities between the AF and Re curves calculated from the polynomial regression, with curves of order 5 and 6, respectively. A. The AF data range from 0 to 35. Peaks within the original curve do not reveal a clear trend; however, a slight increase towards the north (MeF and WAT) is noted. B. The Re data range from 0.45 to 0.87, with a slight increase similar to the AF index. Both curves indicate a slight correlation between basin shape and tilting: the higher the elongation, the more tilted the basins are.

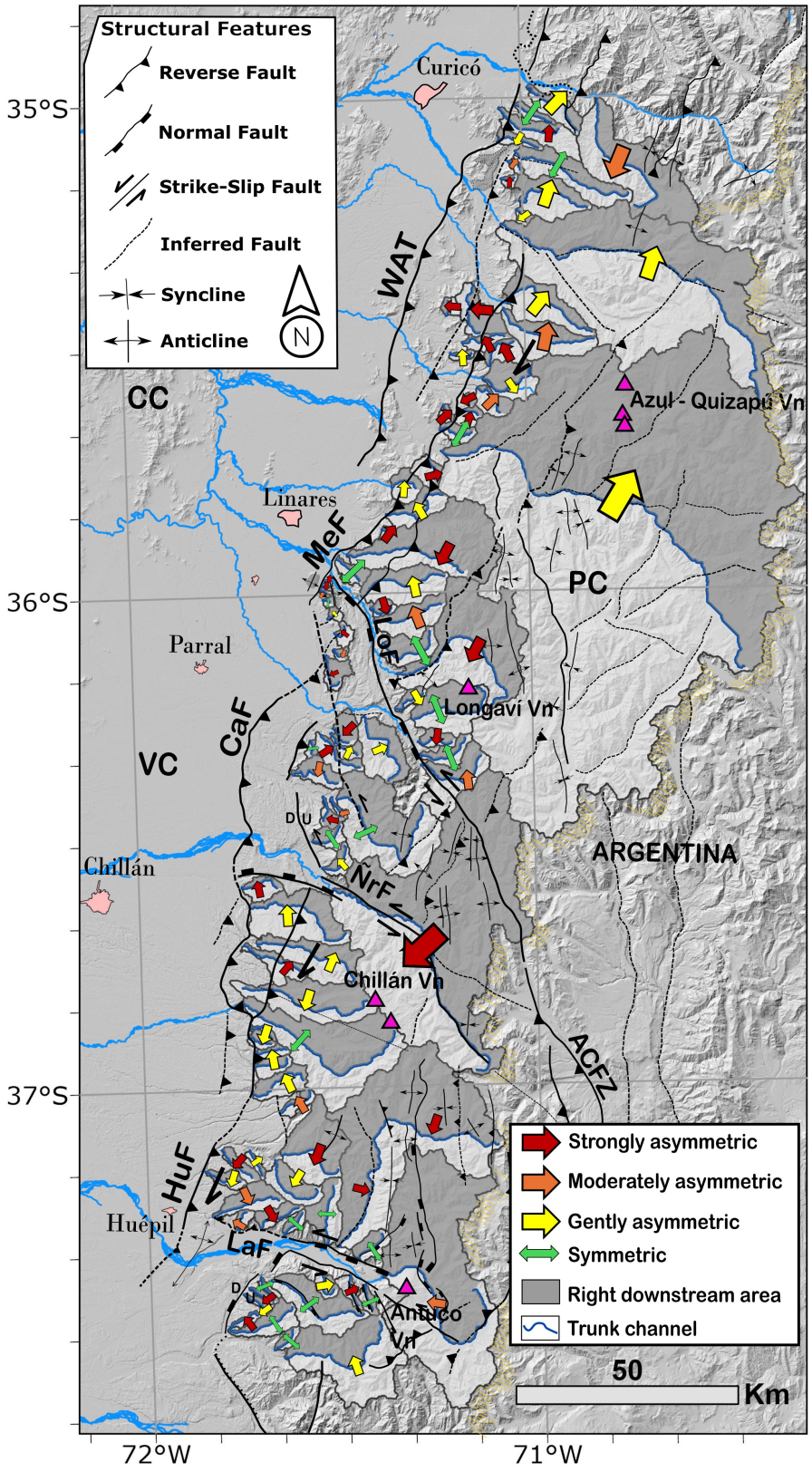


Figure 3-7: Asymmetry factor distribution along the drainage basin in the study area. In dark grey the basins taken on the right are shown below, while the areas on the left are in light grey (see Figure 3-4 to drainage basins position). The size of the arrows does not indicate greater tilting, their size varies to make interpretation easier.

Table 3.1: Basins and related morphometric parameters for the Western Slope of the Principal Cordillera. For the study 97 basins were calculated the following indices: Mountain Front Sinuosity (Smf), Valley Floor Width-to-Height Ratio (Vf), Asymmetry Factor (AF), Basin Elongation Ratio (Re), Hypsometry and Statistical Moments, K_{sn}, Concavity (C_{max}), Concavity Factor (Cf%), and Distance from Source (Δ L) from normalized river profiles. Additionally, the table includes the outlet elevation of basins, area, and Tectonic Relative Index (Iat).

Basin No	Area Km2	Smf	Vf	AF	Re	HI	Skewness	Kurtosis	Density skewness	Density kurtosis	Mean Ksn ($m^{0.9}$)	θ	Cmax	Cf%	dL	Outlet Elevation (m)	Iat
Basin 1	353.73	3.77	0.69	12	0.58	0.35	0.572	2.295	0.348	1.693	138.324	0.525	0.315	39.737	0.266	669	3
Basin 2	59.16	3.77	6.65	10	0.54	0.38	0.497	2.208	-0.002	1.588	82.185	0.651	0.404	48.431	0.439	464	3
Basin 3	19.77	3.77	0.3	2	0.48	0.46	0.546	2.311	0.117	1.677	88.462	0.477	0.213	24.119	0.601	408	3
Basin 4	88.4	3.77	3.05	19	0.47	0.37	0.598	2.348	0.316	1.684	90.866	0.618	0.444	57.595	0.147	342	3
Basin 5	24.23	2.47	1.11	7	0.5	0.37	0.739	2.682	0.488	2.049	62.551	0.695	0.373	42.582	0.467	317	3
Basin 6	149.82	1.51	0.41	2	0.48	0.37	0.557	2.274	0.299	1.64	117.96	0.539	0.258	35.407	0.563	553	2
Basin 7	7.53	1.51	0.92	12	0.67	0.49	0.555	2.333	0.122	1.771	112.222	0.473	0.123	14.54	0.334	577	2
Basin 8	8.84	1.51	0.47	21	0.8	0.45	0.554	2.259	0.389	1.778	99.186	0.548	0.148	17.662	0.468	578	2
Basin 9	116.13	8.81	0.4	7	0.67	0.36	0.527	2.174	0.494	1.76	100.42	0.532	0.291	31.544	0.307	575	3
Basin 10	10.98	8.81	0.42	8	0.81	0.38	0.541	2.271	0.221	1.645	92.07	0.639	0.126	14.537	0.606	621	3
Basin 11	1389.72	8.81	0.62	9	0.58	0.46	0.366	2.088	-0.414	1.808	125.758	0.133	0.169	13.157	0.582	536	3
Basin 12	139.44	8.81	0.15	7	0.57	0.43	0.557	2.306	0.225	1.693	111.027	0.393	0.226	27.712	0.176	653	3
Basin 13	127.49	8.81	0.23	13	0.55	0.43	0.432	2.122	-0.022	1.51	93.99	0.368	0.236	26.457	0.133	728	2
Basin 14	76.5	8.81	0.73	17	0.66	0.35	0.583	2.192	0.804	2.172	52.691	0.644	0.262	21.257	0.171	574	3
Basin 15	14.05	13.06	0.22	17	0.8	0.46	0.451	2.137	0.063	1.512	77.917	0.586	0.229	26.501	0.311	326	3
Basin 16	27.95	13.06	0.25	19	0.51	0.54	0.351	1.976	0.172	1.406	95.249	-0.064	0.056	-2.864	0.333	425	1
Basin 17	9.73	13.06	0.54	9	0.59	0.49	0.449	2.179	-0.169	1.637	75.2	0.123	0.141	5.313	0.672	365	3
Basin 18	38.57	13.06	0.44	26	0.71	0.49	0.503	2.196	0.26	1.7	97.274	0.246	0.038	-2.864	0.394	869	2
Basin 19	83.9	13.06	0.22	7	0.8	0.53	0.374	2.077	-0.278	1.63	136.185	0.165	0.105	-3.806	0.702	623	2
Basin 20	39.93	13.06	0.36	10	0.75	0.41	0.452	2.138	0.05	1.502	115.577	0.425	0.128	12.581	0.2	685	3
Basin 21	6.47	13.06	0.58	21	0.8	0.41	0.606	2.379	0.345	1.778	87.251	0.693	0.133	15.928	0.641	698	3
Basin 22	23.25	13.06	0.83	27	0.78	0.5	0.484	2.218	-0.021	1.614	110.664	0.464	0.155	19.508	0.459	657	3
Basin 23	10	13.06	0.26	8	0.8	0.46	0.468	2.166	0.05	1.522	92.098	0.647	0.244	30.102	0.425	536	3
Basin 24	25.87	13.06	0.07	2	0.66	0.46	0.428	2.101	0.062	1.495	105.028	0.033	0.057	3.759	0.214	460	3
Basin 25	5574.56	13.06	1.64	6	0.69	0.46	0.325	2.012	-0.29	1.549	121.13	0.401	0.249	29.337	0.492	418	3
Basin 26	34.69	13.06	0.2	27	0.81	0.44	0.455	2.134	0.097	1.5	82.989	0.333	0.178	16.352	0.695	429	3
Basin 27	41.56	3.5	0.19	7	0.87	0.45	0.46	2.133	0.119	1.481	110.718	0.505	0.207	26.967	0.358	264	3
Basin 28	67.64	1.94	0.58	7	0.62	0.39	0.57	2.328	0.179	1.651	104.984	0.585	0.291	30.105	0.529	279	3
Basin 29	7.35	1.75	0.08	22	0.71	0.39	0.408	2.06	0.056	1.408	91.699	0.454	0.175	22.014	0.48	394	2
Basin 30	365.25	1.75	8.06	27	0.61	0.33	0.629	2.445	0.295	1.769	108.024	0.606	0.469	60.895	0.217	259	3
Basin 31	29.94	1.54	1.09	2	0.7	0.32	0.355	1.884	0.497	1.464	26.915	0.269	0.209	24.639	0.275	252	3
Basin 32	132.83	1.63	1.17	10	0.63	0.27	0.848	2.748	0.953	2.659	76.74	0.749	0.514	60.435	0.281	329	4
Basin 33	16.94	1.63	0.39	17	0.74	0.4	0.567	2.28	0.362	1.693	59.63	1.083	0.325	42.984	0.416	363	3
Basin 34	96.13	1.63	0.94	12	0.62	0.33	0.649	2.394	0.561	1.913	111.937	0.716	0.439	55.016	0.354	376	3
Basin 35	69.94	1.87	0.85	3	0.7	0.33	0.614	2.321	0.529	1.827	78.01	0.733	0.399	47.999	0.265	434	3
Basin 36	474.68	1.87	1.53	16	0.72	0.45	0.374	2.061	-0.198	1.517	142.863	0.485	0.256	31.704	0.322	530	3
Basin 37	19.96	1.66	0.09	10	0.59	0.44	0.527	2.255	0.165	1.615	113.122	0.583	0.252	31.677	0.469	652	3
Basin 38	153.02	1.66	0.23	4	0.75	0.4	0.433	2.084	0.169	1.469	141.02	0.359	0.219	29.46	0.266	681	3
Basin 39	25.26	1.12	0.1	17	0.64	0.53	0.29	1.943	-0.081	1.351	173.222	-0.145	0	-14.403	0	781	1
Basin 40	41.01	1.12	0.17	2	0.57	0.46	0.417	2.051	0.179	1.425	128.684	0.601	0.339	33.139	0.165	787	2
Basin 41	132.52	1.12	0.38	14	0.66	0.4	0.407	2.041	0.186	1.44	110.395	0.533	0.276	34.001	0.161	825	2
Basin 42	2.24	1.54	0.28	24	0.7	0.36	0.598	2.228	0.762	2.113	26.591	0.291	0.108	2.709	0.287	241	2
Basin 43	2.95	1.54	3.25	18	0.56	0.29	0.908	2.993	0.904	2.842	27.159	0.947	0.18	19.319	0.202	226	3
Basin 44	2.41	1.54	8.36	5	0.54	0.28	1.09	3.72	0.884	3.089	21.612	2.394	0.296	37.148	0.449	215	3
Basin 45	5.88	5.08	0.79	4	0.76	0.49	0.513	2.293	-0.07	1.731	51.106	1.139	0.27	25.043	0.581	231	3
Basin 46	8.32	5.08	0.89	5	0.77	0.42	0.616	2.431	0.264	1.783	24.25	0.755	0.234	12.576	0.148	229	4
Basin 47	16.68	5.08	3.2	29	0.73	0.37	0.603	2.295	0.482	1.737	46.578	0.627	0.361	35.537	0.377	217	3
Basin 48	8.52	5.08	0.26	15	0.81	0.45	0.574	2.341	0.242	1.744	43.312	0.481	0.326	31.591	0.21	245	3

Table 3.1: Continued.

Basin No	Area Km2	Smf	Vf	AF	Re	HI	Skewness	Kurtosis	Density skewness	Density kurtosis	Mean Ksn ($m^{0.9}$)	θ	Cmax	Cf%	dL	Outlet Elevation (m)	Iat
Basin 49	32.72	5.08	1.08	22	0.76	0.43	0.574	2.369	0.145	1.724	43.182	0.727	0.395	48.832	0.316	247	4
Basin 50	121.13	1.45	0.46	8	0.73	0.39	0.466	2.094	0.324	1.515	85.122	0.52	0.357	37.969	0.388	511	3
Basin 51	34.4	2.68	0.68	35	0.76	0.24	0.884	2.762	1.078	2.867	38.32	1.495	0.435	53.699	0.404	364	4
Basin 52	21.57	2.68	1.57	7	0.58	0.35	0.739	2.719	0.422	2.044	55.204	0.783	0.325	43.181	0.434	364	4
Basin 53	45.23	2.68	6.22	25	0.55	0.25	0.915	2.901	1.035	2.871	31.797	0.869	0.389	49.06	0.372	364	3
Basin 54	7.65	2.68	0.6	4	0.65	0.35	0.556	2.186	0.63	1.903	22.387	0.466	0.182	13.177	0.337	331	3
Basin 55	48.45	2.74	0.52	14	0.63	0.29	0.596	2.193	0.738	1.971	28.556	0.882	0.456	52.868	0.146	301	4
Basin 56	358.11	2.74	0.06	0	0.74	0.49	0.408	2.098	-0.097	1.518	109.429	0.483	0.19	24.432	0.096	393	3
Basin 57	8.2	2.74	0.4	12	0.53	0.48	0.496	2.242	-0.026	1.635	118.623	0.513	0.153	17.708	0.422	396	2
Basin 58	16.67	2.74	0.57	20	0.59	0.46	0.483	2.19	0.078	1.556	114.743	0.547	0.197	24.813	0.441	363	2
Basin 59	30.15	1.44	0.38	2	0.76	0.45	0.417	2.096	-0.007	1.498	137.896	-0.116	0	-15.13	0	502	2
Basin 60	26.84	1.44	0.2	7	0.69	0.52	0.357	2.035	-0.165	1.483	113.267	-0.157	0.041	-9.055	0.881	509	2
Basin 61	1635.58	2.01	1.71	16	0.66	0.42	0.351	2.01	-0.075	1.399	117.488	0.485	0.383	47.643	0.146	450	3
Basin 62	36.56	2.19	0.43	21	0.71	0.47	0.362	2.006	0.05	1.395	38.472	0.32	0.149	15.41	0.098	278	3
Basin 63	203.18	2.19	0.39	10	0.67	0.33	0.582	2.197	0.765	2.104	67.755	0.549	0.346	39.188	0.373	300	3
Basin 64	148.32	1.72	0.34	6	0.53	0.41	0.47	2.174	0.046	1.544	101.534	0.433	0.249	35.281	0.491	416	2
Basin 65	54.42	1.72	0.65	20	0.51	0.39	0.503	2.149	0.366	1.587	69.763	0.545	0.274	34.248	0.259	427	2
Basin 66	205.27	2.6	1.21	7	0.52	0.31	0.605	2.268	0.625	1.9	98.159	0.538	0.351	42.107	0.278	459	3
Basin 67	428.88	2.03	2.18	4	0.61	0.34	0.525	2.186	0.334	1.565	89.258	0.529	0.471	54.752	0.219	462	3
Basin 68	7.96	1.26	1.45	9	0.48	0.46	0.54	2.258	0.273	1.689	65.142	0.166	0.086	4.145	0.326	669	2
Basin 69	18.66	1.26	0.82	7	0.73	0.39	0.536	2.195	0.452	1.707	49.398	0.457	0.214	27.366	0.403	597	3
Basin 70	15.15	1.26	0.23	9	0.56	0.43	0.46	2.131	0.136	1.491	74.197	0.018	0.066	2.244	0.797	713	2
Basin 71	31.23	1.28	0.42	10	0.7	0.46	0.454	2.102	0.253	1.526	80.428	0.191	0.108	11.415	0.559	693	2
Basin 72	62.16	1.28	0.28	5	0.62	0.45	0.47	2.159	0.134	1.566	88.472	0.383	0.183	21.913	0.395	627	2
Basin 73	23.85	2.22	0.3	12	0.6	0.47	0.452	2.129	0.154	1.605	63.131	0.255	0.153	-6.367	0.046	966	3
Basin 74	183.17	2.22	0.46	21	0.74	0.5	0.338	2.013	-0.185	1.472	107.401	0.275	0.186	23.456	0.431	615	2
Basin 75	73.84	2.22	0.51	5	0.68	0.53	0.397	2.092	-0.144	1.569	100.006	0.61	0.151	20.461	0.412	585	3
Basin 76	11.91	1.28	0.23	7	0.51	0.42	0.498	2.185	0.204	1.548	82.431	0.493	0.166	19.171	0.415	510	2
Basin 77	28.05	1.28	0.29	17	0.54	0.37	0.552	2.253	0.381	1.736	54.754	0.294	0.156	17.878	0.29	478	1
Basin 78	24.88	1.25	0.32	6	0.56	0.52	0.485	2.225	-0.018	1.744	59.836	0.4	0.199	19.924	0.382	383	2
Basin 79	71.75	1.26	0.63	15	0.56	0.4	0.43	2.119	-0.033	1.502	61.129	0.457	0.244	29.995	0.22	433	2
Basin 80	13.66	1.26	0.81	14	0.7	0.46	0.423	2.092	0.035	1.453	62.013	0.379	0.121	8.724	0.675	497	2
Basin 81	33.83	1.06	0.84	20	0.56	0.46	0.488	2.216	0.028	1.622	96.208	-0.139	0.086	-9.761	0.73	537	2
Basin 82	15.41	1.06	0.2	2	0.58	0.56	0.33	2.031	-0.382	1.681	127.299	-0.099	0	-11.616	0	577	1
Basin 83	78.54	1.51	0.13	4	0.64	0.52	0.336	2.017	-0.223	1.527	98.798	0.417	0.043	2.528	0.6	686	2
Basin 84	902.31	1.51	0.36	19	0.67	0.41	0.411	2.075	0.051	1.463	95.521	0.471	0.334	40.957	0.207	724	2
Basin 85	37.88	1.4	0.27	4	0.73	0.46	0.448	2.163	-0.074	1.587	111.854	0.689	0.228	27.239	0.369	952	3
Basin 86	998.04	1.4	0.19	11	0.58	0.26	0.431	2.065	0.27	1.517	56.42	0.589	0	-11.275	0	1084	2
Basin 87	18.29	1.15	0.12	4	0.64	0.37	0.648	2.358	0.656	2.009	157.216	0.889	0.352	42.433	0.292	1015	3
Basin 88	21.9	1.15	0.31	17	0.56	0.43	0.409	2.089	-0.017	1.509	103.486	0.188	0.071	2.475	0.443	976	1
Basin 89	22.98	1.32	0.33	5	0.8	0.5	0.394	2.07	-0.062	1.477	119.368	0.163	0.06	-2.37	0.211	835	2
Basin 90	154.23	1.4	0.37	1	0.59	0.29	0.476	2.142	0.183	1.49	106.54	0.684	0.462	54.984	0.318	584	3
Basin 91	7.79	1.4	0.45	1	0.45	0.47	0.611	2.435	0.216	1.853	94.967	0.308	0.07	8.458	0.498	566	2
Basin 92	8.03	1.64	0.23	17	0.49	0.49	0.368	2.041	-0.167	1.448	84.623	0.047	0.128	6.242	0.746	632	1
Basin 93	12.09	1.64	0.21	6	0.53	0.5	0.49	2.229	-0.009	1.643	100.069	0.595	0.196	20.772	0.471	586	2
Basin 94	12.67	1.64	0.51	25	0.48	0.39	0.472	2.125	0.211	1.477	66.995	0.515	0.165	20.962	0.515	472	2
Basin 95	65.44	1.64	1.12	4	0.56	0.45	0.514	2.256	0.066	1.625	82.756	0.647	0.299	39.156	0.411	462	3
Basin 96	16.82	1.18	0.43	0	0.6	0.52	0.481	2.232	-0.094	1.718	106.042	0.319	0.214	18.658	0.505	619	2
Basin 97	333.36	1.18	0.36	10	0.74	0.3	0.447	2.061	0.297	1.455	106.957	0.73	0.546	60.294	0.182	581	3

3.4.3 Basin Elongation Ratio

The Re value also shows considerable fluctuation, similar to that observed for the asymmetry factor, but with a higher order in the polynomial regression line (magenta line, Figure 3-6). The Re data range varies from 0.45 to 0.87. About 30.93% of the basins display circular to slightly elongated shapes, 50.52% show elongated basins, and 18.56% are highly elongated. The trend indicates that Re values tend to be higher (indicating more elongation) in the south (0-50 km), center (150-180 km), and north (210-280 km) of the study area. Additionally, lower elongation is noted around similar locations, with one exception at the dataset's edges (LaF and WAT). We observed that elongated basins correlate with asymmetrical drainage patterns; as the basins become more elongated, the asymmetry factor also increases.

3.4.4 Hypsometric curve and integral - statistical moments

Hypsometric integral (HI) values exhibit a general slightly fluctuation according to the distance measures in the Western Andean Front (Figure 3-8). The general trend indicates variability in the central part of the study area along the internal mountain front (parallel to the Cachapoal Fault), LoF, and MeF. Predominantly low HI values are observed in this region, with an increase in both the southern and northern parts of the study area.

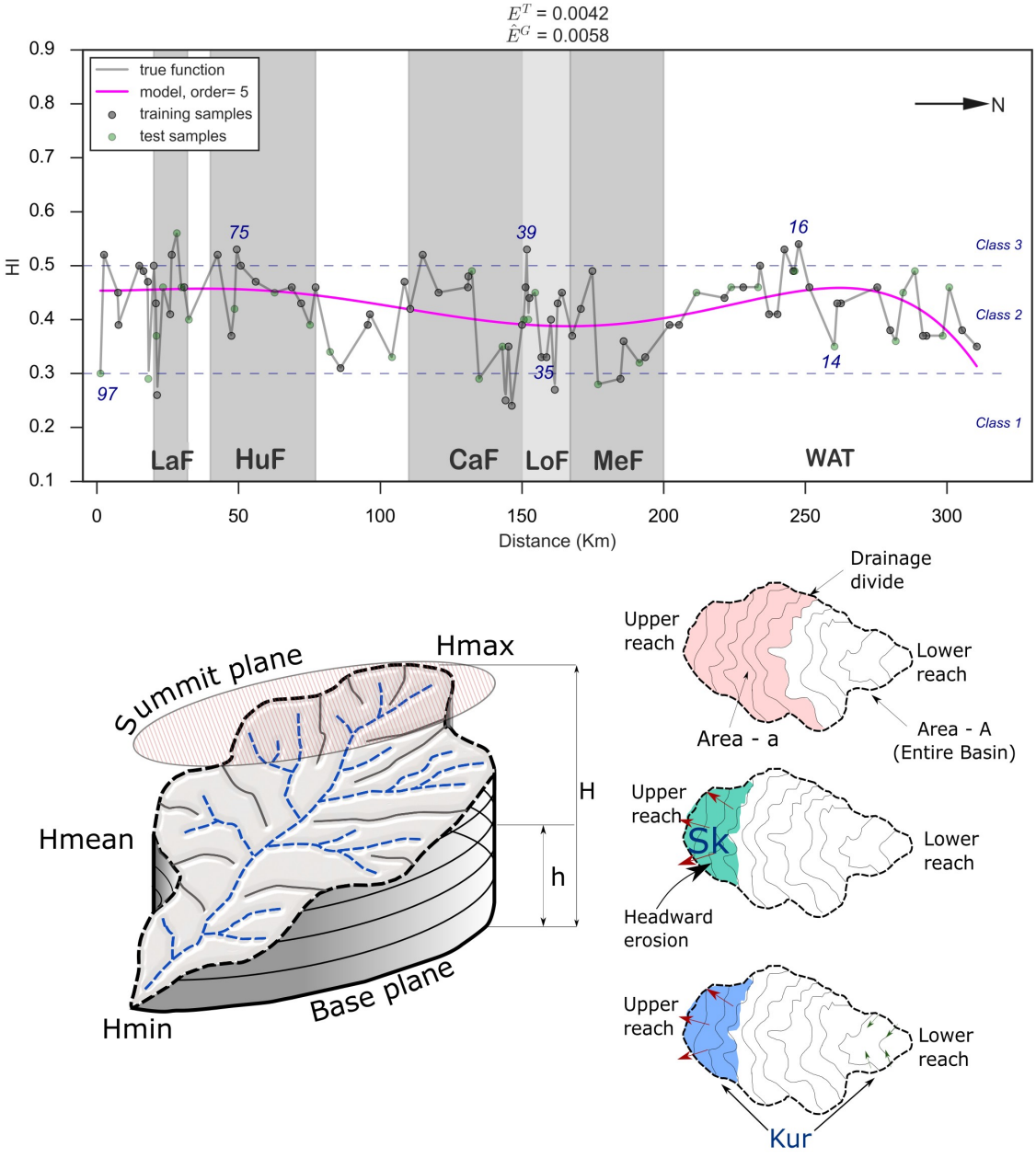


Figure 3-8: Hypsometric Curve and graphical representation of Sk and Kur Statistical Moments (lower part). The IH index data range from 0.24 to 0.56. A set of low IH values is observed towards the CaF, LoF, and MeF sectors, contrasting with high IH values towards both the southern end of the study area and the north.

The classification by HI allowed to differentiate three classes with the following percentages (e.g.,

Matoš et al., 2016: Class 1 (HI $\geq$ 0.5) with the 17.53% indicating regions with weakly eroded basin, found mainly in the intersection between HuF and LaF. Class 2 (0.3 $<$ HI $<$ 0.5): with 76.29%, represents areas with moderate erosion. This class is widespread across most fault zones without representative pattern and Class 3 (HI $\leq$ 0.3) with 6.18% denotes regions of significant erosion, found in the central part of the study area.

The polynomial regressions for skewness, kurtosis, density skewness, and density kurtosis exhibit trends that align with the HI trend (Figure 3-9). Regions with low HI values (CaF, MeF, and LoF) generally show higher skewness and kurtosis values, indicating significant headward erosion in the upper reaches (e.g., Harlin, 1978; Pérez-Peña et al., 2009; Radaideh and Mosar, 2019; Rimando and Schoenbohm, 2020). Conversely, relatively large kurtosis and density kurtosis values may be explained by increased incision occurring not only in the upper reaches but also in the lower reaches of each basin (e.g., Pérez-Peña et al., 2009) (Figure 3-9).

Examining the shape of HC with the methodology proposed here, we obtained a systematic classification of the curves in the WSPC. Notably, preliminary observation using polynomial regression led us to conclude that with spatial distribution of the HC (Figures 3-10 and 3-11), the central segment in the WSPC shows an area with highly eroded basins located in portions limited by NW-NNE faults.

In Figure 3-12, the spatial distribution of HC from north to south reveals the following patterns: north of 36°, over the WAT and the northern extension of the MeF, basins of various sizes (basins 1 to 27) predominantly exhibit convex mouth shapes, with a smaller proportion showing S-shaped basins (Figure 3-11). One of the largest basins in the study area corresponds to the Maule River, with a drainage area exceeding 5000 km^2. Its convex shape towards the mouth may indicate active tectonics. However, we believe that the HC shape is also influenced by lithology (Miocene granitoids), climate (given its relationship with glaciers), and the presence of high volcanic peaks that increase relief from the middle part of the basin.

Additionally, the possibility of reactivation towards the front should not be ruled out, considering its relationship with neighboring basins. In general, the position of volcanoes and granite bodies lies in a central section of the western flank of the Principal Cordillera (Oviedo-Reyes et al., 2024). The rock strength (granitoids) and high peaks of the volcanic systems are consistent with the increasing area-to-elevation ratio in HC and HI. South of 36°S, the predominant basin shapes are convex-mouth to S-shaped, with slight variations towards convex. Only in the sector described towards the central part of the WSPC are concave basins found.

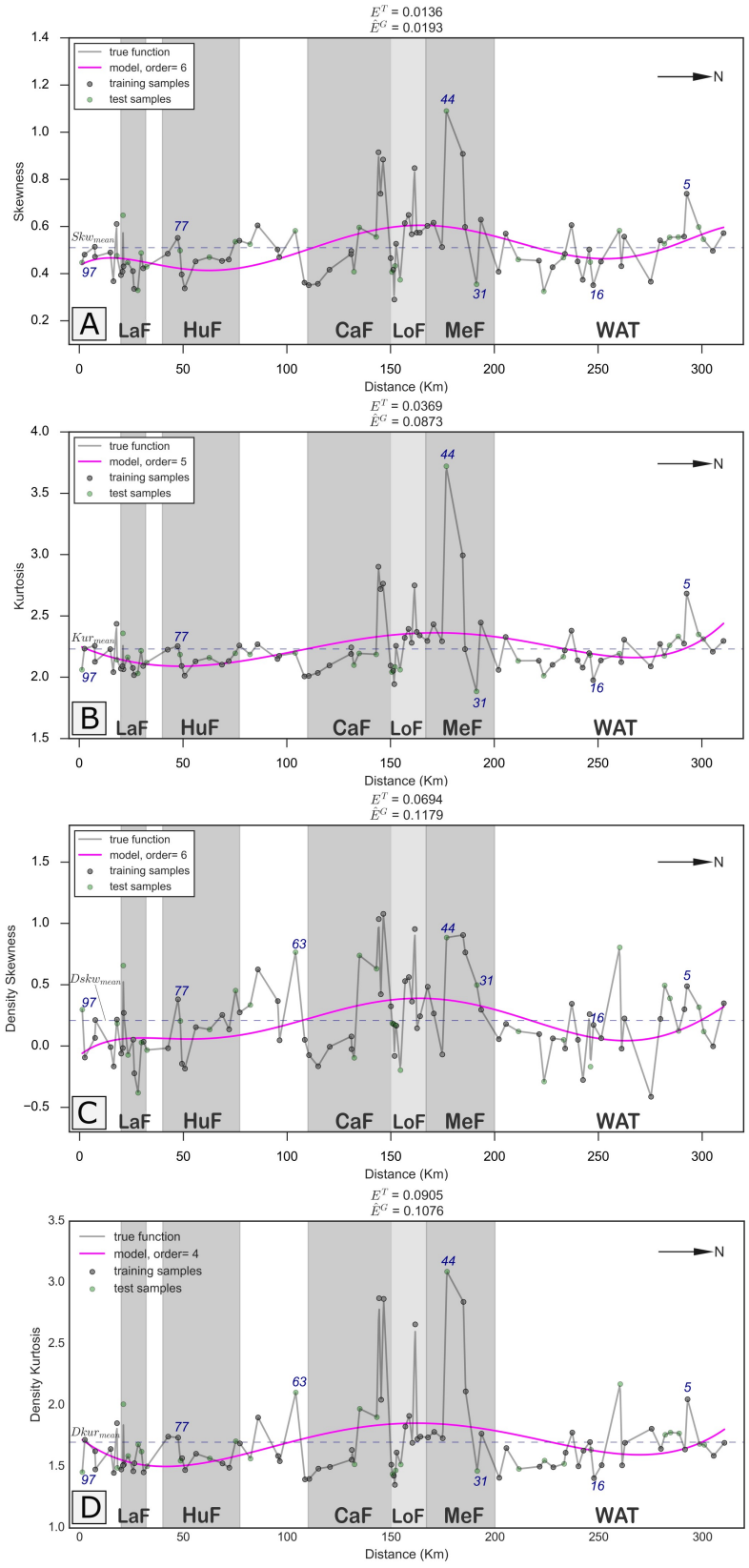


Figure 3-9: Statistical moments and its variations along north-south in the study area. Skewness (Sk) (range of data: -0.382 to 1.078), Kurtosis (Kur) (range of data: 1.943 to 3.72), Density Skewness (Dsk) (range of data: -0.414 to 1.078) and Density Kurtosis (range of data: 1.351 to 3.089) (Dkur) Statistical Moments varying in similar trends over south, central and north sections subdivided here the WSPC. The mean values for each statistical moment are displayed in A, B, C and D plots.

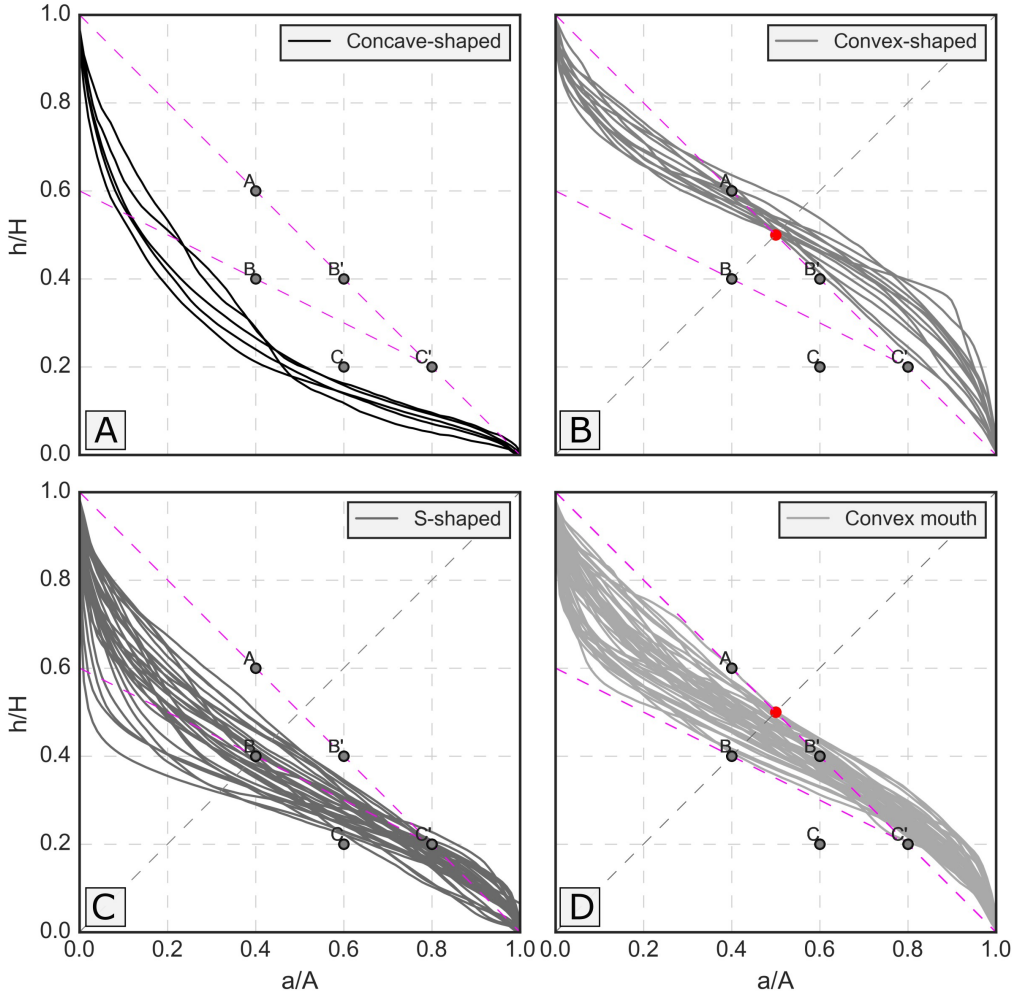


Figure 3-10: Hypsometric curves ranked using their morphological changes along the curve. To classify curve shapes, reference points (A, B, B', C, C') were used. Convex curves rise above the midpoint of AB' and stay above B'C'. Convex mouth curves sit below the midpoint of AB' but remain above BC', staying convex above point C'. S-shaped curves generally lie below AC' and cross over C'C. Concave curves remain below BC.

3.4.5 Topography and channel-steepness index (K_{sn}) and normalized river profiles

The western slope of the Principal Cordillera exhibits a high degree of slope angle variability, indicative of steep and rugged terrain (Figure 3-13A). The with high slope angle variability areas indicate steeper slopes with rapid elevation changes, primarily observed along the middle section of the western flank of the Principal Cordillera. These steep slopes (60 to 80°) are associated with granitic bodies (Miocene), high relief, and erosion processes, including both fluvial and glacial erosion, which contribute to the formation of verticalized landscapes. Additionally, the high elevations of volcanic systems also plays a role in creating these steep and rugged terrains. The local relief presents high values (>1000) mainly north of 36°S, with local variations recorded on volcanic edifices along the WSPC, and rock strength lithologies Figure 3-13B). South of this parallel, the local relief decreases

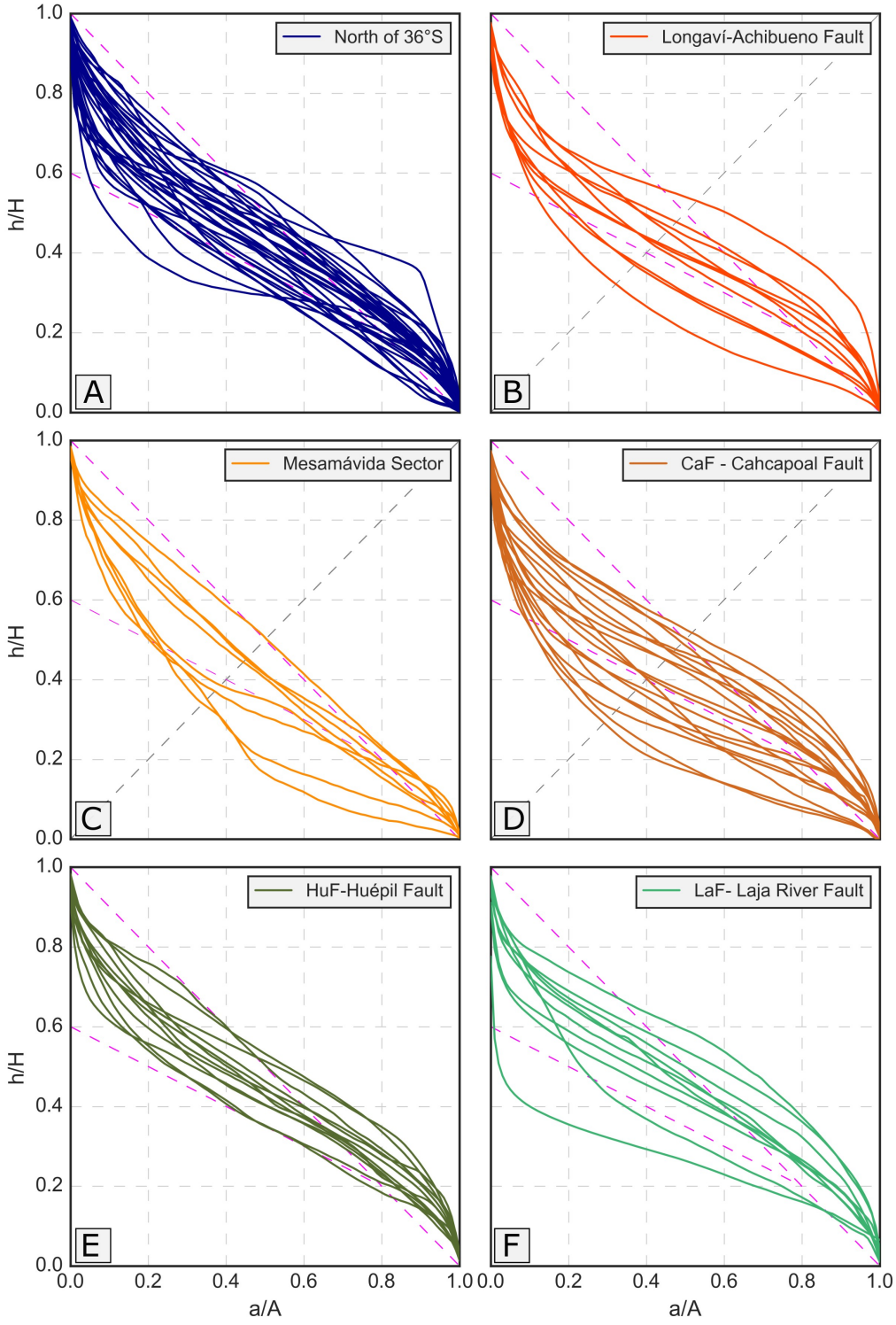


Figure 3-11: Hypsometric curves ranked using their fault location. Note how the Huepil fault sector, the Laja river and WAT present curves from convex to convex to the mouth. In contrast, MeF, LoF, CaF sectors show wider ranges of curves from highly eroded basins (concave) to weakly eroded basins (convex).

(<1000m) as the elevation of the Andes also decreases towards the south (Montgomery et al., 2001). Some areas delimited by very high local relief present moderate to low local relief, which together with lower variability in slope angles would indicate relict surfaces of the landscape (glacial landscapes).

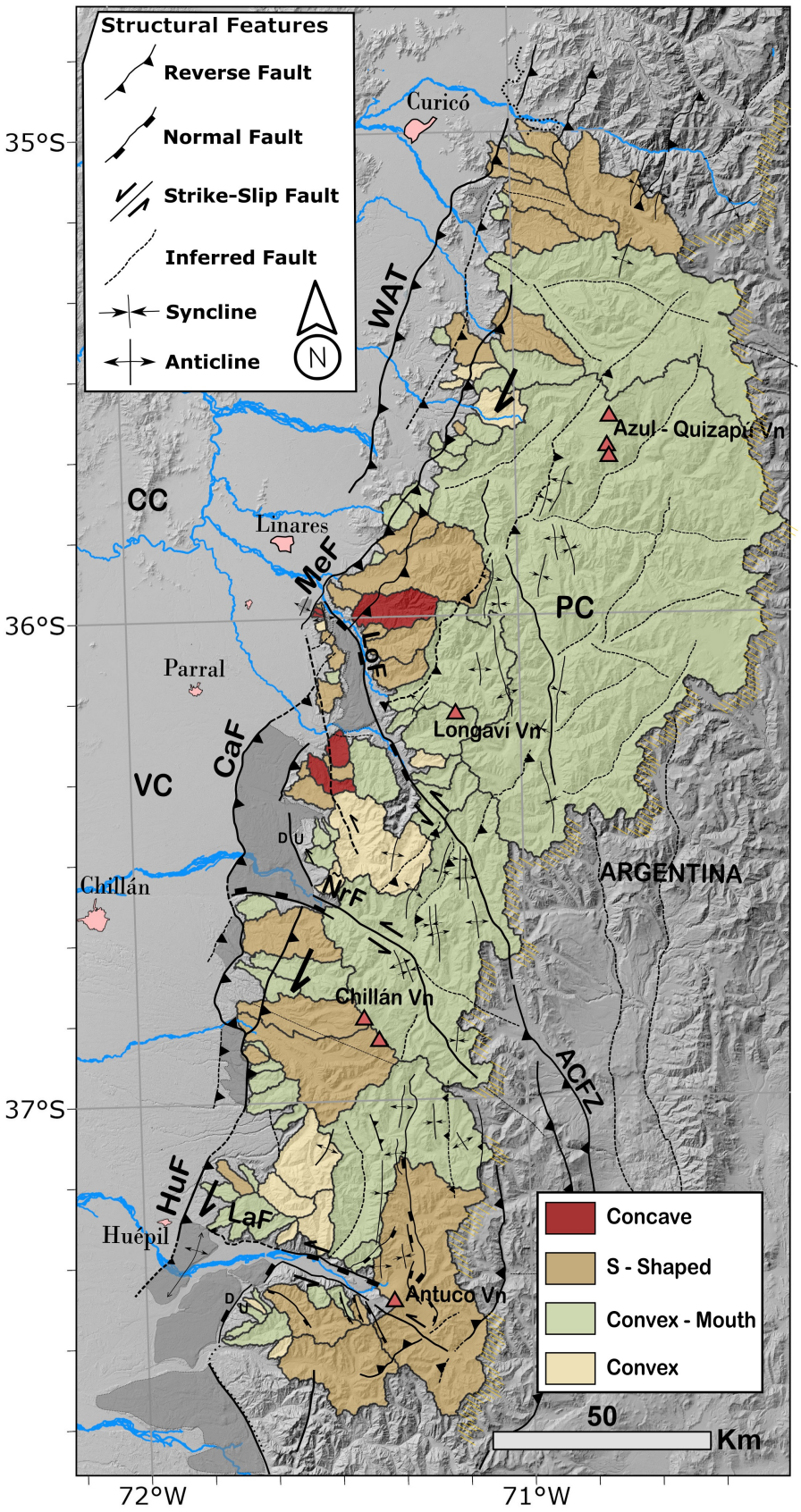


Figure 3-12: Hypsometric curves mapped according to the classification proposed in this study. The hypsometric curves, classified according to the proposed method in this study, highlight that most concave basins are located in the fault sectors of MeF, LoF, and the northern part of CaF. In contrast, other sectors display moderately eroded zones. The presence of convex curves near the mouth suggests a landscape response to tectonic uplift (landscape rejuvenation).

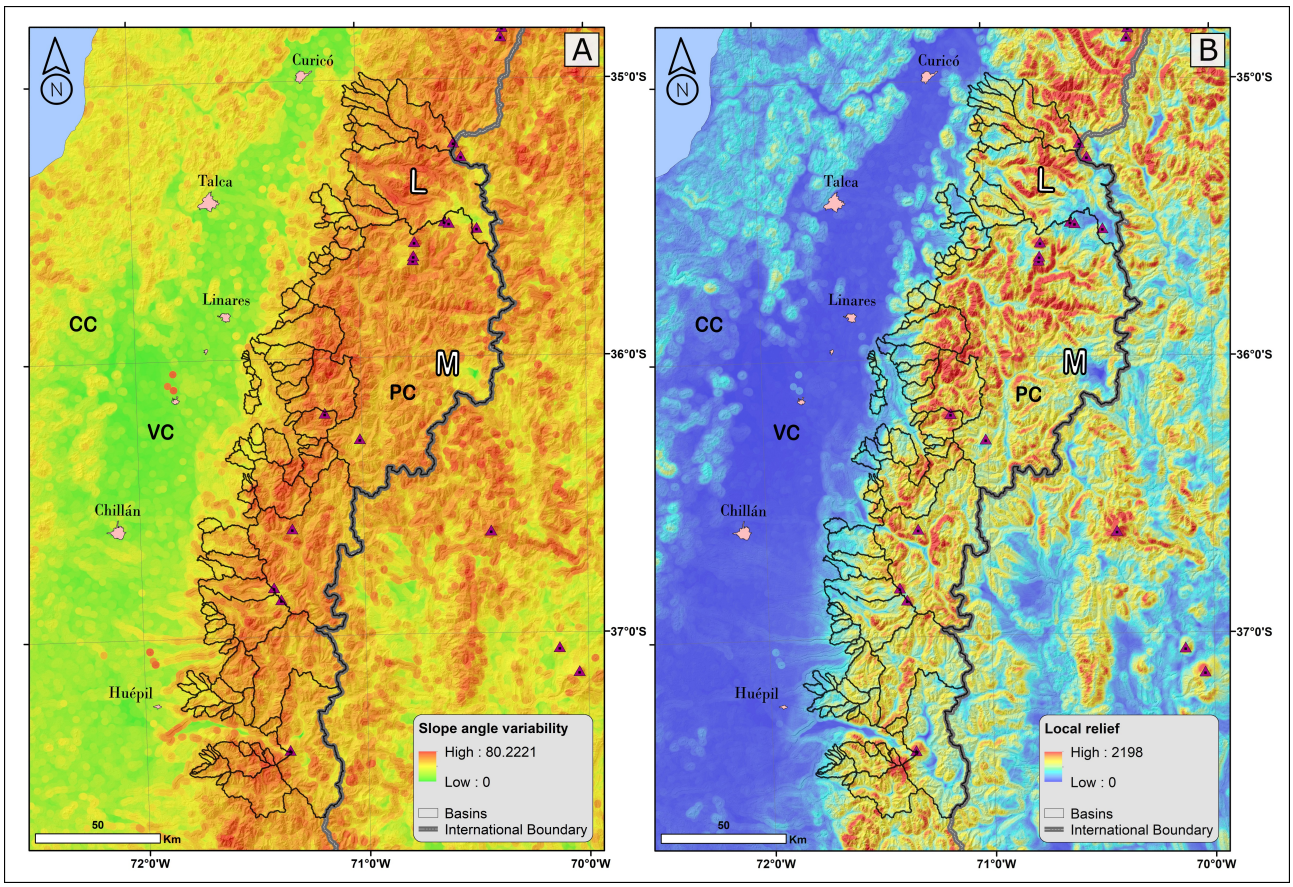


Figure 3-13: Regional topographic metrics in the Western Slope of the Principal Cordillera. A. Slope-Angle Variability. High degree of slope angle variability, predominantly shown in red and orange shades. B. Local Relief. The Maule rivers (M) and Lontué (L) are depicted in both figures to reference. PC: Principal Cordillera, VC: Central Valley, CC: Coastal Cordillera.

As a measure of fluvial incision, the local relief map indicates more significant incision patterns towards the north of the study area (north of 36°), particularly along the hillslopes flanking the fluvial systems downstream. Similarly, high local relief is observed in areas of intense glacial erosion, such as the headwaters of the Achibueno River (Figure 3-4) near the Nevado de Longaví volcano.

The polynomial regression curve of K_{sn} mean values for each drainage basin exhibits a decrease towards the central part of the study area (Figure 3-14), with a peak near the LoF trace sector. Values between 20 to 80$m^{0.9}$ are observed in this central area, characterized previously in this document by several morphometric indexes, is concentrated from the tip of the internal mountain front (CaF, San Fabian Fault) to Mesamávida sector (MeF). Relative high values between 90 to 120$m^{0.9}$, are observed along the trace of LaF, and 90 to 140 $m^{0.9}$ along WAT.

The K_{sn} map shows contrasting channel steepness between the northern and southern segments of the study area (referring to 36°S)(Figure 3-15). The distribution of K_{sn} mirrors the pattern observed in the hack index (SL) reported by Oviedo-Reyes et al. (2024), showing a marked prevalence of high values (up to $K_{sn} > 250$ $m^{0.9}$) north of 36°S. In contrast, these high values are infrequent to the south, where K_{sn} ranges from 100 to 180 $m^{0.9}$. Spatially, low K_{sn} values (<90) are uniformly

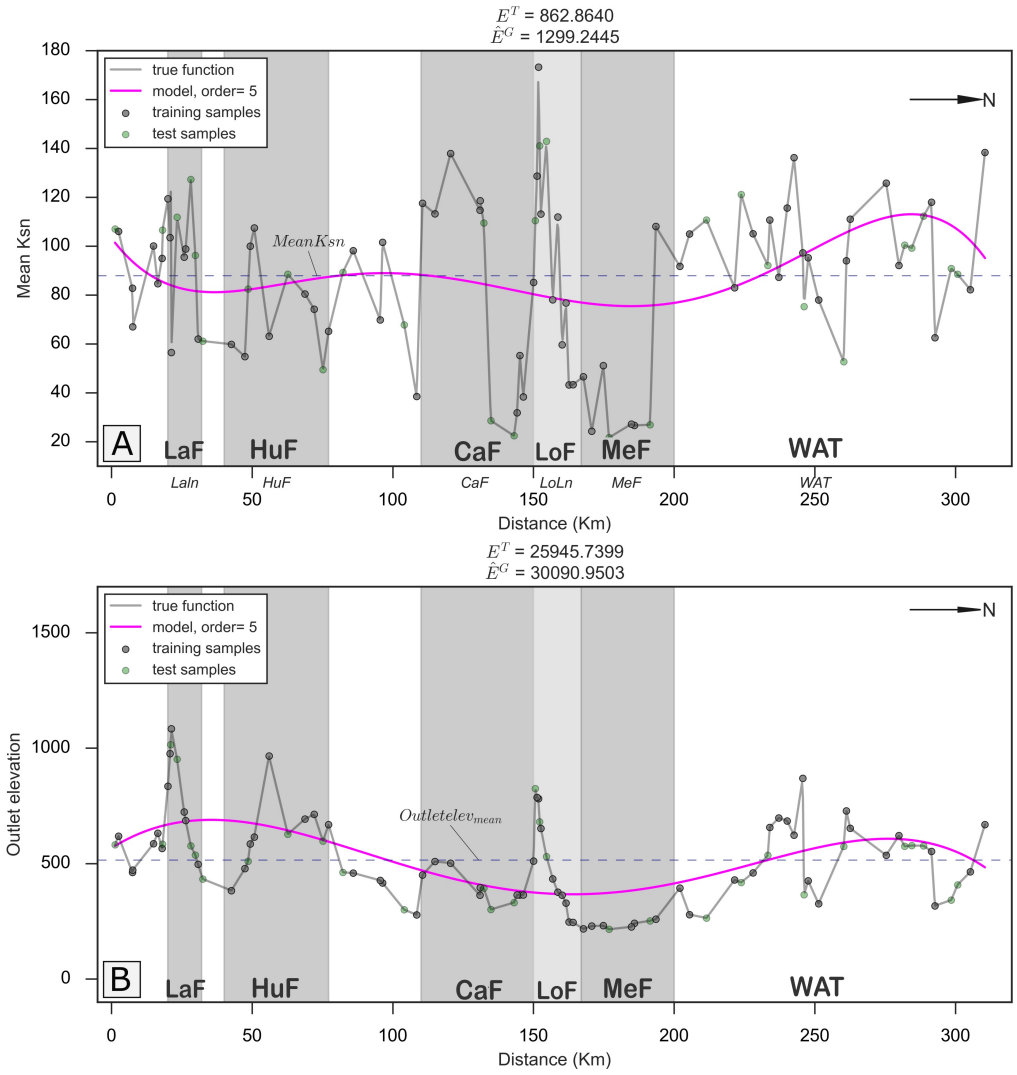


Figure 3-14: K_{sn} variations and outlet elevation of each drainage basin in the study area. A. K_{sn} steepness index show a range of data from 21.612 to 173.222$m^{0.9}$. B. Note how a decrease in the elevation of the drainage basin outlet is observed in the central part of the WAF, with a slight peak over some basins associated with the LoF trace.

distributed in the central sector, as indicated by the polynomial regression curve.

We distinguished a differential uplift in the Ñuble River Fault (ÑrF) and its intersection tip with the San Fabian Fault (SFF) (Figure 3.15B). The knickpoints are detected in the change of K_{sn} values over the same altitude (180 to 250$m^{0.9}$). These downstream portions adjusting to new perturbation can be related to differential uplift such as slope-break knick point (e.g., Wobus, Tucker, and Anderson, 2006; Kirby and Whipple, 2012). Otherwise, we report high K_{sn} values ($>$250$m^{0.9}$) matching with high local relief values along trunk channels in the Maule River (Figure 3-15C). We observed knickpoints when local relief changes from low values to high values ($>$1000 m) up to the channel on bedrock (knickzones) and elevation change of approximately 1200 m concerning the level of the bedrock channel. This non-tectonic distribution is related to a geomorphological transition between a glacial and a fluvial domain. It is pointed out that high K_{sn} values are also consistent with high rock strength levels, similar to those reported with SL by Oviedo-Reyes et al. (2024). Also,

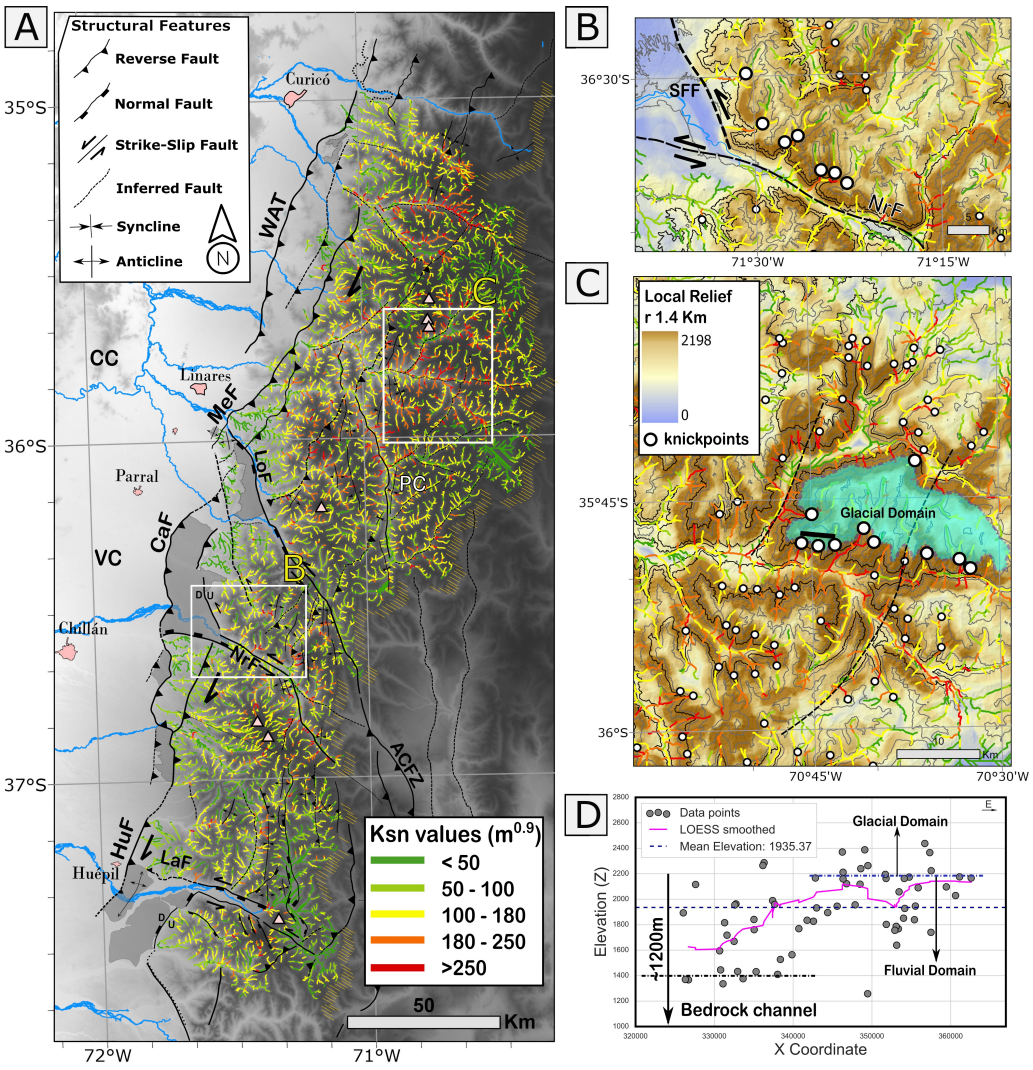


Figure 3-15: K_{sn} map and knickpoints observed in two different sectors in the study area. **A**. Map of K_{sn} patterns on structural map proposed by Oviedo-Reyes et al. (2024) and overlay on DEM- 30m. **B**. The map shows the distribution of K_{sn} and knickpoint values superimposed on the local relief map, with contour lines at 500 meters (gray curves) and 800 meters (black curves). This sector, located along the San Fabian Fault (SFF), is recognized as the internal mountain front parallel to the Cachapoal Fault. Knickpoints are projected where K_{sn} values transition from low to high downstream along the rivers. **C**. The map shows the distribution of K_{sn} and knickpoint values superimposed on the local relief map, with contour lines at 500 meters (gray curves) and 800 meters (black curves). Sector of the Maule River over its trunk channel, where the distribution of the knickpoints can be observed at approximately the same elevation. One of the areas where there is evidence of glacial dominance is highlighted. **D**. Topographic profile approximately along the course of the Maule River (trunk channel) locating the elevations of the knickpoints. The trend of the points is statistically analyzed with Loess (magenta curve).

several knickpoints correspond to lithological changes along trunk channels.

The ranges of the data for the three parameters extracted from the normalized river profiles are as follows: C_{max}: 0 to 0.889, Cf%: 0 to 0.546 and dL: -15.13 to 60.895. The trend observed from the polynomial regression curves indicates low values of C_{max} and Cf% towards the northern and southern extremes along the WSPC (Western Slope of the Principal Cordilelra), with a resurgence of high values at the end of the curve. Additionally, the trend suggests high values for the basins located in the central sector (CaF, LoF and MeF) of the WAF ($C_{max} > 0.3$ and Cf% $> 30\%$) (Figure 3-16). This condition indicates that well-graded river profiles are observed in this area.

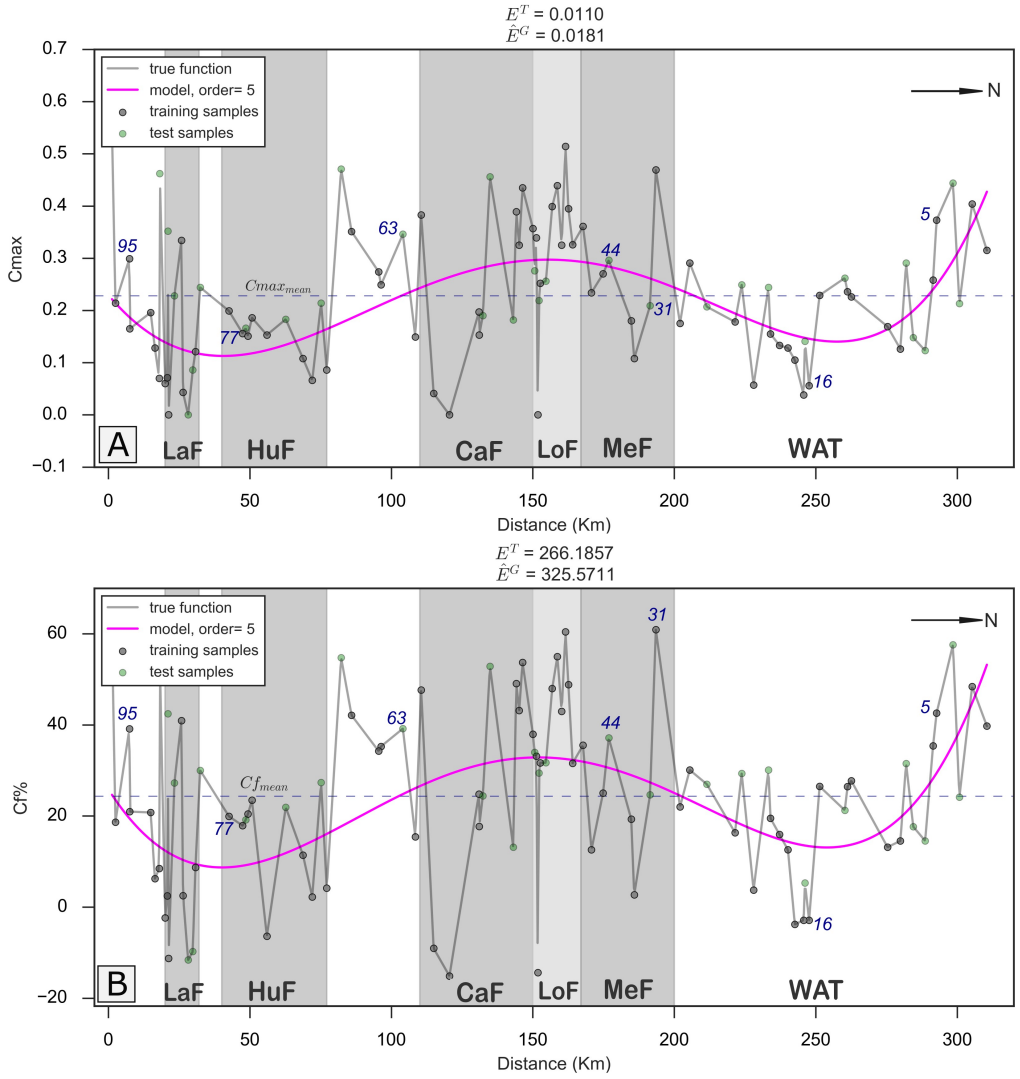


Figure 3-16: Cf% and C_{max} indexes calculated from Normalized River Profiles in the study area. A. C_{max} pattern distribution with polynomial regression curve. The maximum distance between the river profile and the imaginary line between upper and lower reach increase toward the central sector of the study area. B. Concavity factor (%) that represents the area between the curves of the normalized river profile and the line that connects the upper reach and lower reach.

The scatter plot of maximum concavity (C_{max}) against distance from source (dL) (Ruszkiczay-Rüdiger et al., 2009; Matoš et al., 2016) allows for the grouping of different normalized river profiles into five categories relative to the WSPC (Figure 3-17). These categories range from convex profile shapes (CS, Figure 3-17), indicating streams in a young erosional stage, to well-graded profiles (GR, Figure 3-17) representing streams in a state of equilibrium.The classification reveals that graded profiles (GR) represent the largest portion at 31.96% of the total, followed closely by poorly graded profiles (PG) at 27.84%. convex-straight shape profiles (CS) account for 17.53%, while transient profiles (TS) make up 13.40%. The least common are convex mouth profiles (CM), comprising 9.28% of the analyzed rivers.

Furthermore, this classification of profiles (Figures 3-18 to 3-23) enabled the spatial correlation

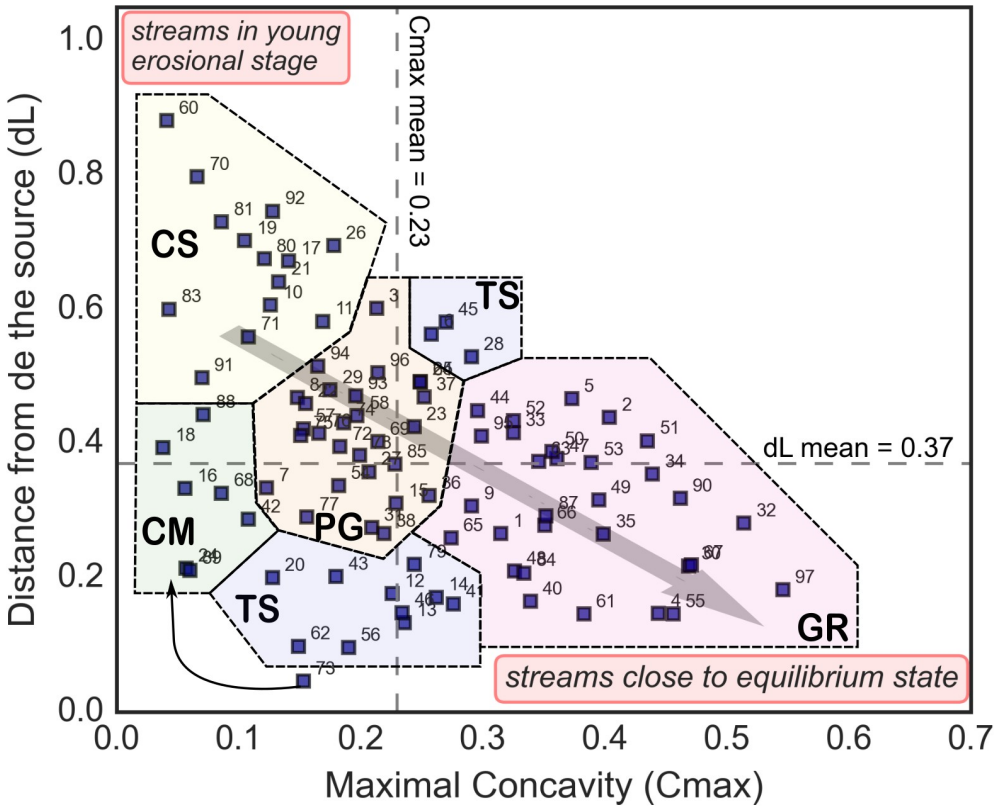


Figure 3-17: Scatter plot of C_{max} and dL of normalized stream profiles for drainage basins of the. Cf% and C_{max} indexes calculated from Normalized profiles from rivers in the WSPC. CS: Convex Shape, CM: Convex Mouth, TS: Transient State, PG: Poorly Graded Profile, GR: Well Graded Profile.

of river basins with faults and deformations along the WSPC (Figure 3-24). The predominance of graded and poorly graded profiles suggests that a significant portion of the rivers are either approaching equilibrium or in an intermediate stage of development. The presence of convex-straight and transient profiles indicates areas of ongoing adjustment, possibly due to recent tectonic activity.

A detailed analysis shows that basins with a convex - straight shape account for 17.53% (n = 17) with an average area of 107.14 km^2. Basins with a convex mouth shape represent 9.28% (n = 9) with an average size of 129.93 km^2. Graded profile basins constitute 31.96% (n = 31) with a mean size of 199.05 km^2. Poorly graded basins make up 27.84% (n = 27) with an average size of 243.44 km^2. Lastly, basins with a transient profile shape comprise 13.40% (n = 13) with an average size of 93.61 km^2. Meanwhile the graded profiles are the most common shape in the WSPC, the poorly graded normalized river profiles constitute the largest average area. However, the average area is high due to the inclusion of the Maule River basin. In that case, the largest average catchments of the WSPC are those represented by the graded profiles.

Close examination of the normalized profiles categorized as transient profiles (TS, Figures 3-17 and 3-21) indicate two types of knickpoints in the study area: first one, a vertical-step knickpoint

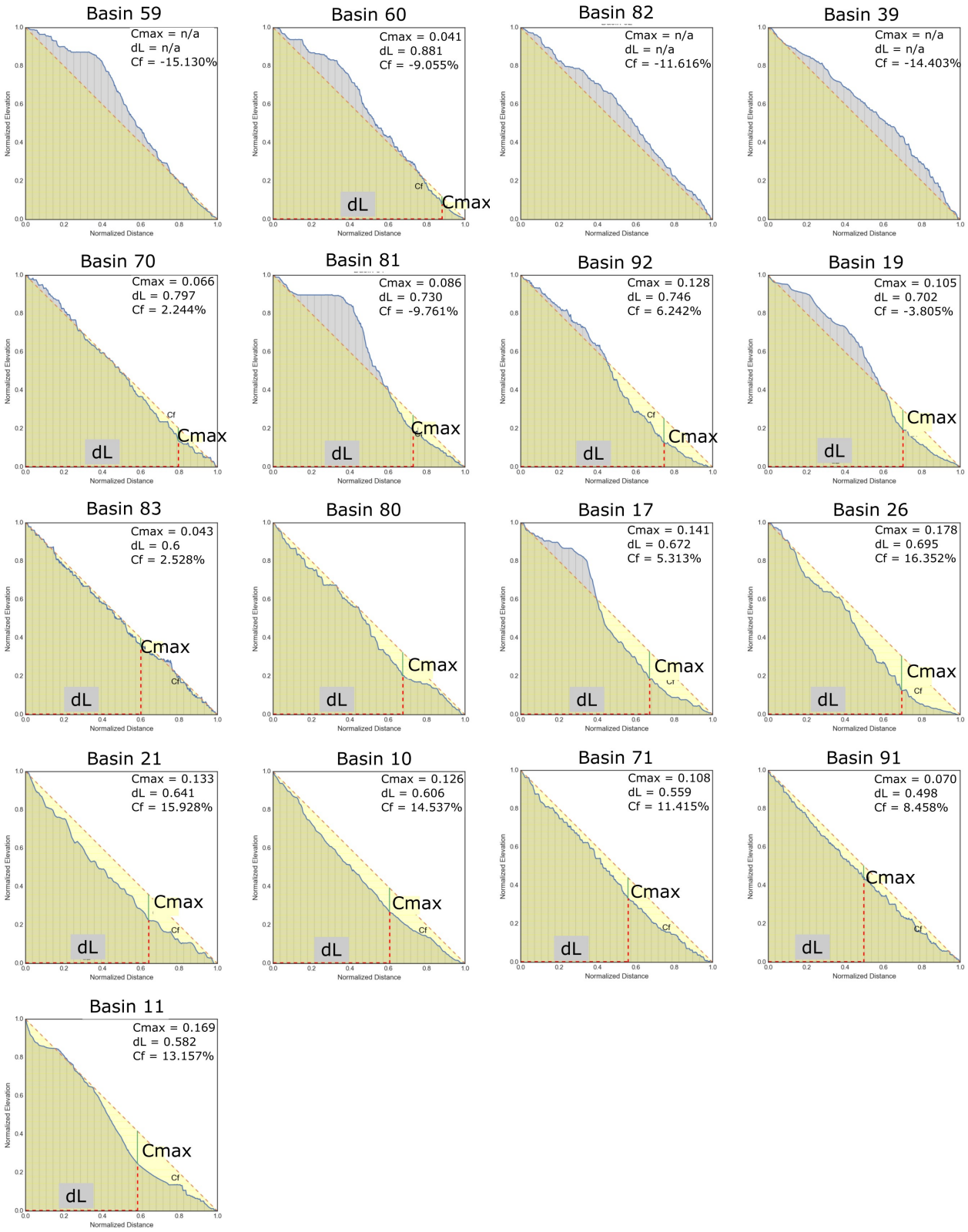


Figure 3-18: Convex to straight profiles in the Western Slope of the Principal Cordillera. Each profile include the position of C_{max}, dL and Cf% (yellow area) and sorted according to the trend in Figure 3-17.

(e.g., Wobus, Tucker, and Anderson, 2006) clearly identified here such as lithological control (e.g., Basin 56, Perquilauquen River), and second one slope-break knickpoint identified particularly in the northern part of the study area (between 35°20'S and 35°50'S). This transient signal is delineated

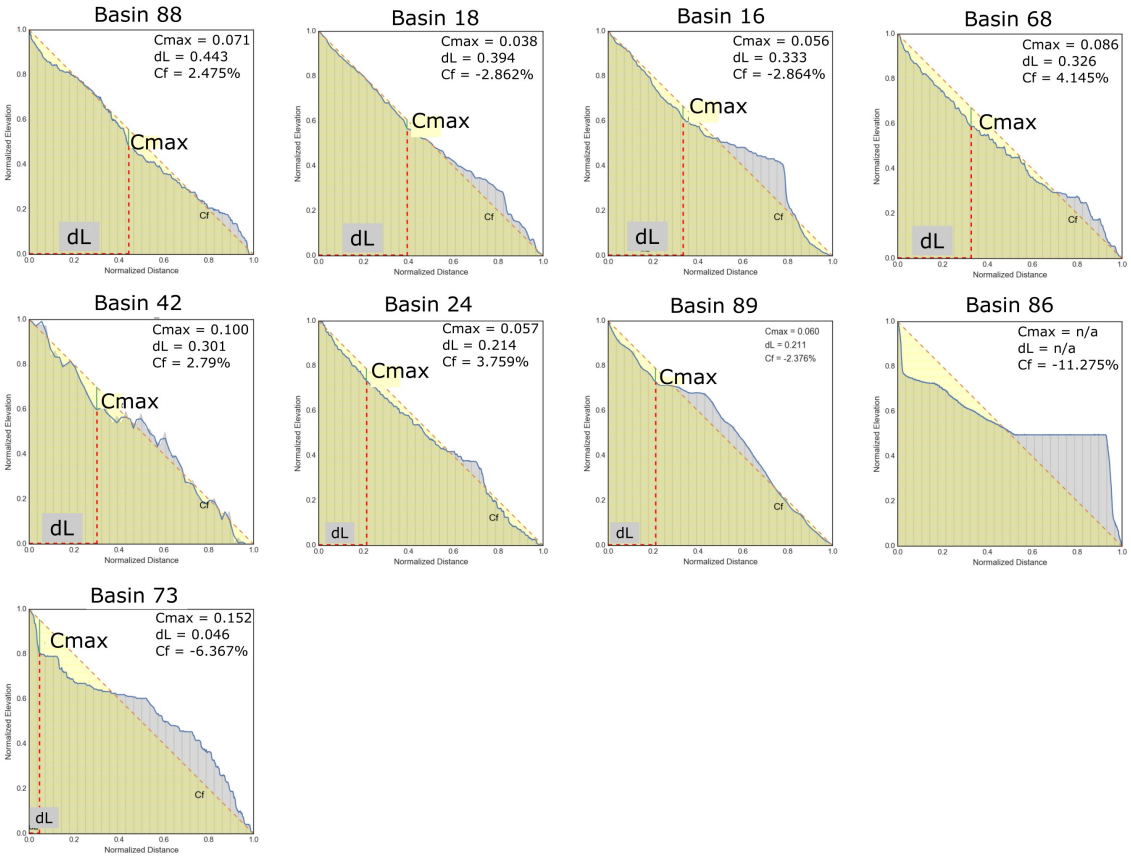


Figure 3-19: Normalized river profiles with convex mouth shape along Western Slope of the Principal Cordillera. Each profile include the position of C_{max}, dL and Cf% (yellow area) and sorted according to the trend in Figure 3-17.

along the trace of the northern extension of the Mesamávida fault within uniform lithology, which together with the K_{sn} provides evidence for possible reactivation of deformation in this area (Figures 3-15 and 3-24). Figure 3-24 highlights two key areas that suggest a possible connection with recent deformation, considering their lithological uniformity (Abanico Formation):1. The Huépil sector at 37°10'S, where the LaF fault terminates and intersects with the HuF fault. This area is characterized by river profiles ranging from convex to straight, poorly graded, and even in a transient state, and 2. The northern sector along the Western Andean Thrust (WAT) at approximately 35°20'S. Here, river profiles exhibit convex to straight shapes, convex mouths, and transient state.

3.4.6 RS-MAP patterns

A prominent high-strength zone (dark gray, Figure 3-25A) dominates the western flank of Principal Cordillera. This zone appears continuous and extends north-south along the entire study area. Specifically, the area is predominantly composed of high-strength rocks, which account for 77% of the study area and include lithologies such as basaltic andesites, andesites, dacites, and ignimbrites. The remaining 23% consists of very high-strength rocks, primarily granitoids (Figure 3-25A). A spatial gradient in rock strength is evident, with strength increasing towards the main drainage divide

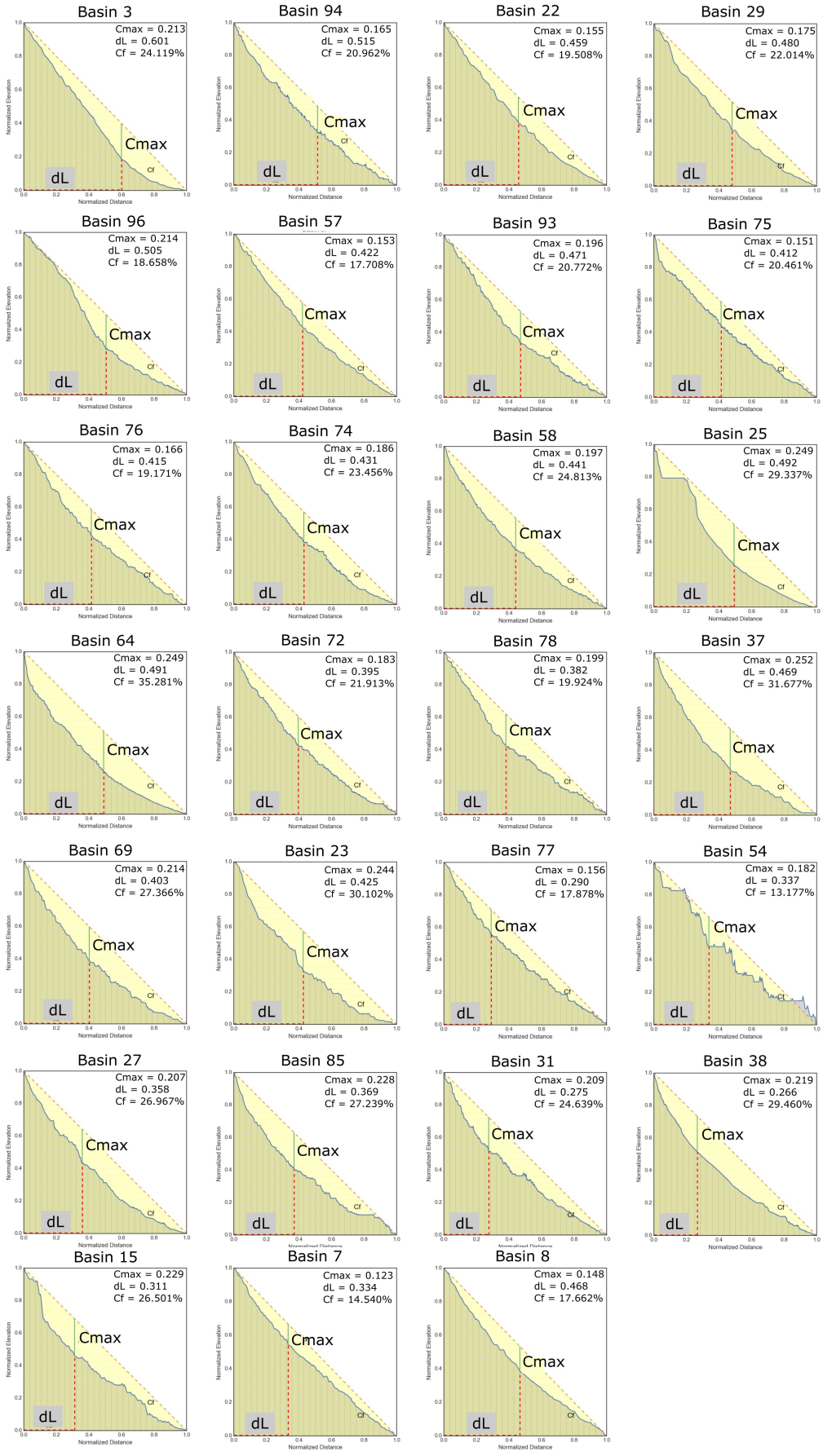


Figure 3-20: Normalized river profiles with poorly graded shape. Each profile include the position of C_{max}, dL and Cf% (yellow area) and sorted according to the trend in Figure 3-17.

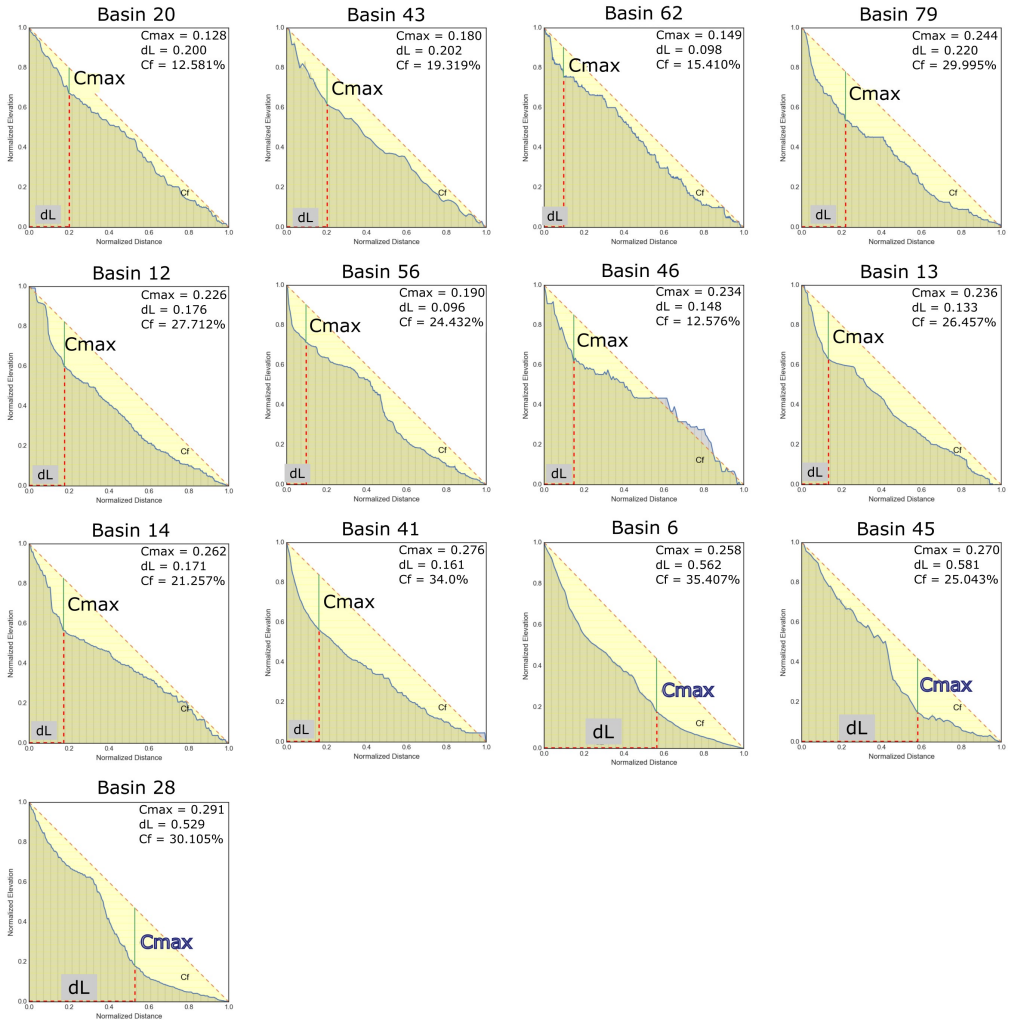


Figure 3-21: Normalized river profiles with transient state signal. Each profile include the position of C_{max}, dL and Cf% (yellow area) and sorted according to the trend in Figure 3-17.

and decreasing in the Central Valley. This lower-strength zone in the Central Valley is characterized by extensive exposures of alluvium and volcanic ash deposits (Oviedo-Reyes et al., 2024).

A striking precipitation gradient is evident from west to east. The western Coastal Cordillera and midportions of Central Valley is dominated by low annual precipitation (possibly <72 mm/year) (Figure 3-25C). Moving eastward, precipitation increases rapidly, transitioning through intermediate MAP values (>72 to 136 mm/year). The precipitation pattern closely follows the topography (volcanic system, e.g., Nevados de Chillán Volcanic Complex), with higher elevations receiving more rainfall (> 173 mm/year). This suggests a strong orographic effect, where the mountain range forces moist air to rise, cool, and precipitate(e.g., Montgomery et al., 2001; Rehak et al., 2010).

In Figure 3-25B, the Central Valley and western part of the Coastal Cordillera are predominantly light green to yellow, reflecting the combination of low rock strength and low precipitation. However, there are scattered darker patches where isolated high-strength rock outcrops coincide with slightly higher precipitation. A transitional zone between the Principal Cordillera and Central Valley shows

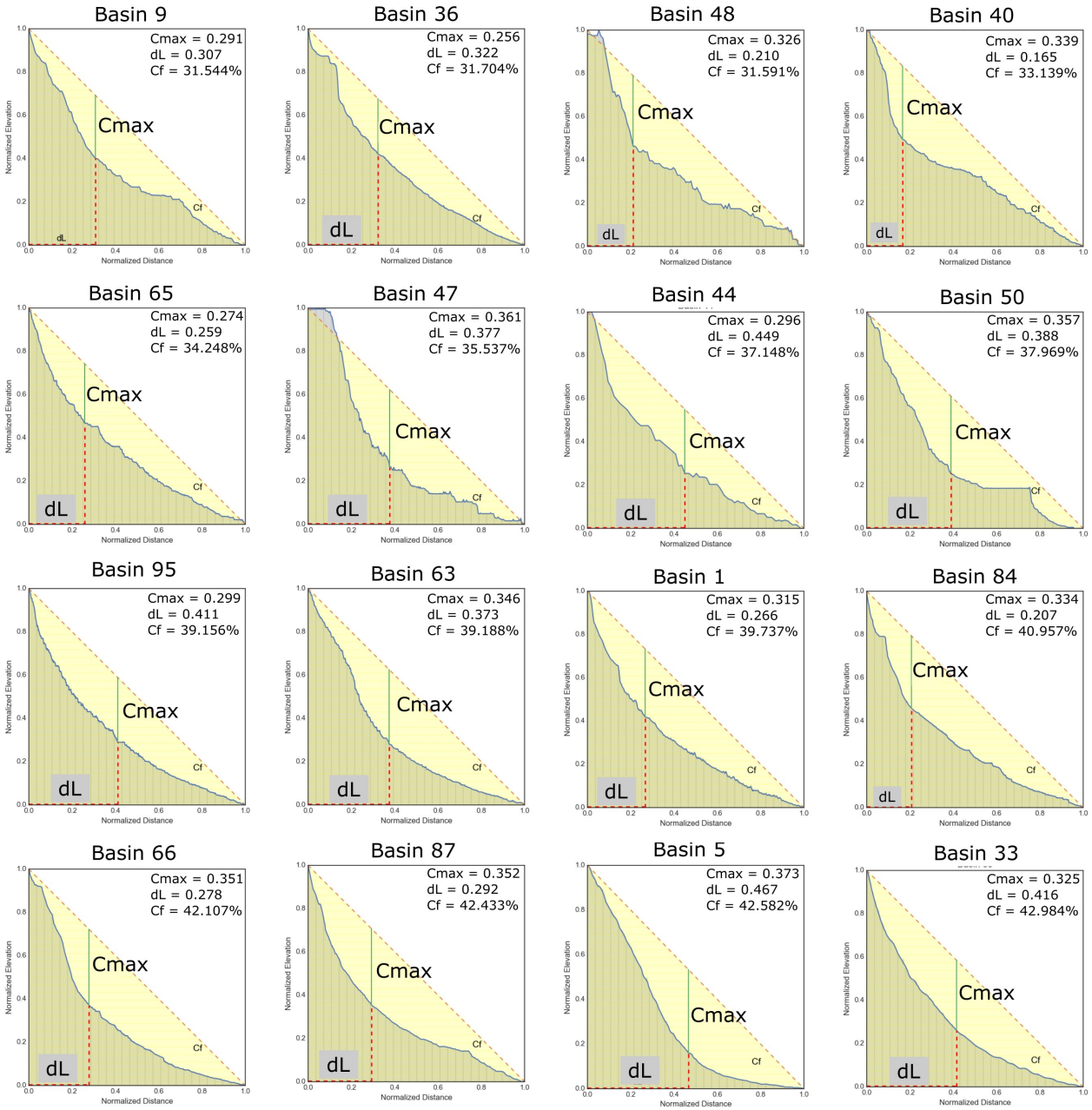


Figure 3-22: Normalized river profiles with graded profile shape. Each profile include the position of C_{max}, dL and Cf% (yellow area) and sorted according concavity factor (Cf%).

intermediate RS-MAP values (light blue to green). This area represents piedmont area with moderate rock strength and moderate precipitation. The RS-MAP map effectively highlights areas where high rock strength coincides with high precipitation. These areas are likely to experience the most intense weathering and erosion, considering the resistant bedrock, we observe a correlation between high probabilities in RS-MAP and local relief patterns (Figure 3-13). Therefore, variations in incision, as distinguished by local relief, may be attributed to differences in lithology or precipitation intensity. Uniformity in both patterns (lithology, climate) would allow to distinguish the signals of active tectonics, however, the signal of glacial erosion is not distinguished here.

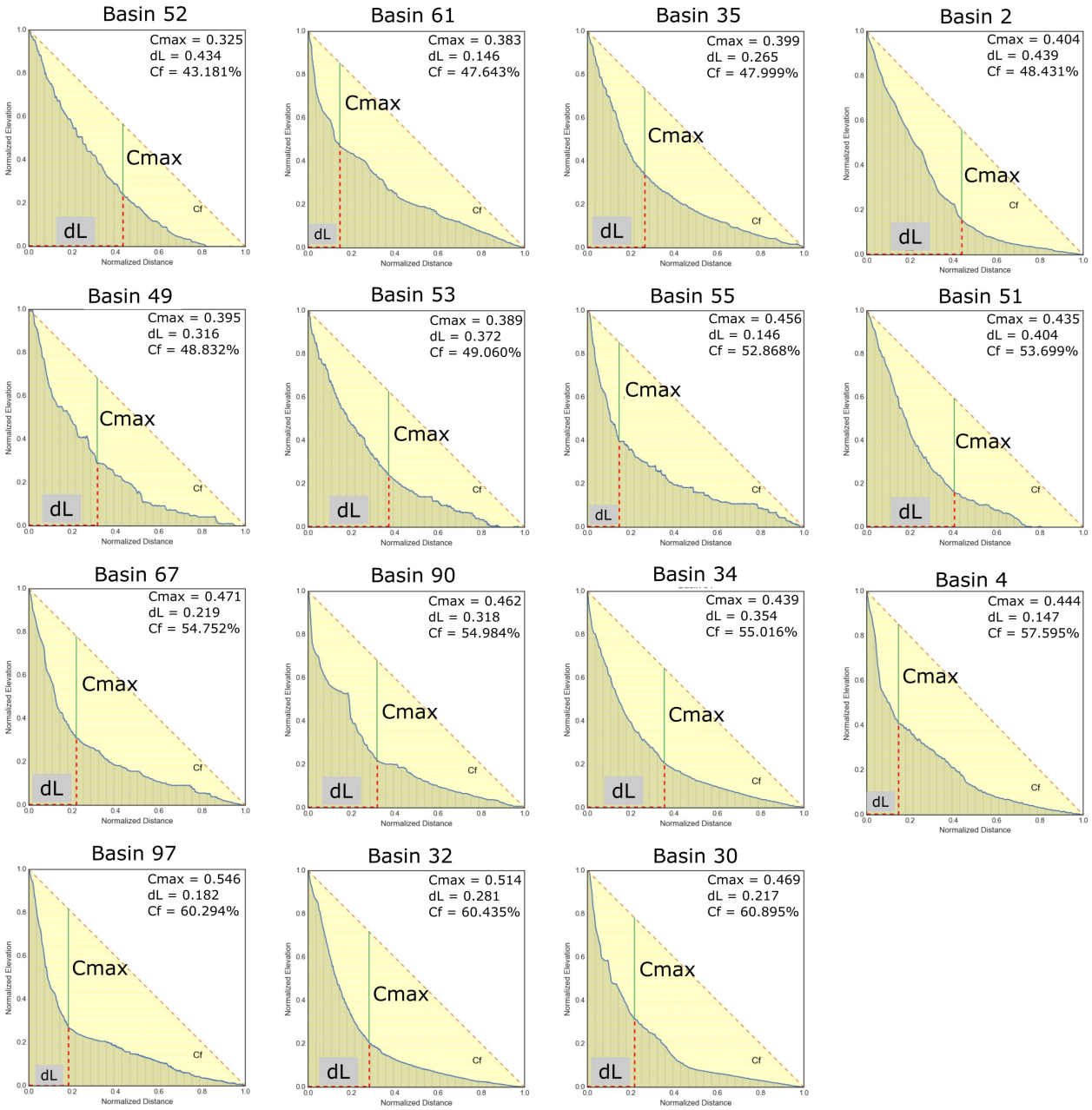


Figure 3-23: Normalized river profiles with graded profile shape. Each profile include the position of C_{max}, dL and Cf% (yellow area) and sorted according concavity factor (Cf%).

3.4.7 Relative tectonic activity index patterns

The tectonic activity classes from Iat reveal that 0.75% of the basins exhibit very high tectonic activity (Class 1, S/n values between 1 and 1.5) covering an area of 126.60 km^2, 20.58% show high tectonic activity (Class 2, S/n values of $1.5 \leq$ S/n < 2) covering an area of 3,390.81 km^2, 77,21% fall under moderately active tectonics (Class 3, S/n values of $2 \leq$ S/n < 2.5) covering an area of 13,087.61km^2, and 1.64% are characterized by low tectonic activity (Class 4, S/n values $\geq$ 2.5) covering an area of 126.6 km^2. These percentages highlight that the majority of the basins are moderately active tectonically, followed by a significant portion exhibiting high tectonic activity,

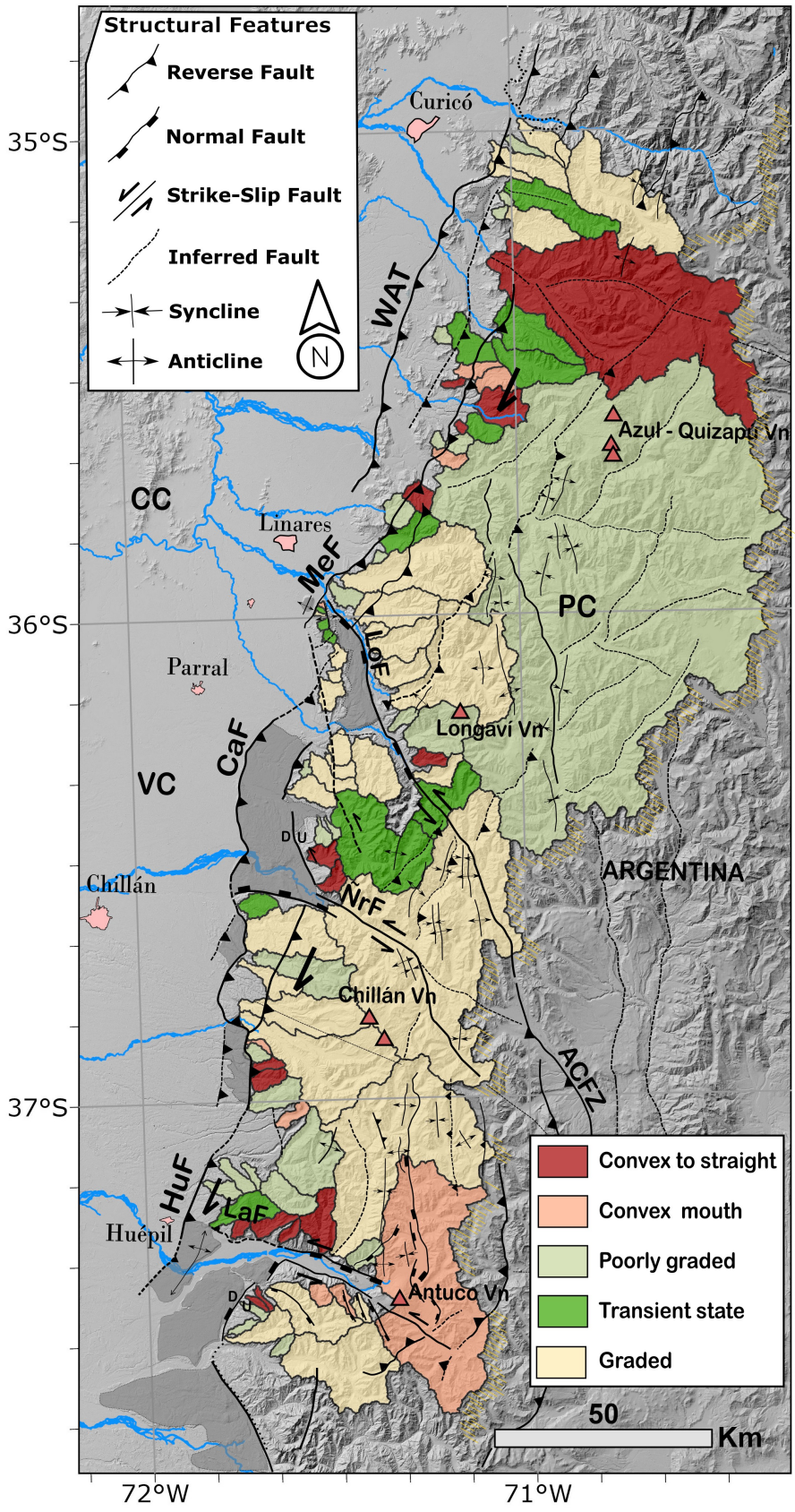


Figure 3-24: Normalized river profiles with graded profile shape. Each profile include the position of C_{max}, dL and Cf% (yellow area) and sorted according concavity factor (Cf%).

while very high and low tectonic activity classes are less represented, each making up a smaller fraction of the total (Figure 3-26A).

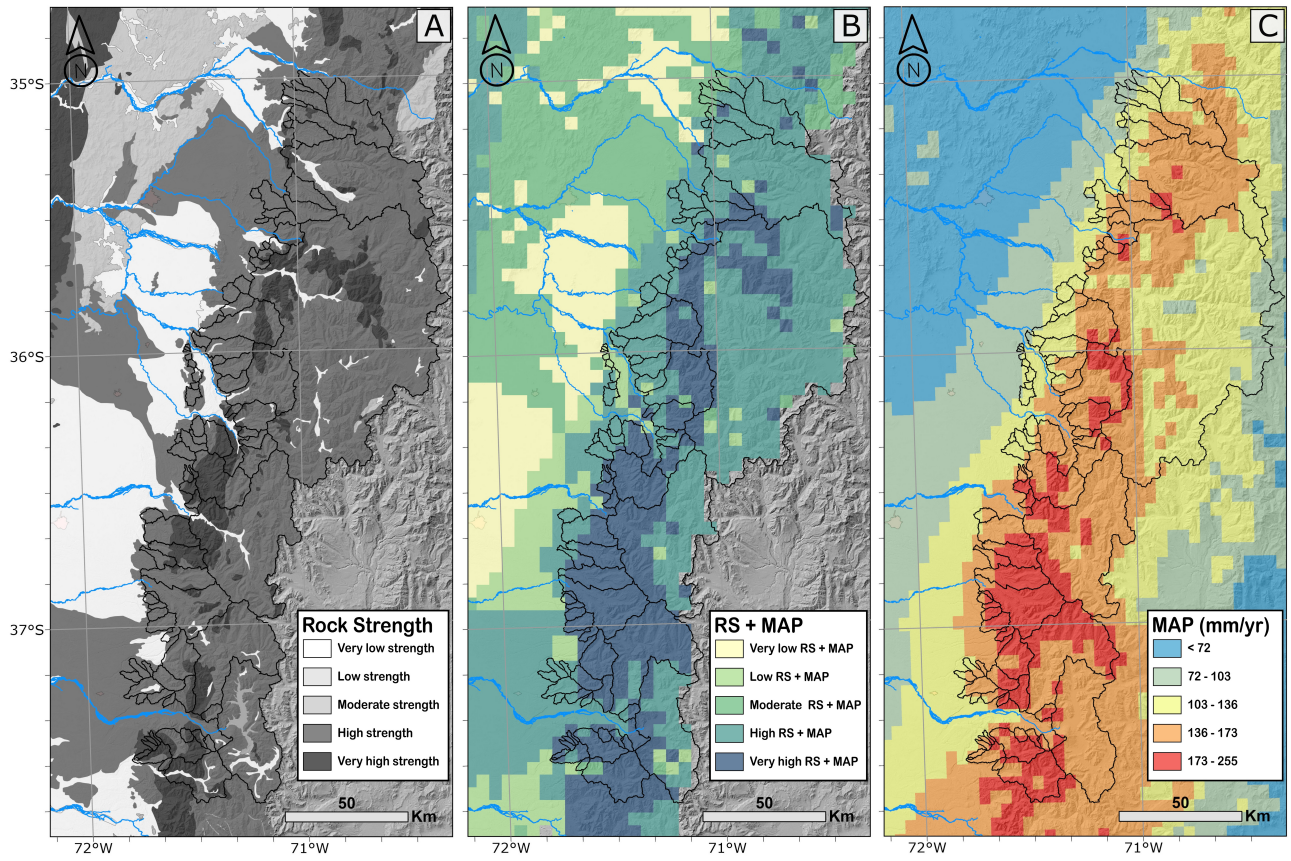


Figure 3-25: Relationships between rock strength (RS) and mean annual precipitation (MAP) along the Western Slope of the Principal Cordillera (WSPC) (modified from Oviedo-Reyes et al. (2024). A. Rock strength levels. B. RS+MAP raster obtained from weighted sum between RS and MAP pixels values (~5km). C. MAP- mean annual precipitation in a 0.05° latitude-longitude grid (approximately 5 km) spanning 1979 to 2019.

Conversely, from the relative tectonic activity index (RTA), it is revealed that 0.52% of the area (88.145 km^2) falls under Class 1, indicating very high tectonic activity, 20.59% (3,488.558 km^2) falls under Class 2, showing high tectonic activity, 65.08% (11,028.293 km^2) falls under Class 3, indicating moderately active tectonics, and 13.81% (2,338.305 km^2) falls under Class 4, characterized by low tectonic activity. These percentages highlight that the majority of the area is moderately active tectonically, followed by a significant portion exhibiting high tectonic activity, while very high and low tectonic activity classes are less represented, each making up a smaller fraction of the total (Figure 3-26B).

The WSPC exhibits a pronounced north-south trend characterized by valley and ridge patterns in polynomial regression curves (Figures 3-4, 3-6, 3-9, 3-14 and 3-16). Despite the predominant Smf index trend north of 36°S (Figure 3-4), the front can be divided into three sectors: southern (Huepil fault to Laja River), central (Cachapoal, Mesamávida, and Longaví-Achibueno faults), and northern (WAT region). Geomorphological indices often show an inverse relationship between the southern and northern sectors, while the central sector behaves oppositely, with the exception of Smf values. Additional parameters, such as basin outlet elevations, follow this pattern, forming a

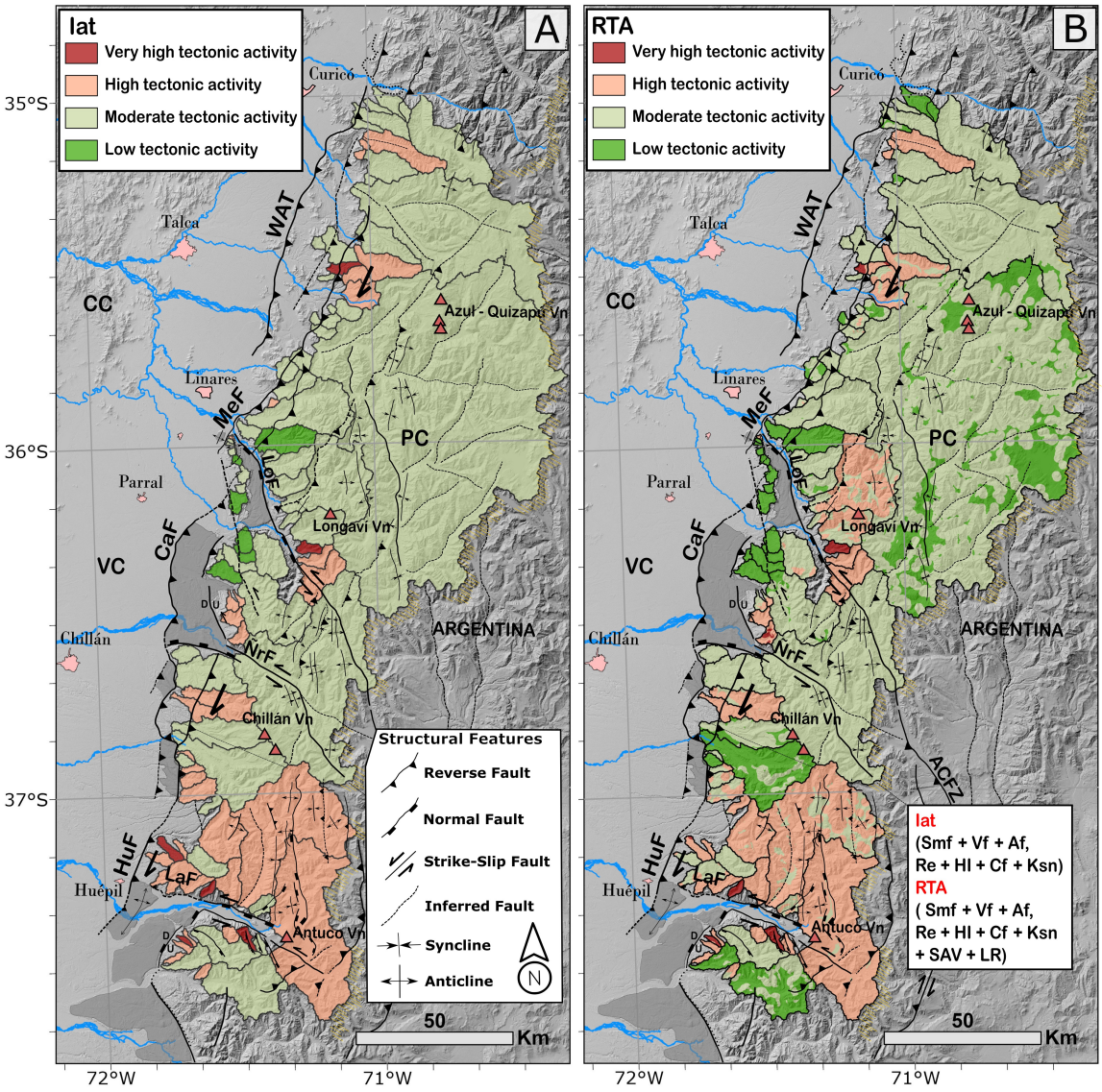


Figure 3-26: Relative active tectonics index for the Western Slope of the Principal Cordillera. A. Iat – defined by El Hamdouni et al. (2008) B. RTA index defined by Matoš et al. (2016). Note the internal mountain front (IMF, white line) and range bounding fault (with younger fault scarps) are depicted in the west of swath profiles (solid white line, c and d). Faults are from SERNAGEOMIN (2003), Melnick and Echtler (2006), Melnick, Charlet, et al. (2006), Folguera et al. (2004), Cembrano and Lara (2009), and Maldonado et al. (2021). **ACFZ**: Antiñir- Copahue fault system; **WAT**: West Andean Thrust; **CaF**: Cachapoal fault; **LoF**: Longaví-Achibueno Fault; **MeF**: Mesamávida Fault; **ÑrF**: Ñuble River fault; **LaF**: Laja River fault; **HuF**: Huépil fault.; **LLFS**: Lago Laja fault system **PC**: Principal Cordillera, **VC**: Central Valley, **CC**: Coastal Cordillera.

low-elevation depocenter between 36°S and 36°30'S.

Normalized river profiles parameters (C_{max} and Cf%) values indicate well-graded profiles in the central sector, contrasting with other areas (Figure 3-24). This trend, with some exceptions like the SFF sector in the Ñuble River (Figure 3-15B), is consistent with relatively stable K_{sn} values and concave S-shaped hypsometric curves. Statistical moments suggest increased remontant erosion in the upper and lower catchments (Sk, Kur, Dsk, Dkur, Figure 3-9) aligning with the normalized river profiles and hypsometric curve shapes.

The Huepil Fault shows high relative uplift rates, with its most significant signal at the Laja

River fault intersection. The Iat and RTA indices reveal recent tectonic activity along the Laja faults (Melnick, Charlet, et al., 2006), potentially extending to eastward-verging faults. However, this activity is also reflected by Lago Laja fault system (LLFS) with an averaged minimum extension rate of 1.2 $\pm$ 0.6 mm/y (Melnick, Charlet, et al., 2006). Also, the metrics indicate decreasing activity northeastward until the Ñuble River fault, consistent with the geometry proposed by Oviedo-Reyes et al. (2024).

3.5 Discussion

3.5.1 Spatial variation in tectonic activity

Most of the mapped area falls under the "moderate tectonic activity" category (class 3, Figure 3-26), especially north of 37°S. Zones of high and very high tectonic activity (classes 2 and 1 respectively, see Figure 3-16) are more localized and typically associated with specific structural features (e.g., LaF, ÑrF, or WAT). This result contrasts with the findings of Oviedo-Reyes et al. (2024), who classified tectonic activity using only the Smf/Vf ratio. The degree of relative tectonic activity proposed here partially aligns with that suggested by the aforementioned author, especially in areas of low to moderate tectonic activity. For example, we propose that the WAT trace and its strands (e.g., MeF) exhibit moderate tectonic activity from 35°S to 35°50'S, whereas the aforementioned study suggests that this segment is an inactive front (e.g., landscape assemblages support this hypothesis). These results may partly be explained by the additional use of morphometric indices tested in active deformation zones (e.g., Krystopowicz et al., 2020; Erbello et al., 2022) due to its potential advantage in differentiation of regions based on comprehensive area-wide morphometrics characteristics (e.g., Re, HI, AF, among other indices) (e.g., El Hamdouni et al., 2008; Dehbozorgi et al., 2010). Despite the novelty of this method, the yields obtained from a single relative active tectonic index generally reflects a moderate level of uncertainty regarding uplift patterns (e.g., Matoš et al., 2016).

We acknowledge that our findings using several geomorphic indices may be somewhat limited by lithological and climate controls over small catchments areas (e.g., Chen et al., 2003). The limitation considered here is that one or more indices may be influenced by controlling factors (e.g., lithology or climate) that result in incorrect assessments of tectonic activity using just one tectonic activity index. Despite this limitation, these indices serve as a preliminary tool for identifying areas with potential for detailed neotectonic studies. If the possible controlling factors are identified and isolated from the tectonic signals (e.g., Radaideh and Mosar, 2019), these indices can become a

valuable resource for regional interpretation of deformation.

The Iat and RTA maps reveals that the region exhibiting the highest relative tectonic uplift is concentrated south of 36°50'S latitude. Within this zone, the most pronounced uplift occurs at the intersection of the northwestern termination of the Laja River Fault (LaF) and the Huépil Fault (HuF), where their tectonic influence converges. These results match those observed in earlier studies which identify the HuF as an active structure with surface expression (Melnick et al., 2006), and the LaF as a NW – trending active structure controlling the course of the Laja river (Oviedo-Reyes et al., 2024). These results provide first evidence of geomorphic response to tectonic uplift from mountain-piedmont junction to drainage basin area scale. Further, Melnick, Charlet, et al. (2006) reported a growth rate of 0.18± 0.07 mm/yr for the central part of the anticline on the east side of the HuF, as well as an averaged minimum extension rate of 1.2 ± 0.6 mm/yr for the LLSF (Figure 3-26). We assume that the fold growth rate east of the Huepil Fault can be used as a proxy for rock uplift rate. Based on this assumption and the morphometric characteristics of the area, we assign an uplift rate of 0.18±0.07 mm/yr to Class 2.

Additionally, there are three other areas of importance regarding their degree of relative active tectonics. The first is located in the San Fabian sector (36°30'S), where the San Fabián Fault (SFF) is proposed as a sinistral fault (Oviedo-Reyes et al., 2024) that originates from the end of the Ñuble River fault. This fault zone shows evidence of transient river profiles (K_{sn} channel steepness, Figure 3-15B) adjusting to differential uplift reflected by knickpoints at the same elevation along both traces (Wobus, Tucker, and Anderson, 2006; Kirby and Whipple, 2012). To the north, the LoF trace shows a releasing bend, which allows the formation of normal faults. In particular, the Longaví River in this sector features a wide valley (1 to 3 km) and straight river course, providing evidence of structural control. And third one, located in the northern extension of the MeF (35°30'S), exhibits the same elements described earlier. However, unlike the other two sectors, it does not display a straight mountain-piedmont junction. Nonetheless, structural control over nearby drainages is evident.

Furthermore, RTA map shows a more detailed and fragmented distribution of tectonic activity levels compared to the Iat map. This is likely due to the inclusion of local relief and slope variability, which capture finer-scale topographic variations. Low tectonic activity areas are more widespread in the RTA map, particularly in the upper reach of Maule basin and sparse locations in the WSPC. This suggests that when considering local relief and slope variability, these areas appear with less incision and slope angle variability. Both maps agree on the location of major zones of high tectonic activity, providing confidence in the robustness of these features across different analytical methods. The Iat map provides a more generalized, regional-scale view of tectonic activity, while the RTA map offers insights into local variations and the influence of small-scale topographic features.

3.5.2 Morphometric properties and their response to climate forcing

This study quantifies the landscape's response to tectonic uplift by integrating multiple metrics into a single index of relative active tectonics. The objective is to gather information on the NNE and NW structures that appear to accumulate deformation at their intersection and to identify signals that may be influenced by lithological and/or climatic controls. Results support the neotectonic character of the Huepil faults, NW-trending faults and shed light into new areas reported with a lower degree in relative active tectonics (e.g., SFF). However, the main hypothesis follows the premise that glacial erosion and precipitation, coupled with isostatic rock uplift and active tectonics, significantly contribute to the morphological response of the valleys and topography metrics in the WSPC (Rehak et al., 2010; Stalder et al., 2020; Harries et al., 2023; Oviedo-Reyes et al., 2024). Stalder et al. (2020) attributed the high Pleistocene erosion rates (over 2 km/Ma) to the complex interplay between these variables in a positive feedback loop mechanism, enhancing the present-day relief. The variables described exert a control in metrics (e.g., Troiani et al., 2014) and some signals can be misleading the significance of patterns in tectonic deformation (e.g., Diercks et al., 2023).

Between 35-38°S a significant change in the local relief can be observed: the northern (above at 36°S) (up to 1700m) and southern (1300m) sectors of the study area. This signal is associated with a glacial imprint on the topography, which was initially thought to extend only to 35°S (Rehak et al., 2010), but evidence now suggests it extends to 36°S (Stalder et al., 2020). Certainly, recent studies have identified typical glacial topographic features at 35.5°S, including glacial cirques (average altitude 2700 masl), glacial valleys (such as Del Indio Valley), glacial striations (Yegüitas Valley), lateral moraines (from the Pleistocene), and volcanic landforms, including stacks of lava flows distributed east-west and the edifice of the Manantial Pelado volcano (Mejías Osorio et al., 2024).

K_{sn} values are strongly influenced by the transition from glacial to fluvial geomorphic systems (Figures 3-15C and 3-15D). We have demonstrated that high K_{sn} values ($250m^{0.9}$) and knickpoints related to channel slope are closely associated with this transition (35°48'S, 70°45'W) (Figure 3-27). The hanging valleys observed in this transition, remnants of former U-shaped glacial troughs, evolve into steeper V-shaped valleys as they adjust to new equilibrium conditions dominated by fluvial erosion.

The observed knickpoints can be mapped over this transition zone over 2200 masl (Figure 3-15D), clearly depicted in the incision patterns of the local relief ($>$ 1300m). Other areas, steep erosional topography (e.g., Singer et al., 1997) in the upper reach of Achibueno River (at 36°S, basin 36) is resulting from glacial cirques which show high K_{sn} values (Figure 3-15). Interestingly,

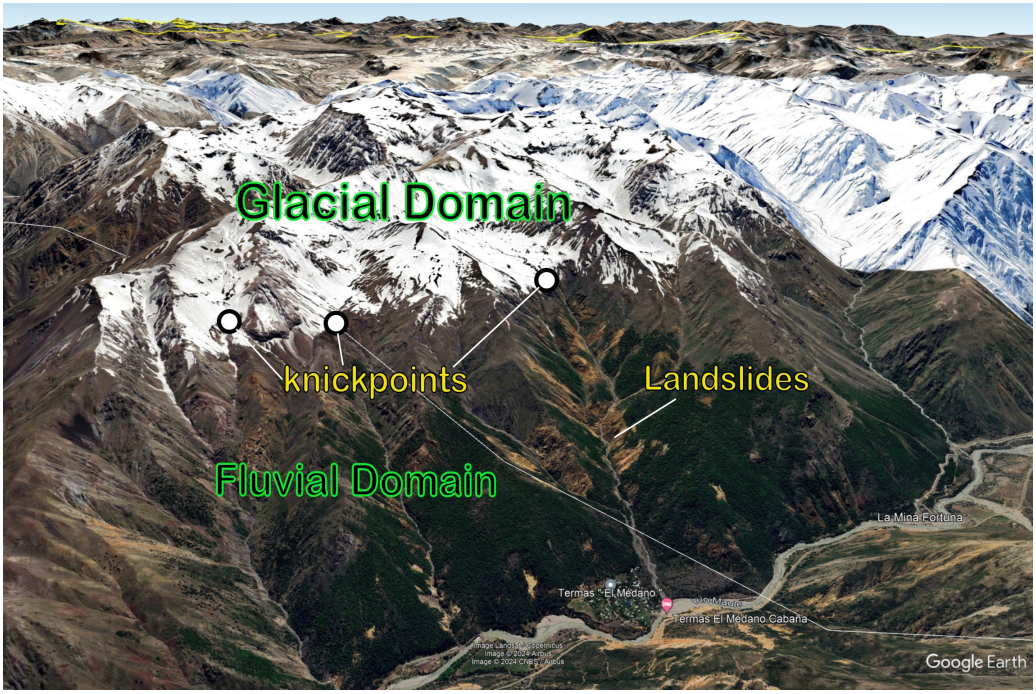


Figure 3-27: Panoramic view looking northeast over the La Mina sector, illustrating the transition between geomorphic domains. The knickpoints, marked by white dots, are situated at 2200 masl, defining the boundary between these domains. At the bottom of the image, the Maule River flows 1200 meters below the knickpoints. (Image modified from Google Earth).

this geomorphic transition is observable both north and south of the Maule River basin, suggesting a remnant surface where Pleistocene glacial activity occurred. Here, we observe that the local relief results from repeated glacial erosion during the Quaternary (Rehak et al., 2010), followed by a transition to fluvial erosional processes. Therefore, the interpretation of K_{sn} as an indicator of active tectonics should be approached with caution, as it may lead to misinterpretations when applied to mechanical uplift models or when inferring transient state information from longitudinal river profiles. Our analysis reveals that variations in the normalized channel steepness index (K_{sn}) across the Western Slope of Principal Cordillera (WSPC, 35°S-38°S) are primarily driven by climatic gradients and differential lithological resistance. This non-tectonic control on channel metrics is reported by Oviedo-Reyes et al. (2024) for the stream-gradient channel SL (Hack Index). However, a critical question emerges: How can erosion rates be so high (e.g., Stalder et al., 2020) while the relief remains relatively uniform between 36°S and 37°S.

The mountain front where the Maule basin is located has been described as an inactive thrust front based on morphometric indices (Oviedo-Reyes et al., 2024), characterized by high sinuosity and a landscape with inselbergs and embayment. However, our results suggest that this front exhibits low to moderate tectonic activity (Figure 3-26), with evidence of high relative uplift rates at 35°30'S. We believe the evidence at the piedmont-mountain junction sufficiently explains the perceived inactivity of this front, and we speculate that the uniformity of the relief is maintained

due to isostatic rebound, possibly reactivating small segments of the Andean front between 35° and 36°S.

Variables describing precipitation such as mean annual precipitation (MAP, Figure 3-25C) increases southward from 36°S (data from 1979 to 2019) (Montgomery et al., 2001; Rehak et al., 2010). This variability is consistent with a decrease in local relief (Figure 3-13B) implying a negative correlation between precipitation and local relief (Rehak et al., 2010). Our data reveal that the glacial imprint proposed by Rehak et al. (2010) ends at 35°S actually extends to 36°S (e.g., Stalder et al., 2020). This significant finding suggests that morphometric index variations should be analyzed from two distinct perspectives: a glacial perspective northward (from 36°S) and a fluvial erosion perspective southward. Local relief values are often elevated in areas with granitoid outcrops (Figures 3-25A and 3-25B), and these variations are reflected in indices such as hypsometric curves and normalized river profiles (e.g., basin 56 at 36°30'S, Figures 3-12 and 3-24). In fact, increasing rainfall correlates with southward-increasing drainage density, leading to more effective denudation of upper catchments (eg. Rehak et al., 2010; Lifton and Chase, 1992).

From 36°20'S southward, we observe a decrease in hypsometric integral (HI) statistical moments (e.g., skewness, kurtosis) with S-shaped and convex hypsometric curves (HC, Figure 3-12) and graded profiles covering around 70% of the area (Figure 3-24). These data suggest erosional states triggered by the southward increase in precipitation. Considering that the topography of the basin is lithologically controlled, we can isolate the lithologic-climatic signal (e.g., Figure 3-25B) from the tectonics using morphometric indices. The sector representing this individualization is the intersection between the Huepil and Laja faults (Figure 3-26).

3.5.3 Fault Segmentation and growth from morphometric properties

Faults in the Western Slope of Principal Cordillera (WSPC) between 35°S and 38°S are predominantly characterized by inferred segments 40 to 50 km in length (e.g., Maldonado et al., 2021), oriented in NNE and NW directions (Oviedo-Reyes et al., 2024). From the structural framework (Figure 3-2), we observe that these segments are often inferred where faults intersect active sediment channels of major rivers. In that case, the Huepil (HuF), Cachapoal (CaF), San Fabian (SFF), and Mesamávida (MeF) faults exhibit morphological segmentation (e.g.,Ellis and Barnes, 2015), where the fault tips limited in some cases by NW-trending structures. From Iat/RTA maps and north-south morphometric analysis (Figures 3-26 and 3-28), we concluded that particular intersection between orthogonal faults are most tectonically controlled segments in the study area.

Fault tips of the studied segments are frequently obscured by Quaternary sediments from active

river channels originating in the Principal Cordillera or tilted alluvial fans (e.g., Huépil area). Our findings provide valuable insights into the understanding of morphological segmentation and fault growth processes in the WSPC. Our analysis reveals that within the study area, NW-trending faults exhibit moderate to high relative tectonic activity. This observation suggests that neotectonic deformation is not concentrated along a single frontal structure but rather distributed across both NNE- and NW-oriented fault systems. The variability observed in the geomorphic indices in the WSPC suggests that NNE-trending faults have a highly segmented morphology. It indicates that these fault segments continue growing and interacting (Densmore et al., 2007).

Analyzing the segments with relatively high uplift rates along the Western Andean Front reveals variations toward the fault terminations (Figure 3-28). In particular, at the northern termination of the HuF, there is a noticeable variability in uplift rates, suggesting a stronger response to uplift. This is evidenced by a rectilinear front (Smf $<$ 1.5) with V-shaped valleys (Vf$<$0.5), highly elongated basins (Re$<$ 0.55), and greater erosion in both the upper and lower parts of the basins due to increased deformation (high values of Sk and Kur). Additionally, a decreasing concavity factor (Cf%) (indicating poorly graded profiles) and an increase in the altitude of basin outlets suggest intensified deformation toward the northern termination. This leads us to speculate that the next rupture could occur in this sector, a hypothesis supported by the significant tilting of alluvial fans further north. We propose, considering morphometric analyses, that the faults in the Western Andean Front grow by segment linkage (e.g., Densmore et al., 2007). This is suggested by our data, which show that deformation propagates at the fault tips. In SFF (Figure 3-29), the rupture is expected to be towards the southern termination, although the most accepted interpretation is the interaction with the Ñuble river fault. Otherwise, in the MeF sector, the data suggest high deformation at the southern termination of the fault (Figure 3-30).

3.6 Conclusions

The spatial variation in tectonic activity along the Western Slope of the Principal Cordillera reveals significant findings. Most areas exhibit moderate tectonic activity, particularly north of 37°S, while zones of higher activity are localized around specific structural features like LaF, ÑrF, and WAT. This aligns partially with previous studies but highlights the advantage of using comprehensive morphometric indices for more accurate regional differentiation. The northern tip of the HuF shows a pronounced deformation zone, suggesting a likely northeast propagation, supported by geomorphic evidence such as V-shaped valleys, elongated basins, and tilted alluvial fans. Additionally, the San Fabian sector (36°30'S) and the northern extension of the MeF (35°30'S) show significant tectonic

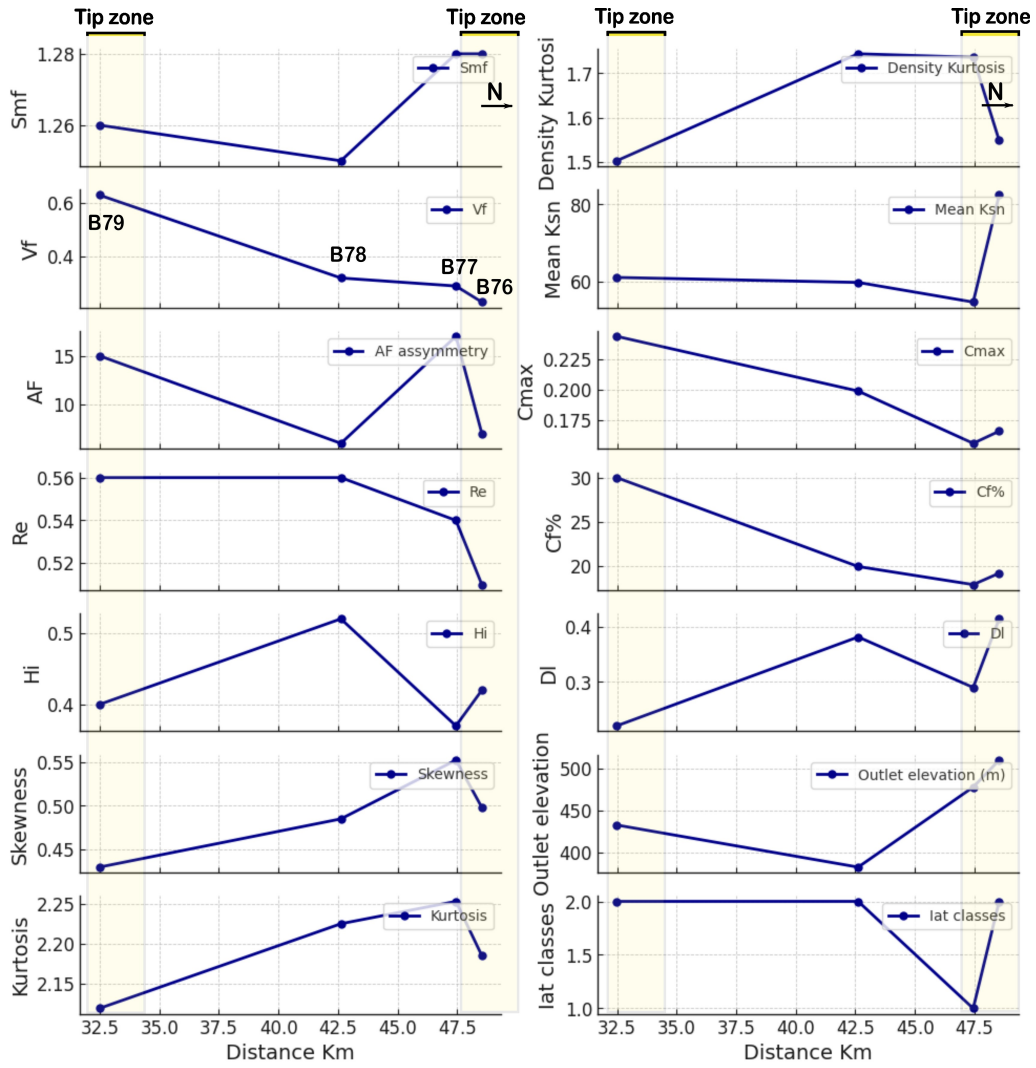


Figure 3-28: Variations in morphometric indices along the Huépil Fault trace. Fault terminations are highlighted (yellow box). Related basins are named e.g. B79 (see Figure 3-4).

activity, with transient river profiles and structural control over drainages indicating differential uplift. The RTA map provides a more detailed view of tectonic activity levels, emphasizing the importance of local relief and slope variability. Morphometric analyses indicate that faults in the Western Andean Front grow by segment linkage, with deformation propagating at fault tips. This is evident in the NNE and NW trending faults, where segments interact and drive rupture, creating a highly segmented morphology. The analysis also suggests that the SFF is likely to rupture towards its southern termination, while the MeF shows high deformation at its southern end.

This study extends the understanding of the glacial imprint on topography from 35°S to 36°S, necessitating a dual perspective in analyzing morphometric index variations: glacial northward and fluvial erosion southward. Normalized channel steepness index (K_{sn}) variations are primarily driven by climatic and lithological factors rather than tectonics alone, emphasizing cautious interpretation of geomorphic indices. Despite high erosion rates and climate-driven fluvial response, uniform relief

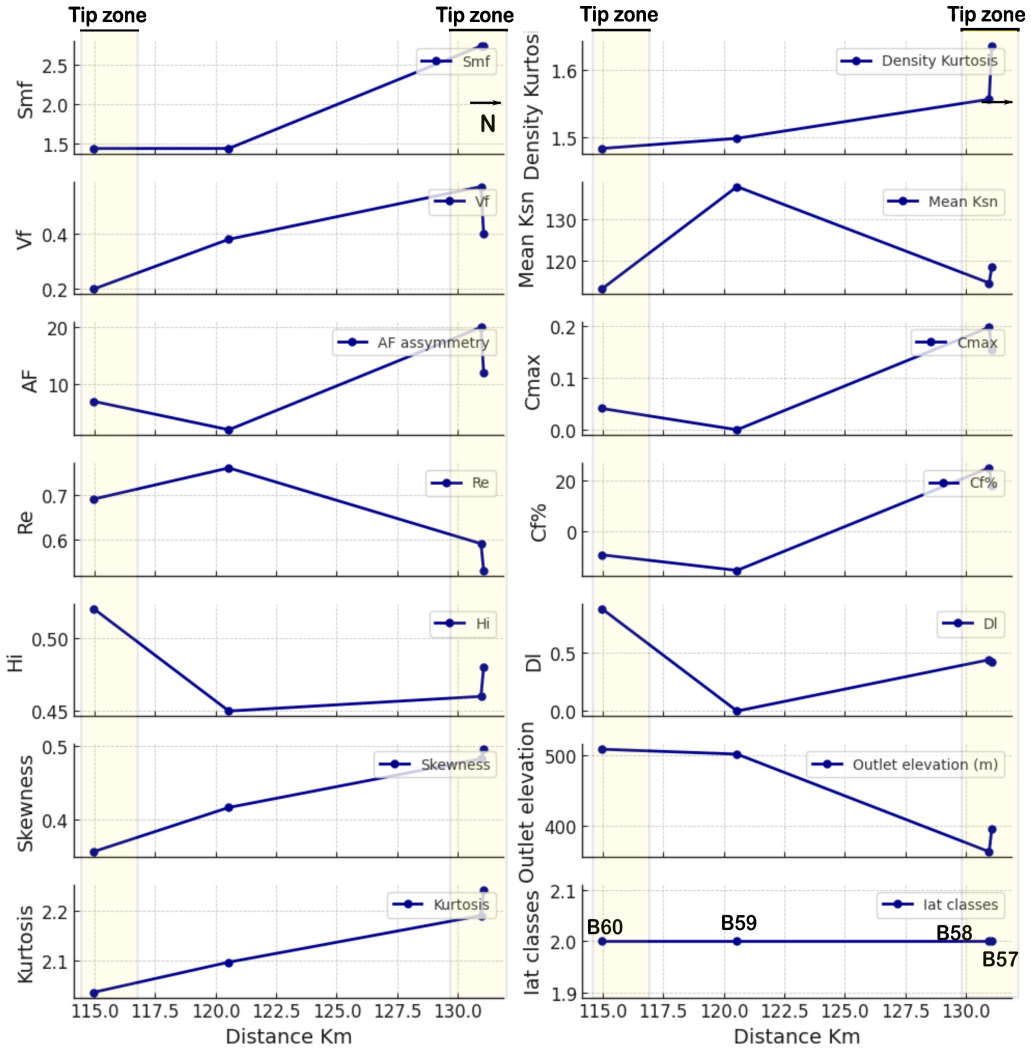


Figure 3-29: Variations in morphometric indices along the San Fabian Fault trace. Fault terminations are highlighted (yellow box). Related basins are named e.g. B79 (see Figure 3-4).

is maintained, possibly by isostatic rebound. By integrating multiple indices and isolating lithologic-climatic signals from tectonic ones, the study provides insights into landscape evolution complexities and sets the stage for future neotectonic investigations.

Overall, these findings underscore the importance of integrating multiple geomorphic indices and considering both tectonic and climatic factors to understand fault growth and segmentation. This comprehensive approach provides valuable insights into the tectonic evolution of the Principal Cordillera and aids in identifying areas for further detailed neotectonic studies.

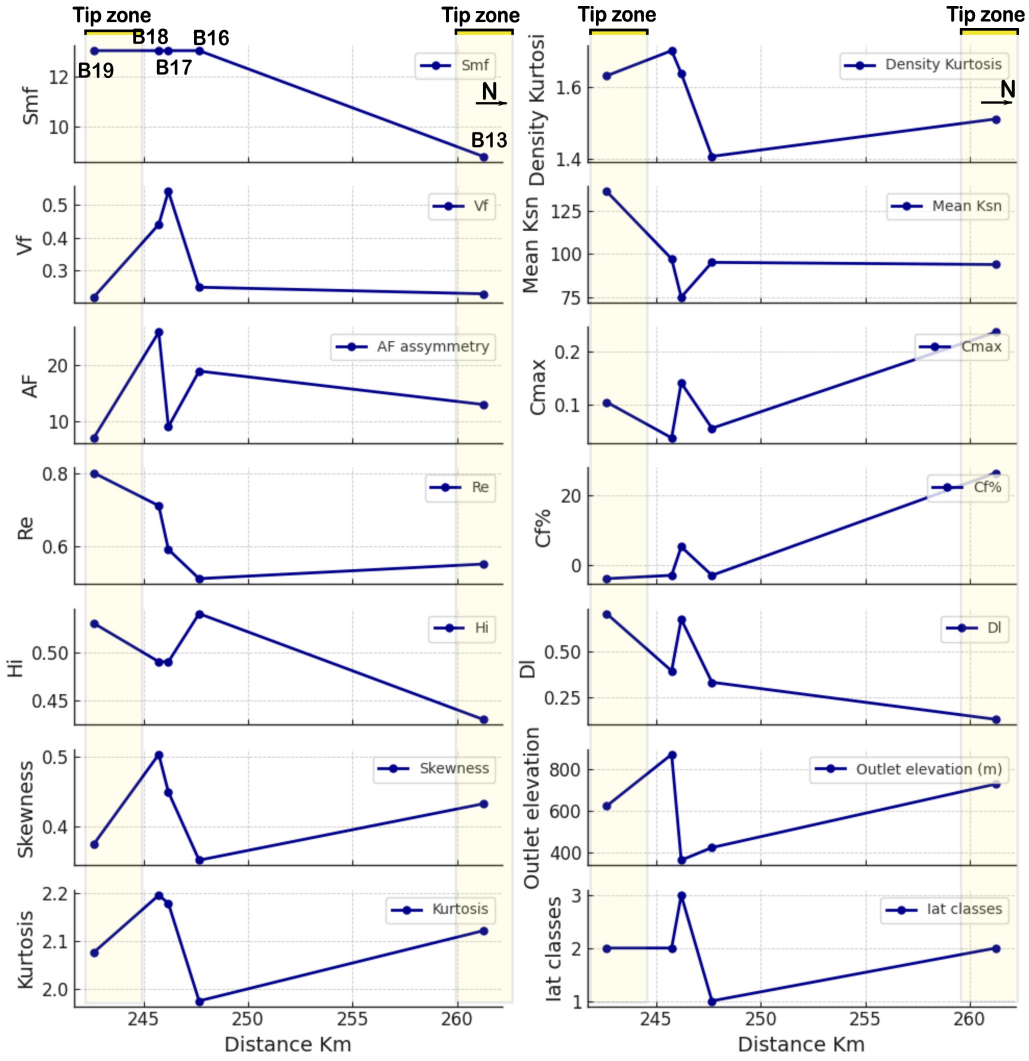


Figure 3-30: Variations in morphometric indices along the Mesamávida Fault trace. Fault terminations are highlighted (yellow box). Related basins are named e.g. B79 (see Figure 3-4).

Capítulo 4

Morphometric analysis detects faulting styles imprinted on geomorphic features: Example from the Western Andean Front (35°S-38°S), central Chile

Morphometric analysis detects faulting styles imprinted on geomorphic features: Example from the Western Andean Front (35°S-38°S), central Chile [1]

Jorge Adrián Oviedo-Reyes[1]; Joaquín Cortes Aranda[1]; Alfonso Fernandez[12]

[1]Departamento de Ciencias de la Tierra, Universidad de Concepción, Concepción, Chile

[2]Departamento de Geografía, Universidad de Concepción, Concepción, Chile

Abstract Logarithmic regressions of morphometric indices- mountain front sinuosity (Smf) and valley floor width-to-height ratio (Vf)- may offer a quantitative approach to infer the style of faulting from landscape morphology (Silva et al., 2003). Here, by using this approach, we analyze neotectonic faulting kinematics of the Western Andean Front (WAF) in central Chile (35-38°S). Regression results reveal two distinct clusters: 1) NW-striking faults with Vf=1.106Ln(Smf)+0.0078, indicating strike-slip to oblique faulting; 2) NNE-striking faults with Vf=1.76Ln(Smf)+0.346, consistent with reverse/thrust faulting. The statistical Kolmogorov-Smirnov test confirms that these Smf/Vf patterns are statistically comparable to other tectonic settings worldwide. NW-striking faults (e.g., Laja and Longaví-Achibueno) exhibit lower Vf values, indicating higher tectonic activity and fluvial downcutting. NNE-striking faults accommodate deformation via thrusting and consequently show slightly higher Vf values in similarly active segments. As tectonic activity decreases along NNE-striking faults, Vf values increase more markedly compared to NW segments, amplifying the contrast between fault orientations. This morphometric analysis confirms that Smf and Vf may serve as first-order proxies for discerning faulting styles from landscape morphology, which is particularly valuable where subsurface data is limited.

KEYWORDS:Geomorphic indices, Logarithmic regressions, Kinematic Proxy, Western Andean Front.

4.1 Introduction

Mountain-piedmont junctions represent a crucial interface where mountainous escarpments meet adjacent basins. Over geological time-scales, these transition zones can be significantly modified by faults in various tectonic settings (Bull, 2007). Fault-generated mountain fronts exhibit numerous geomorphic features indicative of recent tectonic activity (Bull and McFadden, 1977; Wallace et al., 1978), but may also record the imprint of faulting styles (Silva et al., 2003). Both, activity level and fault kinematics, can be elucidated by analyzing geomorphic indices such as the mountain-front

[1]Article Submitted to Journal of Southamerican Earth Sciences- SI Andean Geomorphology

sinuosity (Smf; e.g., Bull and McFadden, 1977) and valley floor width-to-height ratio (Vf; e.g., Bull and McFadden, 1977), which can be obtained from the many Digital Elevation Models (DEMs) that are currently available (e.g., Silva et al., 2003). This approach is particularly valuable in remote or less-studied areas, where detailed geological and geophysical data are sparse, offering a cost-effective and efficient method. Specifically, logarithmic regressions between Smf and Vf provides a quantitative method to describe the mountain front's shape and the possible types of faults (e.g., Silva et al., 2003).

The WAF strip extending from 35°S to ~38°S exemplifies an ideal landscape to test the applicability of these methods. With elevations ranging from ~3000 m ~1000 m towards its southern extent (Montgomery et al., 2001), this physiographic feature is supposed to be controlled by a Late Miocene NNE-striking east-dipping reverse faults (Radic, 2010; Figure 1A). Secondary strike slip NW-striking structures have also been proposed to occur in the area, related to the western termination of the Cortaderas lineament on the western flank of the Principal Cordillera, considered a basement boundary reactivated during Andean deformation (Ramos and Kay, 2006). In this context, one of the open questions concerning the tectonic evolution of the WAF between 35°S and 38°S is related to the Late Quaternary kinematics of the causative faults.

In this research, we build upon our morphometric analysis that unveiled neotectonic structures along the Western Andean Front (WAF) between 35°S and 38°S (Oviedo-Reyes et al., 2024), to provide a comprehensive overview of its potential to reveal fault styles along mountain-piedmont junction (Figure 4-1B). From this analysis of faulting style, we provided a kinematic analysis using aerial/satellite imagery interpretation to characterize surface fault expressions and offset landforms. To do so, we compiled a database of several structural domains (e.g., Rimando and Schoenbohm, 2020), and employ the logarithmic regression methods used by Silva et al. (2003), to examine the relationship between the morphology of the mountain front and the faulting style in the study area. We analytically demonstrate that this kind of morphometric data analysis constitute a proxy for characterizing the faulting style in the studied WAF segment; for the study area, the applicability of this approach will be soon contrasted with structural field data. Likely, this technique will be useful for assessing the Late Quaternary kinematics of faults in other WAF domains and other similar tectonic settings.

4.2 Methodology

Smf reflects the balance between erosional processes and tectonic uplift at a given mountain front (Bull and McFadden, 1977; E. Keller and Pinter, 2002), and it is calculated as the ratio of the

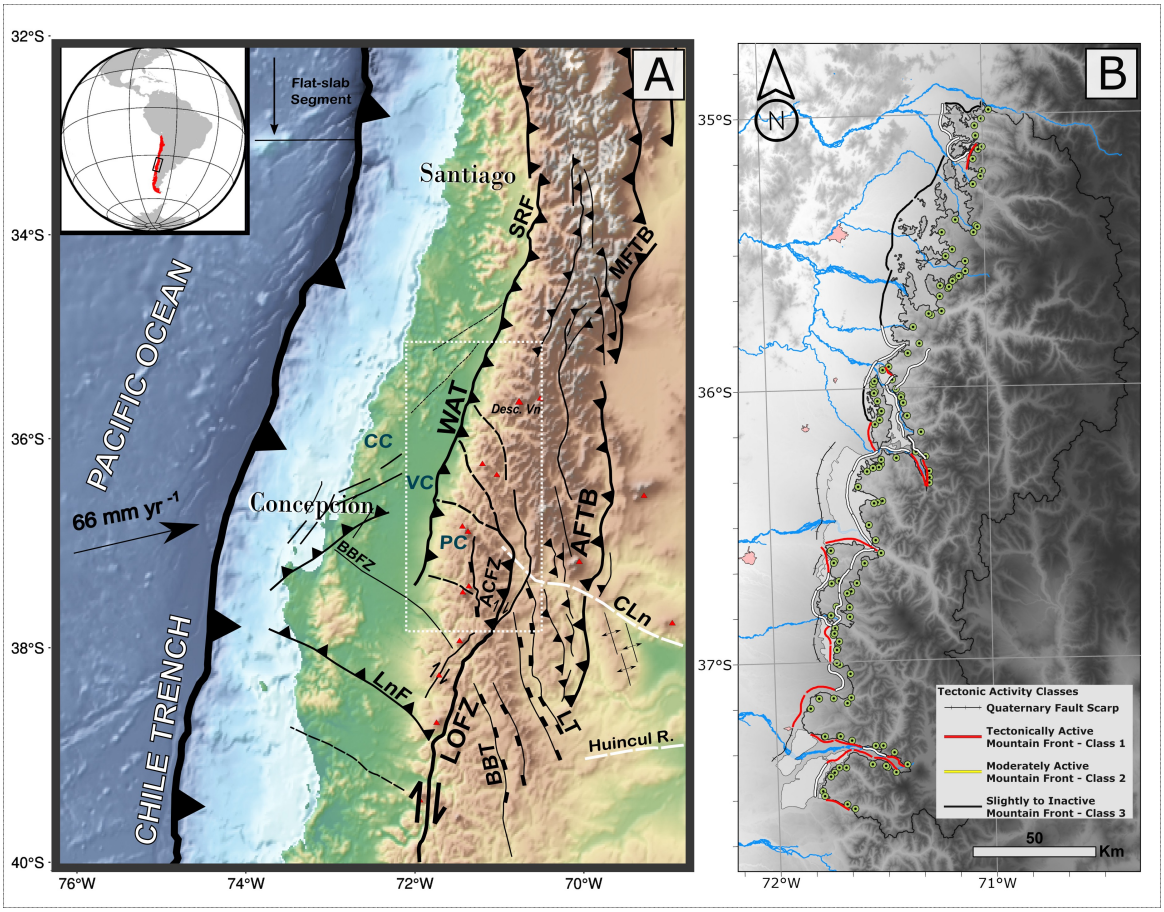


Figure 4-1: Tectonic and structural features for Western Andean Front in Chilean Andes (32-40°S). A. Three main morphotectonics features are displayed: Coastal Cordillera (CC), a 60-80 km wide range with peaks up to 700 m, Central Valley (VC), 20-60 km wide with an average altitude of ∼200 m, filled with Quaternary sediments, and the Principal Cordillera (PC), a 50-100 km wide range with peaks reaching up to ∼3953 m.a.s.l. Main volcanoes are highlighted (red triangles). **SRF**: San Ramon Fault; **WAT**: West Andean Thrust; **ACFZ**: Antiñir-Copahue Fault System; **BBT**: Bío Bío Trough; **LT**: Loncopué Trough; **ND**: Nahuelbuta Range; **LnF**: – Lanalhue Fault; **LOFZ**: Liquiñe Ofqui Fault System; **AFTB**: Agrio Fold Thrust Belt; **MFTB**: Malargüe Fold Thrust Belt; Huincul Ridge; **BBFZ**: Bío Bío Fault Zone; **CLn**: Cortaderas B. Tectonic activity classes for WAF (35-37°S) and location of Vf index measurements (Modified from Oviedo-Reyes et al. (2024)). The mountain-piedmont junction in the study area extends NNE parallel to Principal Cordillera and in agreement with inferred the Western Andean Thrust (WAT).

planimetric length along the mountain-piedmont junction (Lmf) to the straight-line length of the mountain front (Ls):

$$Smf = \frac{Lmf}{Ls} \tag{4.1}$$

Lower Smf values (<1.4) indicate tectonically active fronts, while higher values (>3.0) suggest less tectonic activity. In turn, Vf describes the cross-sectional shape of a valley, V-shaped valleys (Vf<0.5), usually resulting from high fluvial incision related to rapid uplift, from U-shaped valleys (high Vf values) reflecting less incision and degradation processes such as valley widening and ridge-crest lowering (e.g., Bull, 2007; Burbank and Anderson, 2011). According to Bull and McFadden (1977) Vf is the quotient of the valley width to the sum of the heights of the valley sides:

$$Vf = \frac{2Vfw}{(Eld - Esc) + (Erd - Esc)} \tag{4.2}$$

Vf values less than 0.5 typically indicate V-shaped valleys formed by rapid uplift, while higher values suggest U-shaped valleys resulting from slower erosion and degradation processes.

The style of faulting can be discriminated from analysis of patterns in logarithmic regressions between the mountain-front sinuosity index (Smf) and the floor width-to-height ratio (Vf) (Silva et al., 2003). These regressions consist of a plot of Smf/Vf data of the related range-front faults considered in differentiated clusters with a kinematic interpretation. The equation which defines the logarithmic regressions is defined as follows:

$$Vf = AL_n(Smf) \pm B(1) \tag{4.3}$$

where A is the slope and B represent the intercept in Smf/Vf data plot. Silva et al. (2003), in their study of tectonically controlled mountain fronts in SE Spain, noticed that when performing the same regressions with data from other structural domains, they exhibited unique characteristics among data sets. Silva et al. (2003) demonstrated that morphometric data for different structural domains can be reasonably discriminated using this statistical analysis derived. More specifically, the meaning of a logarithmic behavior in this relationship shows variations in the constants A and B: Firstly, constant A value reflects the rate of change in Vf with respect to Smf, where higher values of A indicate a steeper increase in Vf as Smf increases. Parameters A increases from normal faulted fronts to strike-slip faulted fronts, and further to reverse-faulted and bounding folded fronts. Larger uplift events associated with reverse/folding regimes lead to a more rapid increase in Vf with increasing Smf (sinuosity). Secondly, constant B reflects negative values for normal faulted fronts, while it is positive for strike-slip, reverse, and bounding folded fronts. This negative B is interpreted as a morphometric signature of normal faulting, related to the maintenance of V-shaped valleys due to significant vertical slip. The positive B for other faulting styles suggests that Vf starts at higher values, even at low Smf, due to less effective vertical slip in maintaining V-shaped valleys. Therefore, these characteristics were defined by their structural style, which coincided with the observed kinematics between reverse, normal, and strike-slip faults.

Table 4.1: Range of data used to calculate logarithmic regression lines for the Western Andean Front between 35° and 36° S (modified from Oviedo-Reyes et al. (2024)). Some segments do not show Vf values because no major drainage is developed on the studied segment; therefore, no value appears on the Smf/Vf plots (*). ND = No Data.

Mountain Front	Smf	Vf (Mean)	Tectonic activity Class	Fault Trace	Faulting Style
1	3,77	2,673	3	NNE Faulting	Reverse faulting with strike-slip component
2	2,47	1,11	2	NNE Faulting	strike-slip faulting to oblique faulting
3	1,51	*	2	NNE Faulting	ND
4	1,24	0,597	1	NNE Faulting	Reverse faulting with strike-slip component
5	8,81	0,386	3	NNE Faulting	ND
6	13,06	0,473	3	NNE Faulting	ND
7	3,50	0,191	3	NNE Faulting	Strike-slip faulting to oblique faulting
8	1,94	0,576	2	NNE Faulting	Strike-slip faulting to oblique faulting
9	1,75	4,228	2	NNE Faulting	ND
10	1,54	2,003	2	NNE Faulting	Reverse faulting with strike-slip component
11	5,08	1,458	3	NNE Faulting	ND
12	1,31	*	1	NNE Faulting	ND
13a	1,42	1,350	2	NW Faulting	Reverse faulting with strike-slip component
13b	1,22	*	1	NNE Faulting	ND
13c	1,42	1,160	2	NNE Faulting	Reverse faulting with strike-slip component
14	1,63	0,724	2	NW Faulting	Strike-slip faulting to oblique faulting
15	1,87	1,190	2	NW Faulting	Reverse faulting with strike-slip component
16	1,66	0,156	2	NW Faulting	Strike-slip faulting to oblique faulting
17	1,12	0,215	1	NW Faulting	Strike-slip faulting to oblique faulting
18	1,14	*	1	NW Faulting	ND
19	1,45	0,46	2	NW Faulting	Strike-slip faulting to oblique faulting
20	2,68	1,950	2	NNE Faulting	Reverse faulting with strike-slip component
21	2,74	0,388	2	NNE Faulting	Strike-slip faulting to oblique faulting

Table 4.1: Continued.

Mountain Front	Smf	Vf (Mean)	Tectonic activity Class	Fault Trace	Faulting Style
22	1,44	0,291	2	NNE Faulting	Reverse faulting with strike-slip component
23a	2,01	1,631	2	NNE Faulting	Reverse faulting with strike-slip component
23b	1,31	0,402	1	NNE Faulting	Reverse faulting with strike-slip component
23c	1,26	*	1	NW Faulting	ND
24a	1,64	1,392	2	NNE Faulting	Reverse faulting with strike-slip component
24b	1,69	0,498	2	NNE Faulting	Strike-slip faulting to oblique faulting
25a	2,41	1,085	2	NNE Faulting	Strike-slip faulting to oblique faulting
25c	2,09	2,73	2	NNE Faulting	Reverse faulting with strike-slip component
26	1,26	0,830	1	NNE Faulting	Reverse faulting with strike-slip component
27	1,28	0,350	1	NNE Faulting	Strike-slip faulting to oblique faulting
28	2,22	0,425	2	NNE Faulting	Strike-slip faulting to oblique faulting
29	1,28	0,258	1	NNE Faulting	Strike-slip faulting to oblique faulting
30	1,25	0,32	1	NNE Faulting	Strike-slip faulting to oblique faulting
31	1,26	0,72	1	NW Faulting	Reverse faulting with strike-slip component
32	1,06	0,445	1	NW Faulting	Reverse faulting with strike-slip component
33	1,51	0,248	2	NW Faulting	strike-slip faulting to oblique faulting
34	1,40	0,232	1	NW Faulting	strike-slip faulting to oblique faulting
35	1,15	0,244	1	NW Faulting	strike-slip faulting to oblique faulting
36	1,32	0,33	1	NW Faulting	strike-slip faulting to oblique faulting
37	1,40	0,412	1	NNE Faulting	strike-slip faulting to oblique faulting
38	1,64	0,517	2	NNE Faulting	strike-slip faulting to oblique faulting
39	1,18	0,394	1	NW Faulting	Reverse faulting with strike-slip component

Here, we combined the morphometric data that we obtained from morphometric measurements at the piedmont-mountain junction in the WAF (Oviedo-Reyes et al., 2024; see Table 4.1), with

data from different structural domains (e.g., Silva et al., 2003; El Hamdouni et al., 2008; Pérez-Peña et al., 2010; Giaconia et al., 2012; Özkaymak and Sözbilir, 2012; Yıldırım, 2014; Saber et al., 2018; Rimando and Schoenbohm, 2020; García-Delgado and Velandia, 2020; Sançar, 2021) and data previously obtained by Silva et al. (2003), including logarithmic regression lines, to analyze logarithmic regressions between Smf and Vf, and assess the faulting style at the studied segment of the Western Andean Front.

We use 45 segments mapped along the WAF, with segments averaging 20.09 km north of 35°51´S and 11.64 km southwards, while we extracted Vf value points at locations 0.5 to 1 km upstream from the outlet of 97 drainage basins (Oviedo-Reyes et al., 2024; Figure 4-1b). In equation (4.1), values range between 0 to 4 for Vf, and between 0 to 5 for Smf; extreme values are rejected within the analysis due inactive mountain fronts in some cases present very high values that are not significant for the analysis.

To assess whether Smf/Vf data collected for logarithm regressions lines differ statistically (e.g., El Hamdouni et al., 2008; Pérez-Peña et al., 2010; García-Delgado and Velandia, 2020) we applied a two sample-sample Kolmogorov - Smirnov test (KS-test, $\alpha = 0.05$), with the null hypothesis that Smf/Vf values in a given structural domain (here WAF data) have the same distribution as other Smf/Vf values found in a similar structural domain (Table 4.2). The hypothesis is rejected if the p-value is lower than the significance level (p-value <0.05) (e.g., Özkaymak and Sözbilir, 2012; García-Delgado and Velandia, 2020).

4.3 Results

Figure 4-2 (from B to D) shows the logarithmic regression lines following using a total of 230 data for different structural domains discriminated by faulting style and the corresponding regressions lines for the WAF data (Figure 4-2E). Here, we distinguish two main clusters corresponding to different styles of faulting in the WAF (Figure 4-2E). Mostly, segments related to NW-striking faults have an equation of logarithmic regression Vf=1.106 Ln(Smf)+0.0078 (R2=0.83), which shows a similar trend between strike-slip faulting and basin and range normal faulted (oblique faults) (Figure 4-2E). The data along this equation corresponds to the Laja Fault (LaF) (segments 31 to 37, Table 4.1) and the Longaví – Achibueno Fault (LoF - segments 14 to 19), with more active segments from class 1 to class 2 (Figure 4-1B). The constant B in the equation related to NW-striking faults suggests kinematics related mainly to strike-slip faults. However, some segments might likewise present a normal component (B$\leq$0, Silva et al., 2003).

Meanwhile, segments related to NNE-striking faults correspond to an equation Vf=1.76 Ln(Smf)

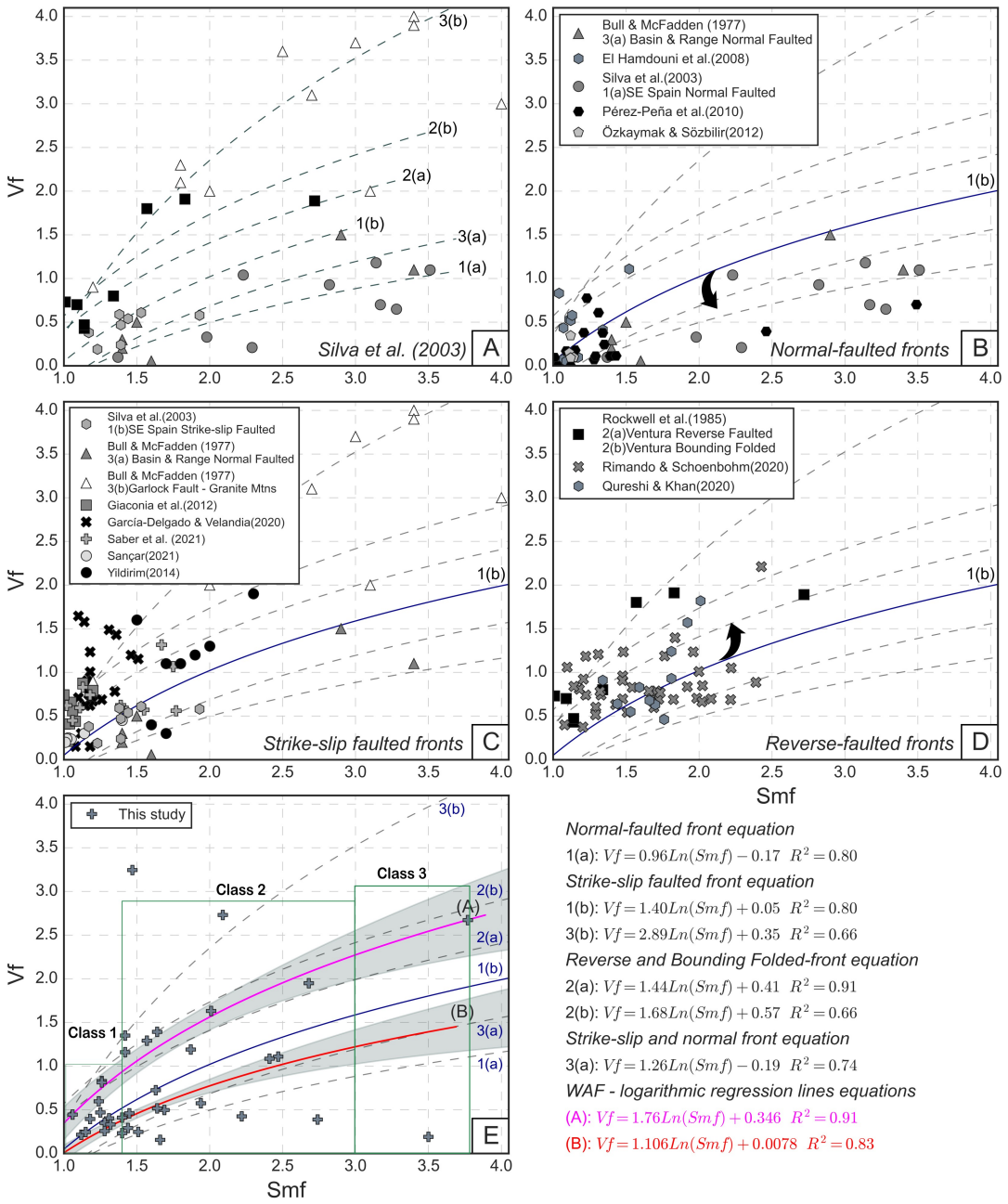


Figure 4-2: Plot of Smf vs. Vf for Western Andean Front in Chile and several authors in different tectonic settings following the procedures from Silva et al. (2003). A total amount of 230 mountain front data have been used for this plot. A. Faulting styles proposed by Silva et al. (2003) from morphometric properties extracted from mountains fronts in different structural domains. Regression lines and equations for different styles of faulting in regional groups are displayed (lower left) B. Data from normal faulted fronts (lines 1a, 3a), the arrow indicates the predominance of the data. The blue line 1(b) highlights the trend of mountain fronts associated with strike-slip faulting. Here used as reference to discriminate the different structural domains. C. Strike- slip faulted fronts data (lines 1b, 3b). D. Reverse faulted fronts data (lines 2a and 2b). E. Western Andean Front morphometric data and tectonic activity classes (green box) (Oviedo-Reyes et al., 2024). The gray zones are the uncertainty (2σ) displayed for the regional groups identified in the WAF between 35° and 38° S and corresponding equations (magenta). Vf values > 4 and Smf > 5 were excluded from this plot.

+0.346 (R2=0.91), which displays a similar trend that fits bounding folded to reverse faulting (Figure 4-1E). Both positive constants A and B increase in value from oblique faults to reverse/bounding folded fronts. Larger A in NNE-striking segments suggests a smaller incision than in the trajectory

highlighted for the NW structures. Therefore, the logarithmic curve has a second interpretation, as it enables us to differentiate the shape of the valleys between the two trends found in the WAF. The valleys of the NNE fronts approach U-shapes while the valleys of the NW front approach V-shaped valleys.

The KS-test results show that the null hypothesis is rejected for most of the Smf/Vf values tested for different structural domains (Table 2). The Smf/Vf data showed a different distribution from the values proposed by Silva et al. (2003) within normal or strike-slip structural domains (p-value = 4,44x10-16), similar to the data provided by Özkaymak and Sözbilir (2012) in normal faulting domains (p-value = 5,2153x10-6). Instead, Smf/Vf are not statistically different (i.e., values fit the same distribution) when these have a similar structural domain. For example, Smf values in the WAF compared with the obtained by Rockwell et al. (1985) (p-value = 0.0962) in the Ventura Anticline region, Rimando and Schoenbohm (2020) (p-value = 0.3406) in the Pampean flat-slab segment, or by Qureshi and Khan (2020) (p-value = 0.3193) at the western margin of the Himalayas.

However, our data have a similar distribution to observations in the Basin and Range group (p-value = 0.6695), controlled by a combination of strike-slip and normal faults (e.g., Bull and McFadden, 1977) or combination of strike-slip and reverse component (p - value = 0.1654) (Saber et al., 2018). Furthermore, the KS-test in the two principal clusters identified fit in the same distribution of Smf values ($p - value = 0.3647$), although the null hypothesis is rejected ($p - values < 0.05$) when tested with Vf index values ($p - value = 0.00355$). This relation coincides with that proposed by Silva et al. (2003) which suggests that for similar Smf values, the Vf index is always higher for reverse faulted fronts than for normal faulted fronts.

4.4 Discussion

Our analysis sheds light onto the neotectonic kinematic style of faults along the WAF between 35°S and 38°S (Figure 4-3). The Smf/Vf data from the WAF clusters into two groups using logarithmic regressions based on key factors (Figure 4-2E): [1] The KS-test shows no statistical differences ($p>0.05$) with Ventura Basin and Basin-Range strike-slip and normal faulted fronts. Comparing the data groups statistically provides insights into the relationship between the morphology of the front and its probable kinematics, and [2] Interpreting the morphometric data using previous studies, and interpreted structures offers clues about the likely structural style (e.g., Oviedo-Reyes et al., 2024). We suggest that faults traces with NNE trend are mainly correlated with a reverse faulting with strike-slip component (trend A), otherwise the faults with a trend NW which cuts the Principal Cordillera orthogonally, show a strike-slip faulting to oblique faulting (trend B in Figure 4-2E).

Moreover, recent analog models using model velocity field inferred from GPS velocities suggest the formation of two fault sets caused by strain partitioning associated with dextral transpression and the orogen-parallel variation in crustal strength. Specifically, these are interpreted as margin-parallel dextral oblique-slip thrust faults and second NW-striking sinistral oblique-slip reverse faults (Eisermann et al., 2021).

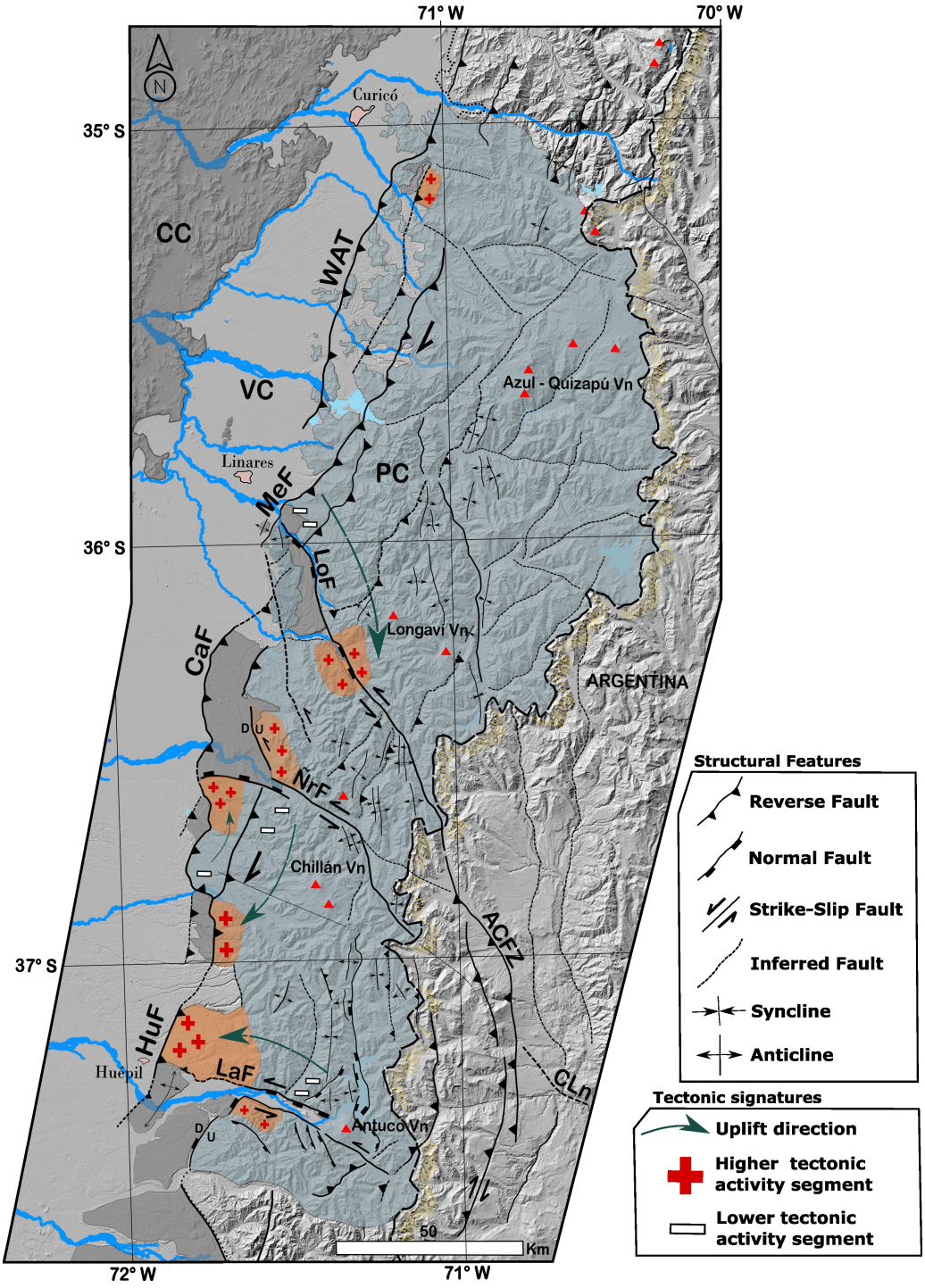


Figure 4-3: Structural Setting and active tectonics interpreted in this study from Smf/Vf ratio (modified from Oviedo-Reyes et al. (2024)). The uplifted areas with higher tectonic activity are highlighted (orange) (See Table 1). **HuF**: Huépil Fault, **ACFZ**: Antiñir- Copahue Fault System, **CaF**: Catillo Fault, **MeF**: Mesamávida Fault, **LaLn**: Laja River Fault, **LnNr**: Ñuble River Fault, **LoLn**: Longaví-Achibueno Fault, **WAT**: West Andean Thrust, **CLn**: Cortaderas Lineament, **U**: Uplifted side, D: Down-Dropped side.

By setting the strike-slip fault line (line 1b, Figure 4-2A) and grouping the data according to the faulting style (e.g., Giaconia et al., 2012; Yıldırım, 2014; Saber et al., 2018; García-Delgado and Velandia, 2020; Sançar, 2021), we obtained a significant pattern in the values of mountain front sinuosity (Smf) and valley floor width-to-height ratio (Vf) (Figure 4-2B, 4-2C, 4-2D). Our data aligns with the hypothesis suggested by Silva et al. (2003) previous work, from Smf/Vf data can be obtained a distinctive clusters related to the kinematics of the related range-front faults. We in fact found that for similar Smf values, the Vf index is always higher for reverse-faulted fronts (Vf $>$ 0.5) than for the normal faulted fronts (0$<$Vf $<$ 1.0)(Figure 4-2B, 4-2D). Additionally, we our results evidence supporting the hypothesis that the horizontal slip in strike-slip faulted fronts favors the record of lower Smf values ($<$ 2), but uplift is not sufficient to maintain V-shaped valleys, the Vf values ($<$ 2) are relatively greater than other structural domains. Conversely, Smf values in normal–faulted fronts tend to display large values (to Smf $\sim$ 3.5) but keep comparatively low values of Vf ($<$ 1) (Silva et al., 2003).

Based on the A and B constants from regression equations, NW-striking structures show a higher prevalence of strike-slip faults compared to normal faults. These structures may also represent a combination of structural domains, including transpressional and transtensional features. Our interpretation is supported by the initial stage of Vf values, which are associated with strike-slip faults (curve 1b), that however gradually decrease. This behavior can be attributed to the geomorphic context of NW-striking faults, which are influenced by erosion processes caused by large rivers trending in the NW direction (e.g., Laja, Ñuble, Longaví). It is reasonable to assume that the incision is slightly more significant on the NW-striking fault traces enhanced by local changes in base level by fluvial erosion than on NNE-striking ones (Oviedo-Reyes et al., 2024), which would keep lower Vf values with similar distributions to other structural domains (e.g., Yıldırım, 2014; Giaconia et al., 2012; Table 4.2).

The obtained p-values provide a statistically consistency between structural domains (Table 4.2). A p-value less than 0.05 indicates that the null hypothesis (which assumes that the two datasets come from the same distribution) can be rejected, and therefore the datasets are considered statistically different. We emphasized the Smf index with p-values greater than 0.05 to establish relationships between the data (Table 4.2) under the assumption that Smf changes occur over extended periods, ranging from the early to middle Pleistocene (125 ka to approximately 1.8 Ma) (Bull, 2007; E. Keller and Pinter, 2002), due to the slow modifications of slopes by geomorphic processes. Typically, the mountain front retreats by about one kilometer over a period exceeding 1 million years (Bull, 2007). In contrast, determining the relationship between the WAF morphometric data and these domains presented a challenge when using the Vf index alone. A possible explanation for this might be that

Table 4.2: Results for KS-test for Smf/Vf values in the WAF and published work worldwide. For the data we used a significance level $\alpha = 0.05$. H0 = Null Hypothesis, H1 = Alternative Hypothesis.* Data grouped by structural domain.

Smf/Vf data source	*Smf values*			*Vf values*		
	KS stat	***p - value***	**H0/H1**	**KS stat**	***p - value***	**H0/H1**
Rockwell et al. (1985) - Ventura Reverse Faulting and folded -USA	0,4512	0,0962	H0	0,3902	0,1887	H0
Rimando & Schoenbohm(2020). West-dipping, thin-skinned Precordillera fold-and-thrust belt, east-dipping, thick-skinned. - Pampean Flat Slab - Argentina	0,1951	0,3406	H0	0,4622	0,0001	H1
Qureshi & Khan (2020). The Himalayan main frontal thrust (MFT) accommodates. Two frontal thrust faults (Khirgi and Jandola) - Manzai Ranges in the Recess Setting. Western Pakistan	0,3060	0,3193	H0	0,4457	0,0442	H1
Silva et al. (2003) - Strike-Slip Faulting -Spain*	0,8431	4,44E-16	H1	0,8431	4,44E-16	H1
Bull & McFadden (1977) - Garlock Fault strike-slip faulting. USA	0,6070	0,0001	H1	0,8469	1,10E-09	H1
Giaconia et al. (2012)- Regional dextral strike-slip faulting and Reverse Faulting. Transpressive regime. SE Spain	0,9024	5,71E-07	H1	0,3415	0,2783	H0
Garcia-Delgado & Velandia (2020). Positive flower structure with Reverse Faults and strike-slip faulting. Northern Colombia	0,6073	3,10E-05	H1	0,4354	0,0072	H1
Saber et al. (2018) - Several parallel and sub-parallel faults which have developed in a right lateral strike-slip system with a reverse component. NW-Iran	0,3570	0,1654	H0	0,4457	0,0442	H1
Saçar(2021). Dextral and Sinistral domains with reverse component. NE-Zagros mountain belt. - western Turkish-Iranian Plateau.	0,8084	0,0001	H1	0,6620	0,0047	H1
Yildirim (2014) - The TGFZ is an oblique-slip normal fault zone with a right-lateral strike slip component. Central Anatolia Turkey.	0,4634	0,0736	H0	0,4329	0,1207	H0
Silva et al. (2003) - Normal Faulting -Spain*	0,8235	4,44E-16	H1	0,8235	4,44E-16	H1
Bull & McFadden (1977) - Basin & Range Normal Faulted-Transtensional pull apart basin. USA	0,2927	0,6695	H0	0,3049	0,6054	H0
Özkaymak & Sözbilir (2012) - E-W trending active normal faulting - laterally terminated by a transversely oriented strike–slip fault zone. Western Anatolia (Turkey)	0,9512	5,22E-06	H1	0,8333	0,0002	H1
Elhamdouni et al. (2008) The study zone linear east–west anticlinal forms, as well as extension with variable vertical rates of normal faulting. Spain	0,6541	0,0004	H1	0,2727	0,4456	H0
Perez Peña et al. (2010). Large-scale open antiformal ridge coincident with the whole extent of the Sierra Nevada and coeval normal faulting. The southern border - WSW–ENE sub-vertical dextral strike-slip fault zone. SE Spain	0,5308	0,0012	H1	0,5638	0,0004	H1

Vf index data in the WAF shows an imprint derived from a climatic control or rapid uplift (Vf<0.5) by a faulting reactivation (Oviedo-Reyes et al., 2024).

Our data show similar Smf values (p-values > 0.05) across reverse faulting, transpressional, and transtensional domains, but Vf values exhibit statistical differences (p-value < 0.05), particularly in the WAF. This suggests a relatively higher incision (lower Vf) in the WAF compared to purely reverse fault-dominated domains. Using both morphometric indexes, complete matches were only observed with Ventura Reverse Faulting (Rockwell et al., 1985) and Basin & Range Normal Faulted-Transtensional pull-apart basin (Bull and McFadden, 1977).

We hypothesize that the NNE and NW structures described here exert the most significant control on the distribution of Smf/Vf data in the WAF (Figs, 4-2 and 4-3). Consequently, the trends observed in Figure 4-2E can explain the geomorphic imprint of the neotectonic activity of these fault-generated mountain fronts in semi-quantitative terms (e.g., Silva et al., 2003), including fault angle, faulting style, and uplift rates. We found that for similar Smf values, the Vf index is always higher for reverse-faulted fronts (Vf > 0.5, trend A) than for the strike-slip faulted fronts (Vf < 0.5, trend B) (Figure 4-2E). The differences between trends can be explained using the relative

active tectonic classes, where NW-trending faults are relatively more tectonically active than NNE faults. Subsequently, in both trends, as the uplift pulse slow down, the Vf values increase due to erosional processes. Thus, NW-striking structures maintain low Smf/Vf values in response to tectonically induced downcutting.

Further, we explored the mathematical relationships of the logarithmic regression and its first derivative (Figure 4-4). Analytically, the dVf/dSmf trend for NNE to NW-striking mountain fronts exhibits a decreasing concave shape. Although both curves are slightly parallel, the initial distances of dVf/dSmf differ, and this difference persists throughout the curves. The rate of change in Curve A (blue line, Figure 4-4) is more pronounced than in Curve B, primarily due to the steeper slope of Curve A in the logarithmic regression. Specifically, Curve A exhibits a faster variation in Vf between classes of active tectonics, such as class 1 (Smf $<$ 1.5) and class 2. Assuming that Vf changes are solely due to tectonically induced downcutting (Bull, 2007), the first derivative of the logarithmic regression equation allows us to interpret these changes in terms of incision or uplift. Therefore, NW-striking fronts maintain V-shaped valleys for a longer duration while experiencing decreasing uplift (from high to moderate classes). In contrast, NNE-striking fronts exhibit a more rapid decay of V-shaped valleys as uplift decreases. In fact, NW segments in the moderate tectonic activity class maintain lower Vf values ($<$0.5) (Oviedo-Reyes et al., 2024).

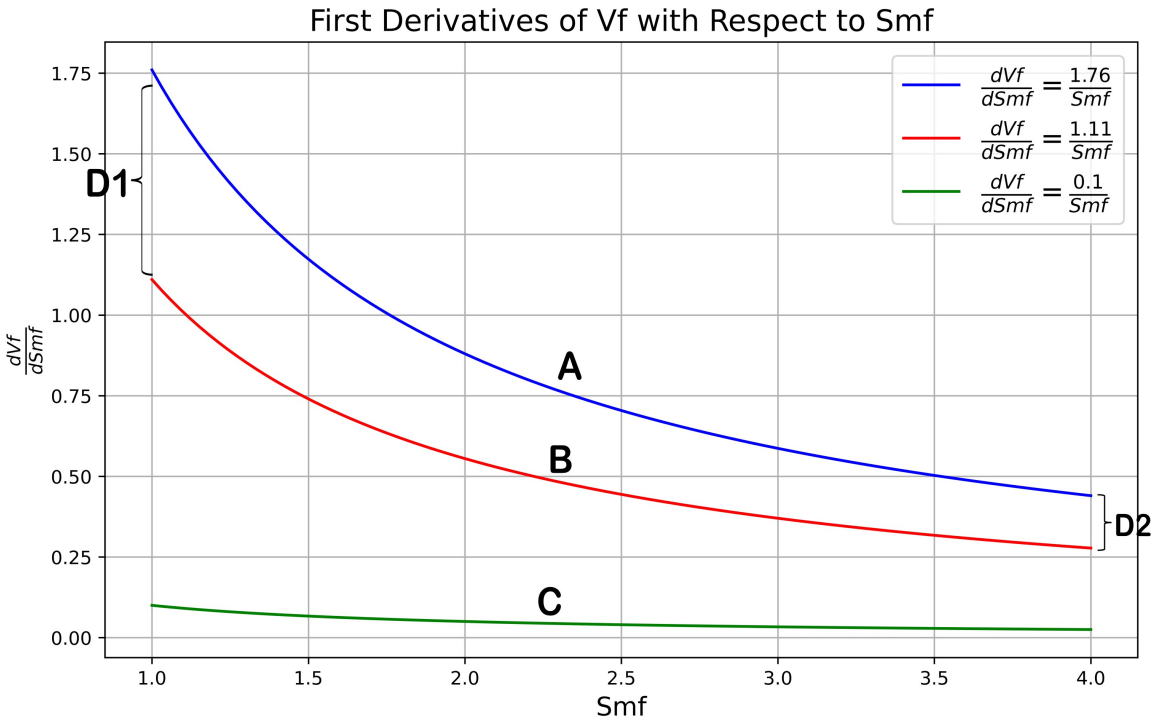


Figure 4-4: Curves of the first-derivatives applied to the two clusters identified in the WAF. A. First-derivative from the equation Vf = 1.76Ln(Smf) + 0.346 related to NNE-striking fronts (blue line). B. First-derivative from the equation Vf = 1.106Ln(Smf) + 0.0078 related to Nw-striking fronts (red line) C. First-derivative which represents a theoretical equation Vf = 0.1Ln(Smf) + 0.1 (green line). Note the distance at the starting point of the curves (D1), and the smaller range at the end of the curves (D2).

Hypothetically, the faulting style influences the Smf/Vf parameters and their relationships. Our approach suggests that NNE-striking front drainage systems quickly reach the base level of erosion, leading to lateral erosion processes that broaden the valleys (Bull, 2007; Burbank and Anderson, 2011). If the reverse faults (including thrust) exhibit higher cumulative uplift (e.g., Nakata, 1989) than other fault systems; Figure 4-4 can also represent cumulative vertical uplift. However, further research is needed to provide deeper insight into the relationships within the Smf/Vf data. Despite the limitations, the arguments presented here could offer additional evidence supporting the findings of Oviedo-Reyes et al. (2024), who contend that the low Vf values ($<$0.5) observed in inactive mountain fronts (Smf $>$ 5) north of 36°S are influenced by non-tectonic factors.

4.5 Conclusions

Our results confirm the potential of morphometric indexes to decipher spatial patterns of faulting styles, while reaffirming our previous findings on the WAF (Oviedo-Reyes et al., 2024). However, we assess that these methods must be combined with other data sources in order to fully describe the landscape evolution and the possible driving mechanisms. In particular detailed lithological, climatic, an erosional data. The data points used in this note represent different mountain front segments that may have experienced varying tectonic histories, leading to potential spatial and temporal variations in faulting styles and deformation patterns. More so over, the mountain front morphology and valley shapes can also be influenced by factors such as lithology, erosion rates, and climatic conditions, which may introduce additional complexities in interpreting the kinematic proxy. Also, integrating field observations, structural data (fault orientations, kinematic indicators), seismicity data, and other geological/geophysical evidence is crucial to validate and refine the interpretations derived from the Smf/Vf logarithmic regression analysis.

Despite the inherent complexity of deciphering faulting styles from morphometric data, our work adds to a growing body of evidence that the faulting style records a geomorphic imprint in the landscape. The mountain-front sinuosity (Smf) and valley floor width-to-height ratio (Vf) indices provide quantitative geomorphic constraints on the faulting style and neotectonic activity along the Western Andean Front in central Chile. Logarithmic regression of Smf/Vf data reveals two distinct trends: NW-striking faults exhibit a trend consistent with strike-slip to oblique faulting kinematics, while NNE-striking faults align with reverse/thrust faulting mechanisms. The results are statistically supported by the Kolmogorov-Smirnov test, which confirms the Smf/Vf patterns are significantly differentiable from other tectonic settings globally and corroborate regional field observations and tectonic models. The morphometric analysis suggests strain partitioning in the

transpressional regime, with NW-striking faults accommodating more tectonic activity and fluvial downcutting, while NNE faults facilitate deformation via thrusting. Our analysis reveals that NW-striking mountain fronts maintain V-shaped valleys longer under decreasing uplift, while NNE-striking fronts decay more rapidly. The first-derivative curves for NNE and NW fronts illustrate incision patterns along different segments in the WAF. The faulting style affects the Smf/Vf relationship, with NNE-striking systems reaching erosion base levels more quickly. Although further research is needed, our findings support the idea that low Vf values in inactive mountain fronts north of 36°S are influenced by non-tectonic factors (Oviedo-Reyes et al., 2024). This approach offers an effective proxy for inferring faulting kinematics where subsurface data is limited. Thus, the kinematics obtained from the Smf/Vf data are consistent with available structural models proposed (e.g., Melnick, Charlet, et al., 2006; Radic, 2010; Eisermann et al., 2021; Oviedo-Reyes et al., 2024).

Capítulo 5

Quantifying Late Quaternary Fluvial Incision Rates in the South-Central Andes ($\sim$36°S): A Record of Uplift, Active Faulting, and Mountain Front Migration

Quantifying Late Quaternary Fluvial Incision Rates in the South-Central Andes (∼36°S): A Record of Uplift, Active Faulting, and Mountain Front Migration [1]

Jorge Adrián Oviedo-Reyes[1]; Joaquín Cortes Aranda[1]; Alfonso Fernandez[12]

[1]Departamento de Ciencias de la Tierra, Universidad de Concepción, Concepción, Chile

[2]Departamento de Geografía, Universidad de Concepción, Concepción, Chile

Abstract This study investigates the west-verging reverse faults in the Western Andean Front (WAF) between $36°15'$ - $36°35'S$, focusing on the San Fabian Fault (SFF), Loma Linda Fault, and Cachapoal Fault (CAF). We aim to characterize the mountain front migration and Quaternary deformation in the south-central Andes. We employed morphotectonic mapping, structural analysis, drainage analysis, and Optically Stimulated Luminescence (OSL) dating. These methods allowed for comprehensive characterization of tectonic markers, terraces, and brittle deformation. Our results reveal significant spatial and temporal variations in tectonic activity. The San Fabian Fault shows rapid vertical uplift of 5.07 ± 0.37 mm/year from 30-13 ka, decreasing to 1.86 ± 0.14 mm/year in the last 13 ka. Shortening rates were estimated at 2.36 ± 0.18 mm/year for the Late Pleistocene, reducing to 0.867 ± 0.065 mm/year in the last 13 ka. The Cachapoal Fault exhibits uplift rates of 1.71 ± 0.22 mm/year for the last 25 ka in the Nahueltoro sector, with lower rates in other areas. The kinematics analysis revealed a complex structural behavior with pull-apart basins in the sector of the San Fabian Fault, enhanced by northwest-striking structures, with a maximum horizontal stress (Sh_{max}) oriented north-south ($006°$) related to Quaternary deformation. The regional stress tensor ($Sh_{max}120°$) describes a reverse faulting regime with a slip component dating back at least to the Late Miocene for the Cachapoal, San Fabian, and Loma Linda faults. The uplifting blocks of the internal range and bounding faults are located in the hanging wall. The mountain front migration in the south-central Andes shows significant spatial variations in tectonic activity along the main traces of the San Fabián and Cachapoal faults, with temporal changes in uplift rates indicating significant tectonic deformation from south to north. The Loma Linda Fault, similar to the San Fabian Fault, controlled the uplifting of the internal mountain front, as recorded in uplifted terraces. These findings are crucial for understanding the long-term slip behavior and seismogenic potential of these faults in the Western Andean Front in a context of oblique subduction zone.

KEYWORDS: Morphotectonic mapping, Deformation indices, Terraces, Optically Stimulated Luminescence (OSL), rates of erosion, uplift, Andean Front Migration

[1]Article in Preparation

5.1 Introduction

A west-verging thrust system (WAT) has been described like a multikilometer structure which controls the uplift in the Western Andean Front (WAF), several authors reports this structures along Chilean margin at 15-20°S (e.g., Muñoz and Charrier, 1996), at 33°S near to Santiago City with San Ramón fault (Armijo et al., 2010; Vargas et al., 2014; Riesner et al., 2017), at 37°10' with the Huépil fault (Melnick, Charlet, et al., 2006) and the Cachapoal fault at 36°10' (Maldonado et al., 2021). However, the most substantial evidence of Quaternary deformation accumulates at 33°S, particularly around the San Ramon and Cariño-Botado faults (also known as the Pocuro system). This evidence encompasses a diverse range of observations: prominent fault scarps (Armijo et al., 2010), detailed field observations (Estay et al., 2023), revealing paleoseismological trench studies (Vargas et al., 2014), distinctive crustal seismicity patterns (Ammirati et al., 2019), and shallow structural boundaries identified through geophysical methods (Yáñez et al., 2002). This comprehensive body of research has, over recent years, convincingly constrained the presence of a tectonically active structure in this region, representing a significant advance in determining the seismogenic potential of the area. This key structure from a mountain building perspective reflecting its current topography in the main Cordillera shows Neogene activity (Farías et al., 2010; Riesner et al., 2017).

Recently, south of 35°S, from topographic analysis it is reported that this structure presents two well-defined segments: between 35-36°S a mountain front with high sinuosity of its piedmont, which allows inferring a quiescence of tectonic activity, and between 36°-37°S a moderately to tectonically active mountain front (Oviedo-Reyes et al., 2024). These authors also suggest that the WAT has two distinctive features, an internal mountain front (IMF) and a range bounding fault (RBF) between 36°15'- 36°35'S (Figure 5-1), probably as structures inherited from ancient extensional basins during the Oligocene-Miocene period. Later, in the Late Miocene, they experienced tectonic inversion, transforming their original extensional nature into compressional features (Radic, 2010).

The range bounding fault is distinctly recognized by linear scarps mainly NNE direction and represent the most clearly evidence of Quaternary deformation. In the other hand, Oviedo-Reyes et al. (2024) reported a moderately tectonic activity over this internal mountain front, and geomorphic imprint of tectonic-fluvial coupling. Despite this attempt, there remains a scarcity of data concerning the deformation nature, its manifestation on the surface, structural style, Quaternary chronology, and rates of uplift.

To better understand of IMF and RBF faults and its role in the Andean Mountain building (Figure 5-1), we mapped and analyzed tectonic markers of recent surface deformation, terraces, and

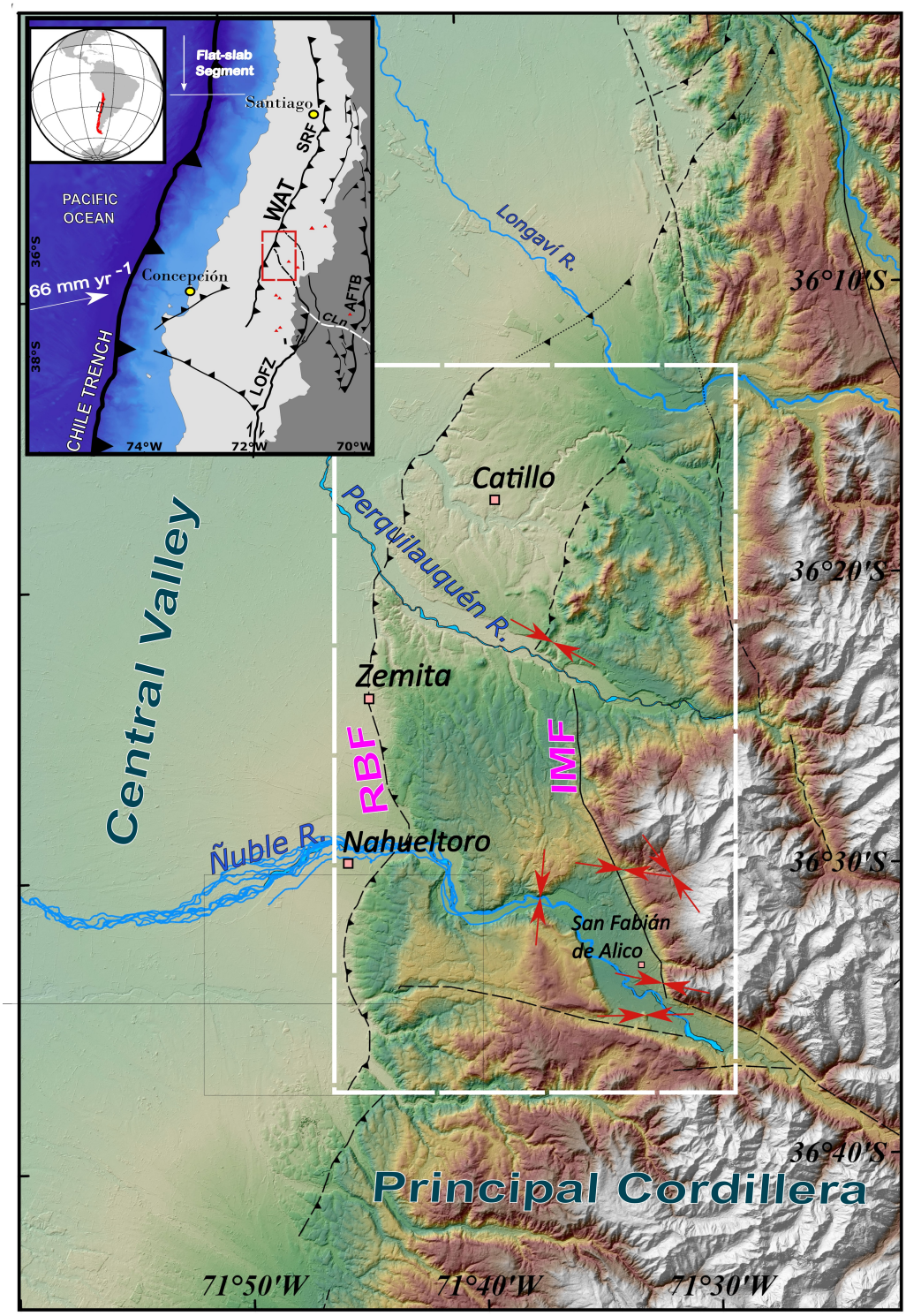


Figure 5-1: Mapped faults and horizontal shortening strain axes calculated in the Western Andean Front (WAF). Internal Mountain Front and Range Bounding Fault are depicted in the main traces.

brittle deformation to characterize the mountain front migration in the south-central Andes. We did this by using morphotectonic mapping (deformation indices, terraces and bedrock), field survey, DEM data, drainage analysis, and optically stimulated geochronology (OSL). Uplift rates for the Quaternary were determined under the assumption that the analyzed mountain fronts are in a state of tectono-fluvial coupling (Oviedo-Reyes et al., 2024).

5.2 Materials and Methods

5.2.1 Morphotectonic mapping

Data derived from ALOS 3WD30 meters, TanDEM X 12.5 meters, Lidar 5m, and 50K-100K topographic maps scale were used to determine the morphotectonic features in the study area. Also, we used UAV (Unmanned aerial vehicle to mapping some features difficult to access). The image provide by UAV supports preliminary observations also find the outcrops to determine age by OSL. The map was prepared in the same scale of topographic sheets (Digua, and San Fabian) and using ArcGIS Pro. We determined structural features, deformation and hydrography indices supported by bedrock and terrace mapping. Standard field mapping led us to collect the OSL samples in the available terraces outcrops and gathering brittle information from bedrock.

5.2.2 Structural Analysis

Data related to brittle deformation in the rocks of the Western Andean Front were collected in the field mapping. The units mainly belong to the Abanico formation. The extracted data were taken using the criteria of Petit (1987) (Figure S6), supplementary data), using false striations and steps to perform the inversion of the paleostresses.

To calculate stress tensors, we employed WinTensor 5.0.1 (Delvaux and Sperner, 2003), a software that enables graphical representation of planes and lines on stereographic projections of the lower hemisphere, and stress axes depicted as arrows. The tensor inversion was performed using data collected from joints and striated planes. The processing followed the supervised mode, adhering to the guidelines provided by Delvaux and Sperner (2003) and Velandia Patiño (2017), utilizing straight dihedral and optimized rotation methods as appropriate. Furthermore, the software recommends verifying each tensor solution using the histogram of the misfit function F5, where values close to zero indicate a good fit. The orientation of the stress tensor, expressed as the maximum horizontal stress (SH_{max}), allows for determining the kinematics of the IMF and understanding their structural style to exhibit aperture, closure, or lateral slip.

5.2.3 Drainage Analysis

Drainage was extracted from the DEMs using photointerpretation and comparing with networks extracted under the D8 algorithm in GIS procedures. From the extraction, a drainage "straightened" method (drainage path rectification) was performed (e.g., Scheidegger, 1979; Hodgkinson et al.,

2006) to know the trend avoiding bias; we used the nodal points where each tributary joins with a new drainage network. This technique allows us to visualize the drainage trend and compare it with the structural data (lineaments, joints) obtained in the field. We mapped the river terraces using the procedures of Angster et al. (2020) to obtain a reliable elevation data of terraces in the study area. We calculated an adjusted fit curve to determine mean elevations at specific terrace levels for comparison with river profile data. Using this analysis, we derived incision rates based on available age constraints obtained through Optically Stimulated Luminescence (OSL) dating. This approach allows for a quantitative assessment of landscape evolution rates for Quaternary time span.

5.2.4 OSL Sampling and Dating of Terraces

The samples were collected considering the finer material within the sand fraction. Due to the nature of the source rocks of the WAF deposits, quartz is very scarce, an additional reason to introduce a careful inspection of the material to be dated, which was a technical difficulty. The sand lenses observed within the gravel-dominated terraces showed very cohesive sediments. To provide a reliable sample, two types of tubes were used: a plastic one and a metal one (height 25 cm, diameter of 5 cm) that allowed a more efficient extraction of the cohesive samples. As part of the tube recovery process, a minimum of 500 g of the surrounding material was gathered to assess the environmental radiation level at the sampling site. Some outcrop material was removed (approx. 15 cm) to remove recently irradiated surface material. Considerations about the material to be dated were made by reviewing the results of the morphotectonic mapping. The plastic tube was marked with a base and top to reference how it was introduced into the outcrop. Previously the base of the tube was sealed with 3M cloth duct tape and sealed with a cap of the same material as the tube. When the sample was removed from the outcrop, it was removed, where the top was processed in the same procedure. The samples consisted of fine to medium sand, with grain sizes ranging from 150 to 250 μm. The equivalent dose (D_e) for the samples were determined using the Single Aliquot Regenerative-dose (SAR) protocol. The annual dose rates varied across samples, with values ranging from approximately 980 μGy/yr to 2080 μGy/yr. Finally, the reliability of the age data was further supported by the results of the recuperation and recycling ratio tests. The recuperation tests showed that residual signals were below 10% of the natural luminescence signal, indicating minimal interference from deep traps. The recycling ratios for all aliquots fell within the acceptable range of 0.90 to 1.10, confirming the consistency and stability of the luminescence signals throughout the SAR protocol. (See supplementary data).

5.3 Morphotectonic mapping and structural style

The internal mountain front (IMF) comprises two faults with distinct styles and kinematics (Figure 5-2): the San Fabian fault (SFF) and the Loma Linda fault (LLF). Field observations, including fault plane measurements, reveal the San Fabian fault as a high-angle reverse fault ($\sim 65^\circ$ dip) with a strike-slip component. This west-verging structure extends 17 km along its main trace between latitudes $36^\circ 30'$S and $36^\circ 35'$S.

Structural control of drainage networks trending NNW suggests the fault may extend up to 25 km. Evidence of deformation is observed through uplifted terraces on the right bank downstream of the Ñuble River. The fault trace is characterized by triangular and trapezoidal facets, with minor pressure ridges, linear ridges, and saddles. Within the fault zone, strain is accommodated by Riedel (and anti-Riedel) shears (from 2.5 to 4 km), segmenting the fault trace. The fault maintains a predominantly NNW direction with an azimuth of 338°, showing slight variations along strike. A fault strand continues in an NNE trend, with deformation indices supporting surface displacement (36°25'S).

Paleostress data along the strike (Figure S6, Table 5.1) reveal Sh_{max} orientations ranging from 102° to 146° (south to north), indicating compressional strike-slip regimes. A pure strike-slip regime is evidenced by an Sh_{max} of 002°. Additionally, pure compressive (Sh_{max} 98°) and extensional strike-slip (Sh_{max} 133°) regimes are observed, dating at least to the Miocene.

This fault accommodates strain from NW structures, including the Rio Ñuble fault (Oviedo-Reyes et al., 2024). Paleostress data from the fault trace south of the study area suggest Sh_{max} orientations between 88° and 177°, transitioning from compressional strike-slip to pure strike-slip regimes (36°35'S). Quaternary records near the mountain front reveal a pull-apart basin (rhomb graben), providing accommodation space for Ñuble River sediments. This basin is bounded by the SFF to the east and a scarp with similar orientation to the west. We hypothesize that this erosional scarp represents a trace of a subparallel fault, further contributing to the complex tectonic geomorphology of the region (Figure 5-3b).

The Loma Linda fault (LLF) (36°20'S), located to the north, is a west-verging, NNE-striking structure (17°) extending 17 km in a straight line. It exhibits a sinuous character marked by triangular facets, linear ridges, saddles, straight drainage networks, river captures, bends, and elbows, as well as wind gaps. Parallel to the LLF, another fault with similar features accommodates deformation in this IMF, showing clearer evidence of a strike-slip component. Paleostress data indicates tectonic regimes ranging from pure compressive to pure strike-slip, with Sh_{max} orientations from 120° to

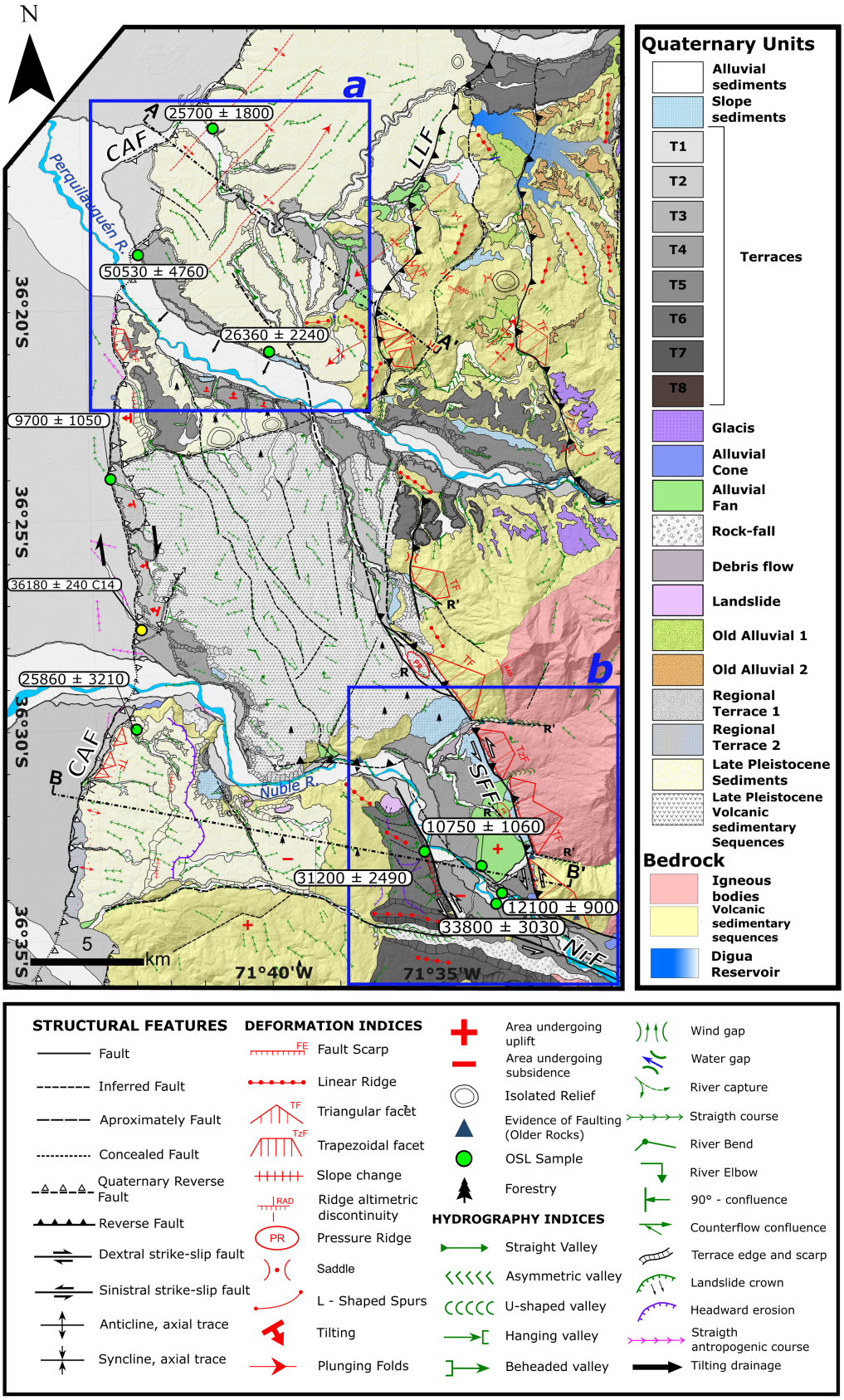


Figure 5-2: Morphotectonic map of the study area. Detailed zoom zones (a and b) are depicted. From bedrock to most recent deposits are displayed in the legend (right side). The symbology include (bottom) tracks all morphotectonic elements and useful information.

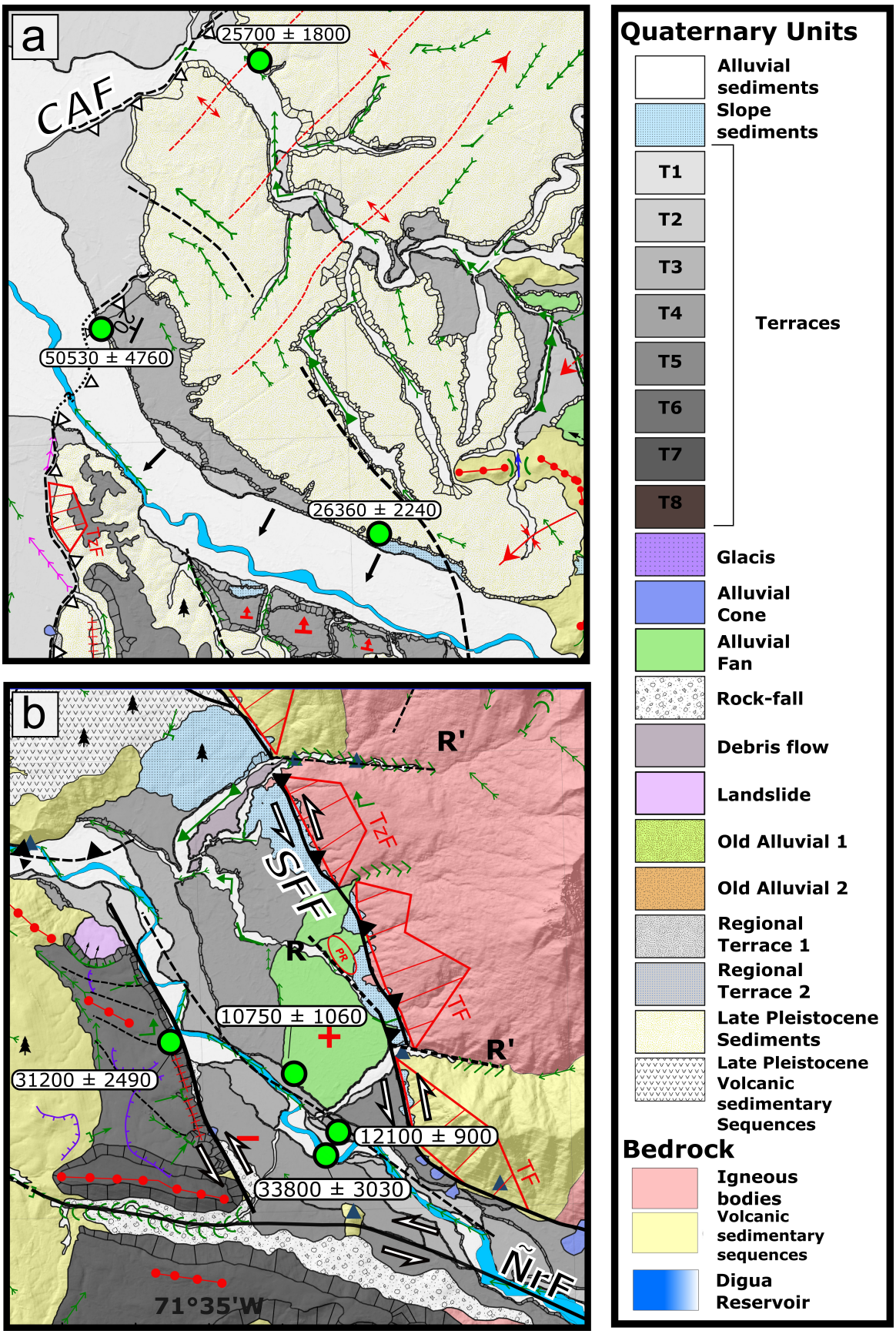


Figure 5-3: Detailed morphotectonic map zooms **a**. Northern sector Cachapoal fault (CAF). **b**. Southern east sector of the San Fabián fault (SFF). Time are depicted with age of deposits (OSL) in terraces.

178°, respectively.

Like the SFF, the LLF's orientation suggests a compressive tectonic regime dating back to at least the Late Miocene. A subset of SFF paleostress data indicates an extensional regime (Table S5.2, supplementary data), which we interpret as corresponding to the Oligocene-Miocene extensional basin period (Radic, 2010). Stress tensor analysis reveals a compressive regime with strike-slip components for both faults. However, their distinct orientations highlight their unique kinematics in shaping the IMF. This complex interplay of tectonic forces contributes to the region's distinctive geomorphological features.

Conversely, RBF is characterized by segmented traces from south to north. The Cachapoal fault (CAF) is defined by linear features forming fault scarps (Maldonado et al., 2021). However, the overthrust of older rocks (e.g., Abanico Formation and local variations) on Quaternary deposits is not detectable. The subtle deformation provides no clear indication of the fault's nature, revealing only information about vertical offset. The Quaternary strip between IMF and these linear scarps stretches approximately 43 km in a NE to NNE direction. Its width varies due to geomorphological segmentation by the drainage system, measuring 16.30 km in the southern Nahueltoro sector (36°30'S), 12.36 km in the central Zemita sector (36°24'S), and narrowing to 8.8 km in the northern Catillo sector (36°15'S). This variability reflects the complex interplay of tectonic and fluvial processes shaping the region's landscape.

The southern Nahueltoro sector exhibits a linear scarp with a 26° azimuthal angle. Scarp heights range from 7 m to 36 m, with two distinct scarps (5 m and 78 m) clearly observed in the north. This sector features a flat area above 550 masl, approximately 300 m higher than the adjacent alluvial plain.

The middle Zemita area comprises linear scarps varying between 348° to 3°, trending predominantly NNE. Scarp heights range from 18 m in the south (36°27'S) (maximum elevation 307 masl) to 64-22 m northwards. A lower altitude strand accompanies these scarps, while tilted surfaces in the north alter the topography up to 82 m (36°22'S). Meanwhile, the northern area maintains a consistent ∼60 m linear scarp with minor variations along its strike (Catillo sector) (Figure 5-3a). The scarp lines morphology hints multiple rupture, but also, we consider a fluvial signatures considering the complex evolution of drainage systems in this sector. However, changes in slope, tilted surfaces (e.g., Zemita sector), subtle triangular facets and orthogonal position of this regionally features can be considering like a linear scarps. No field evidence of deformation in this linear features suggest that this scarps can be interpreted as a flexural scarps without rupture in the surface (Figure 5-4). Man-made straight courses can be detected along the flexural scarp proposed here, we therefore do not rule out that scarps at different heights could have this type of control (e.g., 36°27'S).

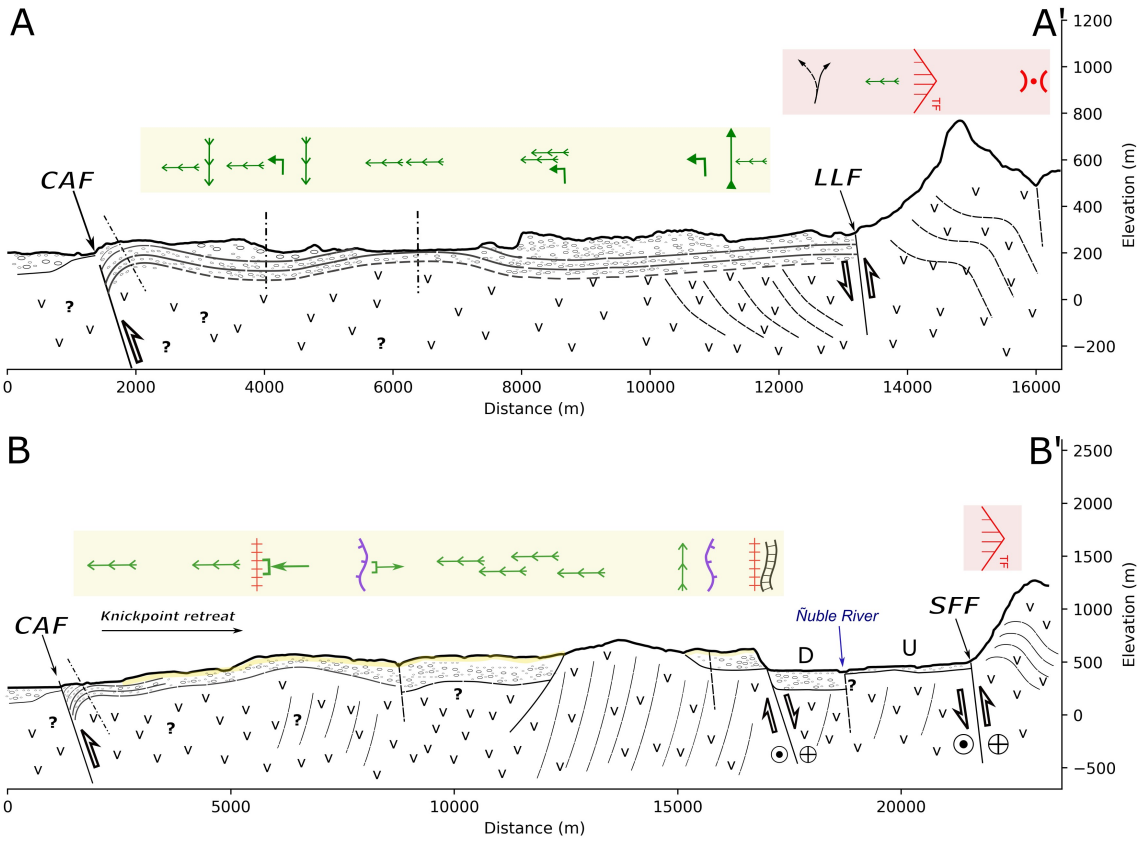


Figure 5-4: Structural and geomorphological sketch of the Internal Mountain Front (IMF) and Regional Basal Front (RBF) in the south-central Andes. For location references, see Figure 5-2. The Catillo sector (upper figure) exhibits Quaternary folding that has produced a flexural scarp, uplifting this area since at least the Late Pleistocene. In the southern Nahueltoro sector (lower figure), a similar pattern is observed, influenced by a strike-slip tectonic regime from NW-striking structures. Geomorphological features related to deformation are highlighted, considering their positions within the IMF and RBF (yellow and pink boxes).

5.4 Geomorphology of Ñuble and Perquilauquén rivers

Along the Ñuble and Perquilauquen rivers (36°15'- 36°35'S), a series of abandoned Quaternary River terraces are found where the rivers cross NNE-trending structures associated with the Western Andean Thrust system. Quaternary deposits are delineated between the Internal Mountain Front (IMF) and Range-Bounding Fault (RBF), and these uplifted surfaces are actively eroded by minor drainages with varying orientations. The Quaternary deposits consist mainly of very coarse pebble gravels, with rounded to subrounded disk-shaped to spherical clasts in a coarse sand matrix, derived from plutonic, volcanic, and sedimentary sources (see supplementary methods). Both north and south of the study area along the Ñuble and Perquilauquen rivers, the unpaired terraces T1-T7 and T1-T6 respectively, are generally fill terraces. However, in some sectors, their limits and relationships were unclear due to high vegetation cover and avalanche debris.

In both drainage systems, the higher elevation fill terraces (e.g., T4 to T7) are observed in the domain of faults controlling the IMF, while closer to the deformation front, only lower fill terraces

(T1-T4) are preserved (Figure 5-5). These hanging terraces are likely a response to base level fall, climatic changes, and erosion processes focused on the IMF. The base level of the Perquilauquen River is approximately 80 m below the Ñuble River (Figure 5-5). From T5 to T7, the terraces show uplift along the IMF controlled by the San Fabian Fault, located 12 km from the Ñuble River's exit from the IMF. Along this reach of the Ñuble River, downstream of the San Fabian Fault control, terraces T5-T7 are absent, with even a gap in T4. This absence coincides with bedrock outcrops of Oligocene-Miocene units (e.g., Abanico Fm) in the river channel. Further downstream, the T1-T4 terrace system reappears where the river exits a confined meander bend (36°30'S, Figure 5-5).

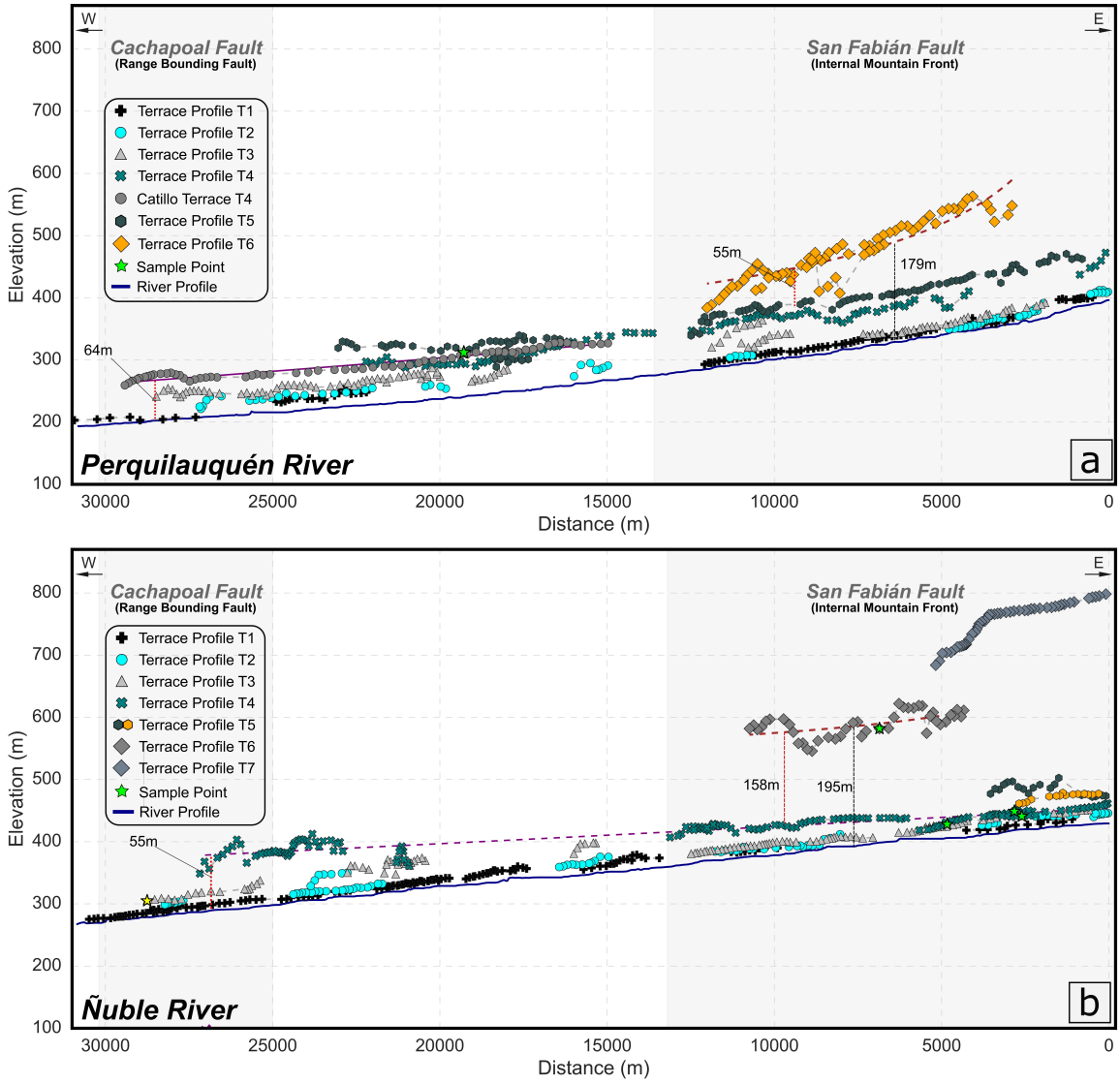


Figure 5-5: Longitudinal profiles of mapped river terraces along Perquilauquén and Ñuble rivers. We followed the procedures of Angster et al. (2020) to obtain terraces profiles. We used 100 m of distance between point elevation extraction. The elevated terraces in the IMF front can distinguished in both river system. Note the difference in elevations between Ñuble and Perquilauquén rivers. **a**. Perquilauquén River in the northern area, T1 to T6 terraces are depicted. **b**. Ñuble River terraces from T1 to T7.

From the extracted drainage networks, we highlighted different drainage patterns along relative flat surface between IMF and RBF (Figure 5-6). Subparallel to parallel drainage patterns with

variations to subdendritic can be distinguished in central and southern sections (e.g., Nahueltoro and Zemita sectors). Particularly, distorted drainages are observed where the likely influence of SFF, with counterflow confluences suggesting a disequilibrium in the erosion processes and promotes piracy (36°25'S-36°30'S). Comparing rectified drainage network and structural data, we distinguished a main trend to NW between lineaments and all orders of drainage (Figures 5-7 and 5-8). Instead, specific trends within joints data can be related to drainage networks but not conclusive.

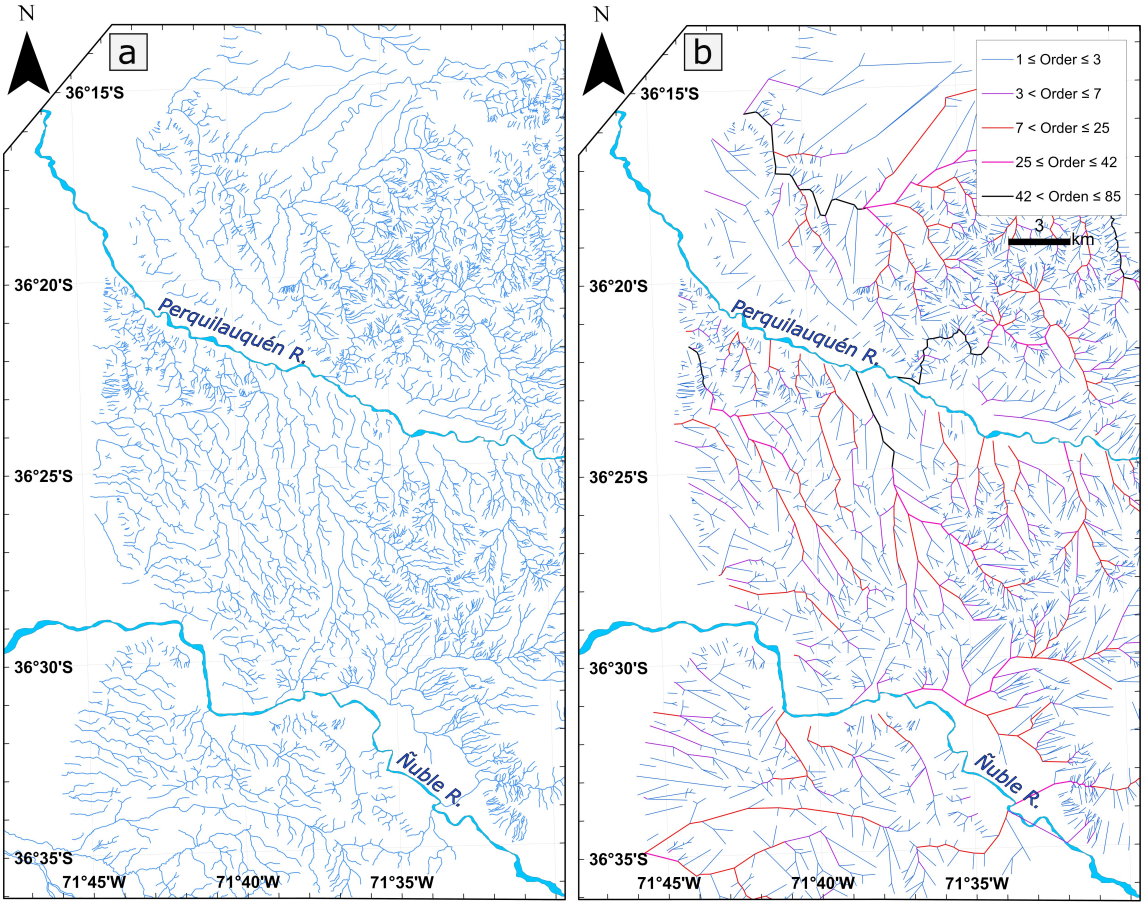


Figure 5-6: Drainage system in the study area. a. Distribution of stream course related to Perquilauquén and Ñuble rivers. Dendrithic, Parallel-subparallel and rectangular drainages can be distinguished. b. "Straightened" method or rectification of the drainage systems using nodes and sense the darainage. The orders come from the rectification procedure, and are grouped by colour.

Detailed analysis of structural data from bedrock proximal to the drainage networks between latitudes 36°24'S and 36°30'S (refer to Figure 5-9) suggests a structural control over the drainage patterns. The orientation of these planes, primarily trending southeast (SE) and extending to northwest (NW), as measured by compass, indicates a likely influence. The aperture of the joints, correlating with the maximum horizontal stress (Sh_{max}) exhibiting a NW trend, implies that the strain from the SFF has caused brittle deformation in the geological units beneath the Quaternary sediments. This deformation is not only evident in the bedrock but is also discernible in the drainage patterns, suggesting potential neotectonic activity or the presence of inherited structural features.

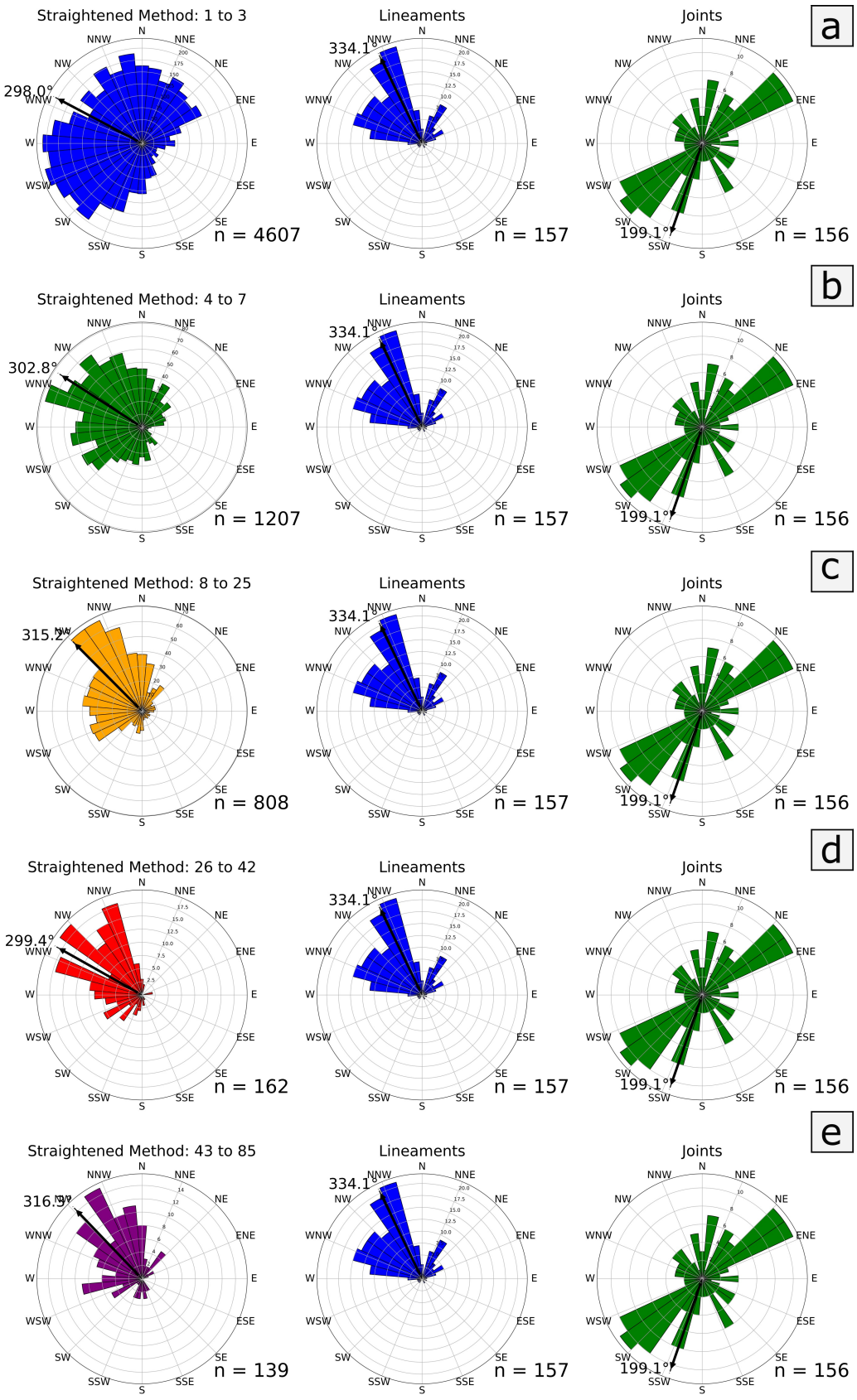


Figure 5-7: Comparison between order classification from "Straightened" method of the drainage system (a to e), lineaments and joints in the study area.

These results would explain similar situation in Nahueltoro area between 36°30'-36°35'S with NW-striking Ñuble River Fault.

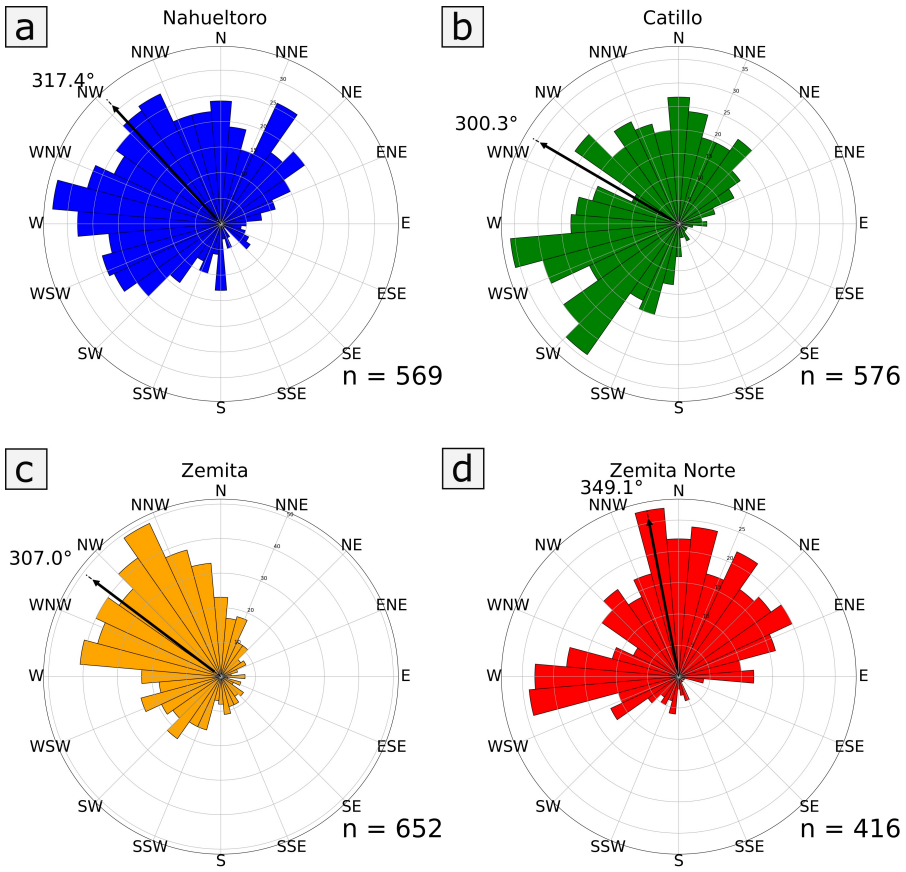


Figure 5-8: Extracted drainage orientations setting by sectors of Quaternary deposits from south to north (a to d). Mean trend vector is depicted for each rose diagram.

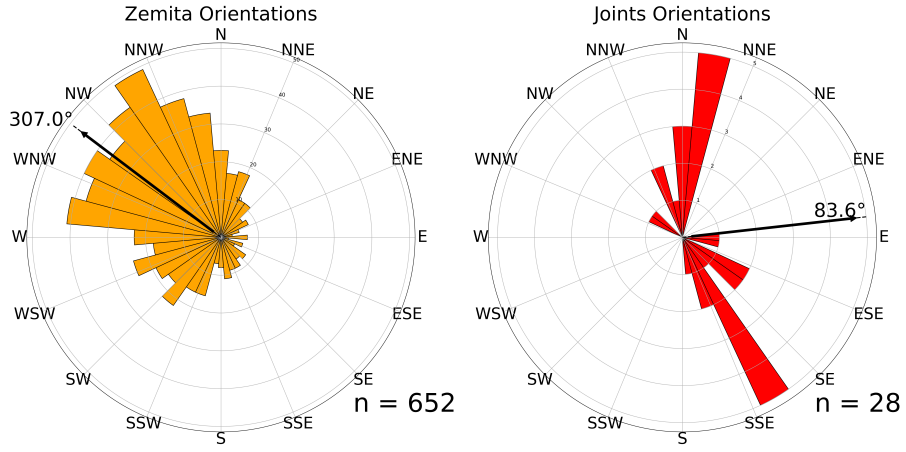


Figure 5-9: Comparison between Zemita drainage network (left) and joints from field data in Abanico Formation (right).

5.5 Fluvial response to low Quaternary active folding

The subtle deformation field evidence can be considering a paleoseismological trenching an overwhelming task. However, we observed changes in the alluvial patterns of Perquilauquen river that suggest warping of folds (e.g., Holbrook and Schumm, 1999)(Figure 5-4), a considerable southern migration of the river course can be detected from IMF to the RBF limits. This alluvial tilting (Fig-

ure 5-3a) can be considered such as evidence of Quaternary active folding. Field evidence shows Quaternary deposits dip 20° to NW in the western flank of inferred anticline fold (36°19'S). The course of river take straight course before to outlet of Central Valley where changes to braided behavior describing a curve in plan view to reach Catillo river. This active folding can be also detected in parallel to rectangular drainage network development on Quaternary Catillo surface (Figure 5-2). We hypothesize that the folds exhibit subtle yet symmetrical geometries, with increasing structural complexity and deformation intensity towards the west (Figure 5-4). This westward trend suggests a gradient in tectonic activity, with the western segments likely representing the most recently active and dynamically evolving portions of the fold system. Considerably patterns incision in drainage network suggest this subtle vertical deformation. This spatial variation in fold characteristics may reflect differential stress distribution and strain accommodation across the region, potentially indicating a westward propagation of the deformation front. Therefore, we propose that the Cachapoal Fault (CAF) is a high-angle blind reverse fault that controls Quaternary folding in the region. This fault geometry results in the formation of flexural scarps, which represent the most significant surface expression of the underlying tectonic activity. Longitudinal profiles of mapped terraces along the Perquilauquén River reveal interesting signals related to this folding, exhibiting terrace warping (e.g., Bullard and Lettis, 1993) (Figure 5-5a).

5.6 River incision and uplift rates

We calculated the fluvial incision rates considering the influence of deformation zones, such as the SFF and CaF, on river systems and the availability of geological material for OSL (Optically Stimulated Luminescence) dating. Sampling for OSL was challenging due to the scarcity of quartz, primarily influenced by the source rock composition. Based on the relative heights of terraces above the current river levels and the inferred OSL ages of fluvial terrace abandonment, we determined the average river incision rates along the Ñuble and Perquilauquén rivers (Figure 5-5) (Table 5.1).

Additionally, we used terrace T4 as a marker due to its continuity along both the Ñuble and Perquilauquén rivers. OSL samples from T4 were collected parallel to the SFF fault trace at a relative height of 37 meters above the modern river channel. Interestingly, the maximum OSL ages for the abandonment of the T4 surface showed two different ages at the same relative height. On the left side of the downstream channel, the age was 33.8±3.03 ka, whereas on the right side, it was 12.1±0.9 ka. This discrepancy is complemented by the age of terrace T6, which is 31.2±2.49 ka and runs parallel to the Ñuble River in the same segment as the two T4 ages.

We propose that the older surface age of T4 could be correlated with the age of T6, suggesting

a collapsed surface that migrated to the IMF (Intermediate Fault) and explaining the rectilinear scarp parallel to the SFF trace (Figure 5-4). This leads us to argue for a pull-apart basin within a complex sinistral (left-lateral strike-slip) system, which creates accommodation space for sediment storage. Initially, oblique faults may have allowed collapse along a normal fault, with the sinistral Ñuble River fault being predominant.

The rates of rapid incision through the SFF from the T6 to T4 surfaces reached up to 5.07±0.37 mm/yr, while from T4 to the modern river, the rate was 1.86±0.14 mm/yr. During the Late Pleistocene, the high rate of incision reflects a response to tectonic uplift (Oviedo-Reyes et al., 2024), which decreases in the Holocene. In the northern Perquilauquén river, the fluvial incision rate was 2.41±0.21 mm/yr during the Late Pleistocene. Comparatively, the T4 terrace in the Ñuble River shows a lower fluvial incision rate than observed in the Perquilauquén River.

Table 5.1: Ages and erosion rates derived from the Perquilauquén and Ñuble river terraces.

Fault	**Sample ID**	**Age (yr)**	**Differences in elevation T6-T4-River Profile (m)**	**Uplift rate mm/yr**
SFF	JAO-046-OSL	31200±2490	158.18	5.07±0.37
SFF	JAO-050-OSL	12100±900	22.46	1.86±0.14
CAF	JAO-048-OSL	26360±2240	63.48	2.41±0.21

In the RBF, uplift rates derived from vertical offset measurements along linear scarps reveal a difference between the southern and northern sectors (Table 2). In the northern sector, the Catillo area (36°16'S) shows an uplift rate of 0.89±0.06 mm/year, whereas the Zemita area (36°24'S) has a lower rate of 0.36±0.04 mm/year. This discrepancy may be attributed to the OSL sample from Zemita being collected from the middle position of the scarp. In the southern sector, the Nahueltoro scarp exhibits an uplift rate of 1.71±0.22 mm/year. This pattern of uplift is consistent with morphotectonic analysis, indicating higher uplift rates and more accumulated relief in the southern sector. The internal mountain front tectonic activity, enhanced by NW-oriented structures, imprints more deformation on the landscape, resulting in a more deformed area.

Table 5.2: Age constraints to CAF linear scarps.

Sector	**Sample id**	**Age**	**Vertical Offset (m)**	**Uplift Rate mm/yr**
Catillo	JAO-034-OSL	25700±1800	22.75	0.89±0.06
Zemita	JAO-048-OSL	9700±1050	3.45	0.36±0.04
Nahueltoro	JAO-051-OSL	25860±3210	44.17	1.71±0.22

5.7 Discussion

The morphotectonic mapping, longitudinal profiles of mapped terraces, and OSL ages of the Ñuble and Perquilauquén rivers reveal significant Quaternary deformation along the San Fabian Fault (SFF) in the Western Andean Front. Our analysis shows rapid vertical uplift of 5.07±0.37 mm/year from 30-13 ka, decreasing to 1.86±0.14 mm/year in the last 13 ka.

Shortening rates were estimated using OSL data and terrace staircases, considering tectono-fluvial coupling in the internal mountain front (Oviedo-Reyes et al., 2024) and assuming homogeneous dip angles (65°) from field data. Treating the SFF as a high-angle fault (65°), comparable to the San Ramón fault (Armijo et al., 2010; Estay et al., 2023), we calculated shortening rates of 2.36 ± 0.18 mm/year for the Late Pleistocene, decreasing to 0.867 ± 0.065 mm/year in the last 13 ka. These rates may explain the higher Quaternary elevated areas in the Nahueltoro sector (36°30'S) compared with adjacent elevated Quaternary surfaces (e.g., Zemita sector, 36°25'-36°30'S). Notably, uplift rates from linear scarps in the CAF (1.71±0.22 mm/year for the last 25 ka) (Figure 5-2) closely match those from terraces (1.86±0.14 mm/year for the last 13 ka), supporting the consistency of our findings from different geomorphological markers (at 36°30'S).

The paleostress data show consistency from south to north along the strike of the San Fabian Fault (SFF), characterizing its kinematics at least since the Miocene. Our findings support that this faulting style is preserved and continues to control neotectonic drainage patterns, as evidenced in the Zemita sector (36°25' to 36°30'S). We hypothesize that the SFF exhibits more intense deformation in certain areas due to its interaction with other structures, particularly where the NW-striking Ñuble River fault intersects it, potentially accumulating strain at this junction. The faulting style of the SFF suggests a pull-apart basin, which explains the rhombic shape of the Quaternary depocenter. This basin configuration also accounts for the age differences observed between adjacent terraces along the Ñuble River near the town of San Fabian de Alico. These observations collectively indicate a complex and ongoing tectonic influence on the regional geomorphology and sedimentary processes.

The geometry of the CAF is poorly constrained, here we provided a geomorphological comprehensive documentation. However, in our interpretation as a flexural scarp needs more interpretation from geophysical methods to constraint the shallow structure. The changes north-south of uplift rates derived from OSL and height of scarps suggest the growth of folding, but likely a rupture in Nahueltoro sector (36°25'S). In this sector, clearly show a headward erosion in response to disequilibrium by uplift. The field evidence presents a challenge given the characteristics of these steep scarps, with outcrops of highly weathered alluvial gravel deposits. Regionally it is observed a volcanic

deposits that could be provide a best tracking of this differential uplift in the study area.

Our approach compares uplift rates and deformation patterns across different sectors in the WAF, providing insights into spatial variations in tectonic activity in this sector of the Chilean Andes.

5.8 Conclusions

The study reveals significant spatial variations in tectonic activity along the San Fabian Fault (SFF). The Nahueltoro sector (36°30'S) shows higher Quaternary elevated areas compared to adjacent regions like the Zemita sector (36°25'-36°30'S). This variability in uplift rates suggests that tectonic deformation is not uniform along the fault, with some areas experiencing more intense uplift than others.

The analysis indicates significant changes in uplift rates over time. The study reports a rapid vertical uplift of 5.07±0.37 mm/year from 30-13 ka, which decreased to 1.86±0.14 mm/year in the last 13 ka. This temporal variation in uplift rates suggests a dynamic tectonic environment where deformation patterns have changed over the Quaternary period. The consistency between uplift rates derived from different geomorphological markers (linear scarps and terraces) at 36°30'S further supports these findings, indicating a reliable record of tectonic activity over time. These temporal changes in deformation rates are crucial for understanding the long-term slip of the SFF and CAF and and their seismogenic potential.

Supplementary Contents

Here we provided additional information about the methodology and other aspects related to this study.

OSL dating parameters

Additional Information:

The OSL dating analysis for the JAO samples was carried out by *Datação, Comércio e Prestação de Serviços LTDA*, located in São Paulo, Brazil. The laboratory is operated by Dr. Silvio Luiz Miranda Brito.

- **Sample Preparation:** Samples were subjected to mineral separation to isolate quartz grains. Chemical treatments involved hydrochloric acid (HCl), hydrogen peroxide (H_2O_2), and hydrofluoric acid (HF) to remove carbonates, organic material, and feldspar contamination, respectively.
- **Instrumentation and Protocols:** The OSL measurements were conducted using a Risø TL/OSL reader following the Single Aliquot Regenerative dose (SAR) protocol. Each sample was measured using 10 aliquots to determine the equivalent dose (De).

Summary of Samples (JAO ID) Aliquots and Reliability of Age Data

The document provides detailed results for the JAO samples using the SAR (Single Aliquot Regenerative-dose) protocol. Here's a summary of the key findings related to the reliability of the age data:

1. Aliquot Tests

- **Recuperation Test:** This test assesses the residual luminescence signal after the sample has been subjected to a regenerative dose of zero. For the aliquots from the JAO samples, the recuperation signals are generally below the threshold of 10% of the natural luminescence signal, indicating that there is minimal residual signal that could skew the age determination.
- **Recycling Ratio Test:** This test ensures that the luminescence response of the aliquots remains consistent throughout the SAR protocol. For the JAO samples, the recycling ratios typically fall within the acceptable range of 0.90 to 1.10. This consistency suggests that the

Table S1: Equivalent dose (De), annual dose rate (Da) and calculated OSL ages for each sample. Ages have been calculated for Quartz grains with size ranging between 180-250 µm.

Sample	Latitude	Longitude	Mineral Separation	Cosmic Radiation Dose Rate (µGy/yr)	Water Content (%)	Equivalent Dose (Gy) - CAM	Annual Dose Rate (µGy/yr)	Age (years)
JAO 033	-33.4489	-70.6693	Quartz	300 ± 30	8.4 ± 0.8	53.3 ± 2.8	2080 ± 90	25700 ± 1800
JAO 034	-33.4489	-70.6693	Quartz	300 ± 30	8.0 ± 0.8	86.7 ± 6.9	1720 ± 90	50530 ± 4760
JAO 035	-33.4489	-70.6693	Quartz	300 ± 30	19.0 ± 1.9	44.6 ± 2.4	1690 ± 110	26360 ± 2240
JAO 045	-33.4569	-70.6648	Quartz	300 ± 30	7.7 ± 0.8	19.9 ± 1.7	1860 ± 90	10750 ± 1060
JAO 046	-33.4569	-70.6648	Quartz	300 ± 30	10.3 ± 1.0	54.4 ± 3.6	1610 ± 100	33880 ± 3030
JAO 044	-33.4619	-70.6508	Quartz	310 ± 30	5.9 ± 0.6	61.4 ± 4.1	1970 ± 90	31200 ± 2490
JAO 048	-33.4619	-70.6508	Quartz	290 ± 30	11.3 ± 1.1	17.5 ± 1.5	1810 ± 120	9700 ± 1050
JAO 050	-33.4670	-70.6444	Quartz	300 ± 30	2.5 ± 0.3	22.3 ± 1.3	1850 ± 80	12100 ± 900
JAO 051	-33.4670	-70.6444	Quartz	300 ± 30	15.7 ± 1.6	25.4 ± 1.8	980 ± 100	25860 ± 3210

luminescence properties of the aliquots are stable, which is crucial for reliable age determinations.

2. Statistical Modeling

Central Age Model (CAM): The equivalent dose (De) values for the JAO samples were processed using the Central Age Model, with overdispersion (OD) considered. In cases where OD exceeds 30%, alternative models like the Minimum Age Model (MAM) or Finite Mixture Modeling (FMM) are recommended. However, for the JAO samples, the CAM appears to be appropriately applied, as the OD values are generally within the acceptable range.

3. Reliability of Age Data

The tests applied to the aliquots from the JAO samples suggest that the OSL age data is reliable. The low recuperation signals and stable recycling ratios indicate that the aliquots have not undergone significant alteration during the measurement process, and the use of the CAM provides a statistically robust approach to age determination. Therefore, the OSL ages reported for the JAO samples can be considered reliable.

Morphotectonic Map

Additional information we gathered from Slope Map and TRI procedures.

Terrain Ruggedness Index TRI

To calculate the TRI, at first the elevation difference between a central pixel (h0) and each of the eight neighboring pixels (h1–8) is determined. The TRI is determined with (Riley et al., 1999):

$$TRI = \sqrt{\sum_{n=1}^{8} (h_0 - h_n)^2} \tag{5.1}$$

As a result, the TRI represents the average difference in elevation between the central pixel and its neighbors as an absolute value. TRI returns more localized information of the terrain as each pixel only contains information on its direct neighborhood. Terrain Ruggedness Index (TRI) highlights the amount of elevation difference between adjacent cells of a digital elevation model (DEM). For example, we can classify the range of data as follows: from level terrain surface to extremely rugged surface. This raster is helpful to detect local fault traces, the resulting maps highlights terrain with abrupt changes (Riley et al., 1999; Diercks et al., 2023).

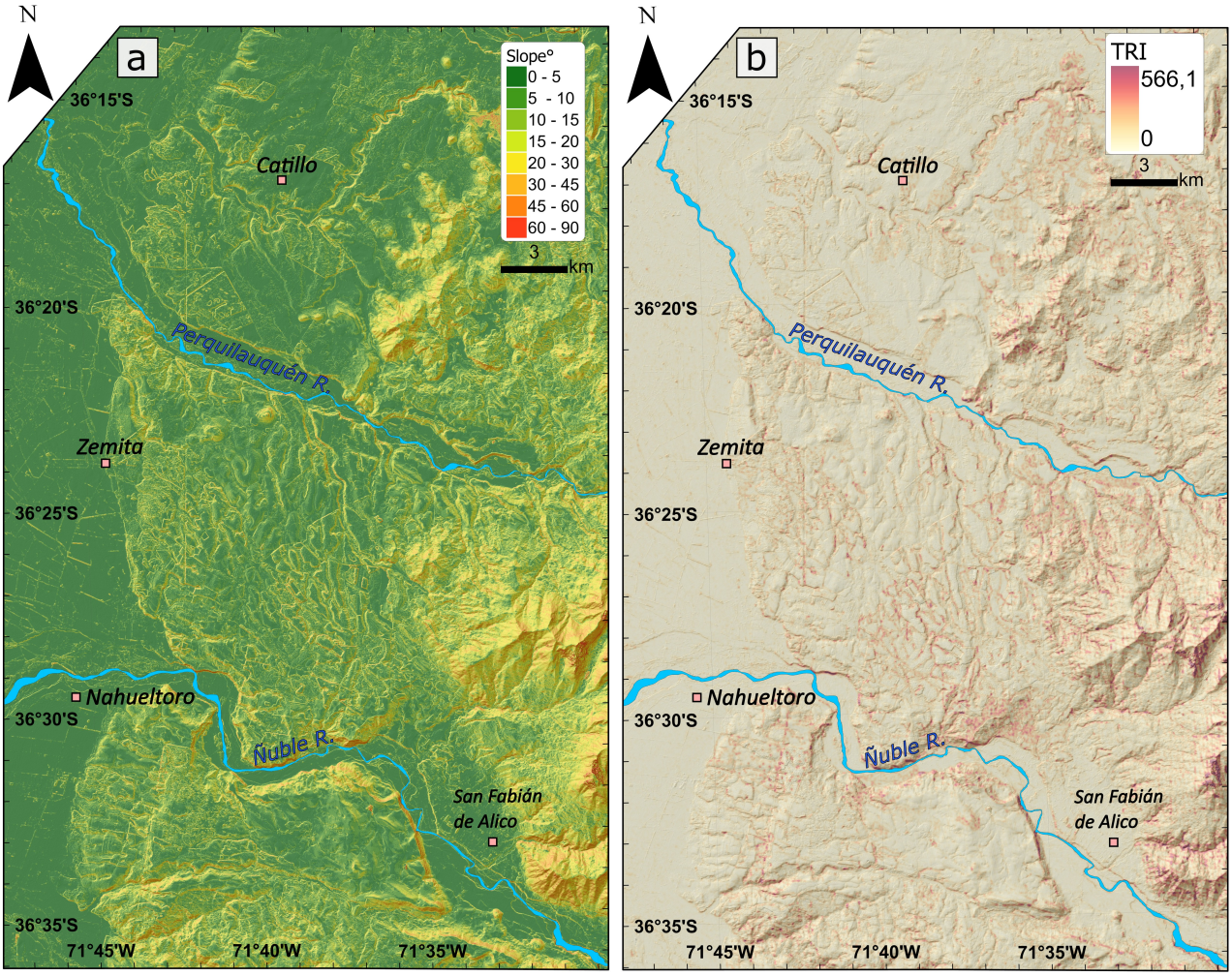


Figure S1: Slope and TRI maps for the study area. a. Distribution of slope in the study area. The highest elevations are located to southeast section. b. TRI permits to mapping structural features adequately. Perquilauquén and Ñuble Rivers are depicted in blue.

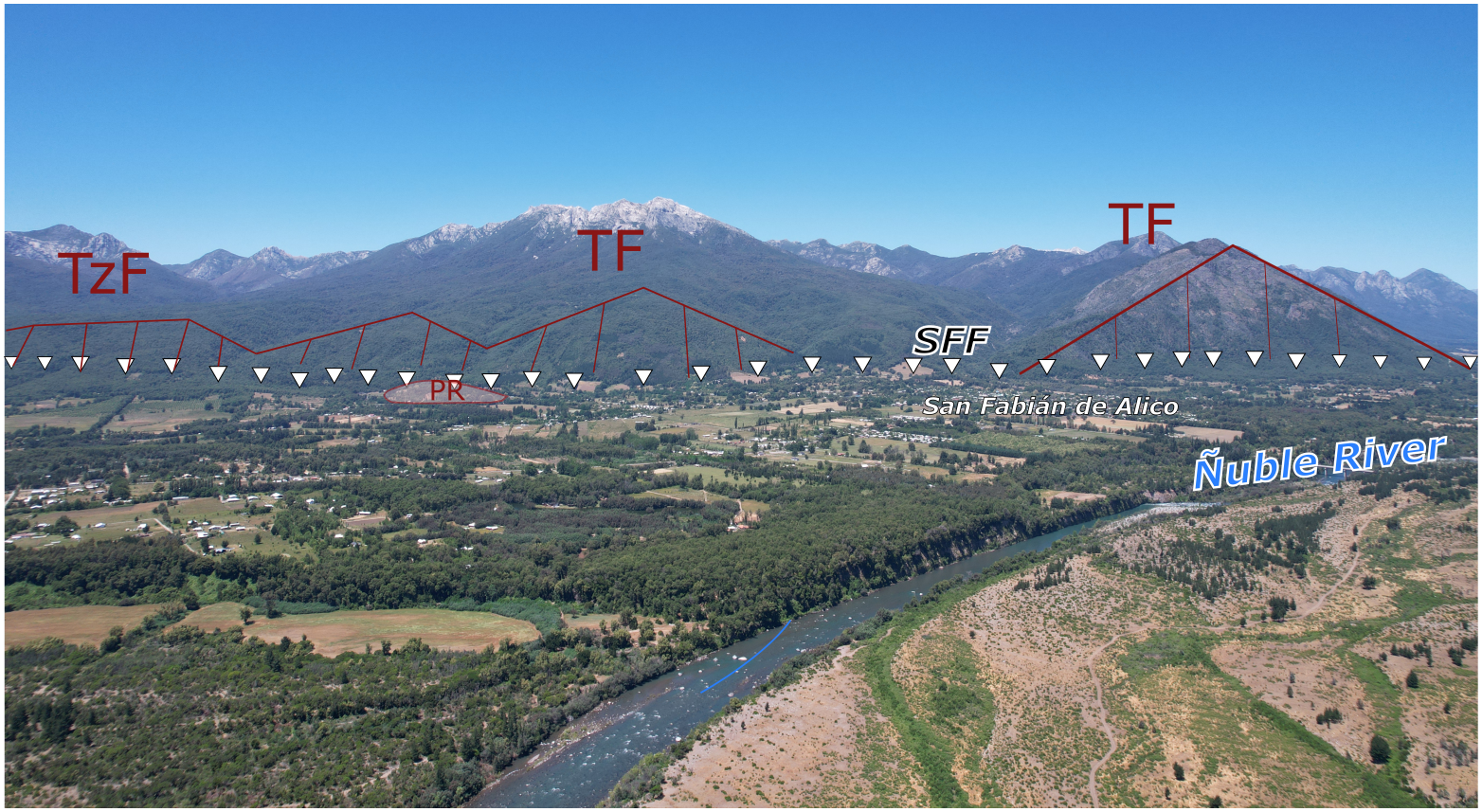


Figure S2: Drone image of the San Fabián fault (SFF) and its morphotectonic deformation indices. View towards the east. Triangular (TF) and trapezoidal facets can be distinguished along the fault trace. An isolated relief is described as a pressure ridge, with a low relief (PR). From left to right, a transition in lithology is observed from Abanico Formation units (andesites) to granitoids, which form the highest elevations.

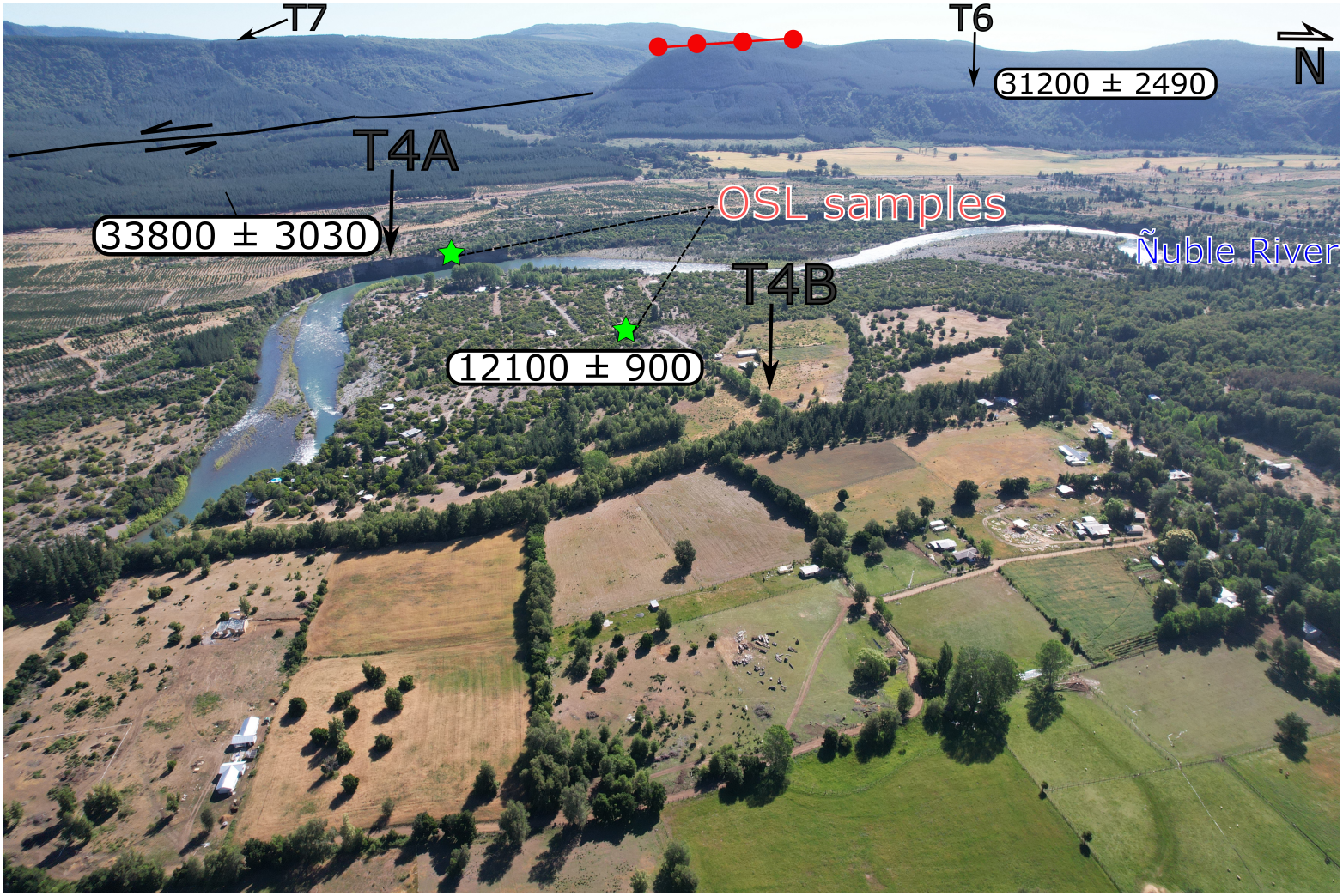


Figure S3: Drone image of the terrace and alluvial gravel deposits of the Ñuble River near San Fabián de Alico. Two positions of the T4 terrace are observed. Meander formation only occurs in this segment, while along this sector, the Ñuble River has a straight course. T6 and T7 terraces are also highlighted. OSL dating of T6 reveals a similar age to T4A.

Sedimentology

To characterize the Quaternary deposits in the study area, we measured the a, b and c axes of clasts from the gravel deposits of the terraces. The proportions (mud, sand, gravel) were also measured according to textural classifications (e.g., Folk (1954)). For each recent deposit, at least three measurements in 50x50 cm squares were taken to obtain an adequate description of the deposit. For each working station, classifications by shape (roundness, clast axes), composition, and stratigraphic relationship were obtained. Where fine-grained sand lenses were observed at the top of the deposit, OSL samples were taken.Sand samples for OSL dating were collected within sand lenses from terraces and recent deposits in the study area (Table S3).

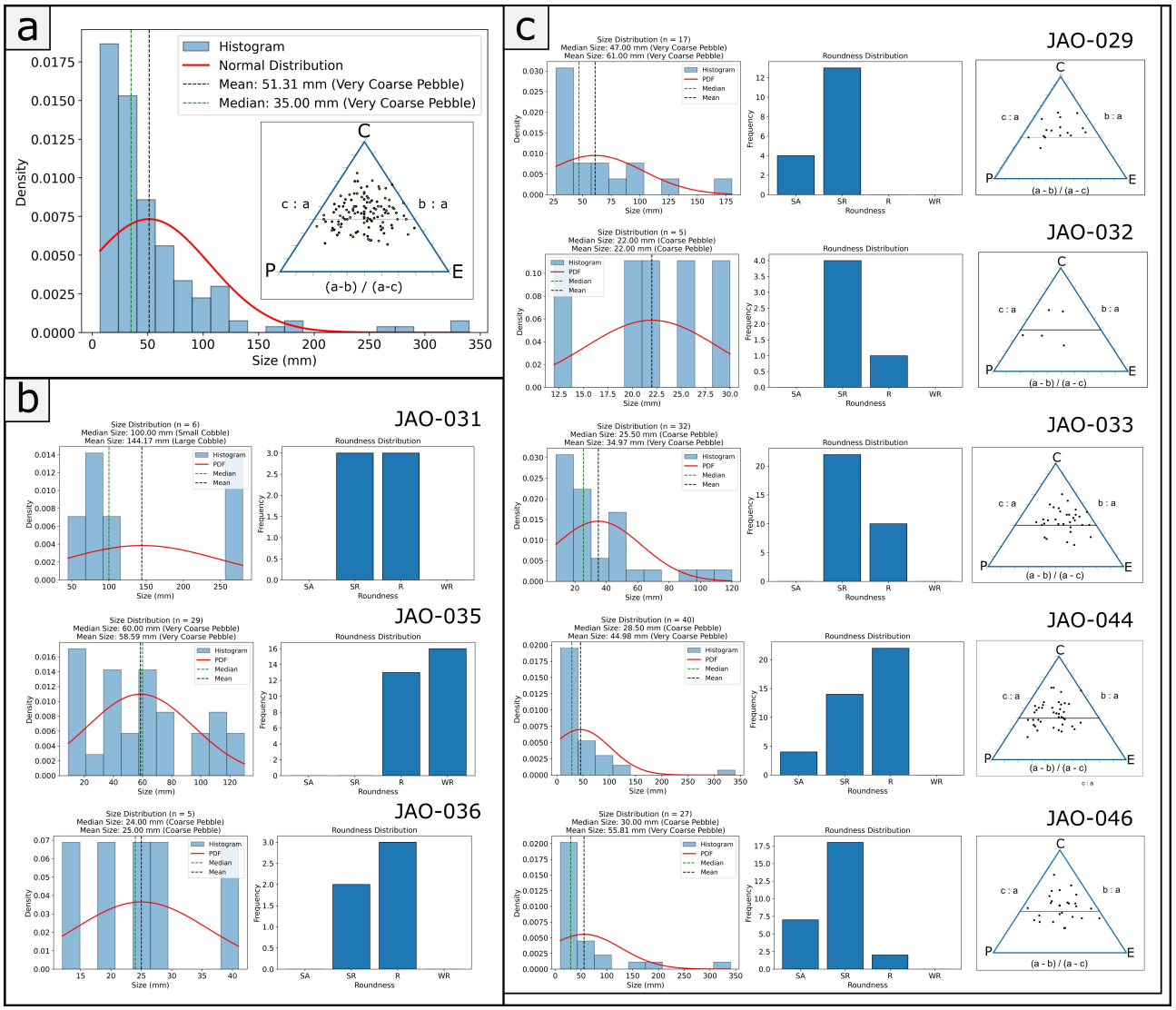


Figure S4: Distribution of particle size of terraces and other deposits in the study area. Triangular diagrams based on Sneed and Folk (1958) from C: Compact, P:Platy, and E:Elongated.Using TRI-PLOT excel spreadsheet from Graham and Midgley (2000). Note the majority of clast range from compact bladed, elongated and platy shapes.

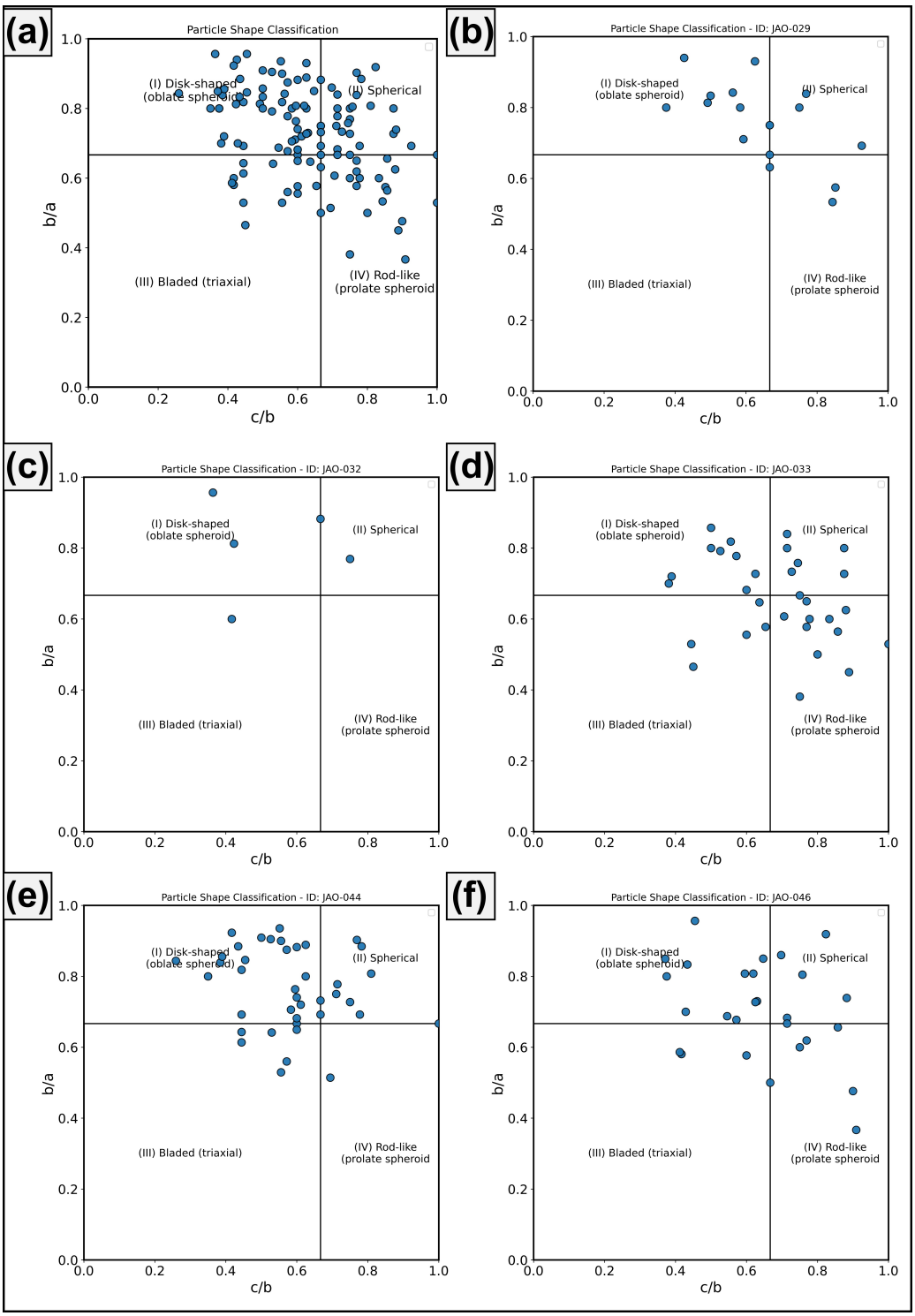


Figure S5: Zingg (1935) particle shape classification using the ratios of the three main axes of a clast a,b and c. Particle shape from disk shape to spherical.

Structural data

To calculate paleostress data in the study area we followed the procedures of (Delvaux and Sperner, 2003) and others author considerations, the Table S1 summarizes the data obtained using WinTensor 5.1 and Table S2 the database obtained from field mapping. The stress tensor analysis encompasses various parameters and methods, including the orientation of principal stress axes and maximum

horizontal stress (SH_m), statistical measures such as Counting Deviation, α and F5 values (for I.R. Dihedr method), and stress ratios R and R'. Analytical approaches involve I.R. Dihedr (Improved Right Dihedra), Enhanced Straight Dihedra, and R. Optimisation (Rotational Optimisation), with quality indicators Q and QRt.

The analysis classifies tensor types according to the World Stress Map (Zoback, 1992) and identifies associated stress regimes. Data characteristics include location, lithology, number of data used per tensor (n), subset population (n subset), and total field station data population (N). The quality factor Q is primarily influenced by data quantity, reliability, percentage, and other factors (Sperner and Zweigel, 2010).

For methods with fewer planes involved (I.R. Dihedr and Enhanced Straight Dihedra), specific values (α, F5, Counting Deviation) are reported separately, providing a comprehensive overview of the stress tensor analysis results.

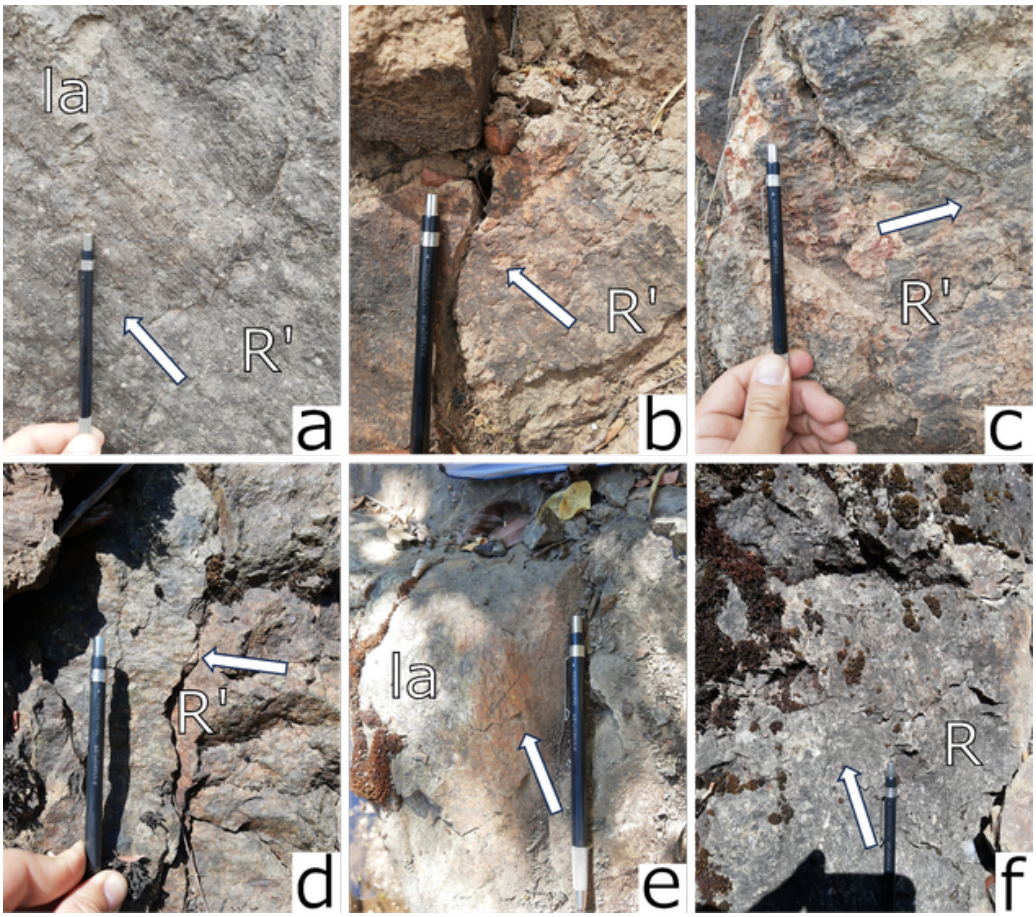


Figure S6: Minor structures on fault planes of the Loma Linda fault (a, b, c) and San Fabian fault (d, e, f). Riedel (R), antithetic Riedel (R'), and lunate fractures (la) are observed across the fault planes. Slip direction is determined using criteria established by Petit (1987). Arrows indicate sense of movement of missing block.

Table S2: Results of the solution of the stress tensors obtained from the analysis of striated planes

ID	Site ID	Coordinates		Age	Lithology	Method	Tensor	Graphical representation	n	n subset	N	Axis			Counting Deviation R.Dihedr	α	F5	R	R'	Shmax	QRt	WSM	Tectonic Regime
		X	Y									s1	s2	s3									
1	JAO - 043	265074	5955706	Oligocene - Miocene	Andesites	R. Dihedron	1		6	8	8	00/187	17/097	73/278	22.5	-	-	0.33	2.5	6	D	TF	Pure Compressive
2	JAO-052	272704	5951426	Oligocene - Miocene	Andesites	R. Dihedron	2a		4	10	10	00/182	81/273	09/092	28.2	-	-	0.5	1.5	2	E	SS	Pure Strike-slip
						R. Optim F5	2b		4	6		04/102	58/006	32/195	-	21.5	18.1	0.12	1.5	102	E	TS	Compressional Strike-Slip
3	JAO-054	271968	5948277	Oligocene - Miocene	Basalts	R. Optim F5	3a		4	8	8	008/89	81/306	006/179	-	25	18.5	0.25	1.5	88	E	TS	Compressional Strike-Slip
						R. Dihedron	3b		4	4		16/356	70/214	12/089	29	-	-	0.5	1.48	177	E	SS	Pure Strike-slip
4	JAO-056	270915	5957526	Oligocene - Miocene	Breccia	R. Optim F5	4a		7	22	22	16/145	60/025	25/243	-	16.4	12.2	0.14	1.50	146	D	TS	Compressional Strike-Slip
						R. Dihedron	4b		7	15		003/278	009/188	80/023	26.5	-	-	0.57	2.5	98	D	TF	Pure Compressive
						R. Dihedron	4c		4	8		32/313	58/138	002/044	26.4	-	-	0.75	0.9	133	E	NS?	Extensional Strike-Slip
5	JAO-058	265484	5971087	Oligocene - Miocene	Lithic tuffs	R. Dihedron	5a		5	13	13	004/121	00/030	86/299	22.8	-	-	0.2	2.46	120	E	TF	Pure Compressive
						R. Dihedron	5b		5	8		16/178	73/006	002/269	24.6	-	-	0.5	1.42	178	E	SS	Pure Strike-slip

Table S3: Database of brittle deformation in the Internal Mountain Front

No	Point	Az	Az d+	Dip Dir	Dip Dir +d	Dip	Rake	Rake WT	Sense	Kinematics	Component	Criteria	Type	Unit	Rock
1	JAO-043	62	65	152	155	56	14	166	SW	Sinistral strike-slip	Reverse	R'-lunate	A	Fm. Abanico	Andesite
2	JAO-043	122	125	212	215	27	27	153	SE	Dextral strike slip	Reverse	R'	B	Fm. Abanico	Andesite
3	JAO-043	125	128	215	218	48	54	126	SE	Reverse	Dextral	R'	B	Fm. Abanico	Andesite
4	JAO-043	98	101	188	191	58	82	98	SW	Normal	Dextral	R'	B	Fm. Abanico	Andesite
5	JAO-043	65	68	155	158	42	85	95	SE	Reverse	Dextral	R'	B	Fm. Abanico	Andesite
6	JAO-043	10	13	100	103	86	19	161	NW	Dextral strike slip	Reverse	Crystal fibers	A	Fm. Abanico	Andesite
7	JAO-043	175	178	265	268	64	20	160	SW	Dextral strike slip	Reverse	R'	B	Fm. Abanico	Andesite
8	JAO-043	230	233	320	323	52	38	142	NE	Sinistral strike-slip	Reverse	R'	A	Fm. Abanico	Andesite
9	JAO-043	315	318	45	48	44	65	115	N - NW	Reverse	Dextral	R'	B	Fm. Abanico	Andesite
10	JAO-043	305	308	35	38	30	30	150	NW	Sinistral strike-slip	Normal	R'	C	Fm. Abanico	Andesite
11	JAO-052	65	68	155	158	73	17	163	NE	Dextral strike slip	Reverse	R'	B	Fm. Abanico	Andesite
12	JAO-052	222	225	312	315	84	34	146	SW	Sinistral strike-slip	Reverse	R'	B	Fm. Abanico	Andesite
13	JAO-052	220	223	310	313	76	50	130	NW	Normal	Sinistral	R'-lunate	B	Fm. Abanico	Andesite
14	JAO-052	216	219	306	309	72	40	140	NE	Sinistral strike-slip	Reverse	R'-lunate	B	Fm. Abanico	Andesite
15	JAO-052	60	63	150	153	71	51	129	NE	Normal	Sinistral	R'-lunate	B	Fm. Abanico	Andesite
16	JAO-052	215	218	305	308	84	9	171	NE	Dextral strike slip	Normal	Crystal fibers	B	Fm. Abanico	Andesite
17	JAO-052	200	203	290	293	64	78	102	NW	Normal	Dextral	R'	C	Fm. Abanico	Andesite
18	JAO-052	195	198	285	288	86	12	168	NE	Dextral strike slip	Normal	R'-lunate	B	Fm. Abanico	Andesite
19	JAO-052	242	245	332	335	50	55	125	NW	Reverse	Sinistral	R	B	Fm. Abanico	Andesite
20	JAO-052	180	183	270	273	38	69	111	SW	Reverse	Dextral	T	C	Fm. Abanico	Andesite
21	JAO-053	110	113	200	203	88	0	180	-	Sinistral strike-slip	-	RM	A	Fm. Abanico	Basaltos
22	JAO-053	110	113	200	203	88	5	175	-	Dextral strike slip	-	R	A	Fm. Abanico	Basaltos
23	JAO-054	248	251	338	341	65	10	170	NE	Dextral strike slip	Normal	R'	B	Fm. Abanico	Basaltos
24	JAO-054	280	283	10	13	88	9	171	NW	Dextral strike slip	Reverse	R'	A	Fm. Abanico	Basaltos
25	JAO-054	220	223	310	313	76	16	164	NW	Dextral strike slip	Reverse	R'-lunate	B	Fm. Abanico	Basaltos
26	JAO-054	295	298	25	28	64	22	158	NE	Sinistral strike-slip	Reverse	R'	B	Fm. Abanico	Basaltos
27	JAO-054	302	305	32	35	80	12	168	NE	Dextral strike slip	Normal	R'	C	Fm. Abanico	Basaltos
28	JAO-054	55	58	145	148	62	25	155	SW	Sinistral strike-slip	Reverse	R' - R	B	Fm. Abanico	Basaltos
29	JAO-054	257	260	347	350	58	1	179	-	Sinistral strike-slip	-	R'	C	Fm. Abanico	Basaltos
30	JAO-055	282	285	12	15	76	28	152	NE	Dextral strike slip	Normal	R'	C	Fm. Abanico	Basaltos
31	JAO-055	159	162	249	252	58	30	150	SE	Sinistral strike-slip	Normal	R	C	Fm. Abanico	Basaltos
32	JAO-055	10	13	100	103	26	40	140	SW	Dextral strike slip	Reverse	R'	B	Fm. Abanico	Basaltos
33	JAO-055	355	358	85	88	34	55	125	NE	Normal	Sinistral	R'	C	Fm. Abanico	Basaltos
34	JAO-055	260	263	350	353	25	82	98	NW	Normal	Sinistral	R'	B	Fm. Abanico	Basaltos
35	JAO-056	144	147	234	237	30	15	165	NW	Sinistral strike-slip	Reverse	R'	B	Fm. Abanico	Breccia
36	JAO-056	318	321	48	51	79	12	168	NW	Dextral strike slip	Reverse	R'	C	Fm. Abanico	Breccia
37	JAO-056	198	201	288	291	62	75	105	NW	Reverse	Sinistral	R'-lunate	C	Fm. Abanico	Breccia
38	JAO-056	178	181	268	271	84	55	125	NW	Reverse	Sinistral	R'	C	Fm. Abanico	Breccia
39	JAO-056	220	223	310	313	35	45	135	NW	Reverse	Dextral	R'-lunate	B	Fm. Abanico	Breccia
40	JAO-056	144	147	234	237	37	62	118	NW	Reverse	Sinistral	R'-lunate	B	Fm. Abanico	Breccia
41	JAO-056	232	235	322	325	52	88	92	NW	Reverse	-	R'	C	Fm. Abanico	Breccia
42	JAO-056	202	205	292	295	36	62	118	NW	Reverse	Sinistral	R'	B	Fm. Abanico	Breccia
43	JAO-056	293	296	23	26	58	40	140	NW	Dextral strike slip	Normal	R'	C	Fm. Abanico	Breccia
44	JAO-056	280	283	10	13	62	8	172	SW	Dextral strike slip	Reverse	R' - R	B	Fm. Abanico	Breccia
45	JAO-056	268	271	358	361	68	8	172	NW	Dextral strike slip	Reverse	R'	B	Fm. Abanico	Breccia
46	JAO-056	155	158	245	248	76	39	141	SW	Sinistral strike-slip	Reverse	RM	A	Fm. Abanico	Breccia
47	JAO-056	290	293	20	23	48	20	160	NW	Dextral strike slip	Reverse	R'	A	Fm. Abanico	Breccia
48	JAO-056	276	279	6	9	49	29	151	NW	Dextral strike slip	Reverse	R'	B	Fm. Abanico	Breccia
49	JAO-056	264	267	354	357	50	75	105	NW	Reverse	Sinistral	RM	A	Fm. Abanico	Breccia
50	JAO-056	206	209	296	299	34	40	140	NE	Sinistral strike-slip	Reverse	R'	B	Fm. Abanico	Breccia
51	JAO-056	196	199	286	289	65	49	131	NW	Reverse	Sinistral	R'-lunate	A	Fm. Abanico	Breccia
52	JAO-057	44	47	134	137	55	70	110	SE	Normal	Sinistral	Crystal fibers	C	Batolito Andino	Tonalite
53	JAO-057	353	356	83	86	32	84	96	NE	Normal	Sinistral	Crystal fibers	C	Batolito Andino	Tonalite
54	JAO-058	25	28	115	118	66	90	90	-	Reverse	-	R'	C	Fm. Abanico	Lithic Tuff
55	JAO-058	65	68	155	158	70	10	170	SW	Sinistral strike-slip	Reverse	R'-lunate	B	Fm. Abanico	Lithic Tuff
56	JAO-058	295	298	25	28	88	22	158	NW	Sinistral strike-slip	Normal	R'	B	Fm. Abanico	Lithic Tuff
57	JAO-058	285	288	15	18	86	8	172	SE	Dextral strike slip	Normal	R'	B	Fm. Abanico	Lithic Tuff
58	JAO-058	220	223	310	313	78	20	160	NW	Sinistral strike-slip	Reverse	R'	B	Fm. Abanico	Lithic Tuff
59	JAO-058	212	215	302	305	80	30	150	NW	Sinistral strike-slip	Reverse	R'	B	Fm. Abanico	Lithic Tuff
60	JAO-058	225	228	315	318	54	30	150	SW	Dextral strike slip	Reverse	R'	B	Fm. Abanico	Lithic Tuff
61	JAO-058	237	240	327	330	42	32	148	SW	Dextral strike slip	Reverse	R' - R	B	Fm. Abanico	Lithic Tuff
62	JAO-058	204	207	294	297	78	52	128	SW	Reverse	Dextral	R'-lunate	A	Fm. Abanico	Lithic Tuff
63	JAO-058	200	203	290	293	54	45	135	NW	Reverse	Sinistral	RM	A	Fm. Abanico	Lithic Tuff
64	JAO-058	165	168	255	258	59	43	137	NW	Sinistral strike-slip	Reverse	R'-lunate	A	Fm. Abanico	Lithic Tuff
65	JAO-058	240	243	330	333	76	24	156	SW	Sinistral strike-slip	Normal	R' - R	B	Fm. Abanico	Lithic Tuff
66	JAO-058	30	33	120	123	56	75	105	SE	Normal	Dextral	R'	C	Fm. Abanico	Lithic Tuff

Fluvial Terrace Profiling

We extracted terrace profiles along the Perquilauquén and Ñuble rivers following the procedures outlined by Angster et al. (2020) and references therein (Figures S6 and S7). Our method involved constructing river terrace profiles by measuring downstream distance along the river center and pro-

jecting preserved terrace tread elevations toward this centerline, accounting for the river's migration path during abandonment. To manage uncertainty, we acknowledged potential projection errors, variations in deposit thickness, and surface modifications. We utilized a 5 m Digital Terrain Model (DTM) to place points at 100 m intervals along the center or riverside, depending on which provided the best representation. While some projection uncertainty onto the river might result in systematic error, the impact was minimized as most terraces in both river systems are confined within their respective valleys. This approach allowed us to create comprehensive terrace profiles while addressing potential sources of error.

Table S4: List of sand samples collected for OSL. The amount of Qz per sample is indicated.

Id Sample	**Coordinate X**	**Coordinate Y**	**OSL age**	**Type Sediment**	**%Qz**
JAO-033-OSL	258766	5983437	25700 ± 1800	Sand	40
JAO-034-OSL	255534	5977860	50530 ± 4760	Muddy sand	30
JAO-035-OSL	261205	5973629	26360 ± 2240	Muddy sand	20
JAO-044-OSL	270634	5951001	10750 ± 1060	Sand	15
JAO-045-OSL	271298	5949322	33880 ± 3030	Sand	15
JAO-046-OSL	268121	5951700	31200 ± 2490	Sand	50
JAO-048-OSL	254280	5968036	9700 ± 1050	Muddy sand	25
JAO-050-OSL	271530	5949820	12100 ± 900	Sand	25
JAO-051-OSL	255434	5957019	25860 ± 3210	Muddy sand	20

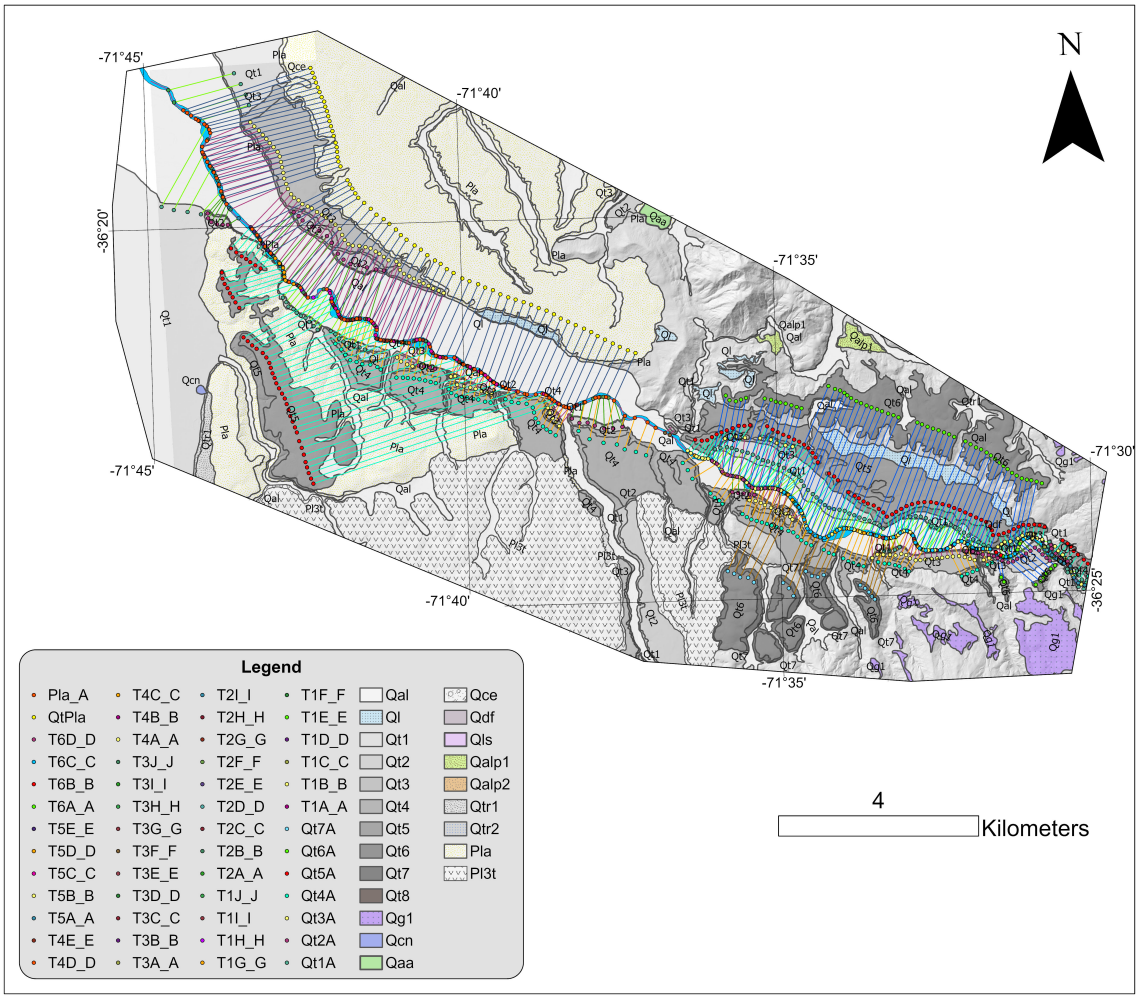


Figure S7: Projection of terrace elevation in the Perquilauquen River.

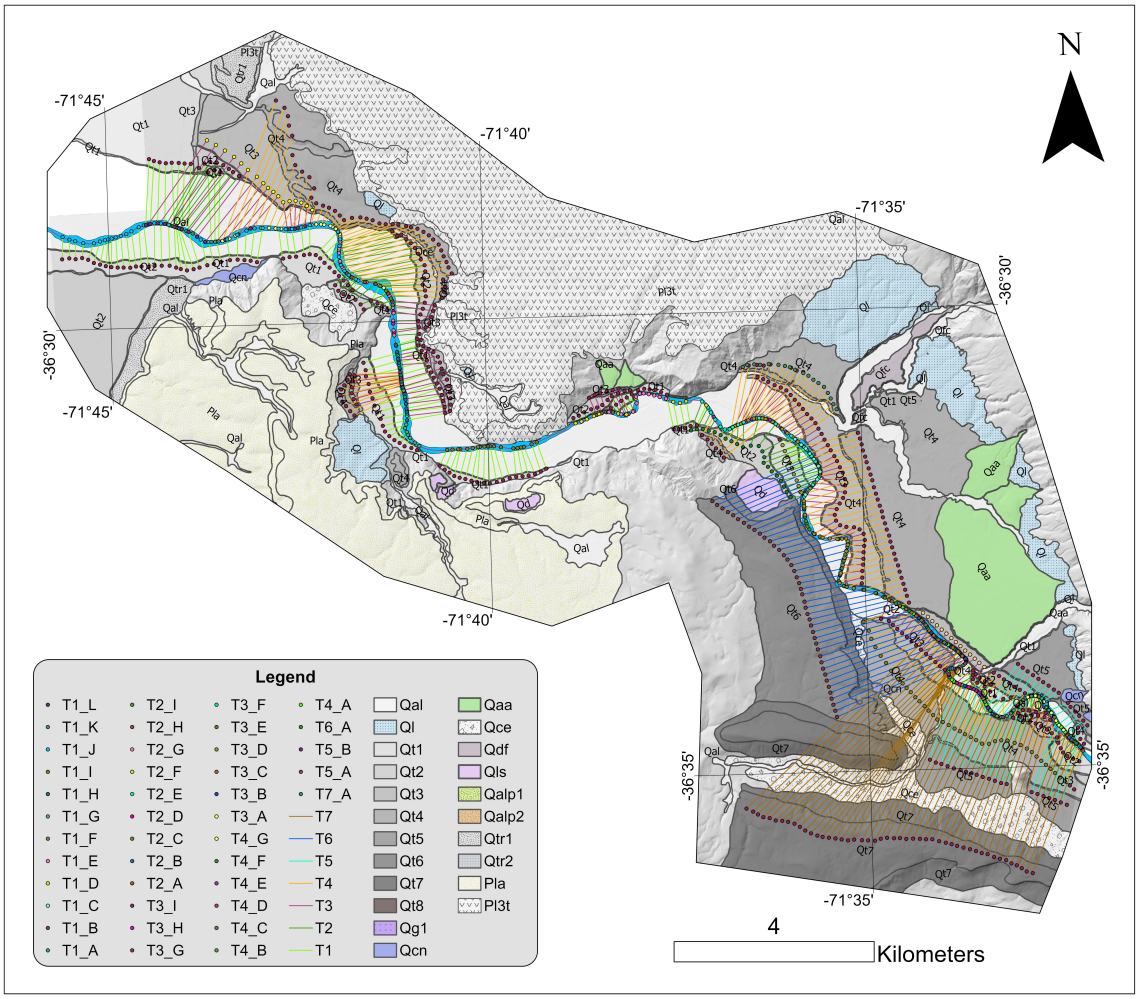


Figure S8: Projection of terrace elevation in the Ñuble River.

Capítulo 6

Discussion

Discussion

In this dissertation, I explored the neotectonic activity and landscape evolution of the Western Andean Front (WAF) between 35°S and 38°S in central Chile. Through comprehensive geomorphic analysis, field observations, and geochronological dating, this study provides new insights into the spatial and temporal patterns of deformation, fault kinematics, and tectonic-climatic interactions shaping this active mountain front.

6.1 Landscape Response to Tectonic and Climatic Forcing

The research identified a distinct north-south variation in neotectonic activity centered around 36°S. North of this latitude, the mountain front appears largely inactive, adjusted to long-term climate-driven fluvial processes. South of 36°S, the landscape is characterized by active uplift and transient topography. The findings pointed out the relevance of the influence of the climate on tectonic evolution in the Chilean Andes. Whipple (2009) discusses the sensitivity of mountain belts to spatial and temporal variations in erosional efficiency, highlighting the importance of understanding how climate interacts with tectonic processes. In this aspect, Rehak et al. (2010) demonstrated a significant relationship between climate and topography, noting that increased rainfall correlates with decreased elevation and relief. This suggests that higher precipitation rates can significantly shape mountainous landscapes by enhancing erosion. These authors defined a segmentation where on the one side glacial erosion dominates (30-35°S), and a fluvial erosion domain (35-40°S). As a consequence, steeper and more rugged topography resulting from glacial erosion, this important signal can be considered a key in the interpretation of the morphometric properties in the study area of this research.

One might wonder why, north of 36°S, the landscape is dominated by isolated hills (inselbergs) and embayments along the mountain front. Are the tectonic processes responsible for shaping these distinctive geomorphic features? From a Davisian perspective, landscape evolution is viewed through the lens of sequential stages of youth, maturity, and old age. Therefore, we could attribute the erosion such a first control in this segment of the mountain front which tends to denude the landscape over time, reducing the topography. The eastward retreat of the escarpment is measured using the mountain front sinuosity index (Smf) (Bull and McFadden, 1977), which indicates tectonic quiescence north of 36°S (Oviedo-Reyes et al., 2024). However, valley shape (Vf-index) and channel metrics applied in this research (e.g., SL-index, Ksn, normalized river profiles) suggest pro-

cesses beyond mere degradation. Regionally, topographically constrained glaciers (valley and cirque glaciers) are observed up to 36°S (e.g., Singer et al., 1997; Mejías Osorio et al., 2024). These glaciers enhance erosion rates, potentially explaining the V-shaped valleys in the piedmont area and increase topographic relief through isostatic uplift of residual peaks (Molnar and England, 1990). Using the channel steepness index (K_{sn}) and local relief, it was demonstrated that high K_{sn} values ($\sim 250m^{0.9}$) correspond to transitions between erosional domains. Lower K_{sn} values are found in glacially modeled valleys, forming knickpoints at their transition to fluvial valleys (high K_{sn}). Further, relevant data can be retrieved from geological charts which reveal high-strength mass rock (granitoids), lavas, and Oligocene-Miocene formations (e.g., Abanico Formation), implying potential lithological controls on these morphometric properties. Thus, the isostatic uplift of this segment would explain how the morphometric signal can be misleading if other factors such as climate or lithology are not considered in the analysis (e.g., normalized river profiles, hypsometry, local relief). Supporting this, Diercks et al. (2023) recently concluded that well-established morphometric indexes alone are insufficient to identify active faults, particularly in areas with low deformation rates. They emphasized that elevated K_{sn} values and knickpoints can result from lithological boundaries, glacial processes, dams, and other non-tectonic influences.

In fact, the question 'Why do valleys exhibit a V-shape in the context of an inactive thrust front?', addressed in chapter two, was explained by climate-driven bedrock incision. However, the findings in chapter 3 allow us to identify how these controls are manifested and what their origin is with greater certainty. Nevertheless, it is not ruled out that there are fault reactivations due to these isostatic uplifts, which is why they are also analyzed in this chapter.

6.2 Spatial Variation in Tectonic Activity

The tectonic activity classes mapped trough different methods can be follow in the chapter 2 and 3. The first one, Smf/Vf ratio solely focus on piedmont-mountain junction (e.g., Bull and McFadden, 1977; Rockwell et al., 1985; E. Keller and Rockwell, 2022) meanwhile the relative tectonic activity indexes (Iat) or RTA (e.g., El Hamdouni et al., 2008; Dehbozorgi et al., 2010; Matoš et al., 2016) evaluating the entire area. By comparison, all classification provides similar results overall in the southern segment (36-38°S). Despite the ability of Iat/RTA indices to detect potential tectonic deformation across areas, the Smf/Vf ratio demonstrates particular sensitivity in describing deformation along mountain fronts with uniform lithology and consistent climate gradients. Though the Smf/Vf ratio is included in the calculation of the Iat/RTA indices, they categorize the mountain front north of 36°S as having moderate tectonic activity. This oversight could be explained by the

sensitivity of some indices (e.g., hypsometry, basin elongation ratio, asymmetry factor) to abrupt lithologic and climatic changes, potentially elevating the assessed level of tectonic activity. Given that Ksn values reflect changes between geomorphic systems and respond to lithologic variations (specifically in the study area), it follows that Iat/RTA indices should also be interpreted with caution.

Nevertheless, both Iat/RTA indices prove to be powerful tools for discriminating relative tectonic activity across areas. They successfully identified regions with high tectonic activity that had previously shown evidence of active deformation, such as the Huepil fault (HuF) and the Lake Laja fault system (LLFS) (e.g., Melnick and Echtler, 2006). Moreover, the San Fabian Fault (SFF), described in Chapter 5 and exhibiting deformation evidence through morphotectonic mapping, is highlighted as an area of high tectonic activity. These indices also emphasized intersection zones between NW- and NE-trending faults, opening avenues for future research on the development of these mechanisms. Furthermore, the resulting maps provide valuable insights into deformation trends and their spatial distribution. The integration of relative tectonic maps provided valuable information regarding the distribution of deformation. In the case study of the western Andean front, this was crucial for identifying areas for field study. As previously mentioned, the San Fabián de Alico area was chosen partly based on the information provided by geomorphological indices and the procedures used to distinguish active tectonic signals from non-tectonic ones (e.g., lithology, climate).

Delving deeper into the orogenic processes underlying the spatial distribution of relative tectonic activity (Figures 2-6 and 3-26) in the study area, we propose several key mechanisms beyond the observed surficial processes. These mechanisms include: (1) variations in subduction angle along 35-38°S, which likely influence the stress regime and deformation patterns in the overriding plate; (2) changes in inherited lithological and structural heterogeneities south of 35°S, potentially controlling the localization and style of deformation; and (3) variations in thickness and composition of the continental crust, which may modulate the mechanical response to tectonic forces.

The slab configuration can be characterized as follows: (1) north of 27°S, the slab dips eastward at approximately 30°; (2) between 27.5°S and 33°S, a distinctive sub-horizontal segment, or "flat slab," is present (e.g., Yañez et al., 2001); (3) from 33°S to 36°S, the slab steepens again to an average dip of 30° eastward; and (4) between 36°S and 46°30'S, the slab inclination increases further, ranging from 30° to 40° (e.g., Cahill and Isacks, 1992; López et al., 1997). The transition between from flat to normal subduction (∼33°S) have been described by slab tear (Yañez et al., 2001) or slab bending (Pesicek et al., 2012) which accommodates this transition in subduction angle. A stepper slab dip in the south (38°S) representing vertical tearing of the slab explained by the Mocha fracture zone (Pesicek et al., 2012), and this would explain the termination of the WAT

at 38°S with the surface projection of the slab tear (Eisermann et al., 2021). This slab tear would explain the tectonic deformation in surface highlighted by the morphometry proposed in this work (Figures 2-6 and 3-26) between 37-38°S. Thus, these tectonically controlled areas would imply a surface response of orogenic processes, due slab tear creates abrupt changes in the stress field at the surface, potentially in the development of new fault systems or reactivation of existing ones. For example, second first-order NW-striking structures (e.g., Laja River Fault – LaF) are regionally related to the western termination of the Cortaderas lineament on the western flank of the Principal Cordillera, which is considered a basement boundary that was reactivated during Andean deformation (Ramos and Kay, 2006; and references therein). However, prominent NW-striking faults appear to form spontaneously as riedel shears in response to dextral transpression, rather than reactivating pre-andean discontinuities (Pesicek et al., 2012). This distributed deformation pattern aligns with observed NNE-NW first-order faults (Figure 2-9) and explains the segmentation of the upper crust into rhomb-shaped domains (e.g., Eisermann et al., 2021). These domains, created by intersecting fault sets, could account for the spatial patterns of high tectonic activity identified in morphometric analyses, including the intersection zones between NW- and NE-trending faults (e.g., San Fabian fault). Quaternary tectonic activity along the WAF is particularly evident in the Huépil Sector (south of 37°S), coinciding with the WAT's southern limit, the LOFZ's northern boundary, and GPS velocity field variations. This tectonically complex area may reflect slab tearing, influencing upper plate crustal strength differences (Eisermann et al., 2021).

Other mechanism to explain the controlled tectonic areas in the south of the study area (37-38°S) may referred to localized uplift due to asthenosphere upwelling; increasing heat flow and potential volcanism (e.g., Antuco volcano, Nevados de Chillán Volcanic Complex), where the shallower dip slab allows more differential uplift (north of 38°S). Crustal anisotropy induced by vertical asthenospheric flow (e.g., Wu et al., 2019) can be reflected in surface deformation patterns, as suggested by morphometric analysis. Given the scope of this study, which primarily addresses surface tectonic deformation during Quaternary times, delving into the nuances of crustal anisotropy would require extensive analysis that may detract from the main themes. As such, this interpretation is introduced as a preliminary hypothesis, framed within the context of the orogenic mechanism, but it remains an area for future research to explore in detail.

Finally, the crustal architecture could lead a differential uplift between north to south in the study area. East of 70°W, high-density crust is observed in the northern (29–34.5°S) and southern domains (37–39°S), with densities around 3000–3050 kg/m^3 (Rodriguez Piceda et al., 2020). This high-density crust is likely to behave more rigidly compared to the lower-density, thicker crust beneath the orogen. As a result, these high-density blocks can resist deformation more effectively, potentially

acting as buttresses or rigid blocks that influence the distribution and style of deformation in the region. Specifically, at (∼33°S) well constrained tectonically controlled mountain fronts in both sides of Andes by active faulting (e.g., San Ramon Fault or Eastern Sierra de la Cantera fault – Sierras Pampeanas) and between 37 to 38°S in the Huépil Fault (Chilean border) and Antiñir-Copahue fault system (Argentinian border) coincides with areas high-density crust areas described. The contrast between the rigid, high-density crust and the more ductile, lower-density crust beneath the orogen can create differential movement along their boundaries. This differential movement can result in the concentration of stress along faults that separate these different crustal domains, leading to increased fault activity, slip rates, or the reactivation of older faults. The deformation patterns observed from morphometry (Figure 3-26) between 35-38°S coincides with the differential densities describe by Rodriguez Piceda et al. (2020) to the east of Principal Cordillera, this limit could be acting such as rigid block, accumulating the deformation in this areas, meanwhile in the central area (34-37°S) the absence of his rigid block may explain the lower tectonic activity described in this research.

In the northern domain (29–34.5°S), along foreland (Pampean segment flat area) the shortening rates range from 0.5 ± 0.1 mm/yr to 0.8 ± 0.4 mm/yr (Rimando and Schoenbohm, 2020; and references there in). Meanwhile, The San Ramón Fault at (∼33°S) has a steep eastward dip, with an estimated total displacement of around 4 km (net thrust slip of approximately 5 km). The minimum average slip rate on this fault is about 0.2 mm/yr (5 km over 25 Myr), while the slip rate on the basal detachment of the frontal system is around 0.4 mm/yr (10 km over 25 Myr) (Armijo et al., 2010; Riesner et al., 2017). The southern domain (37–39°S) (sensu Rodriguez Piceda et al., 2020), a minimum growth rate of approximately 0.18 ± 0.07 mm/yr has been estimated on the Huépil fault (at 37°) for the central section of a fault-propagation anticline (Melnick, Charlet, et al., 2006). Instead, in the Antiñir-Copahue Fault Zone (ACFZ) in the easternmost part of this latitude, along the Reñileuvú section, which represents the central sector of the ACFZ, about 0.5–0.8 km of shortening has occurred since 1.2 ± 0.1 Ma at an average shortening rate of 0.5 ± 0.2 mm/yr (Colavitto et al., 2020). Thus, the likely steep dip angle of the thrust faults in the west could promote more vertical displacement and less horizontal shortening, resulting in higher uplift rates. The higher shortening rates in the east (ranging from 0.3 mm/yr to 0.7 mm/yr) suggest a greater degree of horizontal shortening and compression than in the west promoted by a rigid block in the east.

Finally, these factors collectively contribute to the complex tectonic framework observed in the region, interacting with surface processes to shape the landscape and influence the distribution of relative tectonic activity. Understanding these deep-seated controls is crucial for developing a

comprehensive model of orogen evolution in this segment of the Andes.

6.3 Methodological Contributions

The research demonstrates the power of integrating multiple geomorphic indices (Smf, Vf, NRA, THi*) to unravel tectonic versus climatic impacts on landscape evolution. By isolating lithologic-climatic signals from tectonic ones, the study provides a more nuanced understanding of the factors shaping the WAF. The normalized relief area (NRA) is a significant metric for measuring long-term accumulated incision. In chapter 2, we demonstrated that this technique has potential for describing the landscape in terms of incision and uplift, especially when used alongside valley shapes (Vf index) to differentiate incision patterns in mountain fronts (e.g., WAF). By employing established tools such as swath profiles (SwathProfiler, Pérez-Peña et al., 2017), we integrated relative areas with segments to determine the sinuosity of the mountain front. While previous researchers have used this metric to measure incision with the local relief curve e.g., (Masek et al., 1994; Molin et al., 2004; Azañón et al., 2015), it had not been reported as a method for defining segments across various tectonic-climate driven scenarios.

However, a caveat is necessary: although NRA measures incision, it can be significantly influenced by climate and lithology. Therefore, it should be compared with other metrics (e.g., Oviedo-Reyes et al., 2024) to ensure its relevance. When integrated with other indices, this metric proved to be a powerful tool for identifying areas with active tectonics and understanding possible relationships between uplift and erosion rates, as shown in comparison with the Iat/RTA maps. Nevertheless, it is only applicable to the mountain front. This tool allowed us to conclude that the internal mountain front, controlled by the San Fabián and Loma Linda faults, represents a landscape with a signature of tectonic-fluvial coupling.

On the other hand, by using the Smf/Vf relationship, additional evidence was provided to the hypothesis described by Silva et al. (2003), demonstrating the potential of morphometric indices to decipher spatial patterns of faulting styles. By describing two trajectories of logarithmic curves over the data collected for the study area, it was possible to identify that both clusters corresponded to particularities in the mountain front traces, specifically describing individual NNE and NW faults. It is evident that the structural style seems to influence the values of both metrics. Furthermore, by using the logarithmic curves, we can additionally describe the evolution of valley shapes as tectonic activity wanes and differentiate the types of shapes that can be found in each mountain front.

Considering this control, it was possible to compare the structural style defined in some segments of the WAF through the literature or image interpretations (e.g., DEM, Landsat, Google Earth) with

that determined by this method. With high precision (excluding some fronts without Vf information), similarities were recognized. The NNE trajectory describes reverse faults with a lateral component, while the NW trajectory describes strike-slip faults with a normal component. This match between the morphometric information and the structural style is significant and should be further explored due to its application in areas with uncertain deformation styles. However, its potential must be verified and compared with other information (e.g., structural and geophysical data) to ensure the method's relevance. Nonetheless, this hypothesis is advanced by adding information from other regions worldwide (e.g., El Hamdouni et al., 2008; Pérez-Peña et al., 2010; Giaconia et al., 2012; Özkaymak and Sözbilir, 2012; Yıldırım, 2014; Saber et al., 2018; Rimando and Schoenbohm, 2020; García-Delgado and Velandia, 2020; Sançar, 2021), which reveal marked trends and promise to be a fruitful field of research in the future.

6.4 Uplift Rates and Deformation Patterns

Based on the morphometric analysis (chapters 2 and 3) along the Western Andean Front, an area of interest for detailed studies was identified. The site's relevance was determined by several key factors: the location of tectonically active areas based on active tectonics classes, information documented in the literature such as the active fault map (e.g., Maldonado et al., 2021), and field evidence indicating the potential of the identified areas. From this perspective, it was decided that the area between San Fabián de Alico and Catillo would be the focus for morphotectonic mapping. This zone includes two major rivers, Perquilauquén and Ñuble, which drain to the NW, a Quaternary strip delimited by an internal mountain front and linear scarp.

The fluvial systems of central Chile exhibit varying rates of incision and uplift, reflecting complex tectonic and geomorphological processes. In the Maipo and Mapocho Rivers (Rauld Plott, 2011), incision rates range from 0.06 to 0.98 mm/yr (Table 6.1), with higher rates observed at the mountain front and decreasing upstream. These relatively moderate rates suggest a stable tectonic deformation during the Pleistocene and Holocene. In contrast, the Ñuble and Perquilauquén Rivers to the south show significantly higher and more variable rates. The Ñuble River, influenced by the San Fabián Fault (SFF), experienced rapid incision of up to 5.07±0.37 mm/yr during the Late Pleistocene, decreasing to 1.86±0.14 mm/yr in the Holocene. This dramatic change implies a shift in tectonic or climatic forcing. The Perquilauquén River maintained a high incision rate of 2.41±0.21 mm/yr during the Late Pleistocene. Uplift rates along the Cachapoal Fault (CAF) derived from scarp OSL dating vary considerably in north-south direction, from 0.89±0.06 mm/yr in Catillo sector, 0.36±0.04 mm/yr in the Zemita area to 1.71±0.22 mm/yr at the Nahueltoro scarp, indicating spatial variability

in tectonic activity. These disparities between river systems highlight the heterogeneous nature of tectonic deformation in central Chile, with the southern rivers suggesting a nuanced tectonic deformation compared to San Ramon fault in the sectors of Maipo-Mapocho (Rauld Plott, 2011). The higher rates in the Ñuble-Perquilauquén area may be attributed to the complex interaction of strike-slip faulting, pull-apart basin formation, and differential uplift along fault segments, creating a more tectonically landscape.

Table 6.1: Comparison between structural domains along Western Andean Thrust.

Region	**Fault System**	**Incision Rate (mm/year)**	**Uplift Rate (mm/year)**	**Slip Rate (mm/year)**	**Deformation Style**
Maipo-Mapocho	San Ramón	0.06-0.98	0.2-0.4	N.D.	Reverse faulting (compressive)
Los Andes	Cariño-Botado Fault (CBF)	∼0.1	0.4-1.2	0.6-1.9	Reverse faulting (compressive)
Ñuble-Perquilauquén	SFF.CAF	1.86-5.07 (Ñuble) 2.41 (Perquilauquén)	0.36-1.71 (CAF)	N.D.	Compressional strike-slip faulting

To the north, in the Cariño-Botado Fault (CBF) area, near the Aconcagua River, estimated incision rates are approximately 0.1 mm/year in the Principal Cordillera, based on ∼100 m incision over ∼0.9 Ma. This rate is comparable to the ∼0.15 mm/year calculated for the Maipo River near Santiago. However, the CBF itself shows significantly higher activity, with estimated slip rates between ∼0.6 and ∼1.9 mm/year and tectonic surface uplift rates of ∼0.4 to ∼1.2 mm/year over the last ∼8.7 ka. These rates are derived from a ∼4.9 m slip along a fault dipping ∼40°E, resulting in a ∼3.2 m vertical offset (Estay et al., 2023). Stalder et al. (2020) demonstrated that the western flank of the Andes in the Principal Cordillera (32-36°S) experienced significant changes in erosion rates over time. During the late Miocene to late Pliocene, this region exhibited relatively low erosion rates ranging from 0.1 to 0.25 mm/year. However, a dramatic shift occurred in the Pleistocene, when erosion rates increased substantially, exceeding 2 mm/year.

Interestingly, this acceleration in erosion rates lagged behind a period of intense surface uplift. The major uplift event occurred between 10.5 and 4.6 million years ago, as reported by Farías et al. (2008). The spike in erosion rates followed approximately 2 million years after the conclusion of this uplift phase. This temporal relationship suggests a complex interplay between tectonic uplift and subsequent erosional processes, with a significant delay between the two phenomena. Also, Stalder et al. (2020) argues that the observed phenomena can be attributed to a complex interplay of glacial erosion, intensified precipitation, isostatic rock-uplift, and active tectonics. The influence of glacial processes on landscape evolution emerges as a critical factor when interpreting incision rates in this region. As detailed in chapter 3, glacial impacts have been documented as far north as 36°S latitude, establishing a crucial geographical context for examining the incision rates associated

with the San Fabian fault terraces.

The location of these terraces, south of the 36°S glacial limit, suggests they have likely escaped significant glacial modification. This positioning offers a unique advantage for interpreting incision rates, as it implies that the observed rates predominantly reflect fluvial processes rather than a combination of fluvial and glacial erosion. This distinction is vital for accurately understanding the tectonic and geomorphic processes at work in the region. Furthermore, this scenario strengthens the hypothesis proposed by Oviedo-Reyes et al. (2024) that the preserved landscape represents a coupling between tectonics and incision. This coupling allows for the inference that the observed erosion rates are equivalent to uplift rates, providing a more direct measure of tectonic activity in the area.

However, it's important to consider the possibility of glacial influence extending further south than currently documented. If evidence of glacial erosion is found south of 36°S, it would necessitate a reevaluation of the calculated data. In such a case, the high incision rates observed (e.g., 5.07±0.37 mm/yr) could align with the range proposed by Stalder et al. (2020) for the period between 30-13 ka, suggesting a more widespread glacial influence on landscape evolution in the region.

Leaving aside the aforementioned limitations, the style of faulting in the Ñuble River and Perquilauquén sector plays a crucial role in understanding the calculated incision and uplift rates. The data suggests that the San Fabian fault is an active fault corresponding to an internal mountain front, its activity modulated by the accommodation of the northwest-trending Ñuble river fault. The deformation exerted by this front, combined with the obliquity of the compression, forms a pull-apart basin. This tectonic configuration implies that the deformation is concentrated both in the internal mountain front and the range-bounding fault. The resulting rhomb graben is oblique to the maximum horizontal stress (SH_{max}) calculated for the San Fabian Fault (SFF).

Extending this maximum stress tensor into Quaternary times (oblique shortening), this tectonic setup potentially creates local stress variations due to the flexing of the hanging wall anticline, which could result in crestal grabens, as proposed by Philip and Meghraoui (1983) in similar tectonic settings. However, it is important to note that this interpretation is a hypothesis based on the available data, and further research is needed to conclusively demonstrate this mechanism in the study area.

Capítulo 7

Conclusions

Conclusions

This doctoral thesis investigates the neotectonic activity and landscape evolution of the Western Andean Front (WAF) between 35°S and 38°S in central Chile. Through an integrated approach combining geomorphological analysis and quantitative landscape assessment, this research provides crucial insights into the tectonic, climatic, and erosional processes shaping this dynamic region. The following conclusions summarize the key findings, highlighting significant contributions to our understanding of Andean tectonics, fault kinematics, and the complex interactions between climate and tectonics in mountain building processes. These results have important implications for regional seismic hazard assessment and broader applications in tectonic geomorphology.

1. **Tectonic Transition:** A distinct morphotectonic segmentation was identified around 36°S in the Western Andean Front (WAF), revealing significant variations in Quaternary tectonic activity. North of 36°S, less active tectonics and climate-driven processes dominate, while the southern region exhibits active uplift and transient topography. This transition is evidenced by marked contrasts in multiple quantitative geomorphic indices, including normalized relief area, valley morphology, tectonic classes, and hypsometric variations. The study also uncovered previously unidentified active structures, such as the Mesamávida fault extension. This segmentation provides crucial insights into the differential tectonic processes influencing the Andean landscape evolution, with significant implications for regional seismic hazard assessment and our understanding of the complex interactions between climate, tectonics, and topography in orogenic mountain fronts.

2. **Fault Kinematics:** The study identified two primary fault kinematic trends in the Western Andean Front (WAF): NNE-striking reverse faults with strike-slip components and NW-striking strike-slip to oblique faults. This pattern supports a model of strain partitioning in a transpressional regime, with a distinct north-south neotectonic activity transition centered at 36°S. The distinction between these fault types is corroborated by Smf/Vf logarithmic regression analysis, revealing different trends for NW and NNE-striking faults. NW-striking faults, associated with the western termination of the Cortaderas lineament, show more tectonic activity and fluvial downcutting, while NNE-striking faults facilitate deformation via thrusting. This finding is crucial for understanding the complex tectonic framework of the WAF, providing valuable insights into deformation mechanisms and offering an effective proxy for inferring faulting kinematics where subsurface data is limited. The results are consistent with regional

field observations and tectonic models, supporting the idea of a transpressional regime with strain partitioning.

3. **Geomorphic Indices:** The integration of multiple geomorphic indices proved effective in distinguishing tectonic signals from climatic and lithological influences. However, the study emphasizes the need for cautious interpretation, especially of the Ksn index, which is primarily driven by climatic and lithological factors rather than tectonics alone. This comprehensive approach is crucial in areas like the Western Andean Front, where the tectonic activity classes derived from Iat reveal that a majority of the basins exhibit moderate tectonic activity (77.21%) with significant portions showing high tectonic activity (20.58). The more detailed RTA index also supports these findings, showing that most of the region falls under moderate tectonic activity (65.08%). Both indices highlight that zones of high and very high tectonic activity (e.g., Huepil and San Fabian areas) localized and associated with specific structural features (e.g., Huépil and Cachapoal faults), Confirming the convergence of tectonic signals at key intersections of NNE-NW faults. Despite lithological and climatic influences, these indices offer valuable preliminary insights into areas with potential for detailed neotectonic studies.

4. **Orogenic Processes Reflected in Landscape Morphometry:**The complex tectonic framework in the study area is driven by several deep-seated mechanisms, including variations in subduction angles, lithological heterogeneities, and crustal composition. The transition from flat to normal subduction at 33°S, slab tearing near 38°S, and localized uplift due to asthenospheric upwelling all contribute to the observed tectonic deformation. High-density crust in the northern and southern domains behaves more rigidly, concentrating stress along faults and influencing the distribution of deformation. These mechanisms collectively explain the spatial patterns of relative tectonic activity, highlighting the interaction between deep orogenic processes and surface deformation in this segment of the Andes.

5. **Glacial Imprint:** The research extended the understanding of glacial imprint on topography southward to 36°S, highlighting the complex interplay between tectonic and climatic forces in shaping the WAF landscape. This finding necessitates a dual perspective in analyzing morphometric index variations: glacial northward and fluvial erosion southward. The recognition of this glacial influence is crucial for accurately interpreting landscape features and understanding the relative roles of climate and tectonics in landscape evolution across different latitudes of the study area.

6. **Uplift Rate Variations:** Significant temporal and spatial variations in uplift rates were

quantified, particularly along the San Fabian Fault (SFF). Temporally, uplift rates decreased from 5.07 $\pm$ 0.37 mm/yr between 30-13 ka to 1.86 $\pm$ 0.14 mm/yr in the last 13 ka. Spatially, areas like the Nahueltoro sector (36°30'S) show higher Quaternary elevated areas compared to adjacent regions like the Zemita sector. These variations indicate a dynamic tectonic uplifting where deformation patterns have changed over the Quaternary period, providing crucial information for understanding long-term fault behavior and seismogenic potential.

Referencias

Abraham, E., Rodríguez, M., Rubio, M., Guida-Johnson, B., Gomez, L., & Rubio, C. (2020). Disentangling the concept of "south american arid diagonal". *Journal of Arid Environments*, *175*, 104089.

Alvarez-Garreton, C., Mendoza, P., Boisier, J., Addor, N., Galleguillos, M., Zambrano-Bigiarini, M., Lara, A., Puelma, C., Cortes, G., Garreaud, R., et al. (2018). The camels-cl dataset: Catchment attributes and meteorology for large sample studies–chile dataset. *Hydrology and Earth System Sciences*, *22*(11), 5817–5846.

Ammirati, J., Vargas, G., Rebolledo, S., Abrahami, R., Potin, B., Leyton, F., & Ruiz, S. (2019). The crustal seismicity of the western andean thrust (central chile, 33°–34° s): Implications for regional tectonics and seismic hazard in the santiago area. *Bulletin of the Seismological Society of America*, *109*(5), 1985–1999.

Angermann, D., Klotz, J., & Reigber, C. (1999). Space-geodetic estimation of the nazca-south america euler vector. *Earth and Planetary Science Letters*, *171*(3), 329–334.

Angster, S., Sherrod, B., & Lasher, J. (2020). Constraining the paleoseismic record on the wallula fault in southeastern washington from widespread liquefaction features: Nice scarp, where's the fault..? *AGU Fall Meeting Abstracts*, *2020*, EP031–0004.

Armijo, R., Rauld, R., Thiele, R., Vargas, G., Campos, J., Lacassin, R., & Kausel, E. (2010). The west andean thrust, the san ramon fault, and the seismic hazard for santiago, chile. *Tectonics*, *29*(2).

Asch, G., Schurr, B., Bohm, M., Yuan, X., Haberland, C., Heit, B., Kind, R., Woelbern, I., Bataille, K., Comte, D., et al. (2006). Seismological studies of the central and southern andes. *The Andes: Active Subduction Orogeny*, 443–457.

Azañón, J., Galve, J., Pérez-Peña, J., Giaconia, F., Carvajal, R., Booth-Rea, G., Jabaloy, A., Vázquez, M., Azor, A., & Roldán, F. (2015). Relief and drainage evolution during the exhumation of the sierra nevada (se spain): Is denudation keeping pace with uplift? *Tectonophysics*, *663*, 19–32.

Azor, A., Keller, E., & Yeats, R. (2002). Geomorphic indicators of active fold growth: South mountain–oak ridge anticline, ventura basin, southern california. *Geological society of america bulletin*, *114*(6), 745–753.

Bishop, P. (2007). Long-term landscape evolution: Linking tectonics and surface processes. *Earth Surface Processes and Landforms: the Journal of the British Geomorphological Research Group*, *32*(3), 329–365.

Bohm, M., Lüth, S., Echtler, H., Asch, G., Bataille, K., Bruhn, C., Rietbrock, A., & Wigger, P. (2002). The southern andes between 36 and 40 s latitude: Seismicity and average seismic velocities. *Tectonophysics*, *356*(4), 275–289.

Bookhagen, B., & Strecker, M. (2008). Orographic barriers, high-resolution trmm rainfall, and relief variations along the eastern andes. *Geophysical Research Letters*, *35*(6).

Brigham, C. A., & Crider, J. (2022). A new metric for morphologic variability using landform shape classification via supervised machine learning. *Geomorphology*, *399*, 108065.

Bull, W. (2007). *Tectonic geomorphology of mountains: A new approach to paleoseismology*. John Wiley & Sons.

Bull, W. (2011). *Tectonically active landscapes*. John Wiley & Sons.

Bull, W., & McFadden, L. (1977). Tectonic geomorphology north and south of the garlock fault, california. In *Geomorphology in arid regions* (pp. 115–138). Routledge.

Bullard, T., & Lettis, W. (1993). Quaternary fold deformation associated with blind thrust faulting, los angeles basin, california. *Journal of Geophysical Research: Solid Earth*, *98*(B5), 8349–8369.

Burbank, D., & Anderson, R. (2011). Tectonic geomorphology.

Bursztyn, N., Pederson, J., Tressler, C., Mackley, R., & Mitchell, K. (2015). Rock strength along a fluvial transect of the colorado plateau–quantifying a fundamental control on geomorphology. *Earth and Planetary Science Letters*, *429*, 90–100.

Cahill, T., & Isacks, B. L. (1992). Seismicity and shape of the subducted nazca plate. *Journal of Geophysical Research: Solid Earth*, *97*(B12), 17503–17529.

Camafort, M., Gràcia, E., & Ranero, C. (2020). Quaternary seismostratigraphy and tectonosedimentary evolution of the north tunisian continental margin. *Tectonics*, *39*(11), e2020TC006243.

Cannon, P. (1976). Generation of explicit parameters for a quantitative geomorphic study of the mill creek drainage basin."

Carretier, S., Tolorza, V., Regard, V., Aguilar, G., Bermúdez, M. A., Martinod, J., Guyot, J., Hérail, G., & Riquelme, R. (2018). Review of erosion dynamics along the major ns climatic gradient in chile and perspectives. *Geomorphology*, *300*, 45–68.

Cembrano, J., & Lara, L. (2009). The link between volcanism and tectonics in the southern volcanic zone of the chilean andes: A review. *Tectonophysics*, *471*(1-2), 96–113.

Charrier, R., Iturrizaga, L., Carretier, S., & Regard, V. (2019). Geomorphologic and glacial evolution of the cachapoal and southern maipo catchments in the andean principal cordillera, central chile (34°-35º s). *Andean Geology*, *46*(2), 240–278.

Chen, Y., Sung, Q., & Cheng, K. (2003). Along-strike variations of morphotectonic features in the western foothills of taiwan: Tectonic implications based on stream-gradient and hypsometric analysis. *Geomorphology*, *56*(1-2), 109–137.

Cheng, K., Hung, J., Chang, H., Tsai, H., & Sung, Q. (2012). Scale independence of basin hypsometry and steady state topography. *Geomorphology*, *171*, 1–11.

Cisternas, M., Atwater, B. F., Torrejón, F., Sawai, Y., Machuca, G., Lagos, M., Eipert, A., Youlton, C., Salgado, I., Kamataki, T., et al. (2005). Predecessors of the giant 1960 chile earthquake. *Nature*, *437*(7057), 404–407.

Clementucci, R., Ballato, P., Siame, L. L., Faccenna, C., Yaaqoub, A., Essaifi, A., Leanni, L., & Guillou, V. (2022). Lithological control on topographic relief evolution in a slow tectonic setting (anti-atlas, morocco). *Earth and Planetary Science Letters*, *596*, 117788.

Clubb, F., Mudd, S., Schildgen, T., van der Beek, P., Devrani, R., & Sinclair, H. (2023). Himalayan valley-floor widths controlled by tectonically driven exhumation. *Nature Geoscience*, *16*(8), 739–746.

Colavitto, B., Sagripanti, L., Jagoe, L., Costa, C., & Folguera, A. (2020). Quaternary tectonics in the southern central andes (37°-38° s): Retroarc compression inferred from morphotectonics and numerical models. *Journal of South American Earth Sciences*, *102*, 102697.

Cortés, J., González, G., Binnie, S., Robinson, R., Freeman, S., & Vargas, G. (2012). Paleoseismology of the mejillones fault, northern chile: Insights from cosmogenic 10be and optically stimulated luminescence determinations. *Tectonics*, *31*(2).

Cortes-Aranda, J., Sepulveda, T., Vega, A., Arriagada, D., Aguilera, R., Melnick, D., Espinoza, M., Oviedo, A., Tassara, A., Riedel, M., et al. (2021). The mesamavida fault: A seismogenic fault in the western andean front (waf), central chile (36s). *AGU Fall Meeting Abstracts*, *2021*, T45D–0258.

Costa, C., Audemard, F., Bezerra, F., Lavenu, A., Machette, M., & París, G. (2006). An overview of the main quaternary deformation of south america. *Revista de la Asociación Geológica Argentina*, *61*(4), 461–479.

Costa, C., Murillo, M., Sagripanti, G., & Gardini, C. (2001). Quaternary intraplate deformation in the southeastern sierras pampeanas, argentina. *Journal of Seismology*, *5*, 399–409.

Cressie, N. (1990). The origins of kriging. *Mathematical geology*, *22*, 239–252.

Croissant, T., & Braun, J. (2014). Constraining the stream power law: A novel approach combining a landscape evolution model and an inversion method. *Earth surface dynamics*, *2*(1), 155–166.

Dehbozorgi, M., Pourkermani, M., Arian, M., Matkan, A., Motamedi, H., & Hosseiniasl, A. (2010). Quantitative analysis of relative tectonic activity in the sarvestan area, central zagros, iran. *Geomorphology*, *121*(3-4), 329–341.

Delvaux, D., & Sperner, B. (2003). New aspects of tectonic stress inversion with reference to the tensor program. *Geological Society, London, Special Publications*, *212*(1), 75–100.

Demoulin, A. (1998). Testing the tectonic significance of some parameters of longitudinal river profiles: The case of the ardenne (belgium, nw europe). *Geomorphology*, *24*(2-3), 189–208.

Densmore, A., Gupta, S., Allen, P., & Dawers, N. (2007). Transient landscapes at fault tips. *Journal of Geophysical Research: Earth Surface*, *112*(F3).

Diederix, H., Torres, E., García, L., & Oviedo, J. (2010). Neotectónica del piedemonte llanero entre los municipios de tauramena, monterrey y villanueva (casanare). *INGEOMINAS, Bogotá, Colombia*, 118.

Diercks, M.-L., Mildon, Z., Boulton, S., Hussain, E., Alçiçek, M., Yıldırım, C., & Aykut, T. (2023). Constraining historical earthquake sequences with coulomb stress models: An example from western türkiye. *Journal of Geophysical Research: Solid Earth*, *128*(11), e2023JB026627.

Dixon, H. J., Murphy, M., Sparks, S., Chavez, R., Naranjo, J., Dunkley, P., Young, S., Gilbert, J., & Pringle, M. (1999). The geology of nevados de chillán volcano, chile. *Revista geológica de Chile*, *26*(2), 227–253.

Eisermann, J., Göllner, P., & Riller, U. (2021). Orogen-scale transpression accounts for gps velocities and kinematic partitioning in the southern andes. *Communications Earth & Environment*, *2*(1), 167.

El Hamdouni, R., Irigaray, C., Fernández, T., Chacón, J., & Keller, E. (2008). Assessment of relative active tectonics, southwest border of the sierra nevada (southern spain). *Geomorphology*, *96*(1-2), 150–173.

Ellis, M., & Barnes, J. (2015). A global perspective on the topographic response to fault growth. *Geosphere*, *11*(4), 1008–1023.

Encinas, A., Sagripanti, L., Rodríguez, M. P., Orts, D., Anavalón, A., Giroux, P., et al. (2021). Tectonosedimentary evolution of the coastal cordillera and central depression of south-central chile (36° 30 -42° s). *Earth-Science Reviews*, *213*, 103465.

Erbello, A., Melnick, D., Zeilinger, G., Bookhagen, B., Pingel, H., & Strecker, M. (2022). Geomorphic expression of a tectonically active rift-transfer zone in southern ethiopia. *Geomorphology*, *403*, 108162.

Estay, J., Pinto, L., Easton, G., De Pascale, G., Troncoso, M., Carretier, S., & Forman, S. (2023). Active thrust tectonics along the western slope of the central andes southernmost pampean flat-slab segment (33° s, chile): The cariño botado fault system. *Geomorphology*, *437*, 108801.

Farías, M., Charrier, R., Carretier, S., Martinod, J., Fock, A., Campbell, D., Cáceres, J., & Comte, D. (2008). Late miocene high and rapid surface uplift and its erosional response in the andes of central chile (33–35 s). *Tectonics*, *27*(1).

Farías, M., Comte, D., Charrier, R., Martinod, J., David, C., Tassara, A., Tapia, F., & Fock, A. (2010). Crustal-scale structural architecture in central chile based on seismicity and surface geology: Implications for andean mountain building. *Tectonics*, *29*(3).

Flint, J. (1974). Stream gradient as a function of order, magnitude, and discharge. *Water Resources Research*, *10*(5), 969–973.

Folguera, A., Ramos, V., Hermanns, R., & Naranjo, J. (2004). Neotectonics in the foothills of the southernmost central andes (37–38 s): Evidence of strike-slip displacement along the antiñir-copahue fault zone. *Tectonics*, *23*(5).

Folk, R. (1954). The distinction between grain size and mineral composition in sedimentary-rock nomenclature. *The Journal of Geology*, *62*(4), 344–359.

Forte, A., & Whipple, K. (2019). The topographic analysis kit (tak) for topotoolbox. *Earth Surface Dynamics*, *7*(1), 87–95.

Gaidzik, K., & Ramírez-Herrera, M. (2017). Geomorphic indices and relative tectonic uplift in the guerrero sector of the mexican forearc. *Geoscience Frontiers*, *8*(4), 885–902.

Gansser, A. (1973). Facts and theories on the andes: Twenty-sixth william smith lecture. *Journal of the Geological Society*, *129*(2), 93–131.

Gao, M., Hao, M., Zeilinger, G., & Xu, X. (2023). Recent uplift characteristics of the southeast tibetan plateau, an analysis based on fluvial indices. *Remote Sensing*, *15*(2), 433.

García-Delgado, H., & Velandia, F. (2020). Tectonic geomorphology of the serranía de san lucas (central cordillera): Regional implications for active tectonics and drainage rearrangement in the northern andes. *Geomorphology*, *349*, 106914.

Gelabert, B., Fornós, J., Pardo, J., Rosselló, V., & Segura, F. (2005). Structurally controlled drainage basin development in the south of menorca (western mediterranean, spain). *Geomorphology*, *65*(1-2), 139–155.

Giaconia, F., Booth-Rea, G., Martínez-Martínez, J., Azañón, J., Pérez-Peña, J., Pérez-Romero, J., & Villegas, I. (2012). Geomorphic evidence of active tectonics in the sierra alhamilla (eastern betics, se spain). *Geomorphology*, *145*, 90–106.

Giambiagi, L., Mescua, J., Heredia, N., Farias, P., Garcia Sansegundo, J., Fernandez, C., Stier, S., Perez, D., Bechis, F., Moreiras, S., et al. (2014). Reactivation of late paleozoic structures during the cenozoic deformation in the cordón del plata range and southern precordillera (mendoza, argentina).

González, G., Cembrano, J., Carrizo, D., Macci, A., & Schneider, H. (2003). The link between forearc tectonics and pliocene–quaternary deformation of the coastal cordillera, northern chile. *Journal of South American Earth Sciences*, *16*(5), 321–342.

Graham, D., & Midgley, N. (2000). Graphical representation of particle shape using triangular diagrams: An excel spreadsheet method. *Earth Surface Processes and Landforms*, *25*(13), 1473–1477.

Hack, J. (1973). Stream-profile analysis and stream-gradient index. *Journal of Research of the us Geological Survey*, *1*(4), 421–429.

Hare, P., & Gardner, T. (1985). Geomorphic indicators of vertical neotectonism along converging plate margins, nicoya peninsula, costa rica. w: M. morisawa, jt hack (red.), tectonic geomorphology. *Proc. 15th Annual Binghaton Geomorphology Symposium*.

Harlin, J. (1978). Statistical moments of the hypsometric curve and its density function. *Journal of the International Association for Mathematical Geology*, *10*, 59–72.

Harries, R., Aron, F., & Kirstein, L. (2023). Climate aridity delays morphological response of andean river valleys to tectonic uplift. *Geomorphology*, *437*, 108804.

Hodgkinson, J., McLoughlin, S., & Cox, M. (2006). The influence of geological fabric and scale on drainage pattern analysis in a catchment of metamorphic terrain: Laceys creek, southeast queensland, australia. *Geomorphology*, *81*(3-4), 394–407.

Holbrook, J., & Schumm, S. (1999). Geomorphic and sedimentary response of rivers to tectonic deformation: A brief review and critique of a tool for recognizing subtle epeirogenic deformation in modern and ancient settings. *Tectonophysics*, *305*(1-3), 287–306.

Howard, A. (1994). A detachment-limited model of drainage basin evolution. *Water resources research*, *30*(7), 2261–2285.

Huang, J., Hales, T., Huang, R., Ju, N., Li, Q., & Huang, Y. (2020). A hybrid machine-learning model to estimate potential debris-flow volumes. *Geomorphology*, *367*, 107333.

Ikeda, Y. (1983). Thrust-front migration and its mechanism: Evolution of intraplate thrust fault systems. *Bull. Dept. Geogr., Univ. Tokyo*, *15*, 125–159.

Isacks, B. (1988). Uplift of the central andean plateau and bending of the bolivian orocline. *Journal of Geophysical Research: Solid Earth*, *93*(B4), 3211–3231.

Jewell, P. (2016). Quantitative identification of erosional lake bonneville shorelines, utah. *Geomorphology*, *253*, 135–145.

Keller, E., & Rockwell, T. (2022). Tectonic geomorphology of mountain fronts.

Keller, E., & Pinter, N. (2002). *Active tectonics earthquakes, uplift, and landscape* (Vol. 2). second ed. Prentice Hall, London.

Keller, E. A. (1986). Investigation of active tectonics: Use of surficial earth processes. *Active tectonics*, *1*, 136–147.

Kendrick, E., Bevis, M., Smalley Jr, R., Brooks, B., Vargas, R., Lauria, E., & Fortes, L. (2003). The nazca–south america euler vector and its rate of change. *Journal of South American Earth Sciences*, *16*(2), 125–131.

Kirby, E., & Whipple, K. (2012). Expression of active tectonics in erosional landscapes. *Journal of structural geology*, *44*, 54–75.

Korup, O., Schmidt, J., & McSaveney, M. (2005). Regional relief characteristics and denudation pattern of the western southern alps, new zealand. *Geomorphology*, *71*(3-4), 402–423.

Krystopowicz, N., Schoenbohm, L., Rimando, J., Brocard, G., & Rojay, B. (2020). Tectonic geomorphology and plio-quaternary structural evolution of the tuzgölü fault zone, turkey: Implications for deformation in the interior of the central anatolian plateau. *Geosphere*, *16*(5), 1107–1124.

Lacoste, M., Lemercier, B., & Walter, C. (2011). Regional mapping of soil parent material by machine learning based on point data. *Geomorphology*, *133*(1-2), 90–99.

Lavenu, A., & Cembrano, J. (1999). Compressional-and transpressional-stress pattern for pliocene and quaternary brittle deformation in fore arc and intra-arc zones (andes of central and southern chile). *Journal of Structural Geology*, *21*(12), 1669–1691.

Li, M., Yin, X., Tang, B., & Yang, M. (2023). Accuracy assessment of high-resolution globally available open-source dems using icesat/glas over mountainous areas, a case study in yunnan province, china. *Remote Sensing*, *15*(7), 1952.

Li, T., Fuller, T., Sklar, L., Gran, K., & Venditti, J. (2020). A mechanistic model for lateral erosion of bedrock channel banks by bedload particle impacts. *Journal of Geophysical Research: Earth Surface*, *125*(6), e2019JF005509.

Lifton, N., & Chase, C. (1992). Tectonic, climatic and lithologic influences on landscape fractal dimension and hypsometry: Implications for landscape evolution in the san gabriel mountains, california. *Geomorphology*, *5*(1-2), 77–114.

López, G., Hatzfeld, D., Madariaga, R., Barrientos, S., Campos, J., Lyon-Caen, H., Zollo, A., Giannacone, G., & Kausel, E. (1997). Microsismicidad en la zona centro-sur de chile. *Actas del 7 ° Congreso Geológico de Chile*, *3*, 1771–1774.

Lupi, M., Trippanera, D., Gonzalez, D., D'amico, S., Acocella, V., Cabello, C., Stef, M., & Tassara, A. (2020). Transient tectonic regimes imposed by megathrust earthquakes and the growth of nw-trending volcanic systems in the southern andes. *Tectonophysics*, *774*, 228204.

Mahmood, S., & Gloaguen, R. (2012). Appraisal of active tectonics in hindu kush: Insights from dem derived geomorphic indices and drainage analysis. *Geoscience Frontiers*, *3*(4), 407–428.

Maldonado, V., Contreras, M., & Melnick, D. (2021). A comprehensive database of active and potentially-active continental faults in chile at 1: 25,000 scale. *Scientific data*, *8*(1), 20.

Marcotte, A., Neudorf, C., & Langston, A. (2021). Lateral bedrock erosion and valley formation in a heterogeneously layered landscape, northeast kansas. *Earth Surface Processes and Landforms*, *46*(11), 2248–2263.

Masek, J., Isacks, B., Gubbels, T., & Fielding, E. (1994). Erosion and tectonics at the margins of continental plateaus. *Journal of Geophysical Research: Solid Earth*, *99*(B7), 13941–13956.

Matoš, B., Pérez-Peña, J., & Tomljenović, B. (2016). Landscape response to recent tectonic deformation in the sw pannonian basin: Evidence from dem-based morphometric analysis of the bilogora mt. area, ne croatia. *Geomorphology*, *263*, 132–155.

Mejías Osorio, P., Cortés-Aranda, J., Salas, P., & Mardones, M. (2024). Glacial and volcanic landforms in the upper catchment of claro river, central chile (35.5° s): A late quaternary geomorphological case study. *Earth Surface Processes and Landforms*.

Melnick, D., Charlet, F., Echtler, H., & De Batist, M. (2006). Incipient axial collapse of the main cordillera and strain partitioning gradient between the central and patagonian andes, lago laja, chile. *Tectonics*, *25*(5).

Melnick, D., & Echtler, H. (2006). Morphotectonic and geologic digital map compilations of the south-central andes (36–42 s). In *The andes: Active subduction orogeny* (pp. 565–568). Springer.

Melnick, D., Rosenau, M., Folguera, A., & Echtler, H. (2006). Neogene tectonic evolution of the neuquén andes western flank (37–39 s).

Mere, A., & McPhillips, D. (2024). Fault activity in the san gabriel mountains, southern california, usa: Insights from landscape morphometrics, erosion rates, and fault-slip rates. *Geological Society of America Bulletin*.

Molin, P., Pazzaglia, F., & Dramis, F. (2004). Geomorphic expression of active tectonics in a rapidly-deforming forearc, sila massif, calabria, southern italy. *American journal of science*, *304*(7), 559–589.

Molnar, P., & England, P. (1990). Temperatures, heat flux, and frictional stress near major thrust faults. *Journal of Geophysical Research: Solid Earth*, *95*(B4), 4833–4856.

Montgomery, D., Balco, G., & Willett, S. (2001). Climate, tectonics, and the morphology of the andes. *Geology*, *29*(7), 579–582.

Montgomery, D., & Brandon, M. (2002). Topographic controls on erosion rates in tectonically active mountain ranges. *Earth and Planetary Science Letters*, *201*(3-4), 481–489.

Moreno, M., Melnick, D., Rosenau, M., Baez, J., Klotz, J., Oncken, O., Tassara, A., Chen, J., Bataille, K., Bevis, M., et al. (2012). Toward understanding tectonic control on the mw 8.8 2010 maule chile earthquake. *Earth and Planetary Science Letters*, *321*, 152–165.

Muñoz, N., & Charrier, R. (1996). Uplift of the western border of the altiplano on a west-vergent thrust system, northern chile. *Journal of South American Earth Sciences*, *9*(3-4), 171–181.

Nakata, T. (1989). Active faults of the himalaya of india and nepal.

O'Callaghan, J., & Mark, D. (1984). The extraction of drainage networks from digital elevation data. *Computer vision, graphics, and image processing*, *28*(3), 323–344.

Olivar, J., Nacif, S., García, H., Fennell, L., Heit, B., & Folguera, A. (2022). Controls on crustal seismicity segmentation on a local scale in the southern central andes. *Journal of South American Earth Sciences*, *116*, 103778.

Oviedo-Reyes, J., Cortés-Aranda, J., Fernandez, A., Perez-Peña, J., & Flores, L. (2024). Geomorphic signatures of neotectonic activity along the western andean front in the chilean andes (35° s to 37° s). *Earth Surface Processes and Landforms*.

Özkaymak, C., & Sözbilir, H. (2012). Tectonic geomorphology of the spildağı high ranges, western anatolia. *Geomorphology*, *173*, 128–140.

Panizza, M., Castaldini, D., Bollettinari, G., Carton, A., Mantovani, F., et al. (1987). Neotectonic research in applied geomorphological studies. *Zeitschrift für Geomorphologie. Supplementband*, *63*, 173–211.

Pedregosa, F., Varoquaux, G., Gramfort, A., Michel, V., Thirion, B., Grisel, O., Blondel, M., Prettenhofer, P., Weiss, R., Dubourg, V., et al. (2011). Scikit-learn: Machine learning in python. *the Journal of machine Learning research*, *12*, 2825–2830.

Pedrera, A., Galindo-Zaldívar, J., Ruiz-Bustos, A., Rodríguez-Fernández, J., & Ruiz-Constán, A. (2009). The role of small-scale fold and fault development in seismogenic zones: Example

of the western huércal-overa basin (eastern betic cordillera, spain). *Journal of Quaternary Science*, *24*(6), 581–592.

Pérez-Peña, J., Al-Awabdeh, M., Azan, J., Galve, J., Booth-Rea, G., & Notti, D. (2017). Swath-profiler and nprofiler. *Computers & Geosciences*, *104*(100), 135–150.

Pérez-Peña, J., Azañón, J., Azor, A., Delgado, J., & González-Lodeiro, F. (2009). Spatial analysis of stream power using gis: Slk anomaly maps. *Earth Surface Processes and Landforms*, *34*(1), 16–25.

Pérez-Peña, J., Azor, A., Azañón, J., & Keller, E. A. (2010). Active tectonics in the sierra nevada (betic cordillera, se spain): Insights from geomorphic indexes and drainage pattern analysis. *Geomorphology*, *119*(1-2), 74–87.

Peronace, E., Della, M., Troiani, F., Galli, P., Giaccio, B., Messina, P., & Fredi, P. (2018). Testing geomorphic signal of active normal faulting: The case of the cittanova fault (calabria, southern italy). *Earth Surface Processes and Landforms*, *43*(10), 2256–2270.

Pesicek, J. D., Engdahl, E. R., Thurber, C. H., DeShon, H. R., & Lange, D. (2012). Mantle subducting slab structure in the region of the 2010 m8.8 maule earthquake (30–40°s), chile. *Geophysical Journal International*, *191*(1), 317–324. https://doi.org/10.1111/j.1365-246X.2012.05624.x

Petit, J. (1987). Criteria for the sense of movement on fault surfaces in brittle rocks. *Journal of structural Geology*, *9*(5-6), 597–608.

Philip, H., & Meghraoui, M. (1983). Structural analysis and interpretation of the surface deformations of the el asnam earthquake of october 10, 1980. *Tectonics*, *2*(1), 17–49.

Piacentini, D., Troiani, F., Servizi, T., Nesci, O., & Veneri, F. (2020). Slix: A gis toolbox to support along-stream knickzones detection through the computation and mapping of the stream length-gradient (sl) index. *ISPRS International Journal of Geo-Information*, *9*(2), 69.

Price, B. N., Stansell, N., Fernández, A., Licciardi, J., Lesnek, A., Muñoz, A., Sorensen, M., Jaque Castillo, E., Shutkin, T., Ciocca, I., et al. (2022). Chlorine-36 surface exposure dating of late holocene moraines and glacial mass balance modeling, monte sierra nevada, south-central chilean andes (38° s). *Frontiers in Earth Science*, *10*, 848652.

Prizomwala, S., Solanki, T., Chauhan, G., Das, A., Bhatt, N., Thakkar, M., & Rastogi, B. (2016). Spatial variations in tectonic activity along the kachchh mainland fault, kachchh, western india: Implications in seismic hazard assessment. *Natural Hazards*, *82*, 947–961.

Qureshi, K., & Khan, S. (2020). Active tectonics of the frontal himalayas: An example from the manzai ranges in the recess setting, western pakistan. *Remote Sensing*, *12*(20), 3362.

Radaideh, O., & Mosar, J. (2019). Tectonics controls on fluvial landscapes and drainage development in the westernmost part of switzerland: Insights from dem-derived geomorphic indices. *Tectonophysics*, *768*, 228179.

Radic, J. (2010). Las cuencas cenozoicas y su control en el volcanismo de los complejos nevados de chillán y copahue-callaqui (andes del sur, 36-39 s). *Andean geology*, *37*(1), 220–246.

Ramírez-Herrera, M. (1998). Geomorphic assessment of active tectonics in the acambay graben, mexican volcanic belt. *Earth Surface Processes and landforms: The journal of the british Geomorphological Group*, *23*(4), 317–332.

Ramos, V. A., & Kay, S. (2006). Overview of the tectonic evolution of the southern central andes of mendoza and neuquén (35–39 s latitude).

Rauld Plott, R. (2011). Deformación cortical y peligro sísmico asociado a la falla san ramón en el frente cordillerano de santiago, chile central (33ºs).

Rehak, K., Bookhagen, B., Strecker, M., & Echtler, H. (2010). The topographic imprint of a transient climate episode: The western andean flank between 15 · 5 and 41 · 5 s. *Earth Surface Processes and Landforms*, *35*(13), 1516–1534.

Riesner, M., Lacassin, R., Simoes, M., Armijo, R., Rauld, R., & Vargas, G. (2017). Kinematics of the active west andean fold-and-thrust belt (central chile): Structure and long-term shortening rate. *Tectonics*, *36*(2), 287–303.

Riley, S., DeGloria, S., & Elliot, R. (1999). Index that quantifies topographic heterogeneity. *intermountain Journal of sciences*, *5*(1-4), 23–27.

Rimando, J., & Schoenbohm, L. (2020). Regional relative tectonic activity of structures in the pampean flat slab segment of argentina from 30 to 32 s. *Geomorphology*, *350*, 106908.

Rockwell, T., Keller, E., & Johnson, D. (1985). Tectonic geomorphology of alluvial fans and mountain fronts near ventura, california. *Tectonic Geomorphology. Proceedings of the 15th Annual Geomorphology Symposium. Allen and Unwin Publishers, Boston, MA*, 183–207.

Rodriguez Piceda, C., et al. (2020). Lithospheric density structure of the southern central andes constrained by 3d dataintegrative gravity modelling. *Int. J. Earth. Sci.* https://doi.org/10.1007/s00531-020-01962-1

Różycka, M., Jancewicz, K., Migoń, P., & Szymanowski, M. (2021). Tectonic versus rock-controlled mountain fronts–geomorphometric and geostatistical approach (sowie mts., central europe). *Geomorphology*, *373*, 107485.

Ruszkiczay-Rüdiger, Z., Fodor, L., Horváth, E., & Telbisz, T. (2009). Discrimination of fluvial, eolian and neotectonic features in a low hilly landscape: A dem-based morphotectonic analysis in the central pannonian basin, hungary. *Geomorphology*, *104*(3-4), 203–217.

Saber, R., Caglayan, A., & Isik, V. (2018). Relative tectonic activity assessment and kinematic analysis of the north bozgush fault zone, nw iran. *Journal of Asian Earth Sciences*, *164*, 219–236.

Sançar, T. (2021). Morphometric investigations on the nw bitlis-zagros mountain range (se turkey): Implications for the internal deformation of the western turkish-iranian plateau. *Journal of Asian Earth Sciences*, *216*, 104751.

Scheidegger, A. (1979). Orientationsstruktur der talanlagen in der schweiz. *Geographica Helvetica*, *34*(1), 9–15.

Schwanghart, W., & Scherler, D. (2014). Topotoolbox 2–matlab-based software for topographic analysis and modeling in earth surface sciences. *Earth Surface Dynamics*, *2*(1), 1–7.

Schwanghart, W., & Scherler, D. (2017). Bumps in river profiles: Uncertainty assessment and smoothing using quantile regression techniques. *Earth Surface Dynamics*, *5*(4), 821–839.

Scotti, V., Molin, P., Faccenna, C., Soligo, M., & Casas-Sainz, A. (2014). The influence of surface and tectonic processes on landscape evolution of the iberian chain (spain): Quantitative geomorphological analysis and geochronology. *Geomorphology*, *206*, 37–57.

Selby, M. (1980). A rock mass strength classification for geomorphic purpose: With tests from antarctica and new zealand. *Zeit. Geomorph., NF*, *24*, 31–51.

Sepúlveda, T., et al. (2019). Neotectónica y paleosismología de la falla mesamávida: Evidencia de actividad cuaternaria tardía del cabalgamiento andino occidental (watf) en la región del maule, chile central (36° s).

SERNAGEOMIN. (2003). Geological map of chile: Digital version 1:1.000.000.

Silva, P., Goy, J., Zazo, C., & Bardajı, T. (2003). Fault-generated mountain fronts in southeast spain: Geomorphologic assessment of tectonic and seismic activity. *Geomorphology*, *50*(1-3), 203–225.

Singer, B., Thompson, R., Dungan, M., Feeley, T., Nelson, S., Pickens, J., Brown, L., Wulff, A., Davidson, J., & Metzger, J. (1997). Volcanism and erosion during the past 930 ky at the tatara–san pedro complex, chilean andes. *Geological Society of America Bulletin*, *109*(2), 127–142.

Sklar, L., & Dietrich, W. (2004). A mechanistic model for river incision into bedrock by saltating bed load. *Water Resources Research*, *40*(6).

Sneed, E., & Folk, R. (1958). Pebbles in the lower colorado river, texas a study in particle morphogenesis. *The Journal of geology*, *66*(2), 114–150.

Sperner, B., & Zweigel, P. (2010). A plea for more caution in fault–slip analysis. *Tectonophysics*, *482*(1-4), 29–41.

Stalder, N., Herman, F., Fellin, M., Coutand, I., Aguilar, G., Reiners, P., & Fox, M. (2020). The relationships between tectonics, climate and exhumation in the central andes (18–36 s): Evidence from low-temperature thermochronology. *Earth-Science Reviews*, *210*, 103276.

Strahler, A. (1952). Dynamic basis of geomorphology. *Geological society of america bulletin*, *63*(9), 923–938.

Tarolli, P., & Mudd, S. (2020). *Remote sensing of geomorphology* (Vol. 23). Elsevier.

Troiani, F., Galve, J., Piacentini, D., Della Seta, M., & Guerrero, J. (2014). Spatial analysis of stream length-gradient (sl) index for detecting hillslope processes: A case of the gállego river headwaters (central pyrenees, spain). *Geomorphology*, *214*, 183–197.

Turowski, J., Hovius, N., Meng-Long, H., Lague, D., & Men-Chiang, C. (2008). Distribution of erosion across bedrock channels. *Earth Surface Processes and Landforms: The Journal of the British Geomorphological Research Group*, *33*(3), 353–363.

Vargas, G., Klinger, Y., Rockwell, T., Forman, S., Rebolledo, S., Baize, S., Lacassin, R., & Armijo, R. (2014). Probing large intraplate earthquakes at the west flank of the andes. *Geology*, *42*(12), 1083–1086.

Velandia Patiño, F. (2017). Cinemática de las fallas mayores del macizo de santander-énfasis en el modelo estructural y temporalidad al sur de la falla de bucaramanga. *Departamento de Geociencias*.

Virtanen, P., Gommers, R., Oliphant, T., Haberland, M., Reddy, T., Cournapeau, D., Burovski, E., Peterson, P., Weckesser, W., Bright, J., et al. (2020). Scipy 1.0: Fundamental algorithms for scientific computing in python. *Nature methods*, *17*(3), 261–272.

Wallace, R., et al. (1978). Geometry and rates of change of fault-generated range fronts, north-central nevada. *J. Res. US Geol. Surv*, *6*(5), 637–650.

Wells, S., Bullard, T., Menges, C., Drake, P., Karas, P., Kelson, K., Ritter, J., & Wesling, J. (1988). Regional variations in tectonic geomorphology along a segmented convergent plate boundary pacific coast of costa rica. *Geomorphology*, *1*(3), 239–265.

Whipple, K. (2009). The influence of climate on the tectonic evolution of mountain belts. *Nature geoscience*, *2*(2), 97–104.

Whipple, K., Hancock, G., & Anderson, R. (2000). River incision into bedrock: Mechanics and relative efficacy of plucking, abrasion, and cavitation. *Geological Society of America Bulletin*, *112*(3), 490–503.

Whittaker, A., Cowie, P., Attal, M., Tucker, G., & Roberts, G. (2007). Bedrock channel adjustment to tectonic forcing: Implications for predicting river incision rates. *Geology*, *35*(2), 103–106.

Willgoose, G., & Hancock, G. (1998). Revisiting the hypsometric curve as an indicator of form and process in transport-limited catchment. *Earth Surface Processes and Landforms: The Journal of the British Geomorphological Group*, *23*(7), 611–623.

Wobus, C., Tucker, G., & Anderson, R. (2006). Self-formed bedrock channels. *Geophysical Research Letters*, *33*(18).

Wobus, C., Whipple, K., & Hodges, K. (2006). Neotectonics of the central nepalese himalaya: Constraints from geomorphology, detrital 40ar/39ar thermochronology, and thermal modeling. *Tectonics*, *25*(4).

Wu, C., Tian, X., Xu, T., Liang, X., Chen, Y., Taylor, M., Jiang, M., & Teng, J. (2019). Deformation of crust and upper mantle in central tibet caused by the northward subduction and slab tearing of the indian lithosphere: New evidence based on shear wave splitting measurements. *Earth and Planetary Science Letters*, *514*, 75–83.

Yañez, G., Ranero, C., von Huene, R., & Díaz, J. (2001). Magnetic anomaly interpretation across the southern central andes (32°–34°s): The role of the juan fernández ridge in the late tertiary evolution of the margin. *J. Geophys. Res.*, *106*, 6325–6345. https://doi.org/10.1029/2000JB900337

Yáñez, G., Cembrano, J., Pardo, M., Ranero, C., & Selles, D. (2002). The challenger–juan fernández–maipo major tectonic transition of the nazca–andean subduction system at 33–34 s: Geodynamic evidence and implications. *Journal of South American Earth Sciences*, *15*(1), 23–38.

Yıldırım, C. (2014). Relative tectonic activity assessment of the tuz gölü fault zone; central anatolia, turkey. *Tectonophysics*, *630*, 183–192.

Zhang, L., Liang, S., Yang, X., & Gan, W. (2020). Landscape evolution of the eastern himalayan syntaxis based on basin hypsometry and modern crustal deformation. *Geomorphology*, *355*, 107085.

Zingg, T. (1935). Beiträge zur schotteranalyse. *Schweiz. Mineralog. Petrog. Mitt*, *15*, 39–140.

Zoback, M. (1992). First-and second-order patterns of stress in the lithosphere: The world stress map project. *Journal of Geophysical Research: Solid Earth*, *97*(B8), 11703–11728.